Role of Coupling Conditions for Pattern Formation in Excitable Media: Study of Atrial Fibrillation Mechanisms and Oscillator Arrays in the Belousov-Zhabotinsky Reaction

Dissertation

Dipl.-Ing. Claudia Lenk
Fachgebiet Physikalische Chemie/Mikroreaktionstechnik
Institut für Chemie und Biotechnologie
Fakultät für Mathematik und Naturwissenschaften
Technische Universität Ilmenau

1.Reviewer: Prof. Dr. J. Michael Köhler (TU Ilmenau)
2.Reviewer: Prof. Dr. Philipp Maaß (Universität Osnabrück)
3.Reviewer: Prof. Dr. Oliver Steinbock (Florida State University)

Date of submission: 10.01.2017
Date of defense: 07.06.2017

urn:nbn:de:gbv:ilm1-2017000238

Summary

In this work, the transition between regular and irregular patterns was studied in reaction-diffusion (RD) systems with the ability of pattern formation. The focus of this work lies on the role of the coupling conditions between two or more oscillators for the occurrence of the irregular states and the system-specificity of the mechanisms.

To address this issue, two specific RD systems were chosen: (i) the heart during atrial fibrillation (AF) and (ii) the Belousov-Zhabotinsky reaction (BZR). Numerical simulations of these systems have been performed on the basis of a standard generic model, the FitzHugh-Nagumo model, and system-specific models. Results are compared to experiments of the BZR on silica gels with spatially structured catalyst patterns and medical data from literature for AF studies.

Two mechanisms were studied, which are suggested to yield irregular patterns. The first mechanism, proposed by myself, consists of the interaction of two active sources located in separate regions. In dependence of the relation between the frequencies of the active sources, irregular patterns of different types occurred. One type is a general one, while three other types occurred only in either the generic model or the system-specific one. The proposed mechanism can explain the often episodic occurrence of AF, when considering frequency changes of one active source, which can move the system into the range of irregular patterns. The novel mechanism is relevant also for other RD systems where similar effects situations like detachment of waves and conduction blocks occur.

The second mechanism is based on the diffusive coupling of multiple oscillators. In this case, either a reduced coupling or heterogeneity are thought to cause irregular patterns. Irregular patterns were found in the weak coupling regime due to clusters of synchronized oscillators and the modified dynamics of coupled excitable units. Another type consists of wavefront break-up at the spot centers. The influence of the size, shape and coupling strength of the coupled units on the irregularities was investigated as well as the properties of the irregularities itself. These mechanisms are relevant also for chemical RD systems (e.g. PEM fuel cells) and biological systems as, e.g., the nerve, heart or pancreatic beta cells.

Zusammenfassung

Diese Arbeit beschäftigt sich mit dem Übergang zwischen regulären und irregulären Mustern in Reaktions-Diffusions (RD)-Systemen. Hierbei lag der Fokus der Untersuchung auf der Rolle der Kopplungsbedingungen zwischen mehreren Oszillatoren für das Auftreten des Übergangs und der Systemspezifität der zugrundeliegenden Mechanismen.

Zwei RD-Systeme wurden hierfür gewählt: (i) das Herz im Vorhofflimmer(VF)-zustand und (ii) die Belousov-Zhabotinsky-Reaktion (BZR). Numerische Simulationen dieser Systeme basierten auf einem Standard-RD-Modell, dem Fitzhugh-Nagumo-Modell, und verschiedenen systemspezifischen Modellen. Ergebnisse der Simulationen wurden mit selbstdurchgeführten Experimenten der BZR auf Silikatgelen sowie mit Literaturdaten zu medizinischen Studien des VF verglichen.

Zwei Mechanismen für den Übergang zu irregulären Mustern wurden studiert. Der erste, von mir vorgeschlagene Mechanismus basiert auf der Wechselwirkung zweier aktiver Quellen, welche räumlich separiert sind. In Abhängigkeit des Frequenzverhältnisses der Quellen konnten verschiedene Typen von irregulären Mustern identifiziert werden: ein generischer Typ und drei weitere Typen, welche nur im allgemeinen oder den systemspezifischen Modellen auftraten. Der vorgeschlagene Mechanismus kann das episodische Auftreten von VF erklären, indem Änderungen einer Quellenfrequenz das System in den Zustand irregulärer Muster bringen. Dieser neue Mechanismus ist nicht nur für VF sondern auch für RD-Systeme (BZR, Nervenzellen) relevant.

Der zweite untersuchte Mechanismus basiert auf der diffusiven Kopplung vieler Oszillatoren. In dieser Arbeit wurden irreguläre Muster im Bereich schwacher Kopplung gefunden, für welche als Ursache einerseits die reduzierte Kohärenz zwischen den gekoppelten Oszillatoren identifiziert wurde und andererseits die aufgrund der Kopplung veränderte Dynamik im Falle von anregbaren Einheiten. Ein weiterer Typ irregulärer Muster wird durch das Aufbrechen von Wellenfronten an den Oszillatoren verursacht. Der Einfluss der Größe, Form und Kopplungsstärke auf das Auftreten der irregulären Muster wurde untersucht sowie die Eigenschaften der Muster. Aufgrund der Generalität der identifizierten Mechanismen sind diese auch für andere chemische und biologische RD-Systeme wie PEM-Brennstoffzellen oder Herz-, Nerven- oder Bauchspeicheldrüsenzellen von Bedeutung.

Acknowledgement

This work would not be possible, if it were not supported by my supervisors, colleagues, relatives and friends. Thus, I want to take the opportunity here to thank all of them.
First of all, I want to thank my supervisors, Prof. J. M. Köhler and Prof. P. Maaß for their overall support, great supervision, motivation, advices and helpful suggestions until the very last minutes of completion of this work. In particular, the fruitful and profitable discussions about the work yielded an understanding of the results and helped keeping track of the overall goal of this work.
Dr. Mario Einax, Dr. Alexander Gross and Dr. Mike Günther did a great job in providing ideas, discussing results and giving advices how to handle problems and get finished with the thesis.
I want to thank, furthermore, Steffen Schneider and Frances Möller for their support and help in all questions related to technical equipment, laboratory work and set-up of experiments. For his support in all questions related to computation and using the high performance computing cluster I want to thank Henning Schwanbeck. Dagmar Böhme and Tilo Nicolai, I would like to thank for their help with all questions and problems, not only but in particular administrative-related. Dr. Arne Albrecht and Olaf Marufke, I thank for their support in all questions concerning the work in the laboratories in the Centre for Micro- and Nanotechnologies. Chirag Saraswati helped with the modification of images for better visibility and, partly, with movie production.
For the good working atmosphere, stimulating discussions and helpful advices and ideas I want to thank all my colleagues from the department of Theoretical Physics II (TUI), Physical Chemistry (TUI), Statistical Physics (Uni Osnabrück), Theoretical Physics I (TUI) and Micro- and Nanoelectronics (TUI), in particular, Dr. Hartmut Grille, Christian Trott, Lars Winterfeld, Dr. Thomas Hennig, Yvonne Richter, Dr. Jialin Cao, Dr. Dana Kürsten, Dr. Andrea Knauer, Dr. Nikunjkumar Visavelyia, Dr. Aniket Thete, Lars Hafermann, Prof. Erich Runge, Dr. Wichard Beenken, Dr. Markus Reinmöller, Felix Schwarz and Dr. Adam Williamson.
Special thanks I want to give to Dr. Anja Eisenhardt, Dr. Martin Körner, Dr. Marcel Himmerlich, Dr. Thomas Hänsel and Dr. Patrick Scholz not only for their support by reading drafts, discussing results, providing programs and funny coffee breaks but also for their friendship.

I gratefully acknowledge financial support by the Landesgraduiertenförderung Thüringen and the Carl-Zeiss-Stiftung.
Finally, but most importantly, I want to thank my family (my parents, parents-in-law, my sister and her family), for supporting me, motivating me, taking care of the kids and being there when necessary. Helena and Rosalie, I thank you for your patience and your understanding. Without the help, support and time, spend by my husband Steve Lenk, this work would have never been done and finished. Thank you!

Contents

List of Figures

List of Tables

List of abbreviations

RD Reaction-Diffusion

AF Atrial Fibrillation

BZR Belousov-Zhabotinsky reaction

FHN FitzHugh-Nagumo

TMV transmembrane voltage

AV atrio-ventricular

ECG electrocardiogram

APD action potential duration

CV conduction velocity

ERP effective refractory phase

BCL basic cycle length

FKN Field, Körös and Noyes

HH Hodgkin-Huxley

PEM polymer electrolyte membrane

PExM proton exchange membrane

CRN Courtemanche, Ramirez and Nattel

BOCF Bueno-Orovio, Cherry and Fenton

pBOCF BOCF model describing the physiological state of atrial tissue

rBOCF BOCF model describing the electro-physiologically remodelled state of atrial tissue

pBOCF-re variant of the pBOCF model with reduced excitability

FEM finite element method

FDM finite differences method

PDE partial differential equation

GUI graphical user interface

GPU graphical processing units

CPU central processing unit

PETSc Portable, Extensive Toolkit for Scientific Computation

t.u. time unit

PEG polyethylenglycolnumber behind denotes the molecular weight

PVP poly-vinylpyrrolidon

PVA poly-vinylalcohol

PSSS poly(sodium-p-styrene sulfonate)

PSS-co-PM poly(4-styrene sulfonic acid-co-maleic acid)-sodium salt

DLS Dynamic light scattering

EDX energy dispersive X-ray diffractometry

SEM scanning electron microscopy

UV-Vis refers to the ultraviolet to visible range of the wavelength spectrum

NMR nuclear magnetic resonance

FWHM full width half maximum

FFT fast Fourier transform

WL wave length WL=CV/ERP

CFAE complex fractionated atrial electrocardiograms

FIRM focal impulse and rotor modulation

LAO low amplitude oscillations

HAO high amplitude oscillations

RP Recurrence plots

AP action potential

List of symbols

Model related

ρ	density
u	variable of RD systems, activator, represents TMV or concentration of bromide
v	variable of RD systems, inhibitor,gating variable
$f(u, v_i)$, $g(u, v_i)$	reaction terms of RD systems
∇	spatial derivative $\partial/(\partial r)$
D_i	Diffusion coefficient, index denotes which variable/substance is diffusing
V_m	transmembrane voltage
I_i	ionic currents through the cell membrane, index denotes ion species
r_c	resistance across the cell membrane
C_m	capacitance of cell membrane
n, m, h	gating variables HH model with coefficients α_i, β_i
E_{ion}	Nernst potential of ion
g_{ion}	conductance of ion channel for certain ion species
$\alpha, \beta, \mu, \epsilon$	parameters of the Rovinsky model
h_0	acidity function
q	stoichiometric factor in the Rovinsky model
k_i	rate constants for chemical reactions in the Rovinsky model
A_R	concentration of $HBrO_3$ (Rovinsky model)
B_R	concentration of $CHBr(CHOOH)_2$ (Rovinsky model)
C_R	concentration of $Fe(phen)_3{}^{2+}$+$Fe(phen)_3{}^{3+}$ (Rovinsky model)
a, b, c	coefficients in the FHN model, influencing the refractory period, self-excitability and excitability
z	external stimulus in the FHN model
v, w, s	gating variables in the BOCF model
$\tau_i, v_\infty, w_\infty$	coefficients of the BOCF model (mainly time constants)
τ_{fi}	sodium channel conductance in BOCF model
$H(x)$	Heaviside step function

Simulation general

$u_a(x,t)$	functions of FEM
F, M, K	arrays of system of ordinary differential equations in FEM
h_s	step size in Euler method
pos	linear index of point in CUDA simulation
$\Delta x, \Delta y, \Delta t$	spatial or time discretisation step
N_g	number of grid points

general

M	concentration [mol/l]
T_1	NMR relaxation time
$\varphi(t)$	phase of time series
Φ	order parameter for phase coherence
$C(u_k, u_j)$	correlation
$f_{\max}$	maximal determined frequency in simulation area
v_i	wave front speed
SF	safety factor for wave propagation, above 0 waves can propagate
Q_S	source charge
Q_L	load charge
r_K	curvature radius of wave fronts
C	coupling strength

AF related

R, L, B	right or left part or bridge in simulation area for AF studies
w_B	width of bridge in simulation area for AF studies
κ	conductivity of tissue
f_1, f_2	frequency of primary (index 1) or secondary (index 2) pacemaker
f_{det}	frequency, above which detachment of waves from corners occurs in the FHN model
f_{lim}	frequency, above which pacing can not excite a propagating wave front for each stimulus
f_{cbl}	frequency, above which complete conduction block at the bridge occurs, i.e. no wave can pass the bridge
f_{sbl}	frequency, above which sustained conduction block at the bridge occurs, i.e. waves pass the bridge with a certain transfer rate
f_{tbl}	frequency, above which a transient conduction block occurs, which vanishes after some time
w_{cbl}	critical bridge width, below which waves cannot pass the bridge
Δs	distance between locations of two subsequent annihilations of waves
$\Delta s'$	distance a wave front can propagate before its annihilation
t_{tr}	time until the irregularity type III occurs after start of simulation

BZR related

$d_{\mathrm{BL}}, d_{\mathrm{diff}}$	width of boundary or diffusion layer, respectively
$\bar{b}, N_b \Delta b$	mean and width of uniform distribution for b parameter
r, A_s, U_s	radius, area and circumference of spot
Δr	increase of spot radius per row of array
a_s	side length of square spot
h_s, h_t	height of diamond-shaped (index d) or triangular (index t) spots
l, l_{th}	spot-to-spot distance: between spot centres for experiment or spot boundaries for simulations
Δl	increase of spot-to-spot distance for each row
N_s	number of spots in one row or column in array
N_d	number of applied Ferroin drops per spot in array
ΔN_d	increase of number of drops per row
V_d	volume of Ferroin droplet
c_F	concentration of Ferroin in spot
Δd	increase of spot diameter during experiment
b_c	b parameter, below which spots are self-excitable (oscillating) and above which spots are excitable
l_{crit}	spot-to-spot distance separating the strong from the weak coupling regime
l_{c1}	spot-to-spot distance separating the quiescent from the oscillating regime
l_{c1}	spot-to-spot distance, above which broadening of the frequency distribution occurs
AP	maximum value of action potential in comparison to resting state value

Introduction

Motivation

To handle the huge amount of information, permanently send by the organs of perception, the brain relies on the method of pattern recognition [1]. Patterns are represented by synchronized activation of regions of neurons. This method is so deeply implemented that sometimes pattern are recognized in unpatterned images as e.g. clouds, white noise or trees, monsters in the night [2, 3]. Typically the synchronization between neurons, i.e. recognized patterns, are destroyed to enable the generation of new patterns. The dysfunction, during which recognized patterns are not destroyed, is discussed as underlying mechanism of the disease schizophrenia [4]. Besides these failures, the pattern recognition is extremely successful, also because almost all surrounding systems generate patterns and structures, as, for example, the structure of leaves, patterns on skin or fur of animals or formation of stones. Thereby, objects are recognized by addressing certain categories to the detected pattern [1] as, e.g., an animal with four legs, fur, tail and barking is a dog while one with stripes and a longer neck describes a zebra. Patterns can be used to distinguish between systems. One can discriminate between individual zebras on the basis of their stripes or determine the tree to which a leave belongs on the basis of its structure. Furthermore, properties and dynamics of patterns, i.e. shape, regularity, composition, stability etc., yield information about the state and performance of the system and underlying mechanisms of their pattern formation [5–9]. Regular patterns are mainly associated with a stable state of the system, whereas destruction of regular patterns respectively irregular patterns often describe unstable states. For example, during the excitation of the heart, a planar wave propagates across the heart to initiate contraction, whereas irregular patterns with multiple waves, wave breaks and fragments are related with pathological cardiac fibrillation [10–12]. During embryo genesis only embryos are viable that evolve sufficiently regular structuring, as, e.g., during segmentation of the fruit fly or the formation of extremities in more complex organisms. In both examples the transition from regular to irregular patterns is connected with decreasing performance and stability of the systems. In other cases, the transition to more regular patterns, as, for example, a decreased heart rate variability is connected with pathological states as sepsis or encephalopathy [13, 14]. This transition will be studied in this work.

Many of the systems, mentioned so far, consist of many coupled oscillators like the coupled cells in the heart, brain or pancreas. Another biological system

relying on coupled oscillators is the protozoon Dictyostelium discoideum, a slime mold, which forms a multicellular compound in the case of lacking food [15]. Coupling of oscillators can yield an increase of efficiency due to coherent oscillations or suppression of chaotic dynamics and adjustability of reaction rates and conditions [16]. In this context, an array of small catalyst particles may be as efficient as a homogeneous area of catalyst with the same dimensions. Perturbations of the coupling, however, will have a strong influence on the system. In the case of the heart, they can lead to pathological states [17, 18]. Atrial fibrillation, for example, is thought to be sustained by the so-called 'gap-junction remodeling', which results in a decrease of coupling between the heart cells [19, 20]. Due to its importance for many systems, as, e.g. polymerization, chirping of crickets, the flashing of fireflies, the pancreatic beta cells or the heart, the influence of altered coupling of oscillators on the emergent patterns will be studied in this thesis.

Despite the diversity of systems exhibiting pattern formation and the various mechanisms underlying this pattern formation, most systems can be described in the frame of Reaction-Diffusion (RD) systems. The coupling of an activator with an inhibitor with different time scales or reaction rates describes the pattern formation process. This process is formulated in terms of reaction equations, in particular, of rate equation type. Additionally, the diffusion or propagation of activator and inhibitor is taken into account for spatial systems. Thus, in mathematical terms, the description of reaction-diffusion systems is based on coupled differential equations describing the temporal evolution of activator and inhibitor. The number of equations, involved parameters and exact form of the reaction terms depends on the considered system, thus describing different properties and behaviors. Heart cells, for example, exhibit a restitution behavior, which describes the change of conduction velocity and frequency of excitation waves for increased pacing frequencies. Furthermore, the shape of the excitation pulse differs in different systems. Sawtooth shaped pulses are observed in the Belousov-Zhabotinsky reaction (BZR), whereas pulses with spike-and-dome form, comprising a sharp peak followed by a plateau, are generated by cardiac cells. There are, however, properties which are present in all RD systems, as for example the refractory phase, describing the time after the initiation of an excitation during which the systems cannot be excited again. The analysis of generic and system specific features of pattern formation will be another objective of this work.

Specifically, two different systems will be studied in this thesis. The first system will be the heart during Atrial Fibrillation (AF). The heart cells are an excitable medium [21], whose excitation is triggered by the sinus node as pacemaker. Disturbances of the excitation propagation across the heart may result in diverse diseases as, for example, atrial flutter, excitation block at the atrio-ventricular node, ventricular fibrillation or sudden cardiac death. Atrial fibrillation is the most common arrhythmia of the heart in clinical practice and the major cardiac cause of stroke [22, 23], whose prevalence increases with

the age [24, 25]. During AF, irregular excitation patterns are observed in the atria, resulting in desynchronized and uncontrolled contraction, which can be observed as fast, uncontrolled movement of the atria, resembling shivering or trembling. This decreases the output of the heart and enables the generation of blood clots, which are the reason for the increased risk of stroke.

Due to the complexity of biologic systems like the heart and their challenging experimental accessibility, systems, which can be more easily adjusted, are used to gain an understanding of the occurring processes. Recently a 3D plasma system was developed just for this purpose [26]. In this work, the BZR in structured gel systems is the second system for study. The BZR is an oscillating, chemical reaction and the standard example of pattern formation in chemical systems [27, 28]. Pattern formation can be studied quite well in chemical systems, since the influencing parameters can be controlled relatively easily. The emerging patterns resemble patterns in biological systems, enabling thus the study of pattern formation in biological systems by investigating chemical RD systems.

With these systems the previously raised questions, i.e. transition between regular and irregular state, influence of coupling between oscillators and the differentiation between generic and system-specific effects, will be studied.

Thus, the scientific objective of this work is to study mechanisms responsible for the transition from regular to irregular patterns. Thereby, systems composed of multiple coupled oscillators will be considered and the mechanisms will be analyzed according to their system specificity or generality. To address this objective, two specific RD systems are chosen. Investigations are based on numeric calculations, experiments and results from medical studies. The comparison of the results obtained from the different methods and systems allows the discussion of system specificity and generality.

In part I RD systems and principle mechanisms of pattern formation will be introduced in general, followed by the presentation of the two chosen, specific RD systems (AF and BZR) and the mathematical description of RD systems. In part II the numeric and experimental methods are described as well as the methods used for time series and pattern analysis. In part III results about investigations of local, passive coupling of multiple oscillators (system BZR) and of active coupling between two oscillators (system AF) are presented and discussed. The thesis will be concluded by a summary and outlook.

Part I:
Reaction-Diffusion (RD) systems

Chapter 1

General description

Systems with the ability of pattern formation are often described as Reaction-Diffusion (RD) systems. Here, one or more spatially confined but temporally dynamic reactions are combined with spatial propagation, mainly diffusion. RD systems are extremely diverse and observed in many different research fields. In chemistry the Belousov-Zhabotinsky reaction [29, 30] and catalysis of carbon monoxide at a platinum catalyst [31, 32] are popular examples as well as propagation of electrical excitations in physiology, population dynamics [33] or segmentation of a fruit fly embryo in biology. By now, the inhibitor-activator principle combined with diffusive signal spread, which is the underlying mechanism of RD systems, is applied to many more processes, as for examples plankton dynamics [34], spread of forest fires [35], the functioning of the brain [36] or the spread of epidemics[37].

The term pattern is in general used in a relatively broad context. In biology, one discriminates between internal patterns, like calcium waves in the cell [40], and external patterns as the stripe or dots on the skin or fur of animals [41]. More general, the term pattern is used for an observed order in a system. Emerging patterns are divided into dynamic, according to temporal and/or spatial variations of the system, or static/stationary ones, which are temporal or spatial constant, 'freezed', due to the reaction process. These 'freezed' patterns, i.e. stabilization of afore temporal or spatial dynamic patterns, are usually termed structures. Examples are the stripes of zebras or tigers [42], structures of snails or sea shells [43, 44], segments of the fruit fly embryo [45] or the structures on leaves [46]. The term morphogenesis is often used for the generation of structures. Artificial freezing of patterns can be done by precipitation of reactants [47], for example. Spatial and temporal dynamic patterns are, amongst others, the propagation of sand dunes[48], the growth direction of sunflowers or maize [49], the conversion rate at fuel cells [50], self-organized patterns of gas discharges[26] or social interactions [51, 52]. A special case of dynamic patterns are the so-called Turing patterns [7]. Here, stable, spatial patterns are observed, although reactant transport is ongoing, which can be furthermore temporally changing. Yamaguchi *et al.* [53] showed that

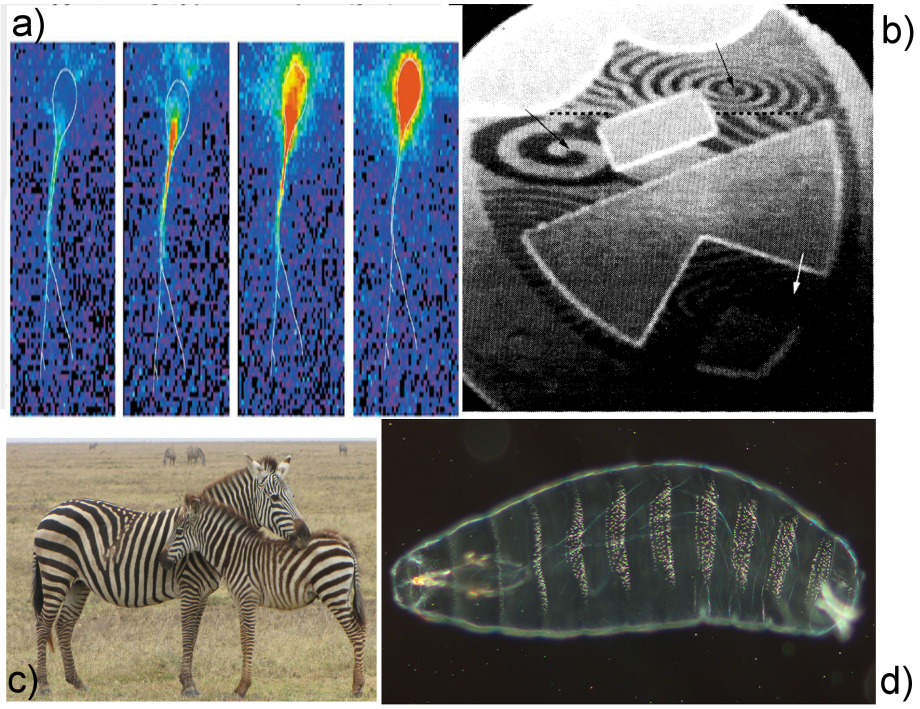

Figure 1.1: Examples of patterns formed in different systems. a) calcium waves in a pyramidal neuron cell (pictures taken from [38]) b) CO oxidation at the Pt catalyst [39] c) stripes of the zebra (by D. Gordon E. Robertson) d) segmentation of the fruit fly embryo.

a disturbance of the stripes of the zebra fish by laser ablation of the pigment cells results in a slow change of the stripe pattern. That means, the stripes, although appearing stationary, are maintained by temporal dynamic processes. In Fig. 1.1 some examples of patterns are shown. Thereby, segments of the fruit fly embryo[1] [Fig. 1.1 d)] and the stripes of the zebra [Fig. 1.1 c)] are examples of stationary patterns, whereas the CO waves during CO oxidation at the Pt catalyst [Fig. 1.1 b)] and calcium waves inside neurons [Fig. 1.1 a)] are dynamical patterns.

Pattern formation is considered in general as a dynamic, self-organizing process, resulting in the formation of periodic patterns. Usually, it is assumed that a phase transition occurs, during which the initially homogeneous state of the system becomes unstable [54, 55]. Thereby, self-organization can occur in the thermodynamic equilibrium, like in the case of micelles or membrane formation, or far away from the equilibrium, which is the case for living systems. For processes far away from the equilibrium energy is consumed and the total entropy of the system increases. The pattern itself can be connected with a local decrease of entropy.

[1] https://upload.wikimedia.org/wikipedia/commons/thumb/2/2b/DrosophilaKutikula.jpg/220px-DrosophilaKutikula.jpg

Alan Turing, after which the Turing patterns are named, first described the pattern formation processes in the scheme of reaction-diffusion processes. In his 1952 published work, 'the chemical basis of morphogenesis' [7], he states that morphogenesis in homogeneous systems can be described by the combination of simple, known physical processes. He recognized that three requirements are necessary for pattern formation: first, two morphogenes are needed, which, secondly, interact with each other and, third, whose diffusion coefficients strongly differ. This is often summarized by short range positive feedback with long range inhibition. This means that an activator (first morphogen) is required, which is self-enhancing (i.e. auto-catalytic). Thus, a small increase of the activator concentration results in a large increase of the activator concentration, which is described as positive feedback. Furthermore, the activator is inhibited by an inhibitor (2nd morphogen), which prevents the strong increase of the activator. The inhibitor diffuses much faster than the activator and acts thus on a longer range. In dependence of the rates of activation, inhibition and diffusion, different patterns can occur. In this model, no pre-patterning is necessary as in previously used descriptions of pattern formation. There, pattern formation was addressed to diffusion of morphogenes from a pre-pattern. This so-called gradient model is a special case of the Turing model for vanishing reaction terms.

Besides its elegance, the Turing model is lacking a biological base. Thus it was considered for a long time as irrelevant for biological systems. However, in 2006 Sick *et al.* [56] could show that the spatial distribution of hair follicles of a mouse is controlled by two substances (activator: WNT, inhibitor: DKK1) in analogy to Turing's model. Furthermore, evidence was found that the patterning of the hard palate in mammals is based on the Turing mechanism [57].

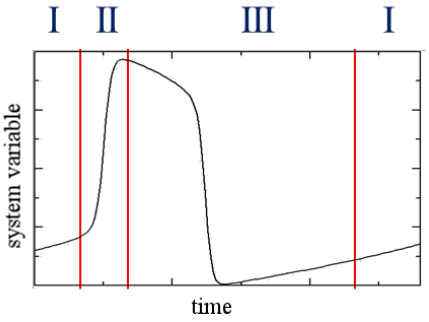

Figure 1.2: Phases of a temporal excitation pulse or action potential: I resting state (system is excitable), II activation (self-enhancement of activator), III inhibition (return to the resting state).

In the model of Turing spatial excitation pulses are generated (local peaks of activator). Temporal excitations are observed for certain ranges of reaction rates of activator and inhibitor as well as coupling between them. Temporal excitations which propagate due to diffusion will be named excitation pulses. In biological systems, in particular for heart cells or neurons, these excitation pulses are termed action potentials. The shape of excitation pulses differs in dependence of the considered system but can be subdivided into three phases

for all systems, as shown in Fig. 1.2. Phase I describes the resting state, i.e. the system is excitable. Activation occurs in phase II. Phase III describes the recurrence to the resting state.

One can differentiate between self-exciting and excitable systems. The first one exhibits an unstable resting state, thus, generating activations by itself. The second one requires a stimulus to initiate an excitation. The stimulus has to be larger than some threshold. If the threshold is overcome, the self-enhanced increase of activator starts. The strength and the speed with which the systems reacts to the stimulus are dependent on the excitability. Excitability can be tuned by the height of the threshold and the strength and speed of inhibition. The self-enhancement effect results in a strong increase of the activator related variable. With time delay the inhibition of the activators starts, thus decreasing the value of the activator variable. The relation between the reaction rates of activator and inhibitor thus determines the shape of the excitation pulse. Due to a higher number of inhibitors, reaction paths or coupling and feedback mechanisms, sub-phases can occur as the plateau phase for action potentials of heart cells. During activation and inhibition the system is refractory, i.e. it is not excitable at all (absolute refractory) or only for larger stimuli (relative refractory). This refractory phase ensures that pulses propagate only in one direction, which is in particular important for action potentials. The system has to return (almost) to the resting state before it can be excited again.

The diffusive instability described by Turing is only one of many mechanisms for pattern formation. The underlying mechanisms for formation of certain patterns comprise a spectrum as broad as the systems exhibiting pattern formation. Growth of systems [58] and their curvatures are discussed for example for the formation of fingerprints and wrinkles of raisins [59]. The geometry of the systems for wave propagation on active tissue [60–62] can yield attachment of waves to obstacles. Mechanical-chemical interaction is thought to underlie pattern formation in cell cultures on gel systems due to strain-stimulated cell traction [63]. Furthermore, in dependence of the distribution of parameters as, for example, gradients [64–68] or stochastic distributions [69, 70] irregular patterns can be generated. Which patterns evolve can be further tuned by choosing the appropriate, initial conditions [71]. A resonant pattern formation is possible by external feedback [72–76]. Further mechanisms are the interaction of multiple active sources [77–80], cross-diffusion [8, 81], i.e. the diffusion of one substance is influenced by the diffusion of another one, or heterogeneity respectively diversity [78, 82, 83]. This list of possible mechanisms for pattern formation is not complete and further informations can be found in a number of review articles, as e.g. [8, 9, 41, 71, 84–86].

Due to the generality and system specificity of RD systems, comparison of different points of view will be taken in this work to allow statements about the applicability of the respective approach. Therefore, two RD systems were chosen (AF and BZR) which, on one hand, can be described in a first approxima-

tion with the same generic mathematical model, the FitzHugh-Nagumo (FHN) model. On the other hand, system specific models will be used and their results will be compared with the FHN model. To decide, which approach is more suitable, experiments of the BZR are conducted and results of clinical studies and medical experiments are considered. In the next chapters the two systems will be described, including already studied mechanisms for the generation of AF and irregular patterns in the BZR. In this work two specific mechanisms supposed to generate irregular patterns will be studied in more detail in the two different systems.

Chapter 2

Human heart during atrial fibrillation

In this chapter, the human heart will be described in terms of RD system. Therefore, the term excitation in the context of the heart is specified and the excitable units (heart cells) as well as the propagation of excitation and the anatomy of the heart described. In the subsequent section, atrial fibrillation will be explained followed by a discussion of the mechanisms for the generation of AF studied so far in the literature. Based on that, a hypothesis for an AF generating mechanism will be derived, which is studied in this work.

2.1 Basic principles of the conduction system of the human heart

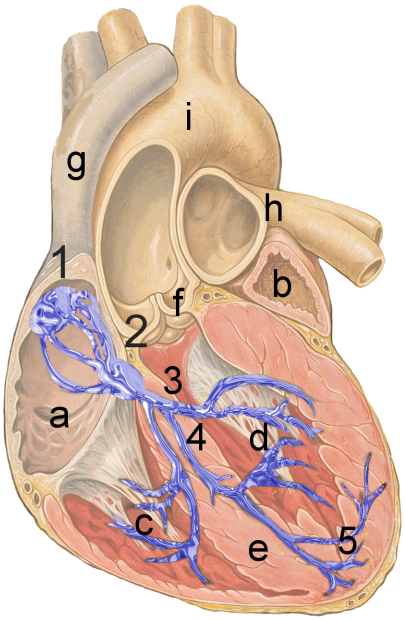

Figure 2.1: Anatomy of the human heart with conduction system (modification of original image by J. Heuser): a) right atrium, b) left atrium, c) right ventricle, d) left ventricle, e) cardiac septum, f) aortic valve, g) superior vena cava, h) pulmonary vein, i) aorta. Not shown are pulmonary artery, mitral and tricuspid valve (between atria and ventricles). The conduction system consists of 1: sinus node, 2: atrio-ventricular node, 3: His bundle, 5: Purkinje fibres.

The human heart (Fig. 2.1[1]) is a hollow organ, which is divided by the septum into a right and left half. Each half consists of an atrium with thin walls and a ventricle with thicker walls. The task of the heart is to pump blood for the pulmonary (right half) and body circulation (left half). It works as a lifting and forcing pump. Blood is pumped with high pressure into the vascular system or the connected ventricle by complete contraction of the ventricles and the atria, respectively. Relaxation of ventricles and atria results in a low pressure/depression. Thus, blood is sucked into the ventricles and the atria, filling them. As shown in Fig. 2.1, the hollow spaces (ventricles, atria) are connected by valves, which prevent reflux of the blood. For an efficient pumping, the tissue of one chamber as well as the various chambers together have to contract synchronously. The sequence of one heartbeat is as follows: first, blood flows into the atria, then the atria contract and thus press the blood into the ventricles. The ventricles contract subsequently and throw out the blood into the pulmonary or body arteries.

Heart tissue consists of myocytes, which can contract, and the fibroblasts, which constitute the extracellular matrix for the myocytes [21]. Mammalian myocytes are approximately cylindrical with a length in the range of 50-150 μm and a diameter of 10-20 μm [21]. The efficient rhythm and synchronisation of the chamber contraction is enabled due to triggering the synchronous contraction of myocytes by an excitation wave propagating across the heart. The excitation wave corresponds to a strong change of the transmembrane voltage (TMV) of the myocyte, named action potential (cf. chapter 1). The TMV or potential arises due to the inhomogeneous distribution of ions inside and outside of the myocyte. Ions can cross the membrane only through pores, called ion channels, or by ion exchange pumps. The structure of the cell membrane including pores and ion pumps is shown in Fig. 2.2.

Not only the work of ion pumps but also permeability of pores and, thus, the ion concentration are controlled by the TMV and other processes, as the attachment of specific proteins or enzymes. A small stimulus results only in a small change of TMV, in which case the membrane acts as a capacitor. A stimulus can be set by external electrodes, mechanical disturbances or the neighbouring cells, if they are activated already. A stimulus above a certain threshold results in a strong, non-linear change of the TMV, as shown in Fig. 2.3, by opening various ion channels. This change is caused initially by opening the sodium ion channels resulting in positive TMV of about +30mV (resting state is in the range of -80 to -90mV). With a time delay potassium channels open. Potassium flows in the opposite direction compared to sodium and acts as inhibitor. Sodium ion channels close if a certain value of the TMV is reached and the ongoing outward potassium flow in combination with the transport of sodium ions inside the cell by ion exchange pumps results in a slow return to the resting potential. Ion exchange pumps work thereby continuously

[1] modification of original image by J. Heuser,
https://commons.wikimedia.org/w/index.php?curid=1686121

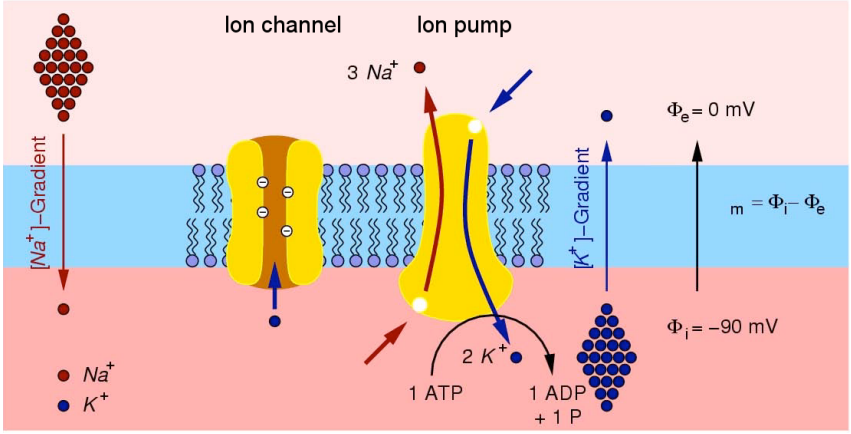

Figure 2.2: Sketch of the structure of the cell membrane showing the ion gradient, ion channel and ion pumps for exchanging sodium and potassium ions (modified from [87]).

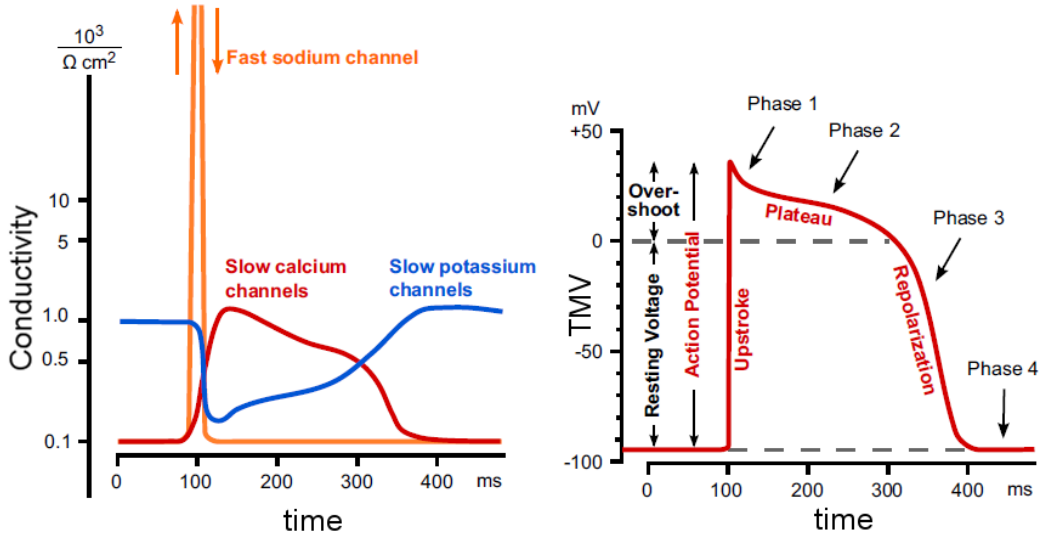

Figure 2.3: Left: Conductivity of ion channels during the course of an action potential. Right: Course of the TMV during an action potential divided into the phases: 'upstroke' = depolarisation (phase 1), plateau (phase 2), repolarization (phase 3), and resting potential (phase 4) (modified from [87]).

to maintain the resting TMV, but can be up- or down-regulated by various substances.

Beside myocytes, neuronal cells, muscle cells and secretory cells can exhibit action potentials to accomplish tasks as communication, contraction and segregation of substances. Depending on the type and place (e.g. atrium, ventricle, sinoatrial node) of a cell the shape of the action potential differs. It is controlled by the time constants for opening and closing of channels and the

number and type of participating ions. Action potentials on neurons typically are generated only by sodium and potassium ions. In the case of myocytes, more ions are involved, in particular calcium. Calcium channels are opened at the peak of the action potential. Thus an additional plateau phase occurs, which is characteristic for cardiac action potentials. The shape of the action potential is named as spike-and-dome.

To trigger the heartbeat synchronously, the action potential of one cell has to propagate in a certain order to the next cell. The development of an action potential is locally confined to one cell and described by the reaction term of the RD system. The transfer of the action potential to the next cell is described by a diffusion term, which can be derived from the cable equation by calculation of the external and internal cell potential under some assumptions. The internal and external potential of the cell is modified by the ion flux through the membrane and by internal or external currents. The currents flow only in longitudinal direction along the cells and axial direction inside the cell, respectively. The difference between internal and external potential is the TMV. The excitation wave propagating across the heart is generated by the interplay of the locally confined action potential and the propagation from cell-to-cell. The action potential transfer from cell-to-cell occurs along gap junctions, which are shown in Fig. 2.4. Gap junctions are channels build

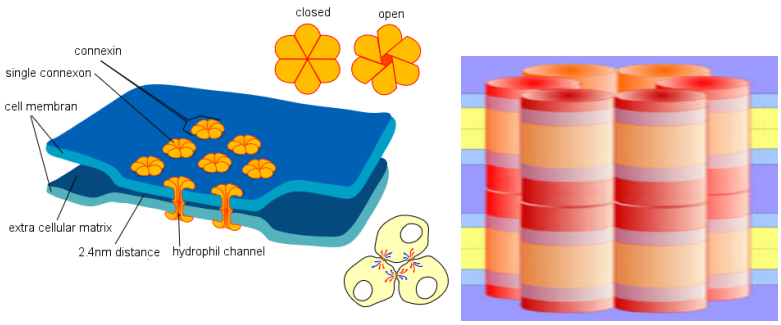

Figure 2.4: Left: scheme of cell-cell-connections via gap junctions, right: scheme of a connexon channel, constituting a gap junction (modified on the basis of image by Mariana Ruiz LadyofHats).

of protein complexes between membranes of neighbouring cells. Each cell contributes one half channel (connexon). Along the gap junctions ions and small molecules, as signal molecules or metabolites, can be exchanged very fast. They activate the neighbouring cell, which then opens their sodium channels to initialise an action potential [88–90]. The conduction velocity of excitation waves depends mainly on the number of gap junctions between the cells and differs in dependence of the place and type of cell. In the ventricular tissue longitudinal gap junctions, located at the longitudinal ends of the cell, are prevalent compared to transversal gap junction, which are located at the lateral membrane. Thus, a macroscopic anisotropy of electrical coupling occurs

[91]. Furthermore, the cylindrical myocytes tend to align along their main axis [21]. Thus a fibre orientation along the main axis of the cylinders can be defined. This anisotropy is enhanced by the alignment of cells into sheets with only a light coupling between different sheets and intersections by connective tissue. Additionally, there are special fibre bundles in the heart, as the Purkinje fibres or Bachmanns bundle, along which the conduction velocity is increased in comparison to normal myocyte tissue. The anisotropy in orientation of cells, coupling between them and between the sheets and the additional fast-conducting fibre bundles yields a strongly anisotropic conduction velocity of excitation waves in the heart. The arrangement of fibres and the corresponding conduction velocities are well determined for the ventricles by histology, optical techniques and diffusion tensor MRI [92–95]. However, there can be local deviations due to locally different expression rates and distributions of ion channels and gap junctions. The main feature of fibre orientation in the ventricles is a slow rotation by 180° from bottom to top. The arrangement and distribution of fibres in the atria is completely different [96–98] and due to increased complexity not yet completely determined experimentally. Thereby, the left atrium consists of a smooth wall but exhibits marked fibre structure changes intramurally. In contrast, an array of pectinate muscles dominates the structure of the right atrium [99].

Due to arrangement of fibres and the anisotropic conduction velocities the coordinated excitation of the heart is maintained. Thereby, the sinoatrial node, a cell compound of specialised, self-excitable cells, generates an excitation. The excitation waves spreads along the right atria. Due to the fast-conducting pathways, here Bachmanns bundle or the coronary sinus, the excitation is transferred to the left atrium almost without time-delay. Thus both atria are almost simultaneously activated and contract synchronously. At the bottom of the right atrium, the excitation wave hits the atrio-ventricular (AV) node, which conducts it to the His bundle and finally into the Purkinje fibres inside the septum of the ventricles. Direct excitation from atrium to ventricle is prevented by the non-excitable valves and septum between them. Purkinje fibres, located in the lower part of the septum with strong ramifications, conduct the excitation wave to the ventricles. The ventricles are thus excited from the bottom to the top and contract in this sequence resulting in a more efficient pumping of the blood into the arteries. A conduction of excitation from the ventricles to the atria is due to the refractory phase and the filter function of the AV node not possible. This secures that the pacing activity of the sinus node is the only excitation source, normally.

The propagation of the excitation wave and the resulting potential distribution can be measured by electrodes placed inside the heart or externally on the body surface, known as electrocardiogram (ECG) with the well-known ECG signal shown in Fig. 2.5 (left) including the common labelling of ECG phases. The excitation of the atria is represented by the P peak, the excitation of the ventricles by the R peak and the restitution of the excitation by the ST

segment. Changes of the excitation sequence due to diseases can be detected by modifications of the ECG signal course. The right part of Fig. 2.5 shows an ECG machine developed in 1911. Nowadays these are much smaller and include electrodes rather than water buckets. In the following chapter diseases of the heart, especially atrial fibrillation, are described.

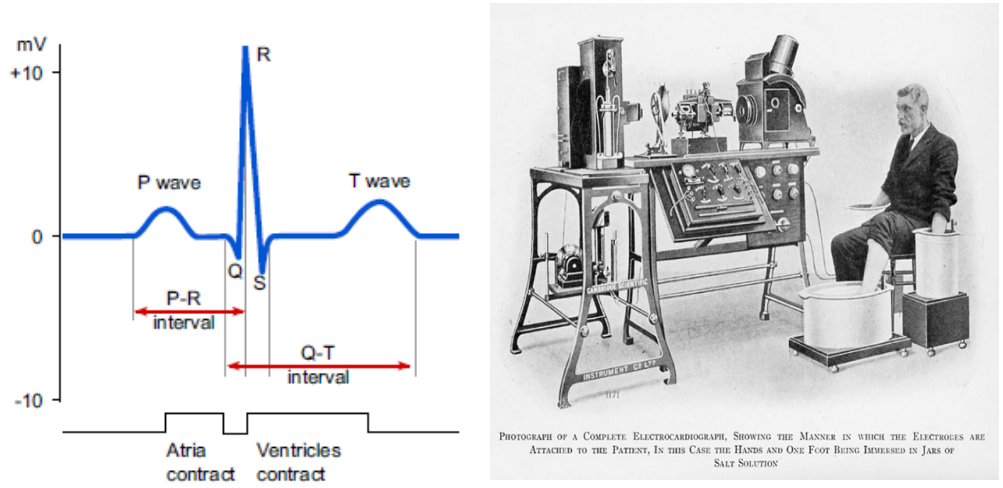

Figure 2.5: Left: scheme of an ECG signal with common labelling. P wave represents the excitation of the atria, R wave the excitation of the ventricles and the ST part the repolarization (modified from [87]). Right: ECG machine from Cambridge Scientific Instrument Company developed in 1911 (from [100]).

2.2 Atrial Fibrillation (AF)

Diseases of the heart are caused by a dysfunction of the electrical conduction, cell supply or the contraction system. One differentiates between

- heart muscle diseases as e.g. myocarditis and myocardial insufficiency combined with a cardiac hypertrophy,
- cardiac valve diseases, which are mainly caused by insufficient closing of the valves,
- coronary artery diseases and heart attack, which are caused by modifications of the blood vessels supplying the heart tissue, and
- arrhythmias, which are due to disturbances of the electrical conduction system.

Arrhythmias are perturbations of the regular heartbeat sequence. They are discriminated by the place of their origin (atrium, ventricle, electrical conduction system), the heart rate (bradycardia means frequency too low, tachycardia means frequency too high and arrhythmia describes irregular beats),

their origin (hereditary or acquired), the underlying mechanism (automaticity, re-entry, triggered), the duration (isolated premature beats, non-sustained or sustained) and the risk for the whole organism (benign, malignant, potentially life-threatening).

The most common arrhythmia in clinical practice is Atrial Fibrillation (AF). The estimated prevalence is increasing with the age of the person and is about 10% above an age of 80 years [25]. Its impact tends to increase due to the demographic development. During AF, irregular, uncoordinated activations with a rate up to 12 Hz are observed, resembling quivering. Thereby, regular excitations of the sinoatrial node do not yield a coordinated activation. The pumping capacity is only maintained by the AV node, acting as pacemaker and activating the ventricles with regular excitations. However, it is not clear in this case, whether the AV node generates excitation pulses, which it is capable of, or acts as a low-pass filter, which conducts only a part of the high-frequency excitation of the atria. It could be shown with conduction models of the AV node that the rate of excitations inside the atria can be calculated from the heartbeat distribution during AF [101, 102]. This supports the hypothesis that the AV node realizes a conduction and filter function. AF is not life-threatening, in contrast to ventricular fibrillation, since activations of the ventricles are regular but occur with a higher rate of approximately 2.5 Hz and the reduced pumping capacitance of the atria influences only slightly the total pumping capacitance of the heart.

Short episodes of AF lead to symptoms as irregular heartbeats, palpitations, fainting, perspiration, dyspnoea, restlessness, fear, exhaustion and/or chest pain. On the same time, AF increases the risk for the occurrence of other, partially life-threatening diseases as embolism[2] or stroke[3], for which the risk is increased by two to seven times [25]. Inefficient pumping of blood by the atria can cause blood clots. These can propagate with the blood flow, thus facilitating embolism or stroke. Furthermore, other serious cardiac diseases are promoted by AF. Persistent AF may cause congestive heart failure. If AF is treated by proper rhythm- or rate control, which describes the treatment of AF by drug or other therapies to control the heart rhythm or rate, respectively, an reduced insufficiency can be obtained [24].

AF is not only promoting other cardiac diseases, it can be caused by them, too [25]. The mechanisms discussed as reason are increased blood pressure in the atria or dilation of the atria. However, the exact mechanism is unclear. AF is classified into lone or idiopathic, if it occurs without other cardiac diseases, or sustained [24]. The term idiopathic AF is used for patients younger than 60 without clinical and echocardiographic symptoms of cardiac diseases, whose prognosis is quite well. Besides other cardiac diseases, there are further factors promoting AF as a previous stroke, hypertension, hyperthyroidism, diabetes mellitus, chronic obstructive pulmonary disease, paroxysmal nocturnal

[2]suddenly blocked vessels

[3]blocked vessels in the brain

dyspnea, vascular disease, genetic predisposition, high age, excessive alcohol consumption and overweight [103].

Atrial fibrillation is a chronic disease but initially occurs in episodes. These episodes end spontaneously within seven days, most often already within 24 h. This type of AF is named paroxysmal. Episodes can be triggered on the one hand by stress, heavy meals or exercise and on the other hand occur in the night or early morning during sleep [103]. Persistent AF is used for episodes not ending spontaneously within 7 days. The rhythm of the heart can be restored by electrical or drug therapy. If these therapies fail, the term permanent AF is used. Not only the individual therapy is based on the classification of AF but also different mechanisms are thought to generate and sustain the different types of AF.

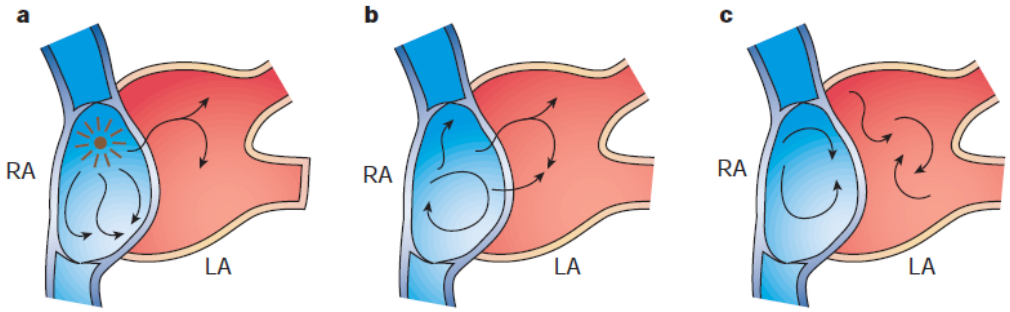

Figure 2.6: Three main theories of mechanisms generating or sustaining AF developed in the 1920s (from [104]). Single ectopic foci (a), single re-entry circuits as spiral waves (b) and multiple re-entry circuits (c) are discussed.

In Fig. 2.6 the three main theories on the generation and sustainment of AF developed already in the 1920s are shown. The theory of Lewis [105, 106] (Fig. 2.6 (a) and (b)) includes a mother wave, a re-entry circuit like a spiral wave, which acts as single, fast pacemaker. Irregular patterns arise due to the propagation of waves, emitted from the mother wave, and the anisotropic conduction properties of the atrium. In the theory of Engelmann, Rothberger and Winterberg [107–109] (Fig. 2.6 (a)) AF is generated on a similar mechanism. Here, one assumes an ectopic[4] focus instead of a re-entry circuit. An ectopic focus is a patch of cells, which are self-excitable like the cells in the sinoatrial node but occur at a different place in the atrium. As in the theory of Lewis, the propagation of waves emitted by the ectopic focus yields irregular patterns due to the anisotropic properties of the AF. In contrast to the single pacemaker, Garrey and Mines [110, 111] (Fig. 2.6 (c)) assumed multiple, simultaneously active re-entry circuits (e.g. spiral waves) emitting excitation waves. Thereby, the interaction between the different re-entry circuits results in the irregular patterns. In both theories including re-entry circuits, these circuits are only

[4]ectopic means 'not at the physiologically right place'

stable if their wave length is smaller than the extension of the tissue, in which it propagates. Additionally, the re-entry circuit has to be large enough to not self-terminate with its own refractory tail.

In 1962, Moe [112, 113] developed the concept of the multiple re-entry circuits further and presented the theory of multiple wavelets. In this theory, re-entry circuits do not necessarily have to be spatially stable, but can be a number of wavelets, i.e. wave fragments circulating around functionally refractory tissue. Functional refractory describes tissue, which is in principle excitable, but due to a permanent excitation refractory most of the time. Wavelets can be extinguished, if they cross a path of reduced excitability, sustain each other or generate so-called daughter wavelets, due to the interplay between each other. Fibrillation would be stable as long as a sufficient number of wavelets is stable.

Diverse experiments tried to reveal the underlying mechanism of the observed AF. Allesie *et al.* [114] studied dog hearts maintaining AF due to acetylcholine infusion and observed multiple wavelets supporting the theory of Moe *et al.* Ectopic activity acting as pacemaker of AF was shown by Haisaguerre *et al.* [115, 116]. Li [117] and Matsuo [118] identified hints for the existence of a mother wave. Concluding, each of the theories seems to describe AF in a certain situation. Thus it is worth to study which mechanism is connected with which situation.

The elucidation of mechanisms underlying the generation and perpetuation of AF is further complicated by the so-called atrial remodelling. This term describes the modification of cell behaviour and electro-physiological properties on organ, cell and molecular level due to the AF itself [20]. Amongst others, an enrichment of calcium inside the cell, a reduced conductivity of potassium channels as well as an altered arrangement and number of gap junctions occur. These result in a modified shape and duration of the action potential and a modified excitability and refractory phase. The typical regulation of high pacing frequencies, normally not sustained by the cells, is reduced and results in higher activation frequencies. Figure 2.7 shows the action potential duration (APD), conduction velocity (CV) and the effective refractory phase (ERP) calculated in the model of Bueno-Orovio, Cherry and Fenton [119] for physiological (black dots) and remodelled tissue (blue triangles). Thereby, the first cell in a linear cell strand is paced with different frequencies and APD, CV and ERP are determined at the last cell of this strand. Typically, the excitation wave cannot propagate for pacing frequencies above a critical frequency, since activation of neighbouring cells is not possible due to the larger refractory phase. This can be seen in Fig. 2.7 by the decrease of the APD and the CV to zero for decreasing basic cycle lengths (BCL), the latter being the inverse of the frequency. That means, action potentials are generated at the first cell (for 2.5Hz) but do not propagate to the last cell. For remodelled tissue (blue triangles), this frequency is strongly increased ($\approx$ 10 Hz). Thus, AF can be sustained or even promoted by the remodelling. The remodelling increases the

complexity and decreases the possibility of differentiation of AF generating mechanisms.

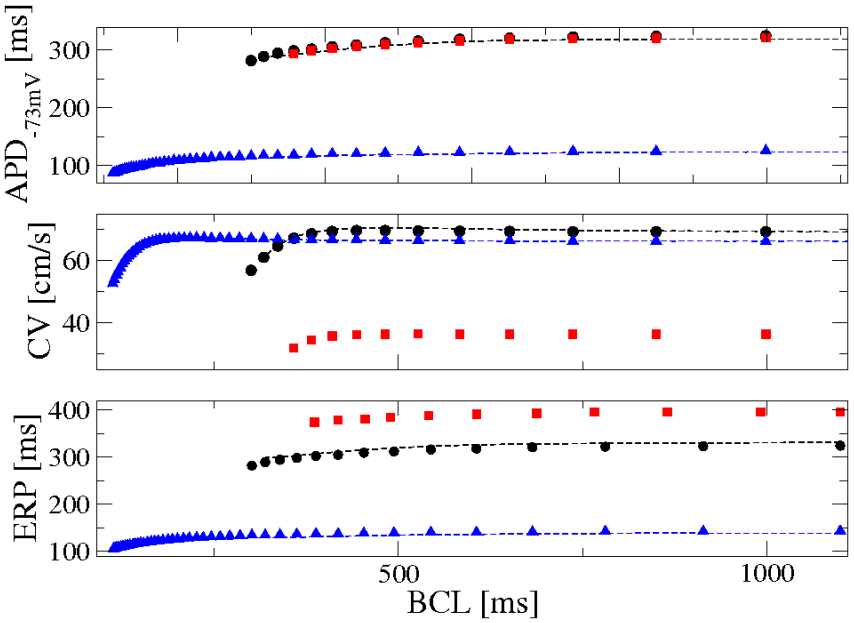

Figure 2.7: APD, CV and ERP of the last cell in a linear cell strand in dependence of the inverse frequency (BCL) of the first cell in comparison for two different states of the tissue: physiological (black) and remodelled (blue). Values are calculated with the BOCF model for atrial tissue with parameter sets according to the corresponding state of the cells. Pacing is observed only until a critical frequency of 2.5 Hz for physiological and 10 Hz for remodelled tissue [120].

The four discussed theories of the generation and perpetuation of AF are quite phenomenological. The sources/causes for the mechanisms were intensively studied in the past 50 years. Suggested were an increased excitability, an increased anisotropy of the atrial tissue or modified cell properties, to mention only a few. Their occurrence could be due to inherited or acquired mutations [121–123], diseases [124, 125], ageing of cells [126], oxidative stress [127], stretch of the tissue [128], malnutrition of cells and perturbed ion, hormone or enzyme balance [25]. The latter three can be treated by restoring the respective balance, which often yields a successful termination of AF.

Most of the discussed modifications are of static nature, i.e. once occurred they can not be removed again. However, the question arises, why AF is typically occurring in (self-terminating) episodes, if cell and tissue properties are modified permanently. The thesis of this work is that the interplay between wave fronts generated by the sinoatrial node and wave fronts emitted from a second, so-called perturbing source (spiral wave or ectopic foci) results in the irregular excitation patterns associated with AF. It is assumed that the second source is located in the left atrium for two reasons. First, a direct influence

of a pacemaker onto a spiral wave, located in the same region, was already studied and results in more regular patterns due to suppression of the spiral wave [77, 80, 129, 130]. Second, mapping of AF patterns of the human heart [131–136] and experiments with cardiac tissue and animals [137–140] revealed that additional pacemaking sources are more often located in the left atrium and exhibit a more critical role in the generation and perpetuation of AF. The thesis, assumed in this work, differs from previous theories with respect to the following points

- first, explicitly two pacemaker (sinoatrial node and perturbing source) are taken into account,
- second, the tissue is assumed as homogeneous; thus irregular patterns cannot be addressed to anisotropic tissue properties, and
- third, it is assumed that the relation of frequencies of the two pacemaker is essential for the generation of the irregular patterns. A frequency change could result in generation or termination of AF explaining thus the episodic occurrence of AF.

In Fig. 2.8 a schematic representation of the proposed mechanism for the generation of AF is shown.

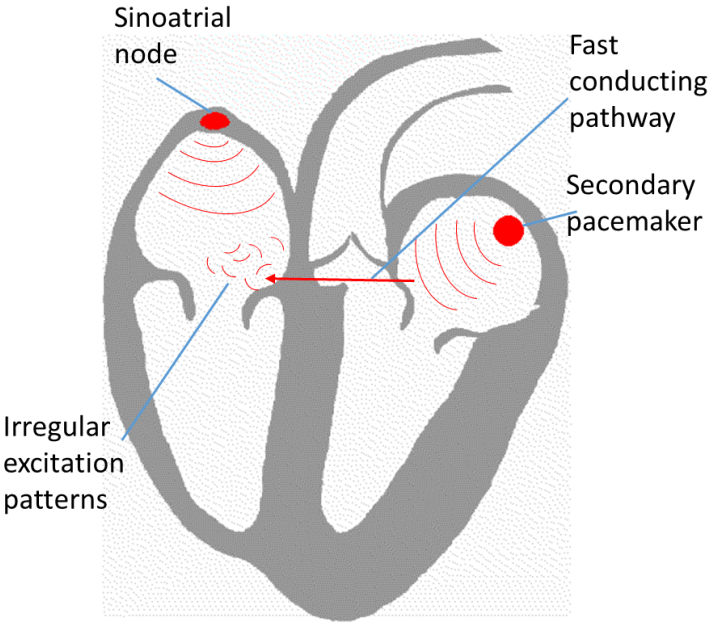

Figure 2.8: Schematic representation of mechanism, proposed in this work, for the generation and perpetuation of AF (the underlying picture was taken from Marquod (link: '//commons.wikimedia.org/wiki/File:Heart_conduct_explain.gif') and modified by me).

Chapter 3

Belousov-Zhabotinsky reaction (BZR)

3.1 Basics

The Belousov-Zhabotinsky reaction (BZR) comprises a family of oscillating, chemical reactions commonly viewed as the experimental standard example of RD systems. B. P. Belousov discovered the BZR around 1950 as he noticed periodic colour changes during the oxidation of citric acid with sulphuric bromate solution and Cer ions as catalysts. However, he could publish his observations only in 1959 since homogeneous, oscillating reactions were assumed to be impossible and it was argued that the oscillations occurred due to some gas bubbles or other inhomogeneities. A. M. Zhabotinski worked on detailed studies of the described phenomena, starting 1961. The BZR was named to account for their research.

Patterns emerging due to the BZR can be differentiated according to the considered system. In homogeneous systems, e.g. stirred reaction solutions, temporal patterns can be observed. In particular interesting for these patterns are multi-stabilities, periodic oscillations and chaotic behaviour [142–144]. Spatial patterns occur, amongst others, in gel systems or thin layers of reaction solutions. Patterns comprise travelling waves, spiral waves, point sources emitting circular waves, segmented waves, quasi-stationary patterns like the Turing patterns or spatio-temporal chaos [8, 71, 145–148]. Three-dimensional (3D) spatial patterns, as e.g. so-called scroll waves, can be studied in thicker (gel) layers [149, 150] or micro-emulsions of BZR solution in oil [151]. Scroll waves can yield irregular patterns [150, 152] due to the Winfree turbulence [153], a mechanism discussed to generate ventricular fibrillation. Beside the mentioned waves, corresponding to colour changes of the catalyst, mechanical waves can be obtained in special gels, where the catalyst is incorporated into the gel matrix [154, 155]. Soaking these gels with the BZR solution results in a periodic swelling and de-swelling of the gel.

The classical BZR solution contains the following reactants: malonic acid as

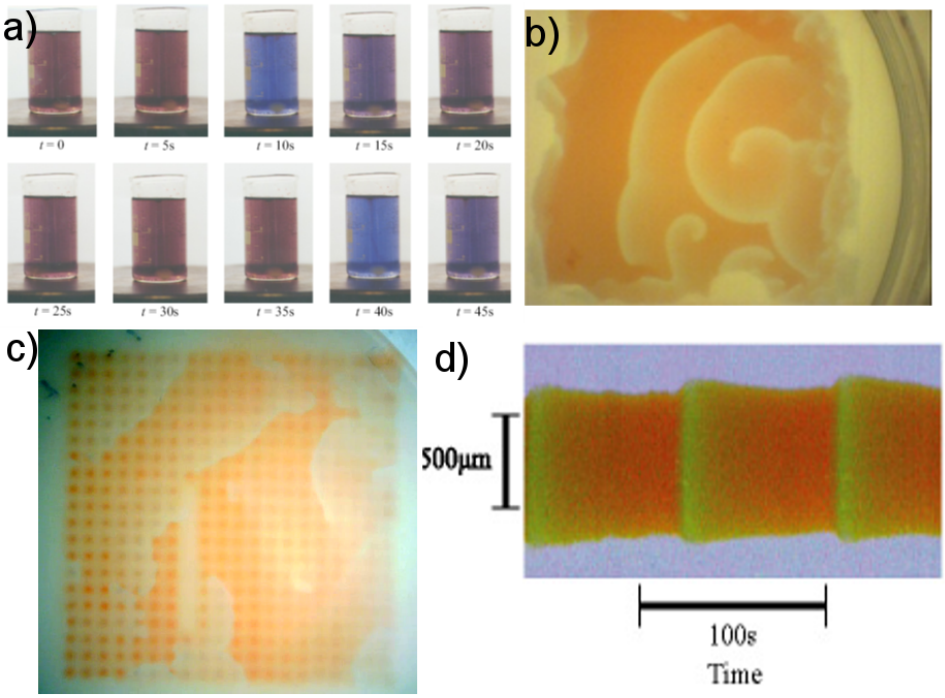

Figure 3.1: Differentiation of BZR systems: a) temporal oscillations (picture from J. Krieger, Wikipedia), b) spatial patterns (wave fronts) on homogeneous systems, c) spatial patterns on inhomogeneous systems (here: coupled oscillators), and d) periodic swelling of gel prepared with BZR solution (from [141]).

reducing agent, sodium bromate as oxidizing agent, sulphuric acid to tune the pH value, and Ferroin[1] as catalyst. Other reducing agents, as, e.g., citric acid or cyclohexanedione, as well as other catalysts based on the transition metals Ce, Mn, Ru, Co, Cu, Cr, Ag, Ni, or Os can be used for the BZR. The colour change of the catalyst, indicating the oscillation, depends on the applied catalyst: for Ferroin an alternation between red and blue is observed (see Fig. 3.1 (a)), for Cer ions a transition between yellow and colourless occurs, whereas for Mn ions pink and colourless are the interchanging colours. Sometimes the colour change is associated with fluorescence. Before possibilities to influence the emerging pattens are described, the reaction mechanism will be depicted.

3.2 Chemical mechanism

The BZR consists of many sub-reactions, sometimes up to 20 reactions are listed, which are not studied all in detail yet. The chemical mechanism can be described with the help of the model of Field, Körös and Noyes (FKN) [156–158]. Therein the reactions are classified into three groups:

[1] chemical compound with the formula $[Fe(o\text{-}phen)_3]SO_4$

- Process 1 contains mainly non-radical processes, where malonic acid, abbreviated by Mal, is brominated under consumption of bromide ions (Br^-) and bromate ions ($BrO_3{}^-$). Furthermore, bromous acid is produced, which will be important for the subsequent processes. The catalyst does not take part in process 1. Process 1 can proceed as long as the concentration of bromide $c(Br^-)$ is larger than a critical concentration $c(Br^-)_c$. The net equation for this process is:

  $$2\,Br^- + BrO_3{}^- + 3\,H^+ + 3\,H_2Mal \longrightarrow 3\,HBrMal + 3\,H_2O$$

- Process 2 consists of radical processes. The most important reaction in process 2 is the auto-catalytic production of bromous acid constituting the basis for the oscillating behaviour (fast activation of the activator, see ch. 1). For higher concentrations of bromous acid, it reacts further to hypobromous acid HBrO. During process 2, the catalyst Ferroin is oxidized resulting in a colour change from red to blue. Process 2 proceeds if $c(Br^-) < c(Br^-)_c$. The net equation is:

  $$BrO_3{}^- + 5\,H^+ + 4\,Fe^{2+} \longrightarrow 4\,Fe^{3+} + HBrO + 2\,H_2O$$

- Process 3 provides the basis to return from process 2 to process 1. Therefore, the concentration of bromide has to be raised above $c(Br^-)_c$. Malonic acid, mono-bromomalonic acid and hypobromite react by reducing the catalyst (change from blue to red) and producing bromide. This process is the time-delayed inhibition of process 2. Furthermore, the final reaction products, carbon dioxide CO_2 and water H_2O, not taking part in the BZR anymore, are produced by decomposition of hydroxmalonic acid ($HOCH(COOH)_2$ with bromate. This reaction results in the overall consumption of bromate and malonic acid. The net equation without production of CO_2 and H_2O can be summarized as

  $$2\,Fe^{3+} + 2\,H_2Mal + HBrMal + HBrO + 2\,H_2O \longrightarrow$$
  $$2\,Fe^{2+} + 2\,Br^- + 3\,HOCH(COOH)_2 + 4\,H^+$$

Concluding, process 1 represents the resting state of the system, process 2 resembles the activation and process 3 the refractory state or inhibition (repolarisation in the cell context). In the terms of excitable media, bromide acts as inhibitor and bromous acid as activator. Considering the total process, the reactants malonic acid and bromate are consumed and carbon dioxide, water and formic acid are produced. Thus the oscillation ends after a certain time.

3.3 Influences on pattern formation

Pattern formation can be influenced, in general, by the concentration of the reactants or by modification of the reaction solution due to replacement of reactants or addition of substances. For example, fructose-biphosphate, acetylacetate or etylacetoacetate can replace malonic acid. The latter two reduce

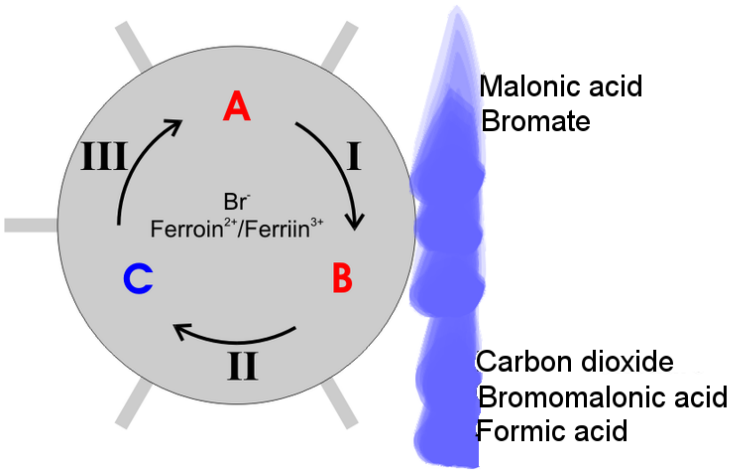

Figure 3.2: Schematic representation of the reaction mechanism as discussed for the BZR (from J. Krieger, translated here).

the generation of gas bubbles, which occur in the classical BZR due the production of carbon dioxide. By addition of methanol excitability and frequency of the oscillation can be tuned [159, 160]. Besides modifications of the reaction solution, temperature [68, 71, 161], gravitation [162], electric and magnetic fields [66, 163], oxygen concentration [64, 164] and illumination [165–168] influence the pattern formation, too. In particular for the ruthenium-catalysed BZR, illumination modifies the excitability locally. By spatially confined illumination a feedback-loop can be realized, enabling, e.g., the stabilization of wave fragments or the positioning of spiral waves [165, 169]. Furthermore, the dimension of the reaction vessel plays a role for the shape of wave fronts and their propagation velocity [166, 170, 171]. In numerical calculations, the blocking of wave fronts in corrugated channels was shown in dependence of the channel curvature [172].

In systems with one component of the BZR solution immobilized, typically the catalyst, emerging patterns depend on the one hand on the properties of the support for the immobilized species. Pore size, ion permeability, end groups, reactivity, thickness, as well as mechanical interactions modify the shape, conduction velocity and frequency of wave fronts and number of observable oscillations, as studied for different gel systems for example by Yamaguchi *et al.* [173]. On the other hand, spatially structured systems can be obtained by immobilizing the catalyst within different spatial arrangements. Thereby, the structuring can be realized by diverse techniques as printing the catalyst onto a membrane [174] or photo-lithographic structuring. The latter describes the photo-lithographic structuring of a resist on a membrane and subsequent diffusion of the catalyst at these sites into the membrane [175, 176]. Structured arrays were also generated by glass plates with holes where catalyst loaded beads were placed [177, 178]. Studies of structured systems demonstrated, for example, the dependence of the wave front geometry on the catalyst structure

[174] (see Fig. 3.3). Depending on the shape of the catalyst units, different geometries of the wave fronts were observed as hexagonal, diamond-like or more complex ones. Furthermore, the conduction of waves between shaped catalyst regions depends on their geometry. Direction dependent and frequency dependent conduction between two catalyst regions could be shown as well as chemical circuitries like diodes [167, 179, 180].

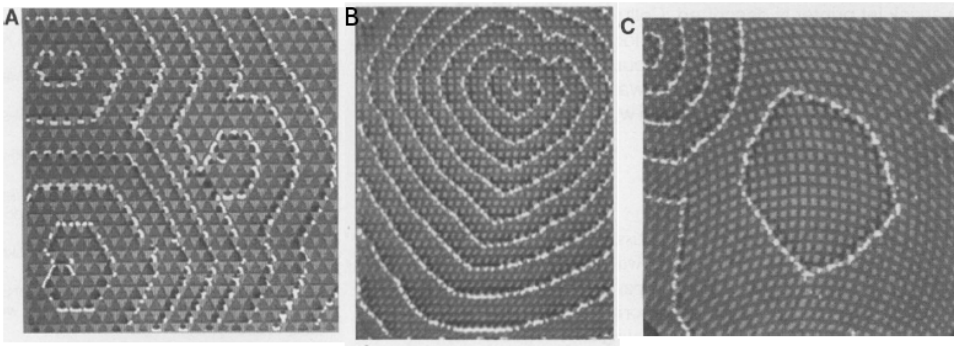

Figure 3.3: Shape of wave front in dependence of catalyst pattern: a) triangular catalyst cells, b) superimposed linear and circular grids, and c) superimposed circular grids resulting in hexagonal (a), diamond-shaped (b), and pentagonal wave patterns (c) (from [174]).

For the generation of irregular patterns, concentration gradients, inhomogeneities and the coupling of multiple reactor units have been mainly discussed in the last years. A gradient of sulphuric acid concentration, realized by coupling two reactors with different concentrations, results in the stabilization of spiral waves, as was shown, experimentally and numerically, by Qiao *et al.* [149]. Resulting patterns are shown in Fig. 3.4.

Even more interesting are patterns observed due to the coupling of many subunits. This is because of their analogy to many biological systems, which are comprised of many cells. The interplay of the subunits yields a larger diversity of patterns, which cannot be observed for single units. For example, determined frequencies of oscillators, which are diffusively coupled to many neighbours, are higher than for single oscillators [181]. Thereby, the oscillators consisted of catalyst-loaded nanoparticles immersed in BZR solution. Globally coupled electrochemical oscillators exhibit synchronized clusters in an ensemble of oscillators as well as chaotic excitation patterns [182]. Introducing boundary layers around the reaction compartments, as in water-in-oil emulsion including the BZR solution in the aqueous phase, results in a further increase of diversity of patterns [183].

The emergence of irregular patterns due to random inhomogeneities was demonstrated by Steinbock *et al.* for printed patterns of batho-Ferroin on polysulphon membranes [174], as shown in Fig. 3.5. Therefore, the catalyst was printed in spots with a pre-defined density. The position of spots inside one row was chosen randomly and the density of spots was increased from left to right.

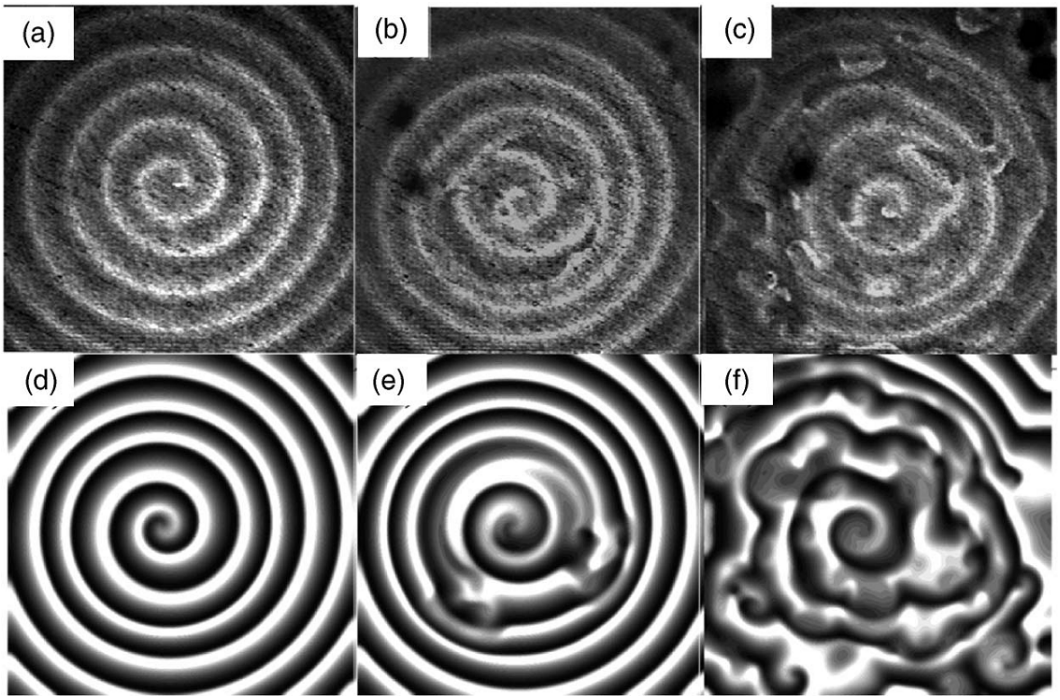

Figure 3.4: Generation of irregular patterns due to a gradient of sulphuric acid concentration, realized experimentally (upper row) and numerically (lower row) by Qiao *et al.* [149].

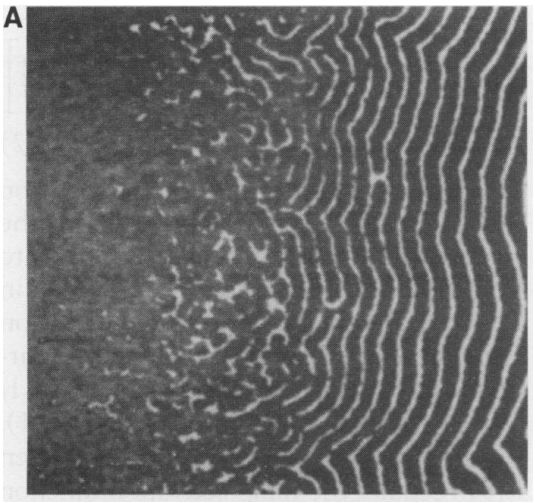

Figure 3.5: Irregular patterns occurring due to random inhomogeneities on polysulphon membranes with printed catalyst. The density of catalyst spots is reduced from right to left. Regular wave front patterns are observed for high densities of the catalyst and irregular patterns for intermediate densities. At low densities, no wave propagation was obtained (from [174]).

It could be shown that above a critical density ρ_1 regular waves occur, whereas below a second critical density ρ_2 no wave propagation is observed but only single active units. In the range of intermediate densities ($\rho_2 < \rho < \rho_1$), wave fragments and irregular patterns are present exhibiting higher frequencies than the regular wave fronts in the high-density region. These wave fragments act as pacemaker for the regular waves. Reducing the excitability by a decreased concentration of sulphuric acid, a qualitatively similar behaviour was observed,

in which the critical density ρ_1 increased in comparison to the experiments with the higher concentrations.

However, it is unclear, if these irregular patterns could be attributed to the heterogeneity or the difference in coupling strength determined by the number of and distance to neighbouring oscillators. In many RD systems, especially biological systems, heterogeneity of subunits, constituting the system, is discussed as reason for the generation of irregular patterns. This question will be addressed in this work, by studying the regularity of excitation patterns in dependence of the coupling strength and heterogeneity of coupled BZR oscillators.

Chapter 4

Mathematical description of RD systems

Besides the enormous differences in temporal and spatial behaviour, emerging patterns and research areas, the dynamics in RD systems can be described within similar mathematical equations. Mathematical models can be divided into two subgroups, depending on the point of view. These groups are macroscopic and microscopic models. In microscopic models, in particular for chemical systems, the interaction of molecules is described by reaction equations. Reaction mechanisms can be described by Markov chains while the diffusion processes are represented by random walk processes. This type of models is often termed 'Lattice-gas model'. The model of Malevanets and Kapral [184] is an example for a microscopic model. In the context of microscopic models, correlations and fluctuations can be taken into account and their influence on the pattern formation can be studied in detail. Suitable coarse graining techniques can yield macroscopic descriptions. The coarsening enables to express the parameters of macroscopic, phenomenological models in terms of experimental accessible variables. In this work, only macroscopic models will be studied.

4.1 Macroscopic models

Models, which can be accounted to the macroscopic point of view, describe RD systems on the basis of coupled, partial differential equations of second order for the system variables. The differential equations are expressed in form of rate equations, thus describing the temporal evolution of the system variables. These are supplemented by diffusion-like terms. In general, these equations can be written as:

$$\begin{aligned} \frac{\partial u}{\partial t} &= \nabla D_u \nabla u + f(u, v_i, z) \\ \frac{\partial v_i}{\partial t} &= \nabla D_{v_i} \nabla v_i + g_i(u, v_i) \; . \end{aligned} \tag{4.1.1}$$

Thereby, u and v_i are the system variables as, e.g., the concentration of reactants or the TMV, and represent activator and inhibitor(s) of the system. They are coupled by the functions $f(u, v_i)$ and $g_i(u, v_i)$ describing reactions and other processes. Since more than one inhibitor can be taken into account, they are indexed with i as well as the reaction terms g_i for these. The spatial propagation is described by the diffusion term $\nabla D_u \nabla u$ or $\nabla D_{v_i} \nabla v_i$, respectively. For constant diffusion coefficients the diffusion term can be simplified to $D_u \nabla^2 u$ or $D_u \nabla^2 v$.

Macroscopic models can be further classified into system-specific models or generic models according to the derivation of the reaction term [21, 185, 186]. In the field of cardiac simulations, generic models are sometimes also termed membrane potential models.

4.1.1 System-specific models

The reaction term in the first group of macroscopic models, the system-specific models, is directly derived from the processes in the systems, e.g, the chemical reactions resolved so far for the BZR. In this work, classification into ionic current models for excitable physiological systems (e.g. brain or heart) and chemical reaction models for chemical systems is used. Further groups, as for processes including enzymes or production of proteins, are existing, but will not be considered here.

At first, we will take a look at ionic current models. Models of this type describe primarily physiological processes during the excitation spread on cells, in particular neurons and myocytes. These models are based on the processes occurring at the cell membrane. Almost all of them are based on the Hodgkin-Huxley (HH) equations, which were developed in 1952 by Alan Lloyd Hodgkin and Andrew Fielding Huxley [187]. From empirical data of the excitation spread along the giant axon of the squid, they derived four coupled differential equations. For this study they were awarded with the noble price in medicine in 1963. The HH equations are:

$$\frac{\partial V_m}{\partial t} = \frac{1}{C_m r_c} \nabla^2 V_m - \frac{1}{C_m} (I_{stim} - I_K - I_{Na} - I_L) \,, \tag{4.1.2}$$

$$\frac{dn}{dt} = \alpha_n (1 - n) - \beta_n n \,, \tag{4.1.3}$$

$$\frac{dm}{dt} = \alpha_m (1 - m) - \beta_m m \,, \tag{4.1.4}$$

$$\frac{dh}{dt} = \alpha_h (1 - h) - \beta_h h \,. \tag{4.1.5}$$

The equations describe the spatial and temporal evolution of the TMV V_m for a cell membrane with resistance r_c and capacitance C_m. The reaction term describes the ion currents across the cell membrane, which are controlled by the opening and closing of ion channels and active pumping through the

membrane. Thereby, I_K represents the potassium current, I_{Na} the sodium current and I_{stim} a stimulating current. A further ion current I_L, the so-called leakage current, which is typically very small, was introduced to account for the influence of further ions as calcium or chloride. The equation for the TMV, Eq. (4.1.2), is coupled with the temporal evolution of the gating variables, Eqs. (4.1.3)-(4.1.5), describing the opening and closing of the ion channels, by the ion currents:

$$\begin{aligned} I_K &= \bar{g}_K n^4 (V_m - E_K), \\ I_{Na} &= \bar{g}_{Na} m^3 h (V_m - E_{Na}), \\ I_L &= \bar{g}_L (V_m - E_L). \end{aligned} \tag{4.1.6}$$

Here, E_{ion} is the Nernst-Potential for the respective ion and g_{ion} the corresponding conductance of the ion channel. The gating variables n, m and h are, on the one hand, voltage dependent, and, on the other hand, the evolution of the TMV depends on the gating variables. They were originally postulated by Hodgkin and Huxley and determined by fitting the experimental data. However, they could be correlated with real structural properties of the ion channels later [188, 189].

All ionic current models describe the ion currents through the membrane. They differ in the number of considered ion currents, the type of ions, the gating behaviour of the individual channels and in the treatment of voltage dependent ion reservoirs. Typical representatives of this group are the models for excitation propagation in the atria from Courtemanche, Ramirez and Nattel [190], Nygren [191], Maleckar [192], Koivumaki [193] or Grandi [194] and the models derived for the ventricles from Luo-Rudy [195] or Noble [196].

Models for excitation spread in atria or ventricles mainly vary in the time constants of the ion channels and partially included additional ion currents. The Courtemanche, Ramirez and Nattel (CRN) model for the atrial excitation includes all known ion currents through the cell membrane. In other atrial cell models, further currents inside the cell are included to account, for example, for the intracellular Ca^+ handling. In Fig. 4.1 the considered ion currents in the CRN model are shown schematically. Besides the sodium, potassium, leakage and stimulating currents of the HH model, calcium and chloride currents as well as the storage of calcium and some more ion pumps are incorporated. The full model consists of 21 variables. Since all known ion currents through the membrane are considered, the CRN model is suited well for comparisons with experiments of cardiac tissue. However, the number of variables and the coupling of the equations complicate the study on underlying mechanisms for the emergence of certain patterns, as wave fragments, spiral waves or irregular patterns. It will be used in this work for comparison with a simpler model for excitation spread in the atria.

In the following, system-specific chemical reaction models will be described. In these models, the reaction term reproduces the chemical reactions. Thus, involved parameters and variables can be directly correlated with concentra-

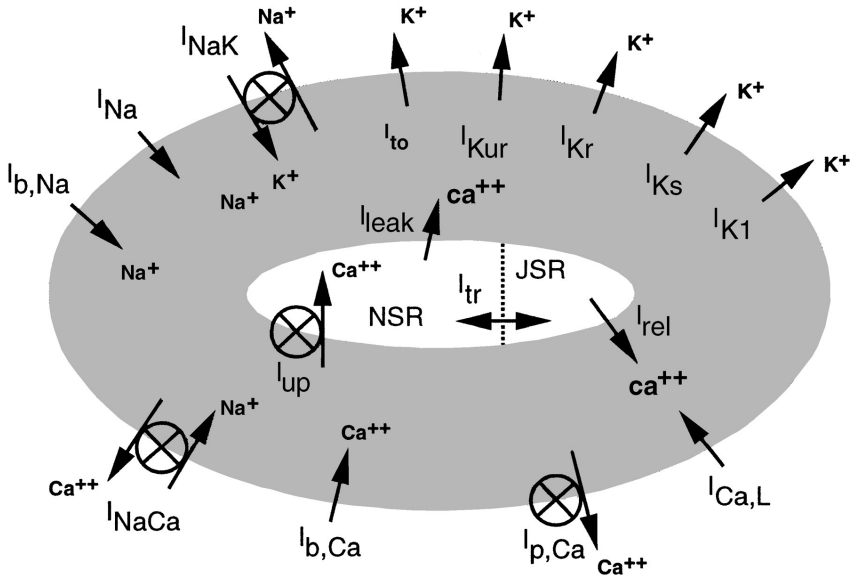

Figure 4.1: Scheme of ionic currents through the cell membrane and inside the cell considered in the CRN model (from [190]).

tions and other influences of the experimental set-up. Typical examples of this group are the Oregonator model [157, 158], the Brusselator model [197] or the Rovinsky model [198]. All were invented to describe the BZR. The system specificity is obvious, when considering the different variants of the Oregonator model, suitable either for the Ruthenium catalysed BZR or the Ferroin catalysed variant. Further representatives of chemical reaction models are the model of Zhang and Datta [199] for Pt/Ru-catalyst polymer electrolyte membrane (PEM) fuel cell or the model of Krischer, Eiswirth and Ertl [200] for the CO oxidation on Pt catalyst.

In this work, the Rovinsky model will be used as system-specific model for the Ferroin catalysed BZR. It consists of two coupled differential equations:

$$\begin{aligned} \epsilon\frac{\partial x}{\partial t} &= d_u\nabla^2 u + u(1-u) - (2q\alpha\frac{v}{1-v} + \beta)\frac{u-\mu}{u+\mu}\,, \\ \frac{\partial v}{\partial t} &= d_v\nabla^2 v + u - \alpha\frac{v}{1-v}\,, \end{aligned} \tag{4.1.7}$$

where

$$\begin{aligned} \beta &= \frac{2k_4}{(k_1 h_0 A)^2}, \\ d_u &= \frac{2k_4}{(k_1 h_0 A)^2} D_u, \\ d_v &= \frac{k_4}{(k_1 h_0 A)^2} D_v\,. \end{aligned} \tag{4.1.8}$$

The parameter β describes the influence of the slow hydrolysis of the bromomalonic acid, while d_u, d_v are the scaled diffusion coefficients. The variables

can be converted into the concentration of substances, used in the experiments, by

$$\begin{aligned} [\mathrm{Fe(phen)}_3^{3+}] &= Cv, \\ [\mathrm{HBrO_2}] &= (k_1 A_R/2k_4)u. \end{aligned} \tag{4.1.9}$$

The constants, $\epsilon, \mu, K_8, A_R, B_R$ and C_R depend on the initial conditions and are given by

$$\begin{aligned} \epsilon &= k_1 A_R/k_4 C, \\ \alpha &= k_4 K_8 B_R/k_1^2 A_R^2 h_0^2, \\ \mu &= 2k_4 k_7/k_1 k_5, \\ K_8 &= k_8 k_9/k_{-8}, \\ A_R &= [HBrO_3], \\ B_R &= [CHBr(CHOOH)_2], \\ C_R &= [Fe(phen)_3^{2+}] + [Fe(phen)_3^{3+}]\ . \end{aligned} \tag{4.1.10}$$

The parameter h_0 is the acidity function, q the stoichiometric factor and $k_{\pm i}$ the rate constants of the reactions.

In contrast to the Rovinsky model, the Oregonator model is composed of three variables. It is typically used for the BZR description and successfully describes, in particular, the Ruthenium catalysed BZR. Despite of this, it seems to describe the Ferroin catalysed BZR not as accurate as the Rovinsky model. Therefore, the Rovinsky model was chosen as system-specific model.

4.1.2 Generic models

The second group of macroscopic models comprises generic or simplified models. These are often reductions or simplifications of the system-specific models and are used for basic or analytical studies. The most prominent representative of this group is the FitzHugh-Nagumo (FHN) model [201, 202], developed in 1961 separately by R. FitzHugh and J. Nagumo. It includes as a special case the well-known van-der-Pol model [203] for description of an oscillator. R. FitzHugh derived this model from the HH model by reduction of the system variables, which was possible due to the different time constants of the variables. J. Nagumo created an electronic circuit, exhibiting the same dynamics. The FHN equations are given by

$$\begin{aligned} \frac{\partial u}{\partial t} &= \nabla D \nabla u + c(v + u - u^3/3 + z)\ , \\ \frac{\partial v}{\partial t} &= -\frac{1}{c}(u - a + bv)\ , \end{aligned} \tag{4.1.11}$$

The variables u, v as well as the parameters a, b and c of the equations cannot be calculated from parameters or properties of the experiment anymore. They

rather describe properties of the system in a summarizing way. The detailed influence of the parameters a, b and c onto the action potentials cannot be determined very easily due to the mutual interdependence and non-linearity. In a first approximation, a regulates the length of the refractory period, b controls the stability of the resting state and c the excitability and strength of the response to a stimulus. D is the diffusion coefficient, describing the spatial coupling. The variable u represents the activator of the system and v the inhibitor. Their interpretation depends on the considered systems, since, although derived from the HH model, the FHN model does not only describe propagation of action potentials on cells, but it can be applied to diverse RD systems like the BZR. When considering the action potential propagation in the heart, u represents the TMV and v summarizes the ion currents through the cell membrane. In the context of the BZR, u represents the concentration of bromide, whereas v describes the catalyst concentration. The variable z represents external stimuli, as for example stimulating currents or illumination. The microscopic model of Malevanets and Kapral is a microscopic version of the FHN model.

Further representatives for generic models are the van-der-Pol model [203], descriptions by the Swift-Hohenberg equation [204], the Gierer-Meinhardt model [205] and models developed by Aliev and Panfilov [206], Pertsov and Panfilov [207], Barkley [208], and Biktashev [209].

In this work, the model of BOCF, a generic model, will be applied as a more system-specific description for the excitation propagation in the heart, since it matches numerical calculations of the system-specific CRN model very well [87, 120]. The BOCF model was developed from the CRN model with the intention of finding a minimal model, still describing all important properties of excitation generation and propagation, in particular, the action potential shape and the conduction velocity and action potential duration in dependence of the pacing frequency. The latter two belong to the restitution properties, describing properties which differ in dependence of the excitation frequency. A direct conversion of the variables into system-specific, measurable quantities as, e.g., ion concentrations at the membrane, is not possible. Favourably, the parameters and the dynamics can be tuned to resemble atrial or ventricular tissue in different situations as, for example, in the physiological state or for remodelled tissue. The differential equations for the four system variables are given by

$$\begin{aligned}
\frac{\partial u}{\partial t} &= \nabla \cdot D \nabla u - \left(I_{fi} + I_{so} + I_{si}\right), \\
\frac{\partial v}{\partial t} &= -\frac{1}{\tau_v^+} v\, H(u-\theta_v) + \frac{1}{\tau_v^-} \left(v_\infty - v\right) \left[1 - H(u-\theta_v)\right], \\
\frac{\partial w}{\partial t} &= -\frac{1}{\tau_w^+} w\, H(u-\theta_w) + \frac{1}{\tau_w^-} \left(w_\infty - w\right) \left[1 - H(u-\theta_w)\right], \\
\frac{\partial s}{\partial t} &= \frac{1}{\tau_s} \left[\frac{1}{2}\left(1 + \tanh[k_s(u-u_s)]\right) - s\right] . \qquad (4.1.12)
\end{aligned}$$

with the ionic currents

$$\begin{aligned} I_{fi} &= -v\,(u-\theta_v)\,(u_u-u)\,H(u-\theta_v)/\tau_{fi}\,, \\ I_{so} &= (u-u_o)\,[1-H(u-\theta_w)]/\tau_o + H(u-\theta_w)/\tau_{so}\,, \\ I_{si} &= -w\,s\,H(u-\theta_w)/\tau_{si}\,. \end{aligned} \tag{4.1.13}$$

Here, $H(x)$ is the Heaviside step function. By scaling the variable u, a TMV equivalent

$$V_m = 85.7u - 80.9$$

(in mV) can be calculated. The current I_{fi} represents the fast, inward-directed sodium current, I_{si} represents the slow, inward current of the calcium ions, and I_{so} describes the slow, outward current of potassium ions. The gating variable v regulates I_{fi}, and the gating variables w and s regulate I_{si}. Due to these three gating variables, the models exhibits the restitution behaviour and the typical spike-and-dome shape of cardiac action potentials. The time constants τ_v^-, τ_w^-, τ_{so}, τ_s, τ_o, v_∞ and w_∞ are functions of the four state variables and can be found in [119].

4.2 Summary

The model, which is applied for the study of a certain RD system, depends not only on the specific system but also on the problem to be studied. Complex, system-specific models, as ionic current models or chemical reaction models, enable the direct comparison with measurements. However, their complexity hampers the study of underlying mechanisms. For this purpose and for analytical considerations, the generic models are more suitable. Additionally, the relevant system properties need to be considered, since physiological models, for example, differ also in the shape of action potentials, restitution properties and conduction velocities. Thus, from calculations with different models it can be derived reversely, which properties are relevant for the studied problem and system. Here, the FHN model will be used for the generic description of both systems. To deduce system-specific mechanisms and features, calculations will be compared with the Rovinsky model in the case of the BZR and the BOCF model for AF studies. Since the BOCF model is actually a generic model, certain cases will be simulated also with the CRN model to test if the observed results are model dependent or a real feature of this system.

Part II:
Methods

In this part the methods are presented, which were used for the study of coupled oscillators. Methods and optimizations are divided into three groups: numerical calculations incorporating the simulation of the mathematical RD models, experimental investigations, in particular experiments of the BZR, and analysis, i.e. time series analysis and pattern description, of the resulting data gained from experimental and theoretical studies. Since some methods are used only for the study of one of the proposed mechanisms, the corresponding chapter will be denoted with the type of the RD system (AF, BZR) for clarity.

Chapter 5

Numerical calculations

Numerical calculations comprise the simulation of the mathematical RD models on simulation areas and conditions suitable for the study of the proposed mechanisms. First of all, different methods for solving the RD models will be presented and compared. Subsequently, the chosen set-up of simulation area and conditions for each RD system will be described.

5.1 Solution methods for the RD equations

To solve the RD models, i.e. the FHN, BOCF and CRN model for the RD system AF, as well as the FHN and Rovinsky model for the system BZR, three different methods and programs were used: first, the finite element method (FEM) with a program written in Matlab and based on the pdetoolbox, second, the finite differences method (FDM) written in CUDA for graphic card usage, and, third, the modular package acCELLerate written in C++, enabling usage of FDM and FEM. Advantages and disadvantages of each method and basis of programming will be described in combination with the methods' principles in the following sections.

The macroscopic models described in chapter 4.1 are in general coupled, non-linear partial differential equation (PDE) of the following type:

$$\begin{aligned} \frac{\partial u}{\partial t} &= \nabla D_u \nabla u + f(u, v_i, z)\,, \\ \frac{\partial v_i}{\partial t} &= \nabla D_{v_i} \nabla v_i + g_i(u, v_i)\,. \end{aligned} \tag{5.1.1}$$

To solve these equations for a certain problem, the simulation area can be divided, on the one hand, into points (1D) or grids (2D) and, on the other hand, into finite sized elements. Depending on the applied method of discretization, the method is termed finite-differences or finite-elements.

5.1.1 Finite Element Method on the basis of Matlab (AF)

The finite element method (FEM) is a numerical method to solve partial differential equations on complex geometries. The complex geometry is fractionated into simple, geometric elements. On this elements, the differential equation can be solved easily with simple, known functions $u_a(x,t) = \sum_{i=1}^{N} c_i(t)P_i(x)$ like polynomials P_i with constants c_i. The real solution $u(x,t)$ is approximated by linear combinations of the functions $u_a(x,t)$. Inserting this into the differential equation $\frac{\partial u}{\partial t} = \nabla D_u \nabla u + f(u, v_i, z)$ yields a system of ordinary differential equations $\mathbf{M}dc/dt + \mathbf{K}c = \mathbf{F}$ [210, 211]. In this way, the problem is reduced to the determination of the parameters c_i by solving a system of linear equations. The number of degrees of freedom is given by the number of degrees of freedom of the physical model multiplied with the number n of functions u_a, which is equal to the number of elements. For small systems, the linear equation system can be solved by direct methods like the Gaussian elimination method. Larger systems are calculated predominantly with iterative methods like the Jacobi or Gauß-Seidel method, multiple grid methods or the method of conjugated gradients.

Matlab provides the *'pdetoolbox'* for solving partial differential equations. In this toolbox the description of the problem, i.e. geometry, initial and boundary conditions and the differential equation itself, is done by the help of a graphical user interface (GUI) or on the basis of self-written scripts. Here, the function *'parabolic'* was used to solve the PDEs, i.e. the FHN equations. At the time of the simulations, non-linear coefficients, depending on the solution u, v or their derivative, could not be used with the *'parabolic'* function. In the FHN model, however, a non-linearity is present in the reaction term (given by u^3). To solve this problem, the non-linearity $u^3(x,t_i)$ was treated as inhomogeneity $u^3(x,t_{i-1})$ for each time step t_i, by taking the value from the previous time step t_{i-1}. This is adequate, as long as $u(x,t)$ does not change much during one time step. Triangles are taken as finite elements in the *'pdetoolbox'*. An adaptive mesh is generated. That means, triangles are smaller at critical sites (e.g. corners), where large variations of the solution u are expected or found. The adaptive meshing allows a reduction of computation effort compared to evenly sized elements, since less elements are needed. However, adaptive grids may lead to errors, if, e.g., diffusion currents are incorrectly matched to the size of the triangle.

5.1.2 Finite differences method realized in CUDA (BZR)

Another method for numerically solving PDEs is the finite differences method (FDM). Therefore, the simulation area is divided into a finite number of grid points, corresponding to rectangular grids for multi-dimensional areas. The differential equation is approximated by the difference quotient at the grid points. The resulting system of difference equations can be numerically solved with various algorithms.

The simplest method is the forward or explicit Euler method. Considering an equation of the type $dy/dt = f(t, y)$, this will be approximated by

$$y_{k+1} = y_k + h_s f(t_k, y_k)\,. \tag{5.1.2}$$

Here, a discretization of the time is given by $t_k = t_0 + kh_s$ with $k = 1, 2, ...$ and the step size h_s. As a result, one obtains approximative values y_k of the function $y(t_k)$. The difference between the approximate and the exact value is the error of the method. It is influenced by the stability[1] and the consistency[2]. Stability describes the summation of the error occurring due to imprecise input values, for example because of rounding, thus corresponding to the robustness of the system/algorithm. Consistency describes how good the problem can be solved by a certain algorithm, i.e. what deviations between approximate and exact solution occur for exact input values. Both, consistency and stability, depend on the step size of the algorithm. Thus, one has to determine for each problem and algorithm the maximal step size, for which the variation of the solution is bounded. The explicit, forward Euler method has a consistency order of one, which means the error is in the same range as the step size. With almost the same calculation effort the second order of consistency can be achieved by applying the central difference quotient $y_{k+1} - y_{k-1} = 2h_s f(t_k, y_k)$ instead of the simple, forward one [Eq. (5.1.2)]. Another possibility to enhance the consistency is to replace the explicit calculation of the difference quotient with an implicit one. Thereby, rather than the actual value of the variable y_k, the value y_{k+1}, which has to be calculated, is used for determination of the function value $f(t_k, y_k)$. The equation to solve for the implicit method, in analogy to Eq. (5.1.2), is given by

$$y_{k+1} = y_k + h_s f(t_{k+1}, y_{k+1})\,. \tag{5.1.3}$$

For this method, one has to solve, in general, a non-linear equation. The advantage is an algorithm which is often more stable than the explicit method for stiff problems[3]. Hence, larger step sizes and consequently smaller calculation time are needed than for the explicit method. Further improvement can be achieved by applying the Crank-Nicolson method. Thereby, the mean between the forward and backward Euler method is used:

$$y_{k+1} = y_k + \frac{1}{2h_s}(f(t_{k+1}, y_{k+1}) + f(t_k, y_k)). \tag{5.1.4}$$

The advantage is a numerically stable algorithm, which goes along with the disadvantage of calculating non-linear, algebraic equation systems if non-linear problems have to be solved.

In this work, the explicit, forward Euler method was chosen to solve the simple RD models (FHN, BOCF and Rovinsky). This is typically not well

[1] How much deviations occur due to the algorithm for disturbances?

[2] How exact is the problem solved for exact initial values by the algorithm?

[3] Stiff means that large step size result in a small change of the function values only.

suitable for stiff differential equations like the RD equations, because very small step sizes are needed for stability of the algorithm. However, in comparison with implicit and more complex algorithms, no significant difference in the maximum value of the step size and in calculation time was observed. This fact might be caused by the fact that the differential equation in the chosen parameter range is not so stiff. A strong decrease of calculation time could be obtained by usage of graphical processing units (GPU) of the graphic cards since it allows a parallelisation of the problem.

As an example, the algorithm for graphic card usage will be explained for the FHN model [code of CUDA program for BZR system can be found in the Supporting Material]. In the first step, the simulation area is discretized into a rectangular grid. An array is generated for each spatially varying quantity, i.e. the variables u, v and the parameters a, b, c. The arrays are transferred from the central processing unit (CPU) to the GPU. Therefore, a block size has to be defined, which groups a certain number of threads, to take all points of the array into account. The dimension of the blocks is given by $[n_1, n_2/\text{number of threads}, 1]$ if array size is $[n_1, n_2]$. Each thread evaluates the same equation simultaneously, since GPUs were developed for parallel array operations. If different equations have to be calculated for the different threads, for example, if the difference quotient differs for points at the boundary, these are evaluated successively. To optimize calculation time on the GPU, every split-up into different equations, which have to be calculated by the threads of one array should be avoided. These split-ups are, for example, caused by if-queries.

The calculation of the FHN equations was performed in two steps. First, the right part of the equation is evaluated as follows:

$$\begin{aligned} du[pos] &= \frac{D}{dx^2}(u[pos-1] + u[pos+1] + u[pos+n_2] + u[pos-n_2] - 4u[pos]) \\ &+ c[pos] * (u[pos] - u[pos]^3 + v[pos])), \\ dv[pos] &= -cstar[pos] * (b[pos] * v[pos] + u[pos] - a[pos]), \end{aligned} \tag{5.1.5}$$

where *pos* denotes the actual position or point considered by the thread. The index of the point $[x, y]$ within the array is converted into a scalar one. Thus, the next neighbour in x-direction is given by $pos \pm 1$, whereas the next neighbour in y-direction is given by $pos \pm n_2$, according to the next column in the array. This step of computation has to consider the boundary conditions. In the simulations of this work, von-Neumann boundary conditions are applied. Thus, the difference quotient for a certain boundary point lacks the difference to the points behind the boundary, i.e. for points at the edges only three differences are calculated whereas for points in the corner one has to calculate only two differences. This is taken into account for by if queries to determine the differences to sum up. Note, that due to this split-up, threads will not finish simultaneously this step of the calculation.

The second step of the algorithm is the update of all points to the next time step, i.e. to calculate $u(t+\delta t, x, y)$ by multiplying the whole array $du(x, y)$

with the time step δt and then adding this to the array $u(t, x, y)$. Here, the calculation is similar for all points. The values $u(t + \delta t, x, y)$ form the starting array for the next evaluation of Eq. (5.1.5). The two-step process guarantees that all threads have the actual values of their next neighbours, since the second step is evaluated only after completion of the first step for all threads. Otherwise, if the calculation would be done in a one-step process, i.e. evaluation of the whole equation in one step, some threads would not have the actual value of their neighbours, but ones from previous time steps. After a pre-defined number of time steps, the array $u(t, x, y)$ is copied to the CPU to save the values in a file for subsequent evaluation, since files can be addressed by the CPU only. The calculation on the GPU continues after the copying process.

In comparison with the CPU, the GPU is faster for this type of calculations, since the difference quotient is evaluated simultaneously for a large number of points in the parallel running threads, thereby only excluding the points at the boundary. In the CPU the evaluation is done successively. However, calculations on the CPU are not as slow as expected, since diverse optimization algorithm, in particular for array operations, are implemented already in most of the complex scripting languages like Matlab. If one considers only the real calculation time, the GPU is faster than the CPU for equal calculation operations, which can be evaluated simultaneously. This advantage is reduced by the communication time between the CPU and GPU for copying arrays, between the threads to exchange the updated values of the neighbour points or between different graphic cards, if the problem size is larger than the memory of a single graphic card. By calculation and comparison of the communication time and the evaluation time on either CPU or GPU, one can decide which processor is more suitable for the problem under consideration.

5.1.3 acCELLerate (AF)

The programming package acCELLErate [212] was used within a cooperation with Dr. Seemann, then working in the group of Prof. Dössel, Institute of Biomedical Technology at Karlsruher Institute of Technology, and now in the Universitäts-Herzzentrum Freiburg. It is organized in modules. In the geometry module geometry, tissue class, fibre orientation and, optional, heterogeneity can be defined. Small, isotropic sections of tissue as well as the whole heart can be simulated. When generating the arrays, one can choose between FDM or FEM. Different RD models for cardiac tissue and different parameter sets, according to different physiological states, are implemented as well as the possibility to use mono-, bi- or multiple domain models. acCELLerate is implemented in C++ and uses routines for solving and parallelisation of the problem from the Portable, Extensive Toolkit for Scientific Computation (PETSc) [213–215]. Besides the many advantages (multiple geometries and RD models), a disadvantage of acCELLerate is the necessary transformation of geometries and equations into PETSc arrays and vectors, which

is very time consuming. Thus, in comparison of the three applied programs (Matlab, CUDA, acCELLerate), acCELLerate is faster, when considering only the calculation time, particularly for the more complex models, but due to the transformation the total calculation time including saving data is approximately the same as for the CUDA based software. The main advantage of the package is the possibility to calculate different RD models, parameter sets and solver without the need for programming.

In the acCELLerate package, for the interplay of two pacemaker, mainly the explicit Euler method was used. Comparisons with the implicit Euler method were conducted, but no significant differences in the step size were observed. The BOCF model with different parameter sets, according to physiological and electrically remodelled tissue and tissue with reduced excitability were utilized.

5.2 Geometric model for simulations

5.2.1 Interplay of two pacemaker (AF)

A two-dimensional simulation area (Fig. 5.1) is considered for the study of the interplay between two pacemakers in active tissue as model for AF generation. It is thought to resemble, for example, isolated sections of cardiac tissue as often used in experiments [216–218]. The two-dimensionality is based on the small thickness of atrial tissue in comparison to ventricular tissue. Thus, excitation waves propagate mainly in two-dimensions and not through the tissue in z-direction. The so-called 'break-through', i.e. excitation wave propagating from inner side to outer side of the tissue in z-direction, is discussed as one possible mechanism for fibrillation, in particular for ventricular fibrillation, but is not considered here. The size of the simulation area is 21×10 in spatial units^2.[4] It consists of three regions: the region R ($11 \leq x \leq 21$, $0 \leq y \leq 10$), resembling the right atria, the region L ($0 \leq x \leq 10$, $0 \leq y \leq 10$), representing the left atria, and the small bridge B ($10 < x < 11$, $5 - w_B/2 < y < 5 + w_B/2$, with width w_B), connecting regions R and L. The bridge is thought to represent a fibre bundle connecting the two electrically isolated atria like Bachmanns Bundle [219–221]. Its width is varied between 0.01-4 spatial units. There are often more connections between the atria, like the Fossa Ovalis or the coronary sinus [222, 223]. However, most of the conduction is thought to be passed along Bachmanns Bundle. For simplification, only one conduction path is considered here.

The regular pacemaker, representing the sino-atrial node and termed primary pacemaker here, is located outside of region R in this model. Thus, waves

[4] Spatial unit in the BOCF model is 1cm, whereas in the FHN model the spatial unit can not be transformed into physical units. Transformation of units may be approximately be deduced by comparison of conduction velocities. But due to a different AP shape, restitution behaviour and other deviations from the biological systems, this can be only a quite rough approximation.

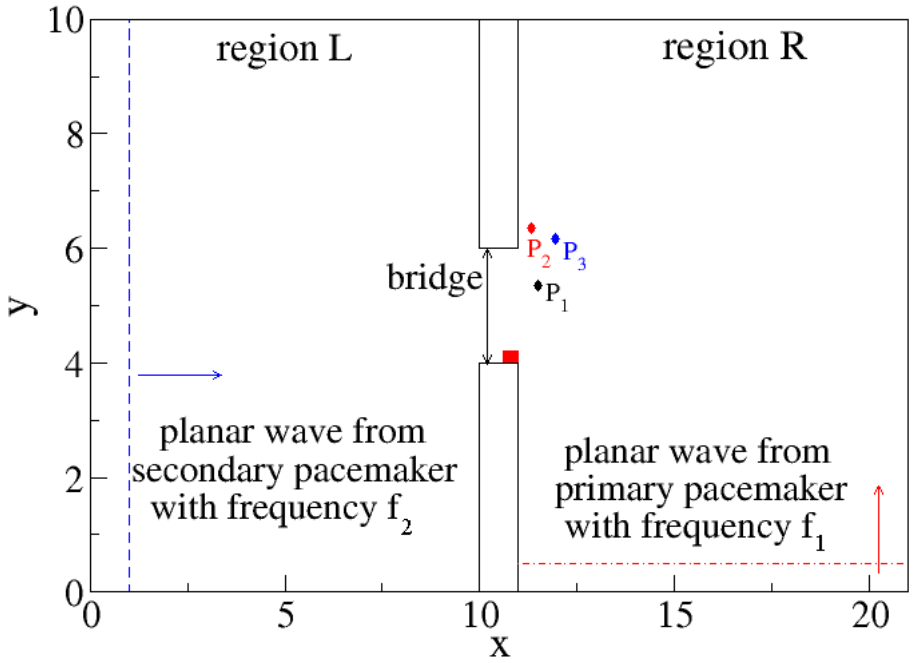

Figure 5.1: Simulation area for studying the interplay of two pacemakers in active tissue as model for AF. The primary pacemaker generates planar wave fronts with frequency f_1 and the secondary pacemaker (region L) with frequency f_2. Time series of marked points (P_1, P_2, P_3) are used to show representative temporal patterns later.

emitted by the primary pacemaker, called primary waves, are assumed to be planar. To periodically generate the primary waves, a current $z = -1$ (equal to 10pA in the BOCF model) is applied for the duration of one time unit[5] and with a frequency f_1 in the region $11 \leq x \leq 21$ and $y \leq 0.5$. The same assumption is valid for the perturbation source, e.g. ectopic focus or spiral wave, in the left atrium, termed secondary pacemaker. It is assumed to be localized outside of region L. Waves emanating the secondary pacemaker are termed secondary waves and are planar inside the simulation area. A periodically injected current of amplitude $z = -1$ for a duration of 1 time unit (t.u.) and with a frequency f_2 in region $x \leq 0.5$ and $0 \leq y \leq 10$ generates the secondary waves.

In the set-up, von-Neumann boundary conditions $\partial u/\partial n = 0$ are applied with $\partial/\partial n$ being the derivative in direction of the normal vector at the bound-

[5] One time unit is equal to 1000 time steps in the FHN model for the typically used value of times steps and 50ms in the BOCF model.

Table 5.1: Parameters of the pBOCF and rBOCF model; All times $\tau_{...}$ are given in ms (except τ_w^∞ which is dimensionless).

	τ_{v1}^-	τ_{v2}^-	τ_v^+	τ_{w1}^-	τ_{w2}^-	τ_w^+	τ_{fi}
pBOCF	41.857	1150	1.70	138.69	62.341	177.41	0.045
rBOCF	16.3	1150	1.703	79.963	28.136	213.55	0.084
	τ_{o1}	τ_{o2}	τ_{so1}	τ_{so2}	τ_{s1}	τ_{s2}	τ_{si}
pBOCF	410	64.914	115	6.5	11.457	53.902	7.802
rBOCF	250.03	16.632	73.675	6.554	9.876	4.203	10.699
	τ_w^∞	θ_v	θ_w	θ_v^-	θ_o	u_w^-	u_o
pBOCF	0.050	0.35	0.328	0.126	0.00005	0.055	0.00
rBOCF	0.223	0.30	0.1817	0.1007	0.0155	0.01	0.00
	u_u	u_{so}	u_s	k_w^-	k_{so}	k_s	w_∞^*
pBOCF	0.9205	0.332	0.792	202.66	1.386	1.226	1.0
rBOCF	1.0089	0.5921	0.8157	60.219	2.975	2.227	0.902

aries. This means that no flux of the TMV across the boundaries is possible. Usually, a reflection of waves would occur at the boundaries due to this boundary conditions. This is not true for RD systems with active boundary region, since an activation wave front is followed by a refractory front, which can not be excited. Thus, back-excitation from the boundary into the simulation area is not possible, since the reflected activation wave front is extinguished by the following refractory front. As initial conditions the resting state of the systems is chosen ($u = 1.2; v = -0.6$ in the FHN model). As standard parameters for the FHN model, $a = 0.7, b = 0.6, c = 5.5$ and $D = 0.1$ were chosen. The corresponding values of the variables and the parameters used for the BOCF model are given in Tab. 5.1. The BOCF model describing the physiological state of atrial tissue (pBOCF) refers to the parameter set used to model the physiological state of tissue and BOCF model describing the electro-physiologically remodelled state of atrial tissue (rBOCF) denotes the parameter set to describe the electrically remodelled tissue. Time steps of 0.01 t.u. (FHN) or 0.01 ms (BOCF), respectively, were taken and a spatial discretization of $\Delta x = \Delta y = 0.1$ s.u. (FHN) or 0.01 cm (BOCF). It was checked that the behaviour remains qualitatively the same after three times longer simulation time, which gives confidence that the obtained features, presented in ch. 7.5, are not a transient phenomenon.

5.2.2 Diffusive coupling of multiple oscillators (BZR)

The simulation area is two-dimensional since for the experiments thin gel layers were used. Thus, spread of reactants into the third dimension are negligible. The simulation area is divided into active and passive regions. The active regions represent the oscillators and there the full RD system including the reaction and diffusion term is solved. For the passive regions in between and

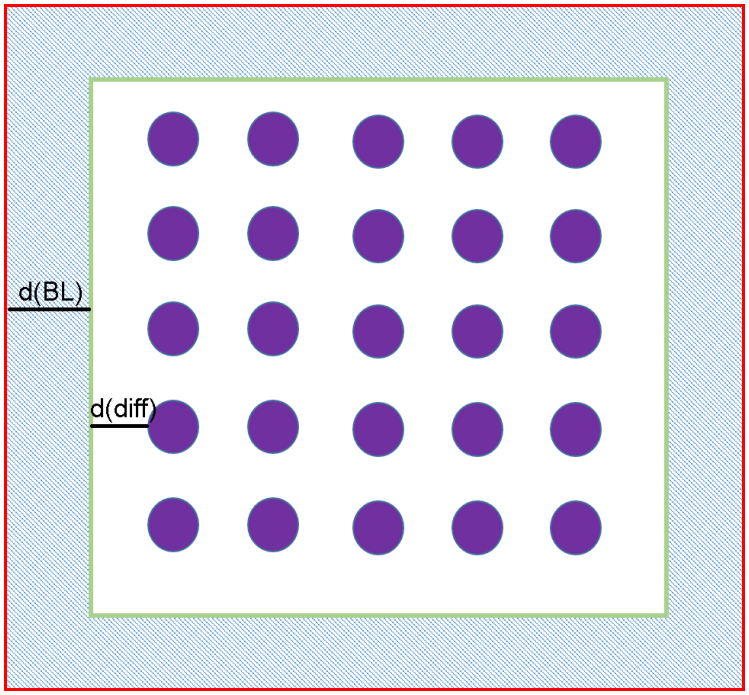

Figure 5.2: Simulation area for the investigation of the diffusive coupling of multiple oscillators as model system for the BZR. The width of the boundary layer is termed d_{BL} and that of the diffusion layer d_{diff}.

around the oscillators only the diffusion term is evaluated, according to a diffusive spread of reactants.

Two types of boundary conditions are applied. In the first set-up, von-Neumann boundary conditions are taken. This describes the situation of a reaction vessel (Petri dish), which is of almost the same size as the reaction area, i.e. gel with catalyst. Thus, in contrast to the active area at the boundaries in the AF model, the concentration of reactants is not reduced at the boundary and an activation of oscillators near the boundary can occur due to this elevated concentration.[6] In the second set-up, an absorbing boundary layer is introduced. Therefore, an additional boundary layer of size d_{BL} is defined, for which, besides the diffusion term, also the reaction term of the RD equations is evaluated. The parameters are chosen in such a way that no activation but a return to the resting state concentration is possible. An accumulation of reactants at the boundary is thus prevented. In this way a situation is described, where the reaction vessel is much larger than the reaction area and reactants diffusing out of the reaction area are not relevant for the further dynamics of the system since their concentration is smaller than inside the reaction area. In Tab. 5.2 the parameters of the FHN model for the different regions of the simulation area are listed.

[6] Concentration is elevated by reaction at the spots and diffuses then outside the reaction area.

Table 5.2: Parameter of the FHN model defined for the different regions of the simulation area (Fig. 5.2). Parameter b for the oscillator region is drawn from a uniform distribution (see description in the main text).

Region	a	$\bar{b}$	c
Oscillator	0.7	b	5.5
passive region	0.0	0	0
Boundary layer	0.7	0.6	1.0

For every oscillator, the parameter b, influencing the self-excitability, is drawn from a uniform distribution with mean $\bar{b}$ and width $N_b \Delta b$. In this way, the experimental fluctuations of oscillator properties and a distribution of oscillator frequencies are introduced into the model. Intrinsic synchronization between the oscillators, occurring without coupling due to equal frequencies, is thus avoided. Initial values of the variables u, v correspond to the resting state $[1.2, 0.6]$, or are drawn from the ensemble of possible values randomly, whereby the probability for the single values are equal. The ensemble of possible values contains always a pair of u, v values to avoid unrealistic combinations of u, v values. It was generated by the sampling 200 equidistant intervals of a representative action potential.

The size of the simulation area depends on the number of oscillator with radius r and distance l_{th}. One side has the length $x = 2 * d_{\mathrm{BL}} + N_s * 2 * r + (N_s - 1) * l_{\mathrm{th}}$, which has not necessarily to be the same in x and y direction. For some simulations, the distance between oscillators and their size was changed along one or both directions. In these cases, the modified size of the simulation area is given by $x = 2 * d_{\mathrm{BL}} + \sum_1^{N_s} 2 * r^i + \sum_1^{N_s - 1} l_{\mathrm{th}}^j$, with r^i the size of the ith oscillator and l_{th}^j the jth distance for N_s oscillators.

Chapter 6

Experiment description (BZR)

The BZR experiments are conducted in several steps. First, a silica gel is prepared. On the one hand, this enables the creation of spatial catalyst distributions to define the single oscillators. On the other hand, it prevents disturbances of the patterns due to, e.g., convection. As precursor, a solution ($15 - 25$ weight %) of sodium meta silicate (Sigma Aldrich) is produced by dissolving it in distilled water. The gelation is initiated by addition of diluted sulphuric acid ($1-2.5$ M[1]) to a small amount of the meta silicate solution. The resulting solution is poured into a Petri dish and given some rest for a certain time (typically one hour) to complete gelation. Subsequently, the resulting gel is rinsed with strongly diluted sulphuric acid (0.25 M) and distilled water. The gel is stored in distilled water to prevent drying.

The next step of the BZR experiment is the generation of single BZR oscillators by immobilization of the catalyst in a predefined pattern inside the silica gel. As described in Ch. 3, the components of the reaction solution are malonic acid, sodium bromate, sulphuric acid and Ferroin. Beside the catalyst, an immobilization of malonic acid can be considered, too. The other reaction components are too small to be trapped by the pores of the gel, since the immobilization is mainly physically by a reduced diffusion due to the pore size. However, attempts to immobilize malonic acid were not successful, meaning that prepared patterns were not stable. Furthermore, the replacement of malonic acid by other substances as glucose, saccharose, novolak, ascorbic acid, polyethylenglycol (PEG), poly-vinylpyrrolidon (PVP) or fructose, which seemed to be more promising with respect to the possibility to immobilize them, did not result in a stable immobilization of the reducing agent. The lacking success was caused either by the precipitation of the substance upon mixing with the meta silicate solution (novolak) or the missing possibility to observe an oscillation (ascorbic acid, PEG, PVP and fructose). Glucose and saccharose could be immobilized and oscillating patterns were observed, but the period of oscillation was too large for the observation of a sufficiently large number of oscillations during the experimental time. Thus, only the

[1]M=mol/l

immobilization of the catalyst was applied for the definition of single oscillators.

Spatial inhomogeneous distributions of the catalyst were created by plotting the catalyst with the aid of the 'Nanoplotter NP 1.2' (GeSim) onto the gel. The 'Nanoplotter' enables to apply small amounts of Ferroin (0.4 nl per drop) at pre-defined positions of the gel. The size of the Ferroin spots, their distance and the Ferroin concentration can be selectively tuned by changing the number of droplets per spot, their position and the concentration of Ferroin solution. After application of the catalyst, it is given about ten minutes time to diffuse completely into the silica gel. An example of an array of Ferroin spots (red) in a silica gel (white) is shown in Fig. 6.1.

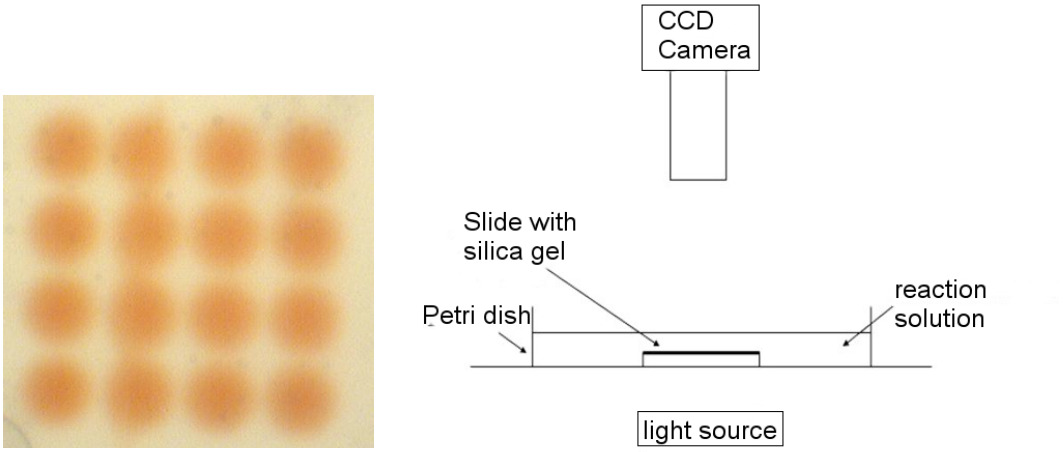

Figure 6.1: *Left:* Array of Ferroin spots (red colour) shortly after plotting on the silica gel by the aid of the 'Nanoplotter'. *Right:* Schematic representation for the experimental set-up used for BZR experiments.

In the next step the reaction is started by addition of the previously mixed, remaining reaction components (malonic acid, sodium bromate and sulphuric acid). Composition of the standard reaction solution is given in Tab. 6.1. The Petri dish is placed on a luminous plate and JPEG pictures of the silica gel are recorded with a CCD camera every 10-30 s. Subsequently, time series of the colour of the catalyst are extracted and evaluated as described in Ch. 6.2. Figure 6.1 shows schematically the experimental set-up and Fig. 6.2 pictures the nanoplotter NP 1.2 from GeSim together with the micro-structured pipette head used for plotting. To experimentally investigate the coupling of multiple oscillators, in particular two steps had to be optimized: first, the immobilization of the catalyst and, second, the image analysis to identify the spots and extract the time series for further analysis. This optimization will be described in the following section.

Table 6.1: Compositions of standard reaction solution for BZR experiments and the range for sodium bromate and sulphuric acid, varied to address the dependence on reaction solution composition.

component	malonic acid	H_2SO_4	$NaBrO_3$	H_2O
standard values	1.1ml (2M)	0.412ml (2.5M)	0.4375ml (1M)	3.2ml
variation (a-d)	1.1ml (2M)	0.412ml (2.5M)	0.4175-0.4575ml (1M)	3.2ml
variation (e-h)	1.1ml (2M)	0.392-0.432ml (2.5M)	0.4375ml (1M)	3.2ml
pure silica gel	1.5ml (2M)	1.5ml (1M)	0.9ml (1M)	3.9ml

Figure 6.2: *Left:* Nanoplotter NP 1.2 from GeSim[3]. *Right:* Micro-structured pipette head made of silicon.

6.1 Optimization of the catalyst immobilization

The quality of the immobilization describes the temporal stability of a pattern inside the gel and the reproducibility of this stability for multiple executions of spotting. Both can be determined by the help of test arrays. Therefore, spots were created on a gel and the evolution of the spot size with time was tracked. A small deviation of the spot size with time is a measure for a good stability. The homogeneity of size inside a spot array and the similarity of the temporal size evolution for repeated executions of the experiments (gel and spot preparation) stands for a good reproducibility. Good stability means here less than 10% size change during the time of one BZR experiment ($\approx$ 2 h) and good reproducibility means spot sizes varying only by ten percent.

Immobilization times, i.e the time for which the spot size changed only slightly, are in the range of minutes up to hours for pure silica gels of equal compositions. Due to this range, it is clear that a large deviation between immobilization times is observed and the reproducibility is quite low. This low reproducibility can be addressed partially to the ageing of the meta silicate solution, which can be explained by the titration curves of sodium meta silicate with sulphuric acid shown in Fig. 6.3. Typically, adding small amounts of sulphuric acid does not change the pH value of the meta silicate solution (≈ 14) much. For larger amounts, a strong reduction of pH value down to 1-2 is observed, corresponding to the acidic range. The amount of sulphuric acid, for which the switch from basic to acid regime occurs, changes with age of the meta-silicate solution. Preparing a gel by the same protocol could yield different gel properties. This may explain the low reproducibility. A possible explanation of the ageing effect could be the slow acidification of meta-silicate solution by diffusion of carbon dioxide into the solution. However, even silica gels produced from the same, freshly prepared meta-silicate solution and with the same protocol exhibit a low reproducibility, which can not be explained yet. The dryness and the roughness of the surface are another influences on the

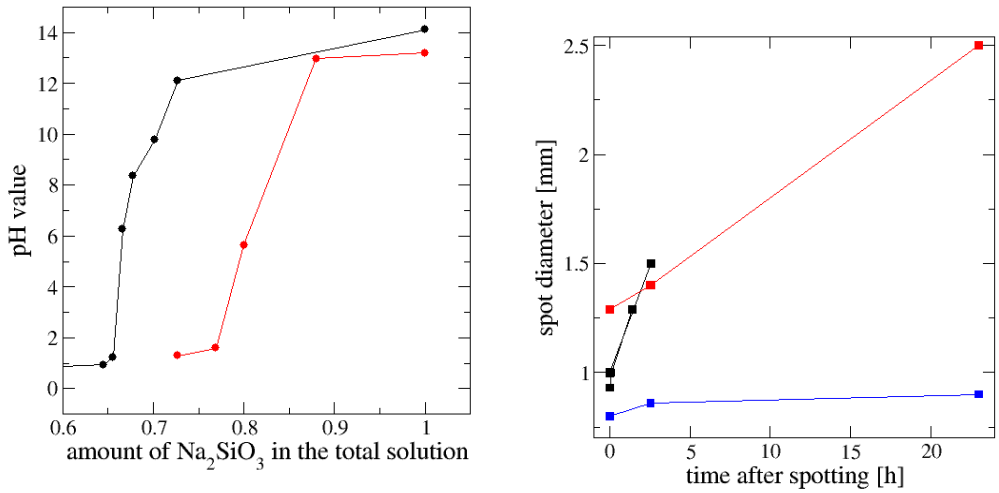

Figure 6.3: *Left:* Titration curve of Na_2SiO_3 solution, either freshly prepared (black) or three months old (red), with H_2SO_4. A shift of the curve to lower values of sulphuric acid is observed for the three months old solution. *Right:* Temporal evolution of spot size for silica gels stored in water in dependence of the concentration of metasilicate solutions: 15% (black), 18% (red) and 25% (blue). The increase of stability of immobilization with increasing concentration can be clearly observed.

immobilisation of the Ferroin spots. If the surface is too wet, a fast, symmetric bleeding of the spots is observed. For rough surfaces, asymmetric spot shapes evolve from the initially symmetric spots.

To improve the immobilization of Ferroin different approaches as modification of the mixture of the gel precursors, addition of substances and usage of gels different from silica were pursued. At first, the modification of compactness and homogeneity of the silica gels was studied by varying the concentration of the meta-silicate solution or modifying the gelation time due to varying the sulphuric acid concentration and amount. Increasing the concentration of the meta silicate solution results in a decrease of the spot size growth with time, possibly due to the higher compactness and smaller pore size of the silica gel. However, silica gels prepared from meta silicate solution with concentrations above 25% were in general more inhomogeneous. Thus, 25% concentration are considered as optimum for the silica gels with respect to immobilization. Changing the amount of sulphuric acid added to the meta silicate solution, modifies the time necessary for completion of the gelation process. Small as well as high gelation times resulted in increased inhomogeneity of the gels compared to the median regime. For 2.5 M sulphuric acid, gelation of meta silicate solution occurs for a ratio of 1:3 to 1:2 of sulphuric acid to meta silicate solution. A ratio of 1:2.5 turned out to be optimal in terms of gelation time and homogeneity of the silica gel. The immobilization time and reproducibility was slightly modified by the composition of the gel solution but it could not be improved sufficiently by this approach.

Table 6.2: Compositions of gels used for immobilization studies

	Na_2SiO_3 solution	H_2SO_4 (2.5 M)	polymer	specialities
Sil-gel	2 ml	0.85 ml	—	—
PEG gel	2 ml	0.75 ml	PEG200, PEG400, PEG600 (0.25-1.0 ml)	dissolved in water (50-100% PEG content)
PSSS gel	2 ml	0.85 ml	PSSS (0.05-0.1 g)	ultra sonic irradiation necessary for homogeneous mixing
PSS-co-PM gel	2 ml	0.85 ml	PSS-co-PM (0.05-0.1 g)	—

The second approach is based on the addition of substances, particularly polymers, to modify the gel network. The idea is to improve immobilization of Ferroin either by reducing the pore size of the gel or by increasing the interaction of the gel with the Ferroin on physical or chemical basis (e.g. charge effects, dangling bond, specific end groups). As additives, PVP, poly-vinylalcohol (PVA), Polyethylenglycol (PEG, Merck, Molecular weight [MW]=200, 400, 600g/mol), Poly(sodium-p-styrene sulfonate) (PSSS , Alfa,

MW 7000g/mol) and Poly(4-styrene sulfonic acid-co-maleic acid)-sodium salt (PSS-co-PM, Aldrich Chemistry, MW=20000g/mol) were tested. PVP and PVA could not be introduced into the gel, since they precipitated upon mixing with the meta silicate solution. PEG, poly(4-styrene sulfonic acid-co-maleic acid)-sodium salt (PSS-co-PM) and PSSS could be mixed with meta silicate solution and the gels could be prepared from this mixture. For mixtures with PEG, the interesting effect that a aqueous two-phase system evolved in dependence on the chain length and mixing ratio, occurred. Thereby, two phases evolve although both phases are aqueous and can be mixed, in principle. In one of these phases, silica nanoparticles were detected, whose size could be determined by Dynamic light scattering (DLS) to be in the single nanometre range. The quality of immobilization was determined with the help of 5x5 spot arrays which were rinsed in distilled water after spotting. Each spot array was recorded over ten minutes and the change of spot diameter was determined from these pictures. The compositions of analysed gels is summarized in Tab. 6.2.

Table 6.3: Spot diameter d and stability in dependence of composition of the gel. The spot size change Δd_1 defines the increase of d in the first hours (1-5h) and Δd_2 for the subsequent 1-2 days after spotting. The abbreviation std d refers to the standard deviation of the diameter distribution in the array and reproducibility describes the variation in spot size mean between different executions of the experiment.

	d (std (d))	reproducibility	d vs t
Sil-gel	0.5-1.5 mm (0.48 mm)	0.5 mm	$\Delta d_1 = 0.6$ mm, $\Delta d_2 = 0.1 - 0.7$ mm
PEG200 gel (50% 0.5ml)	0.5-1.5 mm (0.58 mm)	0.3 mm	$\Delta d_1 = 0.5$ mm, for 0.75 ml: $\Delta d_2 = 0.1 - 0.2$ mm for 0.5 ml, 1 ml: $\Delta d_2 = 0.2 - 0.7$ mm
PEG400 gel (50% 0.5ml)	0.5-1.5 mm (0.9 mm)	0.4 mm	$\Delta d_1 = 0.2$ mm $\Delta d_2 = 0.2$ mm
PEG600 gel (50% 0.5ml)	0.5-1.5 mm (0.8 mm)	0.4 mm	$\Delta d_1 = 0.1$ mm $\Delta d_2 = 0.1$ mm
PSSS gel (0.05g)	0.5-0.8 mm (0.04-0.28 mm)	—	$\Delta d_1 = -0.5$ mm max. 4h measurable
PSS-co-PM gel (0.05g)	0.5-1.5 mm (0.04-0.28 mm)	0.3 mm	$\Delta d_1 = 0.5$ mm, $\Delta d_2 = 0.2$ mm

Analysis of these experiments (Tab. 6.3) revealed that PSS-co-PM and PEG with a molecular weight of 200 to 400g/mol could improve the immobilization compared to pure silica gels. In contrast, the addition of poly(sodium-p-styrene

sulfonate) (PSSS) yielded an increase of bleeding of Ferroin. To study the improved immobilization, different measurements were performed. With energy dispersive X-ray diffractometry (EDX) on dried gels[4] only for PSS-co-PM gels a significant amount of carbon and sulphur could be detected. This indicates that only PSS-co-PM is embedded into the gel. UV-VIS spectroscopy[5] of the dissociation of Ferroin in meta silicate solutions with or without polymer addition revealed that the dissociation rate is decreased if PSS-co-PM is added. One can conclude from these results that PSS-co-PM is incorporated into the gel during gelation and interacts with the Ferroin, when added to the gel. This interaction and incorporation is thought to be the reason for the improved immobilization.

In contrast, UV-Vis spectroscopy with PEG addition revealed an increased dissociation of Ferroin compared to the pure meta silicate solution. Incorporation of PEG in the gel and interaction with Ferroin seems to be not occurring, as indicated by the EDX and UV-Vis spectra. SEM[6] was performed to test if the micro-structure of the gels was changed. SEM images of dried gels (see Fig. 6.4) showed a modified micro-structure of PEG gels in comparison to pure silica, PSS-co-PM and PSSS gels. This micro-structure is characterized by an increased grain size[7] and reduced pore size. This relation between micro-structure and diffusion could be confirmed by nuclear magnetic resonance (NMR) measurements, done and analysed by Dr. Carlos Mattea (Department of Technische Physik II, TU Ilmenau), since a reduced diffusion coefficient of water was identified for PEG gels (see Fig. 6.5). PEG gels are, therefore, considered to improve the immobilization of Ferroin by a reduced pore size and modified micro-structure of the gels, which is a different mechanism than for PSS-co-PM gels. However, due to the formation of the aqueous two-phase system, PEG gels are often more inhomogeneous and less reproducible than the PSS-co-PM gels. Thus, the latter were chosen for the investigations of coupling of multiple oscillators. The standard composition of the gel was thereby 2 ml Na_2SiO_3 (25%), 0.1 g PSS-co-PM and 0.85 ml H_2SO_4 (1 mol/l).

As third approach to optimize the immobilization, exchanging silica gels by other gels was tested. Agarose exhibited an even worse immobilization, whereas commercial Nafion membranes N117 showed an improved immobilization. Thereby, smaller spots and almost no diffusion of Ferroin was observed. However, an oscillating reaction was not seen. Either a stable resting state

[4]EDX spectra were recorded with a detector attached at a Hitachi S 4800II and analysed with Thermos Software.

[5]UV-Vis spectra in the range of 350-600 nm were recorded every 60 seconds for 30 minutes with a Specord 400 of a 1:10 diluted solution of 0.01 ml Ferroin, 1 ml of 25%-metasilicate solution and the polymer (0.5 ml of PEG200-50% solution, 0.05 g PSS-co-PM or 0.05 g PSSS).

[6]SEM images were measured at a Hitachi S 4800II on dried gel, which were sputtered with Platinum for 3 min at a current of 20 mA to avoid charging.

[7]grains are the particles constituting the gel network

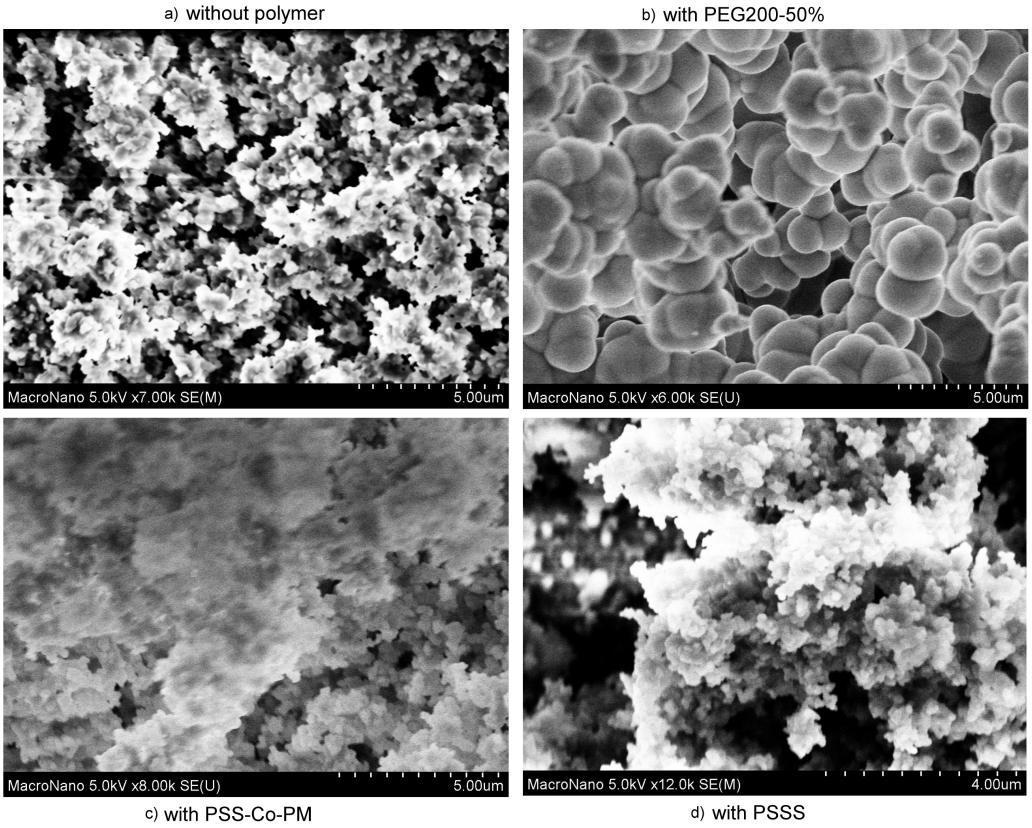

Figure 6.4: SEM images of silica gel with different additives: a) pure silica gel, b) 0.3 ml PEG200(50%) ($\approx$ 10 vol% of the gel solution before gelation), c) 0.05 g PSS-co-PM (Na_2SiO_3:PSS-co-PM $\approx 1:10$), and d) 0.05 g PSSS (Na_2SiO_3:PSSS $\approx 1:10$) (from [224]).

(Ferroin red) or a stable excited state (Ferroin blue) occurred, although different compositions of the reaction solution were tested. This behaviour could be caused by the strong interaction of Ferroin with the sulphonic groups of the Nafion membrane or the selective conductivity for ions, i.e. cations propagate through the membrane and anions do not.

Concluding, adding PSS-co-PM to the silica gel was the method of choice for the BZR studies, because these gels exhibited the best pattern stability and reproducibility. Results from this study about the immobilization of Ferroin in silica gels and its improvement were published in [224].

6.2 Image analysis: Spot detection and time series extraction

The images recorded with the CCD camera have typically a size of 1392 pixel $\times$1082 pixel. The time step between the pictures can be chosen between 0.5 –

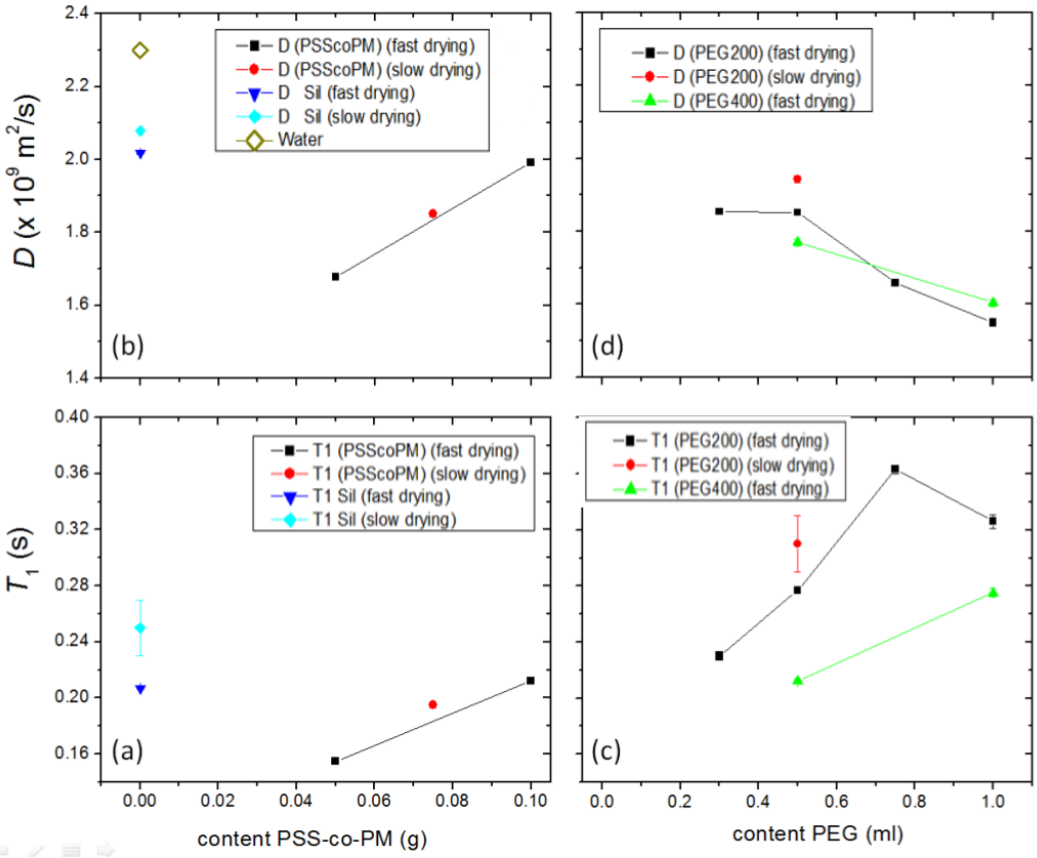

Figure 6.5: Results of the NMR measurements (Diffusion coefficient D and T_1 relaxation time) of protons in silica gels with different amounts of additives: (a)+(b) PSS-co-PM gels and (c)+(d) PEG gels (from [224]). NMR measurements and evaluation of data were done by Dr. Carlos Mattea (TU Ilmenau).

30 s. Per experiment around 500-1800 pictures are recorded (according to $\Delta t = 5$ or 0.5 s, respectively). To analyse the patterns in dependence of spot size and distance, the Ferroin spots in the recorded images have to be detected. This is needed, to correlate the patterns with the real spot size and distance, measured in the experiment. The length of one pixel is determined by capturing an image of a ruler before each experiment. The number of pixels corresponding to the distance of 1 mm in the image is measured 10 times, which yields the conversion between pixel and mm. The demand of memory for generation of the time series of all pixel would be tremendous ($1380 \times 1080 \times 1800$ time steps $\times$ 3 colour values $\approx$ 32GB). Thus, only pixel, which coincide with Ferroin spots, are used for time series extraction. By the help of spot detection, the real spot size and the relevant pixels for time series extraction are determined. Since a large number of experiments are performed, automatic spot detection would be favourable. Therefore, a program was written in Matlab, consisting of multiple steps. First, the image is cut to the interesting

region. The boundaries for this are set manually. Cutting the image reduces the memory demand and facilitates the extraction of the background from the image by reducing disturbances due to particles or bubbles, which are outside of the region of interest. For further analysis, the second colour value of the image array is typically applied. This is possible, since the course of the three different colour values is similar (see Fig. 6.6). Only the difference between the minima and maxima depends on the chosen colour value. The second colour value exhibited the best contrast.

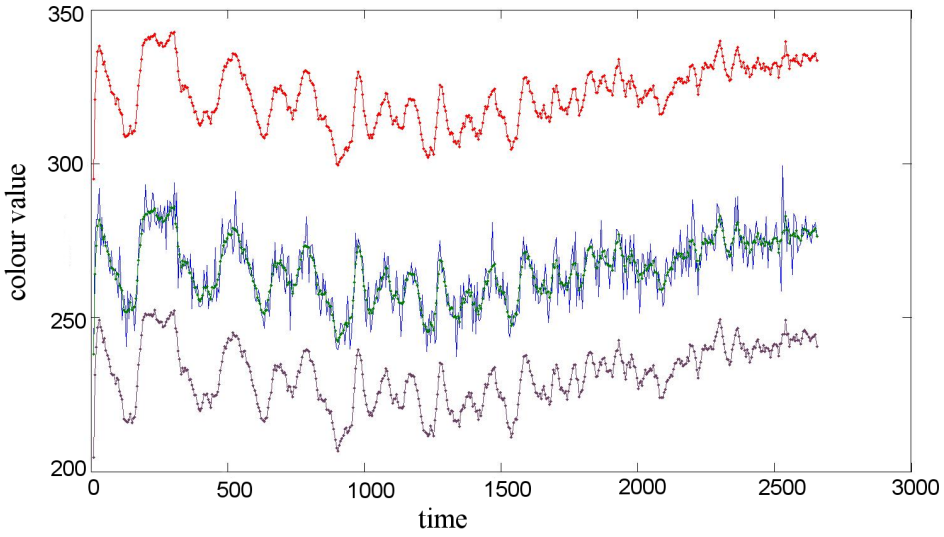

Figure 6.6: Time series extracted for the three different colour values of the RGB images. Upper and lower curves were smoothed with a moving average filter.

The next step in image analysis is the background subtraction. Therefore, the background is determined by applying a moving average filter with a subset larger than the spot size. The result is subtracted from the image. Than, the image is transformed into a binary one according to the following rule. If the colour value $col(x_i, y_i) < col_{\mathrm{th}}$ for point $[x_i, y_i]$, than $col(x_i, y_i) == 255$ (maximum of colour scale). Otherwise, $col(x_i, y_i) == 0$. The threshold col_{th} is set manually, since the images of different experiments differ in the colour range due to changes of the illumination and concentration of the Ferroin. Subsequently, the spot size, spot area and some more properties of the regions with $col = 255$ are determined by the help of the *'bwconncomp'* function, which identifies connected regions. Pixels, whose colour value was set to zero, are considered as background.

To avoid artefacts, i.e. particles, bubbles or other inhomogeneities, different queries are included. First of all, the mean $\bar{A}_s$ and the standard deviation σ_A of the spot area of all spots in one array are calculated. Then, detected spots with $A_s^i < \bar{A}_s - 2\sigma_A$ or $A_s^i > \bar{A}_s + 3\sigma_A$ are identified as artefacts.

This accounts for the fact that the spots inside the array should be quite similar in size, consequently strong deviations from the mean size correspond to bubbles, particles etc. Next, the boundary of the spot is determined with *'bwboundaries'*. Artefacts are spots, whose circumference is too large, $U_s > 2\bar{U}_s$, or too small $U_s < 0.5\bar{U}_s$ compared to the mean value $\bar{U}_s$, since artefacts usually exhibit a ragged boundary.

In Fig. 6.7 images of the different steps of spot detection are shown for a representative spot array image. In some cases, the determined spot size

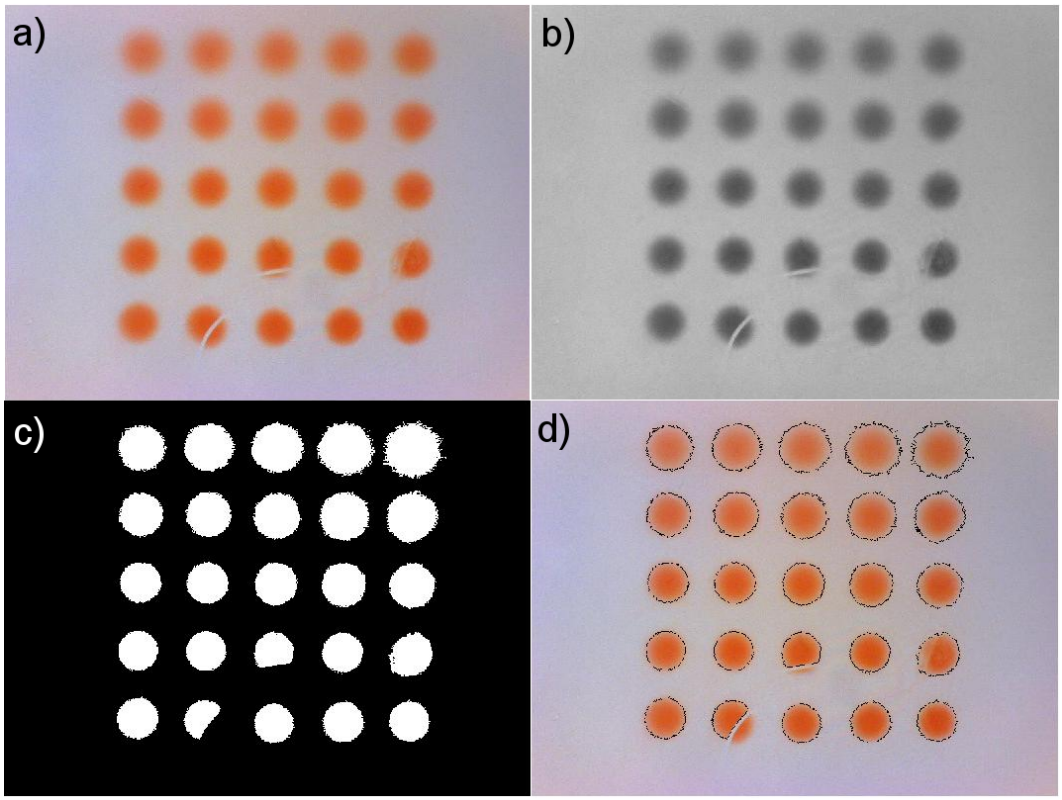

Figure 6.7: Illustration of image analysis steps for detection of spots. The image analysed is shown for different steps of the process: a) original image recorded with CCD camera, b) after cutting and reduction to one colour value, c) upon conversion into binary image, where pixels with colour value smaller than a threshold are set to 255, and larger ones to 0, d) detected spot boundary (black), determined with *'bwboundaries'* from the detected, connected regions, which were identified with *'bwconncomp'*.

corresponded poorly to the real spot size, since its determination strongly depended on the manually set threshold. Gradients of the colour values, e.g. due to the background illumination, can yield over- or underestimated spot sizes. Unfortunately, this problem could not be solved simply by background subtraction. To address this problem, a second method was implemented to check the determined results for the spot size. Therefore, profiles of the colour

value are extracted along the x and the y direction, which cross the spot centre and are 2.5 times the previously determined spot size. The spot centre was either taken from the previous detection or, if detection of the spot failed, given manually. The minimum of this profile line, corresponding to the actual spot centre, was determined. The spot size, i.e. the diameter, was taken as the full width half maximum of this peak. For the whole spot detection routine, one image per experiment had to be analysed.

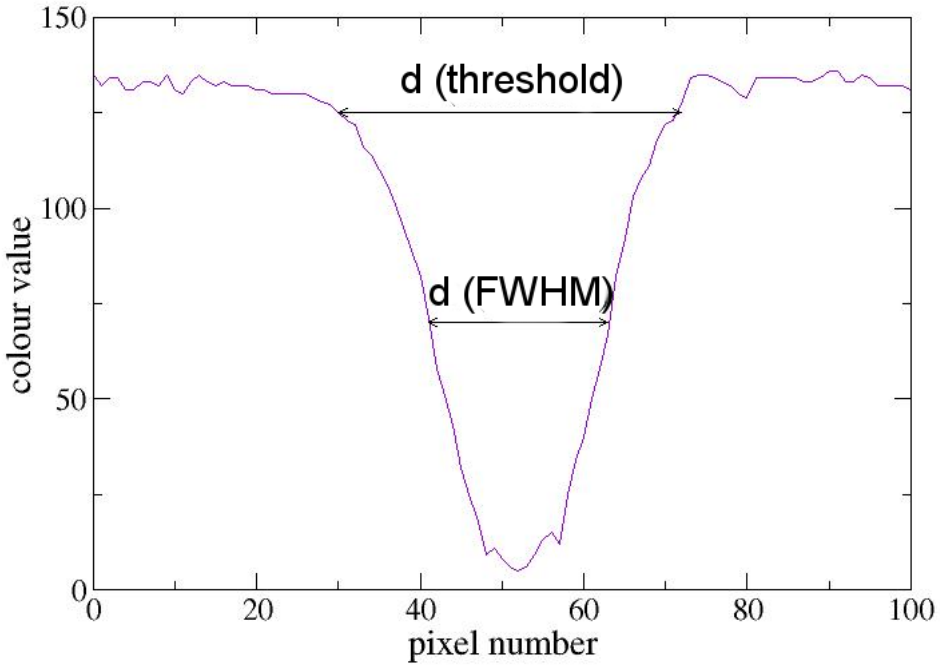

Figure 6.8: Profile line across spot centre (see text for description) used for extraction of spot size. d(threshold) is the value of the spot diameter determined from the connected areas according to the manually set colour threshold. d(FWHM) is the spot size as detected by finding the minimum in the profile line and taking the FWHM values as spot diameter.

Following the spot detection, extraction of time series was performed. Therefore, the colour values of relevant pixels, i.e. corresponding to a spot, for the different time steps were merged into one time series per pixel. The resulting time series are quite noisy, as can be seen in Fig. 6.6 for the time series in the middle panel. To allow easier analysis, the time series were smoothed with a moving average filter. The upper and lower curve in Fig. 6.6 are examples of smoothed times series. A further reduction of noise and an increase of signal-to-noise ratio is obtained by averaging five time series, consisting of the spot centre pixel and its four nearest neighbours. The time series in Fig. 6.6

exhibit a clear oscillation between red (maxima) and blue (minima) colour of Ferroin, corresponding to the resting state (reduced state of Ferroin) and excited state (oxidized form of Ferroin). A variation of the mean value of the time series is visible, as well as a shortening of the oscillation period and amplitude. These occur due to changes of the illumination, bubbles, consumption of reactants, a warming of the reaction solution and the bleaching of Ferroin by the diffusion and the involved acids. As trend correction the routine *'detrend'* was used. Furthermore, jumps in the times series as caused by sudden changes in illumination or similar, are filtered. Therefore, phase jumps in the time series are detected, which are smaller than 2π but larger than 1.5π. The time series before and after the phase jump is averaged and the mean values are compared. If these mean values differ much, the phase jump is identified as an amplitude jump in the time series. Then the time series is analysed separately before and after the jump. Otherwise, an incorrect frequency and phase would be calculated.

In the next chapter, the methods to determine properties of the time series (phase, frequency) and to analyse the coupling between the oscillators (synchronisation regularity of patterns) are described. The methods are applied to the data from the experimental and numerical studies.

Chapter 7

Data analysis techniques (AF+BZR)

With the methods presented in the following the time series from the experimental and theoretical studies are analysed and their properties, such as phase, frequency and fractal dimension, are determined. By calculating the distribution of local frequencies as well as correlation and phase synchronisation for all pairs of oscillators or points of the simulation area, respectively, the regularity of the patterns and coupling strength can be determined. While for the distribution of local frequencies only the minima of the time series are taken into account, phase synchronisation and fractal dimension are sensitive also to the signal shape. Thus, these parameters should be more appropriate to detect small variations. Due to their high sensitivity, their application to the experimental data was not favourable.

7.1 Phase

The phase of the time series is calculated on the basis of the Hilbert transform from the quasi-continuous signal, i.e. the time series with intervals equal to the inverse detection rate. For a continuous, real signal $x(t)$ the corresponding imaginary part $\tilde{x}(t)$ is given by

$$\tilde{x} = \frac{1}{\pi} \text{P.V.} \int_{-\infty}^{\infty} \frac{x(t')}{t - t'} dt' \tag{7.1.1}$$

according to the Hilbert transform with P.V. denoting the Cauchy principal value. For the quasi-continuous signal the transformation is done in three steps: (i) fast Fourier transform (FFT) of the original signal $x(t)$, (ii) multiplication of the spectral components $x(f)$ by $-i\text{sign}(f)$ of frequency f and (iii) back-transformation of the signal into the time domain by applying inverse FFT, finally yielding $\tilde{x}(t)$. The phase of the signal is then determined from

$$\varphi(t) = \arctan\left[\frac{\tilde{x}(t)}{x(t)}\right]. \tag{7.1.2}$$

7.2 Frequency

The frequency is determined in two different ways, one way is based on the phase and the second one on FFT. The direct detection of minima for frequency determination is not successful, in particular for the experimental signals due to the high noise level. Thus, the minima are identified by the phase. The phase increases linearly from 0 to 2π within one period of the oscillation and than jumps back to 0. These jumps are used for the detection of the minima. Due to the discretization and the noise, jumps will not be exactly 2π. Thus the threshold is set to 1.5π for the phase difference. The frequency is given by the inverse mean of the intervals between the detected phase jumps. Only the second part of the time series is used for the frequency determination and the averaging is done over the ten last detected intervals. The reason for this is to ensure that the frequency is determined from stationary patterns. In cases, where the temporal evolution of the frequency needs to be taken into account, a moving average containing five intervals is applied.

The second method consists of the FFT of the time series, smoothing of the frequency spectrum and determination of the first maximum. The influence of noise results in difficulties for detecting the maximum. The determination on the basis of phase jumps has proven as the most stable and reliable method for both data sources (simulation and experiment).

7.3 Correlation

Correlation of pairs of time series is based on the calculation of the empirical correlation coefficient given by:

$$C(u_k, u_j) = \frac{\sum_{i=1}^{n}(u_k(t_i) - \overline{u_k})(u_j(t_i) - \overline{u_j})}{\sqrt{\sum_{i=1}^{n}(u_k(t_i) - \overline{u_k})^2 \sum_{i=1}^{n}(u_j(t_i) - \overline{u_j})^2}} \tag{7.3.1}$$

Indices k, j represent the grid points, index i numerates the different time steps t_i and $\bar{u} = 1/n \sum_{i=1}^{n} u(t_i)$ is the mean value of the time series. The function *'corrcoeff'* of Matlab is used for calculation.

7.4 Phase synchronisation

To determine the phase synchronisation between two signals the phase difference between them is calculated for every time step and subsequently the distribution of these phase differences. For regular propagation of periodic signals, i.e. high synchronisation, a constant phase difference or a sharp maximum of the distribution of phase differences will be observed. In the case of no synchronisation, the distribution broadens and exhibits no pronounced maxima, approaching a uniform distribution. The strength of synchronisation can be quantified by different synchronisation indices derived from the distribution of

the phase differences, as described in [225]. In this work, an order parameter for the phase coherence was applied, given by:

$$\Phi = \frac{2}{N_g(N_g-1)} \sum_{j>k}^{N_g} \left| \langle \exp[i(\varphi_j(t) - \varphi_k(t)] \rangle_t \right| . \tag{7.4.1}$$

Here, N_g is the number of grid points or oscillators and $\varphi_j(t)$ is the phase at point j, and $\langle \ldots \rangle_t$ describes the time average. In practice, we have taken a moving average $\langle \ldots \rangle_t = T^{-1} \int_{t_0}^{t_0+T} \mathrm{d}t \ldots$ in a time interval larger than the minimal inverse frequency (e.g. f_1 or f_2 for AF studies) and checked that Φ fluctuates around a constant value after evolving the system into a stationary state. The synchronisation is calculated for all pairs of points in the grid (AF) or all pairs of oscillators (BZR). Thus, the order parameter is used to quantify regularity of the excitation pattern for the AF system and the dependence of the synchronisation on the distance between the spots, allowing to draw conclusions about the coupling strength for the BZR system.

7.5 Regularity of excitation patterns

To study the transition from regular to irregular excitation patterns, the regularity of the excitation patterns has to be quantified. This is done on the basis of the Shannon entropy of the distribution of local frequencies. Therefore, the distribution of local frequencies is determined by dividing the frequency range into N_b intervals of width Δ and calculating the probability

$$p_l = \frac{n(f_l \leq f \leq f_l + \Delta)}{N_\mathrm{g}} \tag{7.5.1}$$

to find the frequency f in the lth interval. The normed entropy of the distribution of local frequencies, given by

$$S = -\frac{\sum_{l=1}^{N_\mathrm{b}} p_l \ln p_l}{\ln N_\mathrm{b}} \ , \tag{7.5.2}$$

is an appropriate measure to evaluate the strength of the irregularity. In the case of a single frequency, where the distribution is represented by a delta function, $S = 0$. For a uniform distribution of frequencies, the maximal value of the entropy $S = 1$ is observed. Regular excitation patterns typically exhibit a narrow frequency distribution peaked at about the external pacing frequency or the natural frequency of the oscillators. For irregular excitation patterns with wave breaks or re-entrant circuits multiple frequency bands, a broader frequency distribution is expected with a lower entropy value.

Part III:
Results

Chapter 8

AF induced by interplay of two pacemakers

In this chapter, results about the interplay between two pace-making sources located in two different regions as a generating and maintaining mechanism for AF will be presented. First, results from calculations with the FHN model are described, followed by similar investigations using the BOCF model. Thereby, the comparison between the results from both model is used to elucidate system-specific and generic features occurring due to the interplay of the two active sources.

For clarification, the active source modelling the sinoatrial node will be denoted as primary pacemaker and the perturbing source, representing a spiral wave or ectopic foci, secondary pacemaker. Waves emitted by the primary pacemaker are termed primary waves and secondary waves are emitted by the secondary pacemaker. The frequency of the primary pacemaker is named pacing frequency f_1 and that of the secondary pacemaker perturbation frequency f_2.

It will be tested if, on the one hand, the secondary pacemaker (the perturbing source) will have a destabilizing effect on the previously regular propagation of the waves emitted by the primary pacemaker, i.e. the model of the sinoatrial node. On the other hand, a stabilizing effect regularising irregular propagation patterns of the primary waves can also occur. The regimes for these effects will by analysed with focus on the relation between the pacemaker frequencies and the regularity of the patterns will be quantified with the above described methods, see Ch. 7.4 and 7.5.

8.1 Results from the FHN model

The occurrence of irregular patterns in the temporal domain is demonstrated in Fig. 8.1. There, the time evolution of u is shown for three points near the bridge of the simulation area (Fig. 5.1) for two different perturbation frequencies $f_2 = 0.1$ [Fig. 8.1 a)] and 0.105 [Fig. 8.1 b)]. The irregularity is expressed in

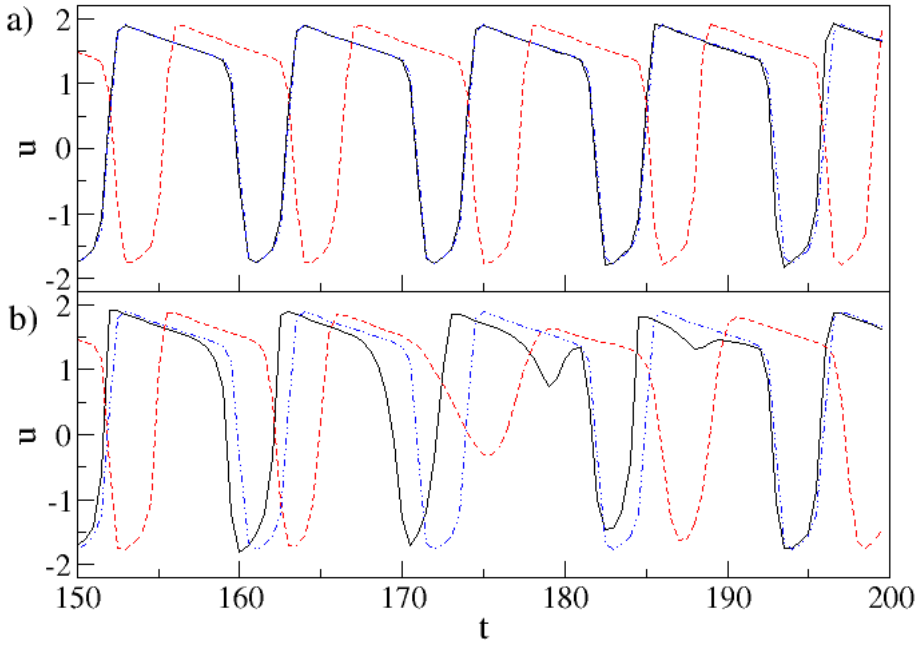

Figure 8.1: Time evolution of u at three points (see Fig. 5.1) $P_1 = (11.49, 5.34)$ (black solid line), $P_2 = (11.33, 6.34)$ (red dashed line) and $P_3 = (11.94, 6.15)$ (blue dash-dotted line), for $f_1 = 0.091$ and two different perturbation frequencies (a) $f_2 = 0.1$, and (b) $f_2 = 0.105$.

changes of the action potential shape $u(t)$ [Fig. 8.1 b)] in comparison to the regular behaviour for the slightly lower perturbation frequency [Fig. 8.1 a)]. Unsuccessful activations ($t = 175$ for P_2 or $t = 189$ for P_1) and a different peak shape ($t = 170$ or 183 for P_1) can be seen. This irregular behaviour is a local phenomenon, since the time evolution of $u(t)$ for point P_3 is not changed besides its small distance to P_1 and P_2. Thus, spatial irregularity is suspected, which would be expressed by wave breaks, wave fragments or re-entrant characteristics. With respect to the patterns observed in region R, three different types of (spatial and temporal) irregularities are distinguishable. Their spatio-temporal characteristics will be described in the following section.

8.1.1 Spatio-temporal patterns in the case of irregularities

Irregularity type I occurs for high pacing frequencies f_1 resulting in a detachment of planar waves from the lower corner of the bridge. A subsequent curling of this open end opposite to the propagation direction is observed. Without

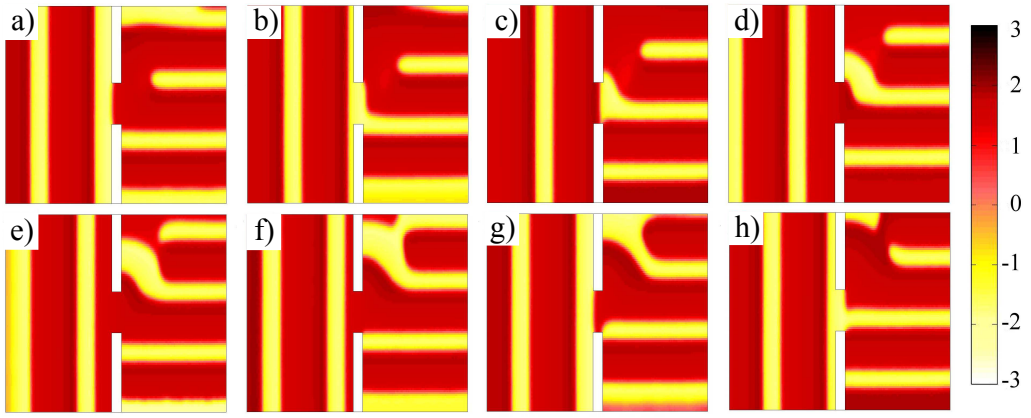

Figure 8.2: Spatio-temporal patterns (u) for irregularity type I ($f_1 = 0.117$ and $f_2 = 0.091$) with $\Delta t = 4$ for (a)-(e) and $\Delta t = 3$ for (f)-(h). Yellow refers to the excited state and red to the excitable/refractory state. Time evolution is shown in Movie S1 in the Supporting Material.

the secondary pacemaker, re-entrant and irregular patterns can be formed. However, in the presence of the secondary pacemaker, the detachment of primary waves and subsequent formation of irregular patterns can be avoided. A typical time evolution of spatial excitation patterns is shown in Fig. 8.2 and movie S1 in the Supporting Material. In a) a detached primary wave front, a primary wave approaching the lower corner of the bridge and a secondary wave approaching the bridge from the left, can be seen. The latter two merge, while the primary wave transverses the bridge [Fig. 8.2(b,c)]. Thereby, the detachment of the primary wave from the bridge with formation of an open end and subsequent curling is suppressed by the secondary wave [Fig. 8.2(d)]. However, since the frequencies of the primary and secondary pacemaker are not similar, not every primary wave front merges with a secondary wave front, as can be seen by the primary wave with an open end in [Fig. 8.2(a-e)]. Thus, the initially regular wave, stemming from the collision of primary and secondary wave at the bridge, is perturbed by the primary wave front with open end which started already to curl [Fig. 8.2(e)]. A fork-type shape pattern results [Fig. 8.2(f)]. Thereby, the lower right part of the fork cannot propagate as fast as the left part due to the refractory area ahead. A rupture of the excitation fronts takes place [Fig. 8.2(g-h)] which is perturbing the subsequent wave front, stemming again from the fusion of a primary and a secondary wave. Hence, despite of the initial stabilization of primary waves by the secondary waves due to avoidance of a detachment, eventually an irregular excitation pattern occurs in the upper part of region R.

Irregularity type II is based on the detachment of secondary waves from the corners of the bridge after passing it. It occurs for high perturbation frequencies f_2. This detachment results in a wave front with two open ends, a wave fragment, which would lead to the formation of two-counter rotating

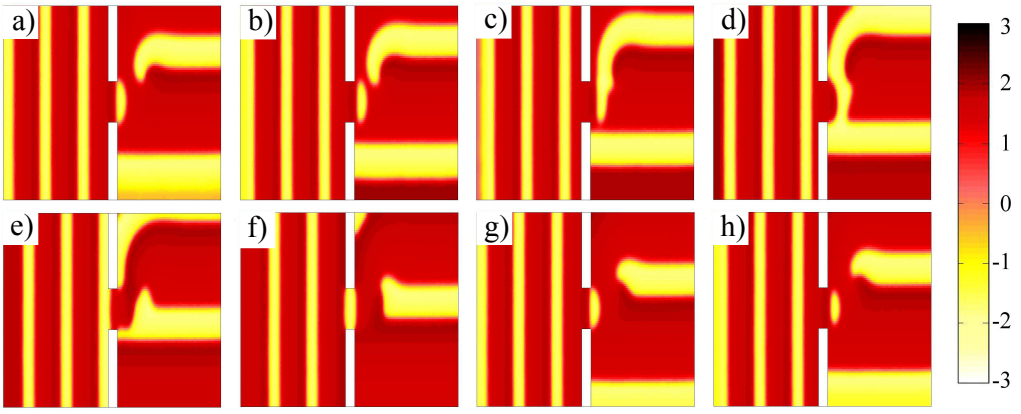

Figure 8.3: Snapshots of spatio-temporal patterns for irregularity of type II ($f_1 = 0.091$ and $f_2 = 0.105$) with $\Delta t = 2$ for (a)-(d) or $\Delta t = 4$ for (e)-(h), respectively. Yellow refers to the excited state and red to the excitable/refractory state. Time evolution is shown also in movie S2 in the Supporting Material.

spirals in the absence of the primary pacemaker. In the presence of a primary pacemaker, complex excitation patterns emerge in region R due to the interplay between the wave fragment and the primary waves. Furthermore, the high frequency excitation at the bridge due to the secondary waves generates even more complex patterns since primary waves are thus forced to detach from the bridge. A representative of spatio-temporal patterns occurring for irregularity type II are shown in Fig. 8.3 and in movie S2 in the Supporting Material. A wave fragment formed by the detachment of a secondary wave can be seen in Fig. 8.3 (a). It merges with the regular, planar primary wave approaching from the lower part of region R [Fig. 8.3 (d-e)] yielding thus a wave front with an open end on the left side [Fig. 8.3 (f-h)]. This periodic wave front pattern with open end in the upper part of region R (compare Fig. 8.3 a) and h)), curls and merges with the upper part of the wave fragment [Fig. 8.3 (b-d)]. A re-entrant like pattern is thus formed. However, this irregularity is spatially confined to the region near the upper corner of the bridge, since wave fronts in the lower and upper part of region R exhibit a regular, planar shape.

Irregularity type III occurs in the lower part of region R for $f_2 > f_1$ and $f_2 < f_{\mathrm{det}}$(representative time evolution is shown in movie S3 in the Supporting Material). No detachment of waves occur. Secondary waves after passing the bridge become circular shaped since both ends are still connected with the boundaries, as can be seen in Fig. 8.4 a)-f). Due to their shape and a higher frequency these circular waves expel the primary waves after a certain time. Without the primary pacemaker, the circular wave fronts would be a regular excitation pattern in region R with the only modification that region R is paced with f_2 instead of f_1. However, due to the ongoing activity of the primary pacemaker, small fragments of primary waves are generated in between the circular secondary waves [see Figs. 8.4 (a), (b), (g), and (h)].

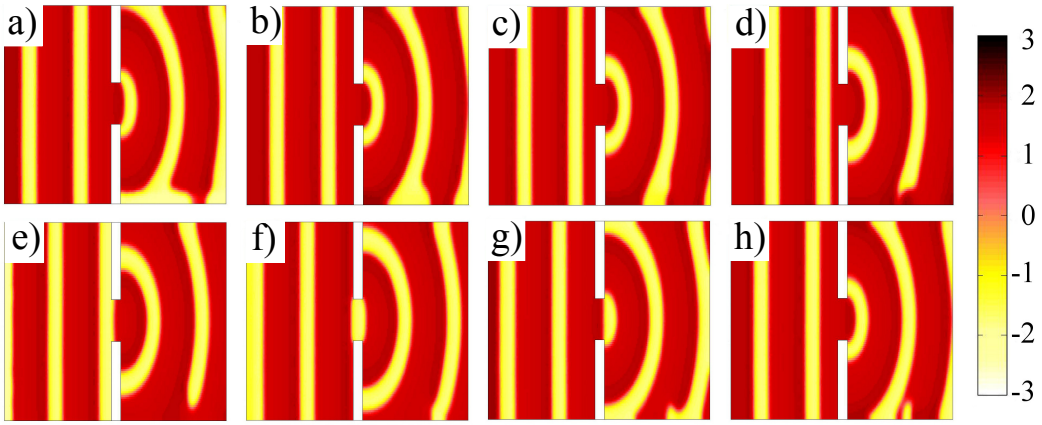

Figure 8.4: Snapshots of spatio-temporal patterns for irregularity of type III ($f_1 = 0.067$ and $f_2 = 0.100$) with $\Delta t = 2$ for (a)-(d) and $\Delta t = 4$ for (e)-(h). Yellow refers to the excited state and red to the excitable/refractory state. Time evolution is also shown in movie S3 in the Supporting Material.

The ongoing activation by the circular waves prevents a spread of these wave fragments. Thus, irregularity type III is confined to the lower boundary layer of region R.

The transient time $t_{\rm tr}$, after which irregularity type III occurs counted from the time of initiating both pacemakers, depends on both, f_2 and f_1. Thereby, the first primary and the first secondary wave front collide and annihilate at half of the path between the primary and the secondary pacemaker, since they are initiated at the same time and propagate with about the same speed. The collision site is moved in direction of the primary pacemaker, if $f_2 > f_1$, since the next secondary wave front is initiated earlier than the next primary wave front and thus can propagate a longer way. The transient time is the time interval from the first initiation of wave fronts until the first secondary wave front reaches the lower boundary of region R. It can be determined by measuring the onset of the irregularity, e.g. by detecting a significant variation of a regularity quantifying parameter as $\tilde{\Phi}(t)$ (Eq. (7.4.1) without time averaging) from its value in the unperturbed system. Thereby, $\tilde{\Phi}(t, f_1, f_2) = \frac{2}{N_g(N_g-1)} \sum_{j>k}^{N_g} \left| \exp[i(\varphi_j(t) - \varphi_k(t)] \right|$ and $t_{\rm tr}$ is the time instant, where $(\tilde{\Phi}(t_{\rm tr}, f_1, f_2 = 0) - \tilde{\Phi}(t_{\rm tr}, f_1, f_2) = 0.2)$ with $\tilde{\Phi}(t_{\rm tr}, f_1, f_2 = 0)$ being the order parameter in the unperturbed system. The resulting dependence of $t_{\rm tr}$ on f_2 for different values of f_1 is shown in Fig. 8.5. For fixed f_1, $t_{\rm tr}$ decreases with f_2, whereas it increase with f_1, if f_2 is kept constant. It is diverging for f_2 approaching f_1. The behaviour of $t_{\rm tr}$ can be intuitively understood if one focusses on the time the secondary waves need to penetrate into region R and expelling the primary waves. This should occur the faster the larger the difference $(f_2 - f_1)$.

The functional dependence on f_2 and f_1 can be determined if one considers

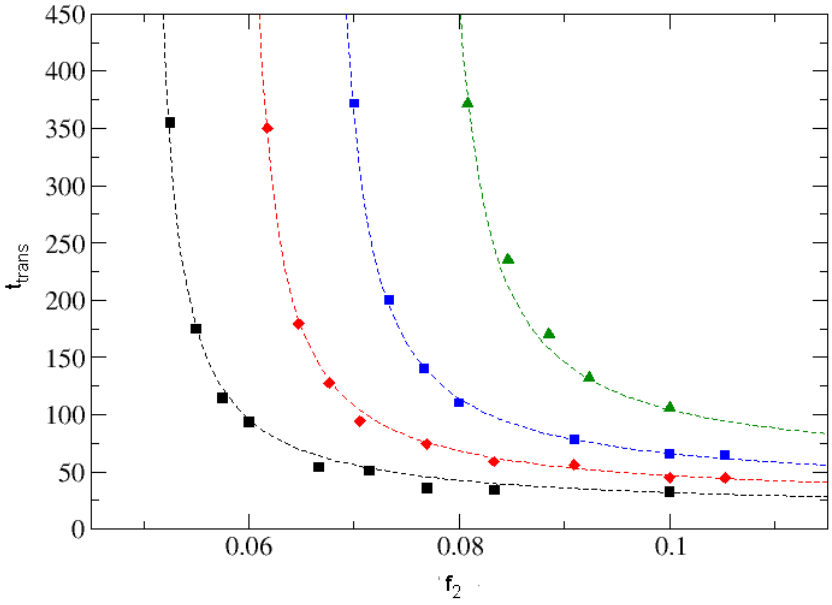

Figure 8.5: Dependence of transient time $t_{\rm tr}$ on f_2 for various values of $f_1 = 0.050$ (black circles), 0.059 (red diamonds), 0.067 (blue squares), and 0.077 (green triangles). Dashed lines are calculated according to Eq. (8.1.4) with $t_a = 0$ for $f_1 = 0.05$ (black line), $t_a = 9$ for $f_1 = 0.0588$ (red line), $t_a = 18$ for $f_{pace} = 0.0667$ (blue line) and $t_a = 36$ for $f_1 = 0.077$ (green line).

two facts (i) secondary waves have to reach the lower boundary of region R and (ii) each secondary wave front is annihilated when colliding with a primary wave. The leading secondary wave front can travel a distance $\Delta s'$ before its annihilation, given by

$$\Delta s' = \frac{v_1 f_2 - v_2 f_1}{f_1 f_2 (1 + v_1/v_2)}\,, \tag{8.1.1}$$

which simplifies to $\Delta s' = (v/f_1 + v/f_2)/2$ if the conduction velocities of both waves are the same, here $v \simeq 1$ for the chosen parameters. The secondary wave front is annihilated and the next one can travel again a certain distance until being annihilated as well. The place of annihilation is moved in direction of the primary pacemaker ($f_2 > f_1$). The distance between the locations of two subsequent annihilations Δs is given by the way$\Delta s'$ the secondary wave travels reduced by the distance between two subsequent secondary wave fronts given by v/f_2 yielding $\Delta s = \Delta s' - v/f_2$. The total distance, the secondary waves have to overcome after the first annihilation to reach the lower boundary in region R, will be denoted by s_0. Here, for equal conduction velocities and starting pacing at the same time instant for secondary and primary waves, $s_0 = 16/2 = 8$, i.e. the half of the total distance between primary and secondary pacemaker.

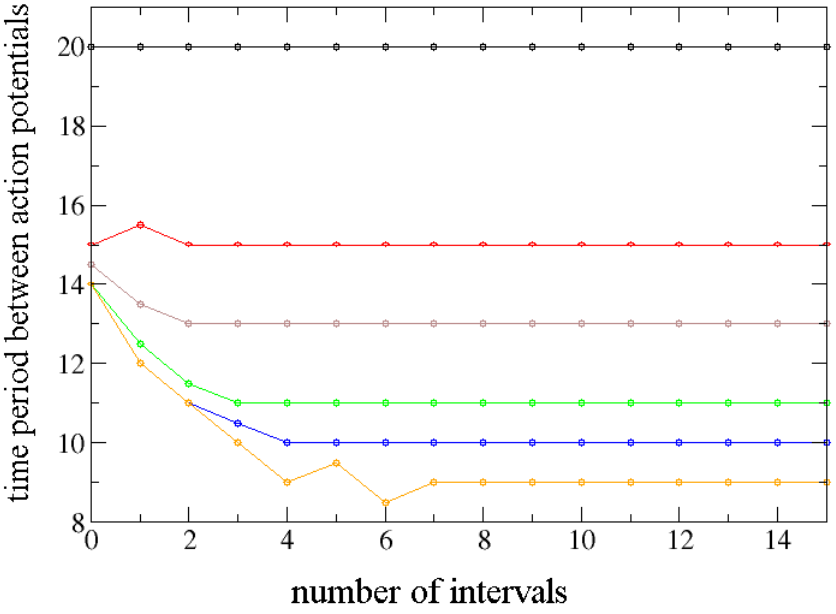

Figure 8.6: Inverse frequency measured at point $[16, 9.9]$ of the simulation area $f_2 = 0$ and $f_1 = 0.050$ (black), 0.067 (red), 0.077 (brown), 0.09 (green), 0.1 (blue) and 0.011 (orange). For higher frequencies, a certain number of intervals is needed to obtain the pacing frequency due to a reduced conduction velocity.

Secondary waves reach the lower boundary of region R after a certain number of annihilations $n = s_0/\Delta s$. For small pacing frequencies ($f_1 \approx 0.05$), the transition time can be calculated by

$$t_{\mathrm{tr}} \sim n/f_1 = 2s_0 f_2/[v(f_2 - f_1)]\,. \tag{8.1.2}$$

For larger values of f_1, a deviation of the simulation results from the equation occurs, in particular in the range of small transient times. This may be a result of a non-negligible contribution of the accommodation of action potential duration and propagation velocity to the excitation frequency. In Fig. 8.6, the time interval between consecutive action potentials at point $[16, 9.9]$ in the simulation area (Fig. 5.1) is shown for $f_2 = 0$ and different f_1. In dependence of the pacing frequency, a certain number of intervals is required until the measured frequency at this point is constant and similar to the pacing frequency. The number of intervals depends on the distance of the point from the pacemaker. This time is due to a reduced conduction velocity for higher frequencies since activations occur in the refractory tail of the previous wave front. However, not the reduction of the conduction velocity causes the deviation of the measured and analytical values of t_{tr}, because in this case an effect depending also on f_2 would be expected but is not observed. The deviation

from Eq. (8.1.2) depends only on f_1. The prolongation of the action potential duration, which incorporates a longer refractory phase, thus seems to be more important for the observed deviation. A longer refractory phase of the primary waves results in an effectively decreased conduction velocity of the secondary waves. Thus, larger values of t_{tr} are observed than expected. This effect can be taken into account in a refined derivation of Eq. (8.1.2) by considering the time dependence of v_2 and the resulting change of Δs:

$$\Delta s = \frac{v_1 f_2 - v_2(i,x,y) f_1}{f_1 f_2 (1 + v_1/v_2(i,x,y)) - v_2(i+1,x,y)/f_2}. \tag{8.1.3}$$

Here, i is the number of intervals and $v_2(i,x,y)$ is the effectively decreased conduction velocity of secondary waves. It is not only dependent on the interval number but also on the distance of the annihilation zone from the primary pacemaker. Neither the relationship of action potential duration nor the conduction velocity of secondary waves on pacing frequency and distance from the pacemaker is known. Due to the interplay of the dependence on the frequency with the dependence on the distance from the pacemaker it is hard to determine from the simulations. This effect can be effectively taken into account by an additive time t_a:

$$t_{\mathrm{tr}} \simeq \frac{s_0}{v} \frac{f_2}{f_2 - f_1} + t_a. \tag{8.1.4}$$

The time t_a was found by fitting Eq. (eq:ttr) to the t_{tr} curves with the result $t_a = 0, 9, 18$ and 35 for $f_1 = 0.05, 0.059, 0.067$ and 0.77, respectively. As shown by the dashed lines in Fig. 8.5, this equation describes well the simulated data.

Patterns in region L remained regular for all frequency ranges. If the perturbing frequency is larger than the pacing frequency, primary wave fronts cannot penetrate into region L and a regular activation due to the secondary pacemaker is observed. For the opposite case, $f_2 < f_1 < f_{\mathrm{det}}$ primary wave fronts could enter the region L and expel the secondary wave fronts. An irregularity type III like behaviour was not obtained since the primary waves arrived as almost planar wave fronts at the left boundary of region L and hence no activation between wave fronts can occur. A regular activation pattern dominated by the primary waves is present in this case. For even higher pacing frequencies, exceeding the critical frequency for detachment, primary waves detached from the bridge in region R could thus not propagate into region L. The regular activation by the secondary pacemaker results in regular excitation patterns for region L.

8.1.2 Occurrence of irregularities in the $f_1 - f_2$ plane

The previously described irregularities occur in three different regimes I-III in the $f_1 - f_2$ plane, see Fig. 8.7. One characteristic frequency, denoted as f_{lim}, sets an upper limit for f_1 and f_2, above which propagating waves cannot be generated for every stimulation. This results in an effectively decreased driving

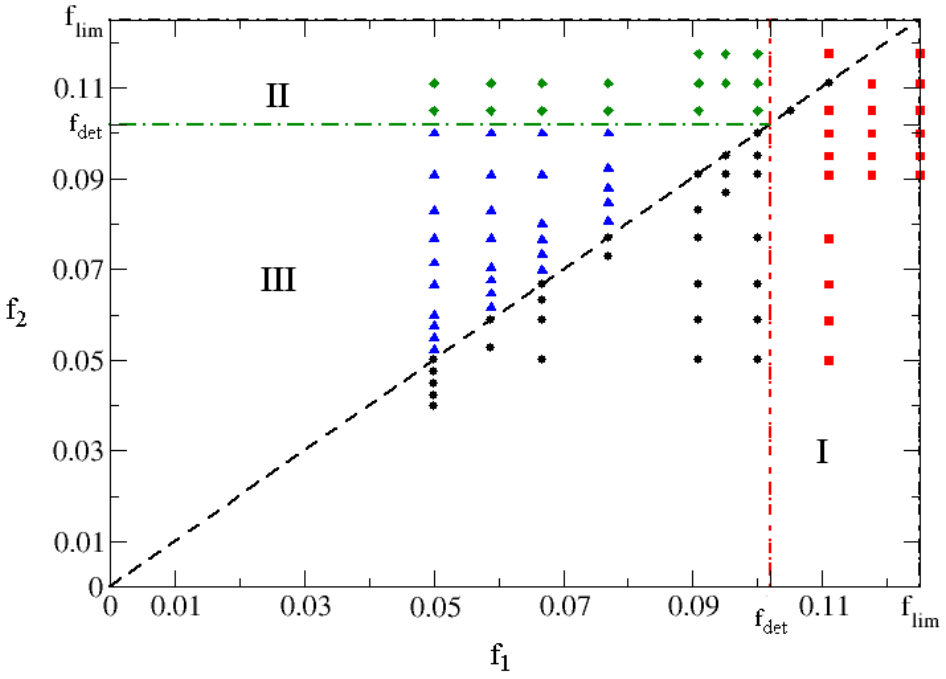

Figure 8.7: Domains of occurrence of the irregularities type I-III in the $f_1 - f_2$ plane. Solutions of the FHN equations (4.1.11) are marked by the symbols: regular excitation patterns (circles) and irregularities type I (squares), type II (diamonds), and type III (triangles). The scale of the frequencies is limited to $f_{\mathrm{lim}} = 0.1176$.

frequency of the propagating waves, which is determined for the parameters used to be $f_{\mathrm{lim}} = 0.1176$. Above the characteristic frequency f_{det} detachment from sharp corners occurs. It is thereby the decisive quantity separating the domains, where irregularities occur. Regime I (irregularity type I) corresponds to high pacing frequencies $f_1 > f_{\mathrm{det}}$, where primary planar waves detach from the lower corner of the bridge. Regime II (irregularity type II) is given by $f_2 > f_{\mathrm{det}}$ and $f_1 < f_{\mathrm{det}}$, whereas for regime III (irregularity type III) $f_{\mathrm{det}} > f_2 > f_1$ applies.

For these simulations, the critical frequency was determined by evaluation of the velocity component $\tilde{v}_x$ in x-direction of the primary waves for different pacing frequencies and $f_2 = 0$. Thereby, the velocity is calculated from the time difference needed for a wave front to propagate between two points near the lower left corner of the bridge ($x \simeq 10.9, 11$ $y \simeq 4.1$). The time instants of the wave front being at a certain point are determined from the peak of the action potential. For small pacing frequencies, a negative value is obtained with decreasing magnitude for increasing pacing frequencies. The velocity

becomes zero if $f_1 = f_{\mathrm{det}} = 0.102$ for the parameters used in this work.

For both, experimental [226, 227] and theoretical studies [226, 228, 229], detachment from sharp corners is well-known. An analytical equation for the critical frequency for detachment was derived by Starobin *et al.* [228] on the basis of the safety factor $SF = Q_S - Q_L$ which sets the source charge Q_S from the wave front in relation to the load charge Q_L, required by the adjacent medium for activation. Thereby, when passing an obstacle, the charge load can be divided into two terms: one accounting for the activation of the wave front into the two directions behind the obstacle and the second one, for increasing the velocity of the wave front propagating parallel to the obstacle from 0 to the normal value. If $SF < 0$, the wave front will detach from the obstacle. Their analysis was based on a dimensionless version of the FitzHugh-Nagumo model with a piecewise linear function, approximating the non-linear reaction term in the equation for temporal evolution of u. Analytically derived equations for RD models including non-linear reaction terms, as used in this work, were not yet presented in the literature. From experiments with cardiac tissue, BZR preparations and computer simulations, it was derived that the detachment depends on the frequency of the pacemaker and the width of the isthmus (here: bridge). Furthermore, changing system properties, as for example decreasing the excitability, resulted in the occurrence of detachment also for larger bridge widths or smaller frequencies, respectively. In the set-up, studied in this work, detachment depends on the frequency of the respective pacemaker but not on the width of the bridge. Here, detachment occurs also for the primary pacemaker before primary wave fronts propagate through the bridge.

8.1.3 Strength of irregularities in regimes I-III

In this section, the excitation patterns, corresponding to frequency regimes I-III will be characterized with respect to *(i)* the ratio of the highest local frequency $f_{\mathrm{max}} = \max f_l$ to the pacing frequency, *(ii)* the entropy S, and *(iii)* the phase coherence Φ, all evaluated only for region R. The maximal local frequency, determined in region R, is shown in Fig. 8.8 in dependence of f_2 for different pacing frequencies f_1. For regular patterns, i.e. $f_2 \leq f_1$, f_{max} resembles mainly f_1. For $f_2 > f_{\mathrm{det}}$ (right of dotted line) or $f_1 > f_{\mathrm{det}}$ (curve marked by the green triangles), which correspond to regime II or I, respectively, a moderate enhancement of f_{max} with respect to f_2 or f_1 is obtained. For regime III, corresponding to $f_{\mathrm{det}} > f_2 > f_1$, f_{max} values in general exceed f_2 slightly. However, in certain cases a quite large enhancement can be observed, as evidenced by the value $f_{\mathrm{max}} \simeq 0.15$ found for $f_1 = 0.05$ (black circles) at $f_2 = 0.1$. It is interesting that the highest local frequencies (up to $3f_1$ and $1.5f_2$) are obtained for moderate values of the pacing and the perturbing frequency in regime II, although one would expect it for regime I or II.

The entropy S and the order parameter Φ of phase coherence are shown in Fig. 8.9 in dependence of f_2 for the same set of fixed pacing frequencies

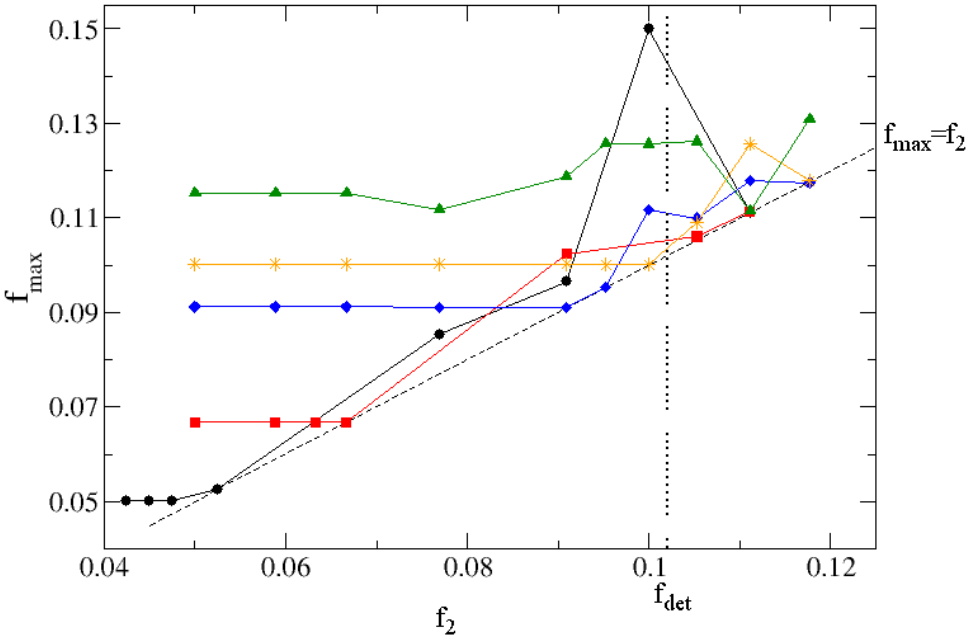

Figure 8.8: Maximal frequency observed in region R in dependence of f_2 for different pacing frequencies $f_1 = 0.050$ (black circles), 0.067 (red squares), 0.091 (blue diamonds), 0.10 (orange stars) and 0.111 (green triangles). The critical frequency f_{det} is marked by the dotted line and $f_{\mathrm{max}} = f_2$ by the dashed line. As a guide to the eye, the solid lines are drawn, connecting the data points.

as in Fig. 8.8. Calculations of both, S and Φ, were performed either for the part of R below the bridge, $y < 4$ (panels (a)+(c)), or for the part of R above the bridge, $y > 4$ (panels (b)+(d)), to differentiate between the different irregularity types. With both measures changes in the degree of regularity of the excitation patterns can be clearly identified. Increases of S and decreases of Φ reflect transitions from regular to irregular states.

The description of the strength of irregularities will be based in the following on the order parameter for phase coherence. For irregularity type I, occurring for $f_1 > f_{\mathrm{det}}$ (curve marked by green triangles), a large constant value of Φ, describing regular excitation, is obtained in the area below the bridge (panel (b)), whereas for the area above the bridge (panel (a)) a small constant value is determined, reflecting the irregular patterns due to the detachment of the primary waves at the bridge. Transition to regime II, where $f_2 > f_{\mathrm{det}}$ (left of dotted line), is reflected in a drop of Φ for the area above the bridge (panel (a)), whereas the behaviour is more complicated for the region below the bridge (panel (b)) and dependent on f_1. Φ is small for small f_1

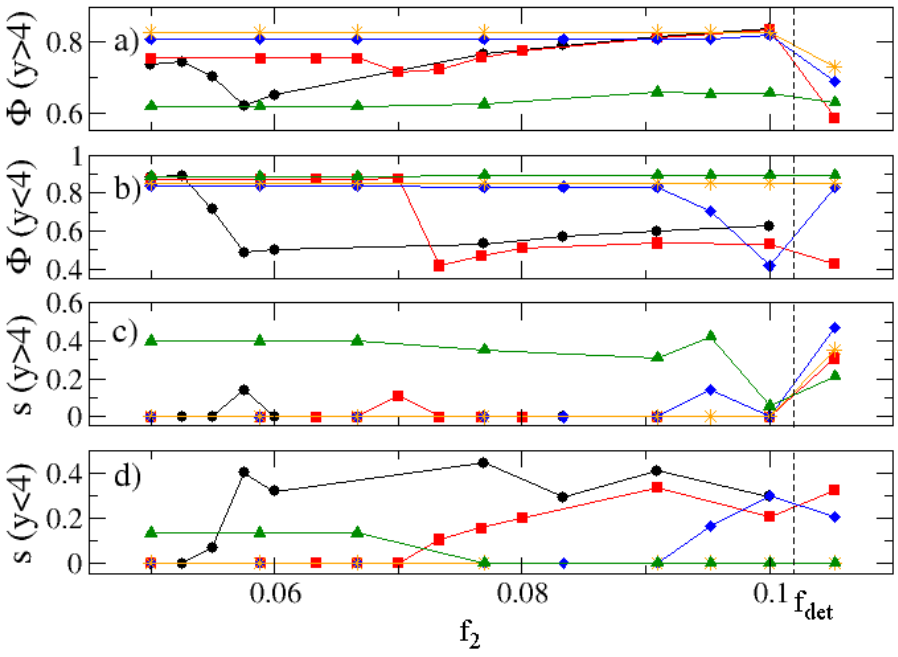

Figure 8.9: Order parameter Φ for phase coherence and entropy S of local frequency distribution are shown as a function of f_2 for areas $y > 4$ (above bridge) and $y < 4$ (below bridge) in region R. Results are obtained for various pacing frequencies: $f_1 = 0.050$ (black circles), 0.067 (red squares), 0.091 (blue diamonds), 0.10 (orange stars) and 0.111 (green triangles). The vertical dashed lines mark the critical frequency f_{det}.

(black, red curves), since the irregularities generated in the upper part of region R can penetrate into the area below the bridge. For larger f_1 (blue curve), an increase of Φ is observed. This can be explained by the fact that the irregularities cannot enter the area below the bridge, due to the higher pacing frequency, and thus more regular patterns are observed there. Transition from regular patterns to regime III is reflected by a sharp drop of Φ, calculated for the lower area of region R (panel (b)). It remains almost constant for further increase of f_2, as long as it is lower than f_{det}. In contrast, the Φ values for the area above the bridge exhibit a less pronounced drop and increase smoothly for increasing f_1, since irregularity type III is confined to the lower boundary of region R. Furthermore, the smooth increase occurs due to suppression of the irregular patterns above the bridge by the fast pacing secondary pacemaker and they become less relevant. In fact, the Φ values for the region below the bridge for regime III are comparable to the ones obtained for regime II for the smaller pacing frequencies (black and red curve). Thus, the transition from

regime III to II cannot be determined from the Φ values.

The transitions between the different regimes can be identified also by considering S. Thereby, drops in Φ are correlate with steep increases of S. However, they can show different behaviour in detail, since the entropy S quantifies the spread in local frequencies, while the order parameter Φ is more sensitive to temporal evolution of u. For example, stronger variations of S are observed for $f_1 = 0.111$ and $y > 4$ if f_2 is approaching f_{det} when compared to Φ. The slow rise of Φ in regime III for small pacing frequencies and increasing perturbing frequencies (cf. panel (a) black and red curve) is not seen in S (panel (c)). For these curves only a small variation in S is observed for the first perturbing frequency larger than the pacing frequency. Upon further increasing f_2 a return to the regular value occurs, indicating a negligible influence of the irregularity onto the frequency distribution in the area above the bridge.

8.2 Results of BOCF model

In this chapter, results obtained with the BOCF model will be presented, including a comparison with the FHN model to determine generic and system-specific effects like the irregularities which are observed in each model and the parameters for their occurrence. It will be investigated how far the findings in the simple FHN model are reflected in the more system-specific BOCF model. Therefore, three different states of the atrial tissue, which are the physiological state, an electrically remodelled state and a physiological state with a reduced excitability, are considered using different parameter sets. The model including the applied parameter set will be denoted by pBOCF, rBOCF and variant of the pBOCF model with reduced excitability (pBOCF-re), respectively, and frequencies and other properties by p, r and pm. The comparison between the three states will yield hints about the necessary requirements for the occurrence of irregular patterns, in resemblance to fibrillation patterns, due to the interplay between the two pacemaker.

As described in ch. 2.2, ongoing AF results in a remodelling of the tissue, which means here a change of electro-physiological properties of the tissue. This is reflected in the rBOCF model by an action potential duration (APD) and effective refractory phase (ERP) much smaller than in the pBOCF model (see Fig. 2.7). The conduction velocity (CV) is only slightly reduced. Furthermore, the dome of the action potential (AP) course is missing (see Fig. 8.10). The limiting frequency in the rBOCF model is much larger, $f^r_{\text{lim}} \simeq 8\,\text{Hz}$, than in the pBOCF model ($f^p_{\text{lim}} \simeq 3\,\text{Hz}$), due to the reduced APD.

Since detachment of waves was the origin of irregularities type I and II in the FHN model, the pBOCF-re variant is introduced. It is known from experiments with sheep epicardial tissue that a detachment of waves from corners can occur for high-frequency pacing [227], as was seen in the FHN model, but also if the excitability of the tissue is reduced, for example by perfusion of the tissue with tetrodotoxin [229]. Furthermore, it was shown for various electro-physiological

models as e.g. the Luo-Rudy model, that a reduction of the sodium channel conductance below 30% of its normal value as well as high-frequency pacing (90% of the maximal frequency) results in detachment of waves [60, 226–229]. However, the range is limited to minimal 20% sodium channel conductance, when describing cardiac tissue. The pBOCF-re variant, where τ_{fi} is increased to 0.11, refers to a reduced sodium channel conductance, thus facilitating the detachment from sharp edges. Different values of τ_{fi} were tested to find the range, where detachment occurs. For $\tau_{\text{fi}} \geq 0.12$ no waves can be generated, while for $0.11 \leq \tau_{\text{fi}} \leq 0.12$ detachment from sharp corners occurs. The change

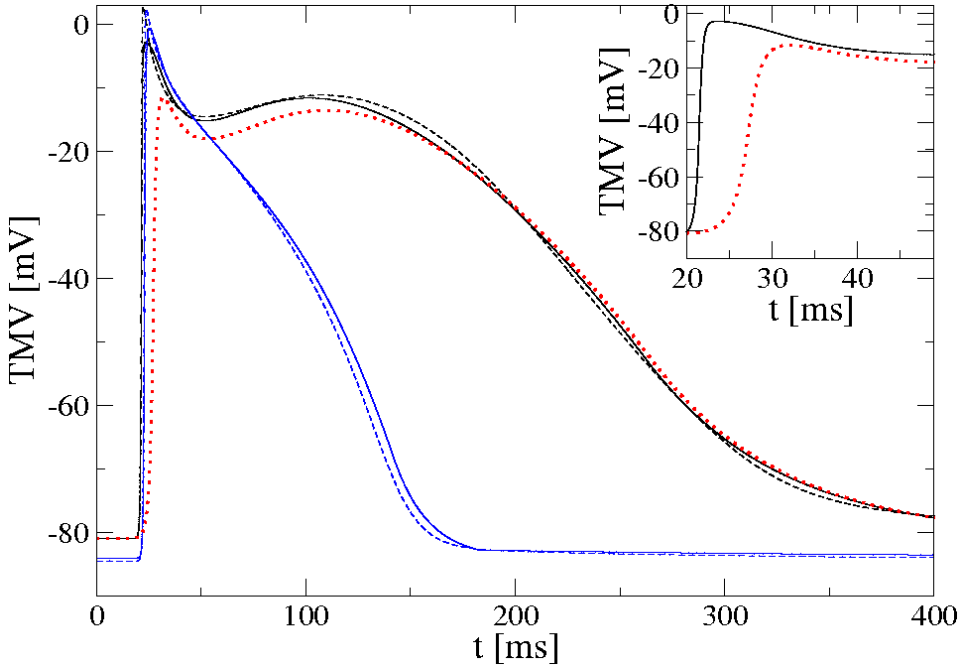

Figure 8.10: AP shape shown for the same pacing frequency obtained in the pBOCF model (black line), the rBOCF model (blue curve) and the pBOCF-re variant (red curve). While in the rBOCF model the dome is missing, in the pBOCF-re variant a slower upstroke of TMV (see inset) as well as a slightly reduced maximal value of the TMV at the peak and the plateau phase compared to the pBOCF model is observed.

of τ_{fi} yields a slightly delayed rise of the transmembrane voltage (TMV), which is correlated with an increased activation current threshold needed to overcome to generate an AP, see Fig. 8.10. Additionally a slightly reduced maximal value of the TMV at the plateau phase is observed. Despite of this small changes, larger modifications occur in the CV and APD. The conduction velocity for the same conductivity of the tissue is decreased by $\approx 18\%$ for the pBOCF-re variant while action potential duration is only slightly decreased from 332ms for the pBOCF model to 328ms for the pBOCF-re variant ($f_1 = 0.8$Hz), as is shown in Fig. 8.11. The overall dependence of APD and CV on the pacing frequency in a linear cell strand is similar for the pBOCF model and the

pBOCF-re variant [see Fig. 8.11]. The limiting pacing frequency f_{lim}^{pm} was decreased to 2.85 Hz in comparison to the pBOCF model ($f_{\mathrm{lim}}^{p} \simeq 3\,\mathrm{Hz}$), in contrast to the rBOCF model, where it is increased.

Furthermore, the effect of structural remodelling was investigated by reducing the conductivity of the tissue, represented by κ in the simulations. Therefore a decrease of κ by up to 30% was studied. In Fig. 8.11 the effect of different conductivities on CV, effective refractory phase (ERP) and wave length WL=CV/ERP (WL) (WL=CV/ERP) is shown for the pBOCF model and the pBOCF-re variant. It can be seen that CV for the same conductivity is strongly decreased in the pBOCF-re variant than compared to the pBOCF model whereas the ERP is increased. The overall dependence on f_1 is similar for both parameter sets but the difference between the CV values for different conductivities is much larger in the pBOCF model than in the pBOCF-re variant.

8.2.1 Irregularities observed in the BOCF model

Because of the presence of many characteristic frequencies and detailed descriptions of the different behaviours in the associated frequency regimes, it can be difficult to keep track of the main points. I will therefore give an overview of the findings for the various models in Tab. 8.1 in the discussion section at the end of this chapter (ch. 8.6).

pBOCF and rBOCF model

In the pBOCF and the rBOCF model, in contrast to the FHN model, a detachment of waves from sharp edges due to high-frequency pacing was not observed. Accordingly, irregularities of type I and II were not occurring in the pBOCF or the rBOCF model.

For $f_2 > f_1$, irregularity of type III appeared in the pBOCF model. A representative spatio-temporal pattern is shown in Fig. 8.12 and in movie S4 in the Supporting Material. As can be seen from the figure, a primary wave fragment appeared at the lower boundary of region R (Fig. 8.12, $t = 8.03\,\mathrm{s}$), which started to curl a bit later (Fig. 8.12, $t = 8.08\,\mathrm{s}$). The fragment was generated by the primary pacemaker in the refractory tail of the secondary wave. The fact, that primary wave fragments curl is different from the observations in the FHN model, where the secondary waves become curled. A reentrant pattern, however, did not arise, because the wave fragment hit the boundary of the simulation area (Fig. 8.12, $t = 8.10\,\mathrm{s}{-}8.13\,\mathrm{s}$) or was annihilated by its own refractory tail. Thus the generation of a spiral wave was suppressed. This is not an effect due to the limited size of the simulation area. Spiral wave cannot be initiated in the pBOCF and rBOCF model by cross-field stimulation, as was shown by Wilhelms *et al.* [230], which is comparable to the initiation here caused by the interaction of secondary and primary wave fronts.

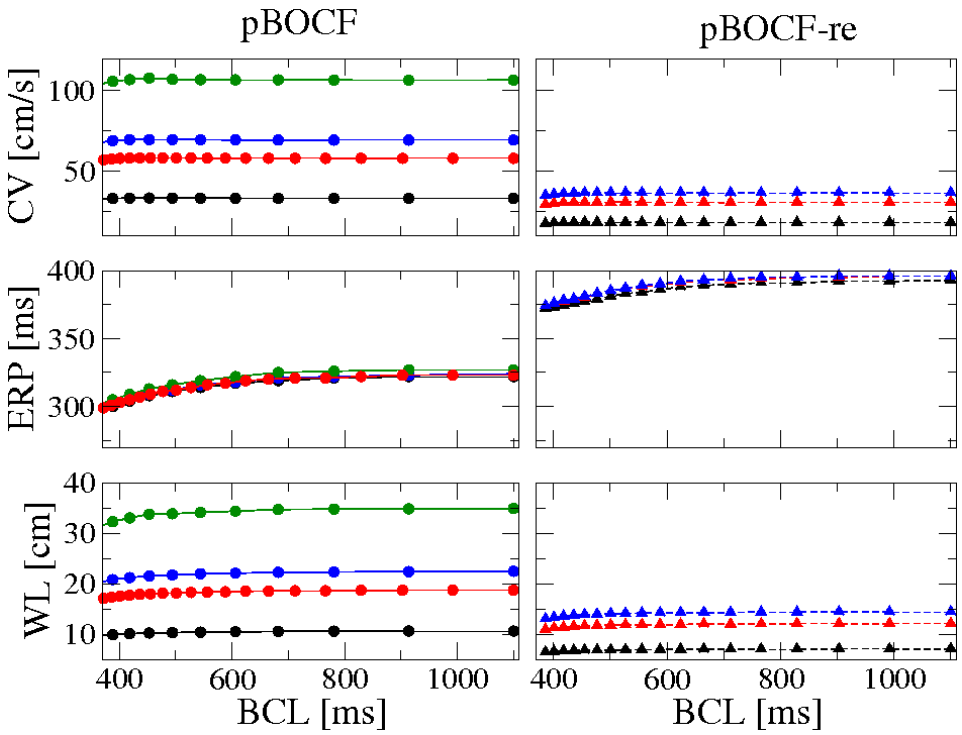

Figure 8.11: CV (upper panel) between the fourth and 8th cell in a linear cell strand, effective refractory phase (ERP) of the last cell in the linear cell strand and wave length $WL = \mathrm{CV}/ERP$ in dependence of the basic cycle length (BCL=inverse of pacing frequency) of the first cell for the pBOCF model (left) and the pBOCF-re (right) variant for different conductivities $\kappa = 0.016$ S/m (black), 0.046 S/m (red), 0.06536 S/m (blue), and $\kappa = 0.1533$ S/m (green). CV for the same conductivity is strongly decreased in the pBOCF-re variant than compared to the pBOCF model whereas the ERP is increased. The overall dependence on f_1 is similar for both parameter sets but the difference between the CV values for different conductivities is much larger in the pBOCF model than in the pBOCF-re variant.

In the rBOCF model in the case of irregularity type III, as in the pBOCF model, primary wave fragments were generated at the lower boundary of region R, which started to curl and hit the boundary or were annihilated by their own refractory tail. In the rBOCF model, the curvature of the wave front with open end was smaller than for physiological conditions. This decreased the probability of finding re-entrant patterns. A representative time evolution is shown in movie S5 in the Supporting Material.

The patterns in region L, for the pBOCF model, remained quite regular for all frequencies. If $f_1 < f_2$, region L was dominated by the regular activation due to the secondary pacemaker. For $f_1 > f_2$, region L was regularly activated either by wave fronts of the primary or the secondary pacemaker, since the secondary and primary wave fronts were almost parallel in region L and thus

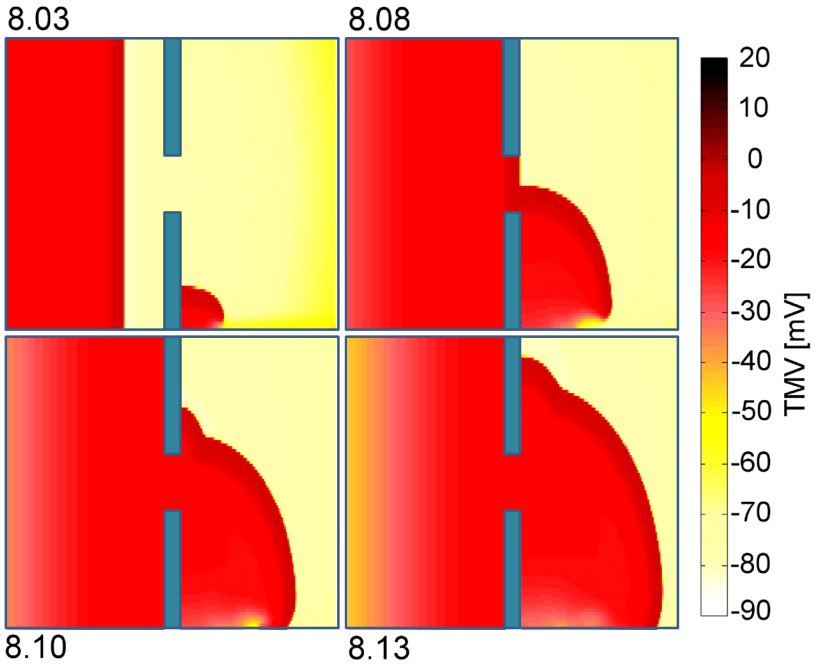

Figure 8.12: Time evolution of the TMV for $f_1 = 1.0\,\mathrm{Hz}$ and $f_2 = 2.27\,\mathrm{Hz}$ in the pBOCF model. Red colour represents the excited state, yellow the resting state. Numbers at the graphs give the time instant in seconds. Time evolution is also shown in movie S4 in the Supporting Material.

no irregularities occurred upon their collisions[1]. In the rBOCF model, as in the pBOCF model, the patterns in region L were regular for all analysed frequencies.

pBOCF-re variant

In the pBOCF-re variant, a detachment of waves from the edges of the bridge occurred for all frequencies, in contrast to the FHN model, where it is dependent on the frequency of waves. Furthermore, in the pBOCF-re model a characteristic frequency can be identified for which a conduction block at the bridge occurs. For f_1 or $f_2 > f_{\mathrm{sbl}} = 2.7$ Hz, a sustained 2:1 conduction block[2] occurs at the bridge, i.e. every second primary or secondary wave front passes the bridge but cannot propagate further into region R or L, respectively. This can be understood, when considering the source-sink relationship. The source is thereby the activated cells of the wave front and the sink are the excitable cells in front of the wave front. In the case of the conduction block, there is

[1] Primary wave fronts exhibit a rounded shape but their ends are connected to the boundary all the time. Near the secondary pacemaker, primary wave fronts are almost planar.

[2] 2:1 means two wave fronts arriving at the bridge result in one wave front successfully crossing the bridge

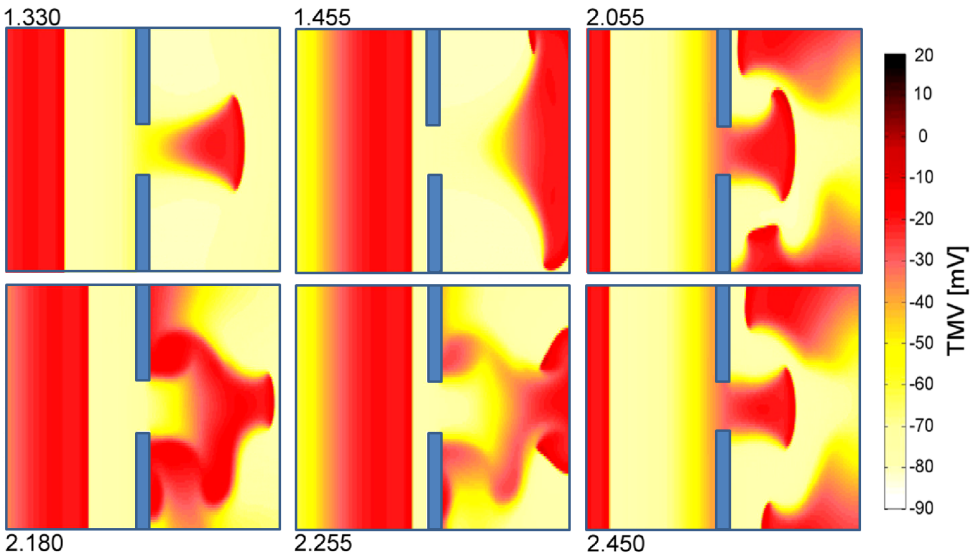

Figure 8.13: Time evolution of the TMV for $f_1 = 1.0\,\mathrm{Hz}$ and $f_2 = 2.5\,\mathrm{Hz}$ in the pBOCF-re model. Red colour represents the excited state, yellow the resting state. Numbers at the graphs give the time instant in seconds. Time evolution is also shown in movie S6 in the Supporting Material.

a source sink mismatch, i.e. the sink is much larger than the source and thus the source can not provide enough current to activate the sink. This results in the failure of propagation. At the border of the bridge to region R or L, the sink increases while the source is comparable. If the excitability is reduced, e.g. due to high frequency pacing, the effective sink is increased furthermore, resulting in the described source-sink mismatch. Due to the restitution, i.e. the modification of APD, CV and ERP with the frequency of waves, and the accommodation time of the tissue for sustaining high frequencies (refer to Fig. 8.6 of the FHN model), additionally a transient conduction block can occur. That means, at the beginning of the stimulation, 2:1 conduction block occurs but after a certain time every wave can pass the bridge. The corresponding characteristic frequency is denoted by f_{tbl} (here: $f_{\mathrm{tbl}} = 2.4\mathrm{Hz}$) and the transient conduction block occurs for $f_{\mathrm{tbl}}^{pm} < f < f_{\mathrm{sbl}}^{pm}$.

The detachment of waves in the pBOCF-re variant leads to a curling of the detached wave fronts, but despite of this, the resulting patterns remained quite regular for $f_1 > f_2$.

In the frequency regime $f_1 < f_2 < f_{\mathrm{tbl}}^{pm}$, excitation patterns occurred, which were a mixture of type III, II, and I irregularity of the FHN model. Detachment of primary waves and secondary waves at the bridge can be identified, as well as the generation of wave fragments at the lower boundary in region R. Short-living re-entrant patterns appear.

A new irregularity, type IV, not observed in the FHN model, was found for $f_1 < f_{\mathrm{tbl}}^{pm} < f_2 < f_{\mathrm{sbl}}^{pm}$. Here, in passing the bridge, every second wave of the

secondary pacemaker looses the contact to the boundaries and propagates as small wave fragment into region R. Dependent on f_2, this wave fragment can either shrink or grow. The wave fragment occurs after a transition from a 2:1 conduction block to a state where all waves propagate after passing the bridge. A typical time evolution of a spatio-temporal excitation pattern for this type of irregularity with a growing wave fragment is shown in Fig. 8.13 and in Movie S6 in the Supporting Material. The open ends of this fragment, at time $t = 1.33\,\mathrm{s}$ in Fig. 8.13, started to curl and after curling at some later time propagated in negative x direction, see Fig. 8.13 at 1.455 s. The interaction of the resulting wave with both, the next primary wave and the next secondary wave passing the bridge, resulted in two wave fragments in the lower and upper part of R (Fig. 8.13 at time 2.055 s). With further increasing time, a pattern appeared at $t = 2.45\,\mathrm{s}$ that resembles the one at $t = 2.055\,\mathrm{s}$. Thus, a quasi-reentrant pattern occurred in region R.

Overall, the excitation patterns resembled fibrillatory patterns in the atria [231], as re-entry [232] (upper part in R), incomplete re-entry [233] (lower part in R) and wave collisions [234] (middle of R) occur. The mechanism could thus be relevant for the generation of AF, if a reduced excitability of cells is present.

If $f_1 < f_{\mathrm{tbl}}^{pm}$ and $f_2 > f_{\mathrm{sbl}}^{pm}$, only $2:1$ conduction across the bridge occurred leading to nearly regular patterns since the effective frequency of secondary wave fronts in region R is $f^{eff} \simeq 0.5 f_2$. Thereby, one secondary wave passes the bridge and propagates regularly in region R without any curling, whereas the next wave front stops its propagation after passing the bridge and vanishes. The overall pattern is dominated by the primary wave fronts due to their higher frequency.

If $f_1 > f_{\mathrm{sbl}}^{pm}$, the primary waves expel the secondary waves and generate irregular patterns in region L, while the pattern in region R remains regular.

8.2.2 Occurrence of irregularities in the $f_1 - f_2$ plane

In Fig. 8.14 the occurrence of the diverse irregularities in the BOCF model are shown in the $f_1 - f_2$ plane for the pBOCF model (left) and the pBOCF-re variant (right). The phase diagram for the rBOCF model is similar to the one of the pBOCF model and is therefore not shown. It can be seen, that for a large range of frequency ratios, i.e. $f_1 > f_2$, the overall behaviour is regular for both BOCF models, as is the case for the FHN model. Irregularity type III occurs in the same region for both BOCF variants. However, in the pBOCF-re variant, the corresponding patterns differ from the pBOCF and the FHN results, since detachment of waves occurs for all frequency ranges. In both, pBOCF and pBOCF-re variant, irregularities type I and II, known from the FHN model, do not occur. An additional irregularity occurs in the pBOCF-re variant, irregularity type IV, which is confined to a small region of the $f_1 - f_2$ plane.

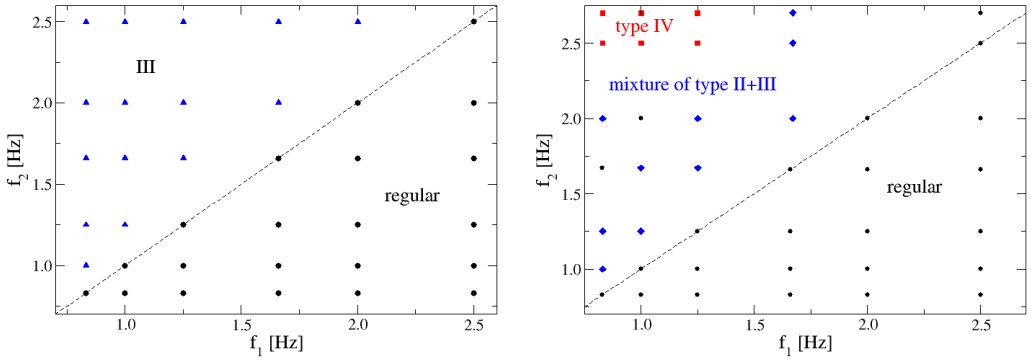

Figure 8.14: Occurrence of irregularities in the $f_1 - f_2$ plane shown for pBOCF model (a) and the pBOCF-re variant (b). The results for the rBOCF model are not shown, since they resemble the pBOCF model results. Regular patterns are observed for $f_1 > f_2$ and irregularity type III for $f_1 < f_2$ in both models, whereas an additional irregularity type occurs only in the pBOCF-re variant in the small range of $f_1 < f_{\mathrm{tbl}}^{pm} < f_2 < f_{\mathrm{sbl}}^{pm}$.

8.2.3 Strength of irregularities in BOCF model

The parameter Φ and the maximal local frequency $f_{\max}$ in region R are shown in Fig. 8.15 in dependence of f_2 for various values of f_1 and the different states of the tissue: pBOCF (upper panels), rBOCF (middle panels), pBOCF-re (lower panels). For $f_2 < f_1$, Φ was close to one, indicating regular patterns. In this range, the maximal local frequency was comparable to the pacing frequency f_1, because the pattern in region R was dominated by the primary pacemaker. If $f_2 > f_1$, Φ decreased slightly with rising f_2 due to the occurrence of type III irregularity. For the pBOCF model, the maximal decrease was only 4% of the maximal Φ value and $f_{\max}$ was comparable to f_2. Hence, in spite of the occurrence of irregularity type III, the overall pattern was quite regular. The decrease of Φ was a bit stronger for the rBOCF model (about 10% of the maximal Φ value) and $f_{\max} \simeq f_2$. The patterns could be classified as almost regular despite the short-living distortions of the wave fronts at the lower boundary in region R. To summarize, in both the pBOCF and the rBOCF model, irregularity types I and II did not appear, and irregularity type III resulted in a weak irregularity. Therefore, it should play no important role in the generation of fibrillatory patterns.

In the pBOCF-re variant, regular patterns are observed for $f_1 > f_2$, accordingly, Φ does not decrease and $f_{\max} \simeq f_1$ (see Fig. 8.15). In the range of irregularity type III, $f_1 < f_2 < f_{\mathrm{tbl}}^{pm} = 2.4\mathrm{Hz}$, the strength of the irregularity (see Fig. 8.15) is comparable to that of the pBOCF model, that is almost regular patterns were observed with Φ close to one and $f_{\max} \simeq f_2$. Thus, like in the pBOCF and the rBOCF models, these irregularities should play no important

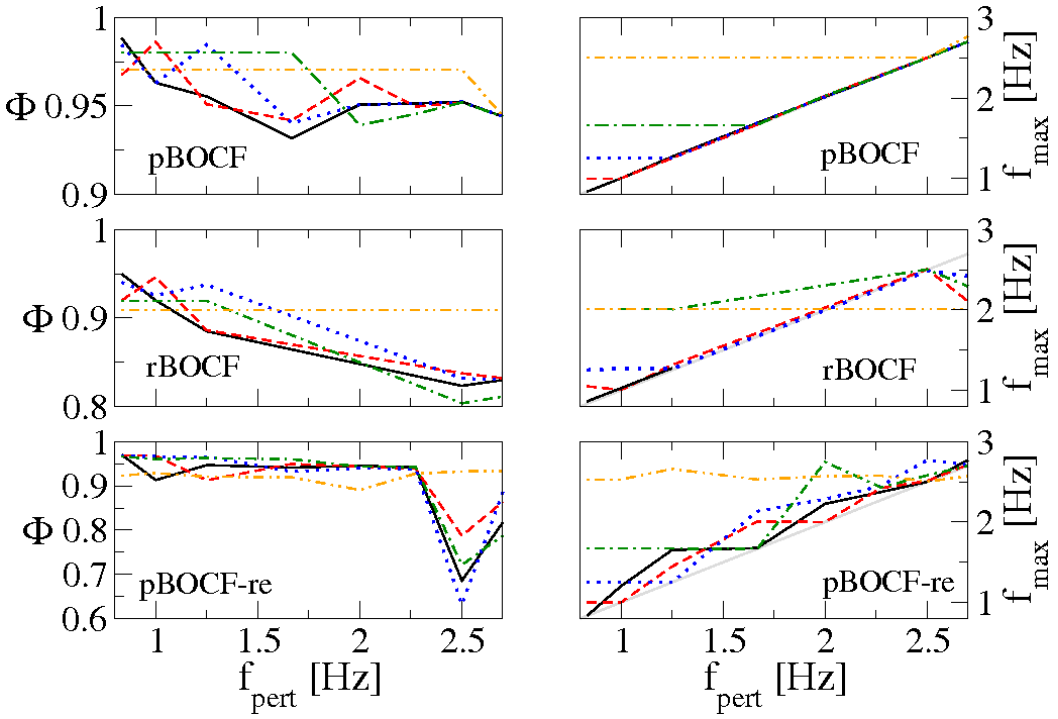

Figure 8.15: Synchronization parameter Φ (left panels) and maximal local frequency $f_{\max}$ (right panels), calculated in the upper part ($y > 4$) of region R (see Fig. 5.1), in dependence of f_2 for $f_1 = 0.83\,\mathrm{Hz}$ (black solid lines), 1 Hz (red dashed lines), 1.25 Hz (blue dotted lines). The green dashed-dotted lines refer to $f_1 = 1.67\,\mathrm{Hz}$ (pBOCF and pBOCF-re model) or 2 Hz (rBOCF model), and the orange dashed-dotted-dotted line to $f_1 = 2.5\,\mathrm{Hz}$ (pBOCF and pBOCF-re model) or 3 Hz (rBOCF model).

role for the initiation of atrial fibrillation.

In contrast, in the range of irregularity type IV, $f_1 < f_{\mathrm{tbl}}^{pm} < f_2 < f_{\mathrm{sbl}}^{pm}$, the strength of the irregularity is large. The measure of synchronization Φ was more than 30% smaller than the regular value and $f_{\max}$ could take values up to $1.5 f_2$.

For larger perturbation frequencies, i.e. $f_1 < f_{\mathrm{tbl}}^{pm}$ and $f_2 > f_{\mathrm{sbl}}^{pm}$, Φ was only slightly varying, and $f_{\max} \simeq \max(f_2^{eff}, f_1)$ with f_2^{eff} as effective frequency of secondary waves passing the bridge. In the range of the sustained conduction block $f_1 > f_{\mathrm{sbl}}^{pm}$ (orange curve in Fig. 8.15), only regular patterns are observed with Φ unaffected by changes in f_2 and $f_{\max} \simeq f_1$.

If additionally a structural remodelling is introduced in the pBOCF-re variant, i.e. decreasing the conductivity κ, this results in a slightly increased reduction of Φ for irregularity type IV patterns. In Fig. 8.16 the strength of irregularity is shown for the pBOCF model (solid lines) and the pBOCF-re variant (broken lines) for different frequencies f_2 of the secondary wave fronts and different conductivities κ. Thereby, $\kappa = 0.06356$ S/m corresponds to the

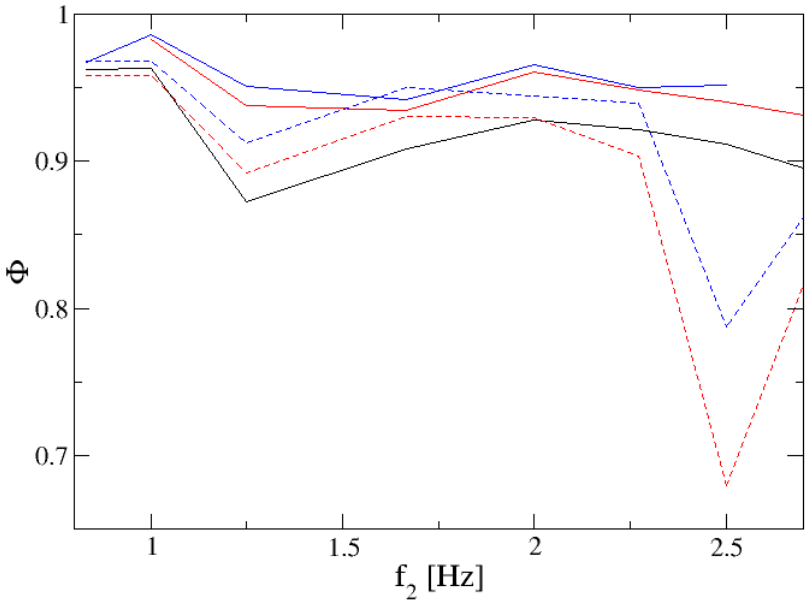

Figure 8.16: Strength of irregularity, measured by Φ, in dependence of frequency f_2 of the secondary pacemaker for various fixed values of the conductivity κ of the tissue: solid lines refer to the pBOCF model and dashed lines to the pBOCF-re variant. The frequency of the primary pacemaker is kept constant at 1 Hz. The conductivity κ varies between 0.016 S/m (black), 0.046 S/m (red), representing structural remodelling, and 0.06536 S/m (blue), which is the standard value used for simulations corresponding to normally conducting tissue.

normal conductivity, 0.046 S/m represents structural remodelling[3] (about 30% reduction of conductivity) and 0.016 S/m is strongly decreased conductivity. The frequency of the primary pacemaker is kept constant at $f_1 = 1$ Hz. In the pBOCF model, reducing the conductivity even to the extremely low value of 0.016 S/m does not increase the strength of irregularity or cause a new irregularity to occur. In contrast, in the pBOCF-re variant a decrease of κ by 30%, to simulate a structural remodelling in the pBOCF-re variant, leads to further reduction of Φ by about 0.1 and only minor changes of $f_{\max}$. A structural remodelling is thus not decisive for the initiation of type IV irregularity, but influences its strength. For $\kappa = 0.016$ S/m propagating wave fronts cannot be initiated in the pBOCF-re variant.

[3]Structural remodelling causes changes in the composition of cells and number and location of gap junctions and, thus, conductivity changes.

8.3 Influence of the direction of secondary wave fronts on irregular patterns (BOCF)

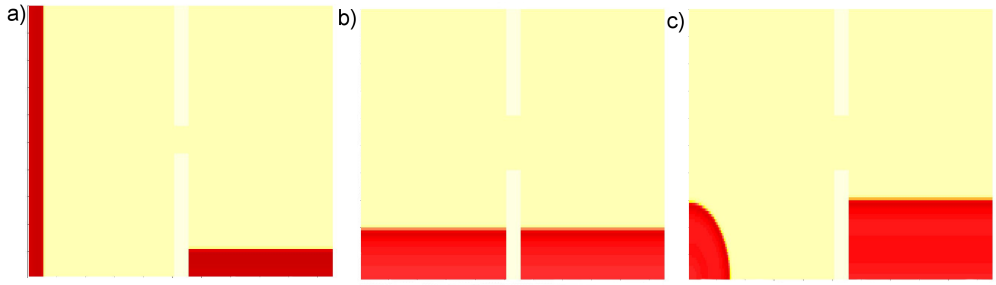

Figure 8.17: Three different orientations of the secondary wave front, shown shortly after initiation. (a) Standard orientation with wave front parallel to the y-axis and propagating in $+x$-direction. (b) 90° rotated orientation of the secondary wave front, i.e. the wave front is parallel to the x-axis and propagates in $+y$-direction. (c) 45° rotated orientation of the secondary wave front, where the front is initiated at line between [0,2] and [2,0].

The influence of the wave front orientation of the (almost) planar secondary waves is studied in the BOCF model. Thereby, three different orientations are tested, which are shown in Fig. 8.17. The first one is the standard orientation, where the wave front is parallel to the y-axis and propagates in $+x$-direction [Fig. 8.17 (a)]. The second orientation is rotated by 90° compared to the standard orientation. That means, the wave front is parallel to the x-axis and propagates in $+y$-direction [Fig. 8.17 (b)]. For the third orientation, the wave front is initiated with an angle of 45° compared to the first variant, i.e. the external current z is applied on the line between [0,2] and [2,0]. After initiation this wave front evolves with a slight curvature due to the interaction with the boundary, but its shape is nearly planar when it reaches the bridge [Fig. 8.17 (c)].

In Fig. 8.18 the strength of irregularity, measured by Φ (upper panel), and the maximal frequency f_{max} (lower panel) determined in region R are shown in dependence of the frequency f_2 of the secondary pacemaker for the three different orientations of the secondary wave fronts. The frequency of the primary pacemaker is kept constant at 1 Hz. On the left side the results are shown for the pBOCF model and on the right side for the pBOCF-re variant. In the pBOCF model, the orientation of the wave front only slightly influences the strength of the irregularity if $f_2 < 2.5$ Hz. For larger f_2, the phase coherence Φ decreases by about 13%. Nevertheless, the corresponding patterns resemble irregularity type III, where short-living re-entrant patterns occur near the lower boundary of region R.

For the pBOCF-re variant, the 90° orientation of the wave front (red curve in Fig. 8.18) results in similar irregularities, i.e. irregularity type IV patterns

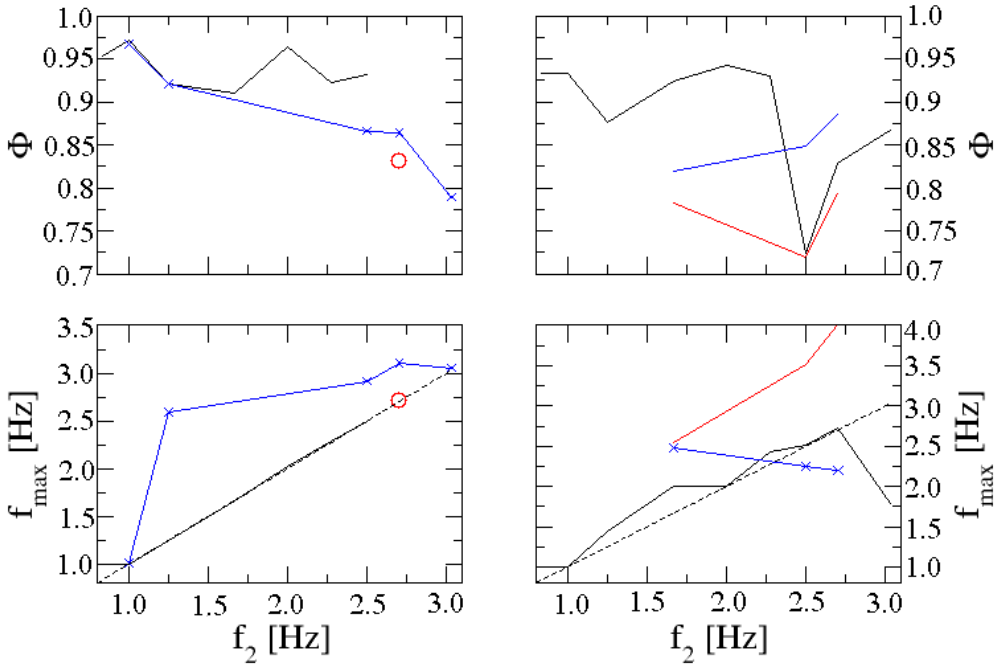

Figure 8.18: Strength of irregularity, measured by Φ (upper panel), and maximal frequency f_{max} (lower panel) in region R in dependence of frequency f_2 of the secondary pacemaker for three different orientations of the secondary wave front. On the left side, the results are shown for the pBOCF model (left) and the pBOCF-re variant (right) and $f_1 = 1$ Hz: normal orientation [black, Fig. 8.17 (a)], 90° [red, Fig. 8.17 (b)] and 45° rotated orientation [blue, Fig. 8.17 (c)] . The dotted line in the f_{max} graphs represents $f_{max} = f_2$.

are observed as well. Thereby, similar re-entrant patterns can be observed (double spiral pattern) and additionally, for a certain time, a stable spiral wave. Irregularity occurs in this case by interaction of secondary wave fronts with each other after passing the bridge. Neither sustained nor transient conduction block is observed.

In Fig. 8.19 two representative patterns are shown, which occur during the simulation for the 90° rotated wave front orientation of the secondary pacemaker (time evolution is shown in movie S7 in the Supporting Material). In the upper panel three snapshots of the spiral wave evolving in region R (after ≈ 9 s of the simulation time), are shown, whereas in the lower panel three snapshots of the re-entrant pattern with two open ends, similar to the one observed in irregularity type IV for normal wave front orientation, can be seen. The maximal frequency observed in this regime (see Fig. 8.18 lower panel), $f_{max} \approx 3.5$ Hz, is larger than for the standard wave front orientation, possibly

due to the spiral wave occurring at intermediate stages of the simulation. Nevertheless, the strength of irregularity is comparable to the values for the standard wave front orientation in this regime of irregularity type IV. The strength of irregularity is larger, i.e. Φ is smaller, in the frequency regime of irregularity type III when compared to the values for the standard orientation.

In contrast to this, for the 45° wave front orientation, irregularity type IV does not occur, only the mixture of type I, I and III patterns (see also time evolution shown in movie S8 in the Supporting Material). Thus the strength is reduced, i.e. Φ is increased in comparison with the values of the other orientations. For smaller f_2, Φ is comparable to the values of the 90° orientation, i.e. smaller than for the normal orientation. Larger values of f_{max} are observed for the two orientations (45° and 90°) than for the normal orientation. This can be attributed to the increased curvature of the wave fragments at the lower boundary in region R, resulting in a short-living re-entrant pattern. In the normal orientation, the wave fragment is extinguished at the boundary, where a small re-entrant pattern occurs, which is extinguished by its tail.

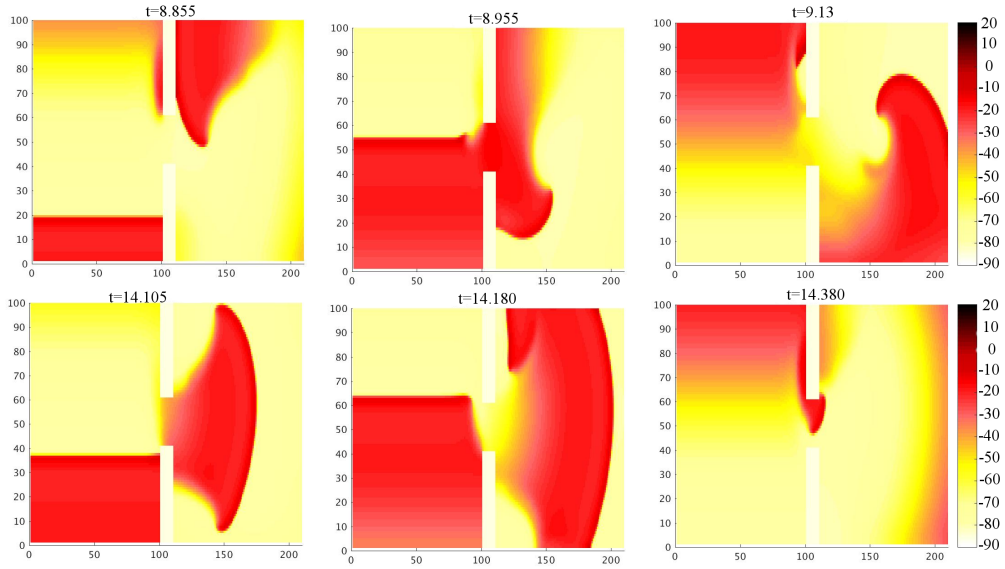

Figure 8.19: Snapshots of two excitation patterns, namely a spiral wave (upper panels) and a wave fragment with two open ends (lower panels), in the frequency regime of irregularity type IV in the pBOCF-re variant for 90° wave front orientation. Red colour represents the excited state, yellow the resting state. Numbers at the graphs give the time instant in seconds. Time evolution is also shown in Movie S7 in the Supporting Material.

8.4 Influence of wave front shape on irregularities

The influence of the wave front shape onto the interplay of the two pacemaker is studied in the FHN model by changing the shape of the secondary pacemaker: first, the secondary pacemaker is assumed to be a point source, representing an ectopic focus, and, second, the secondary pacemaker is assumed to be a stable spiral wave, circulating around functionally re-entry tissue. In the case of the point source, a stimulating current $z = -1$ is applied at a circular area with centre at $[x = 0, y = 5]$ and radius $r = 0.2$. The emerging secondary waves exhibit a circular shape. The frequency of the secondary pacemaker is varied in the same range as for the planar waves. However, a 1:1 pacing is observed only for very small perturbing frequencies ($f_2 < 0.05$). This is due to the circular shape of the wave fronts, which causes a slower conduction velocity of the waves given by

$$v(K) = v_0 - DK, \tag{8.4.1}$$

where v_0 is the conduction velocity of planar waves, D the diffusion coefficient, $K = 1/r_k$ the wave front curvature and r_K is the curvature radius. This relation is well known for active tissue and was derived in 1980 by Zykov [235] for the FHN model for diffusion of the activator only and generalized about 17 years later by Wellner and Pertsov [236] for a broader class of systems, allowing also diffusion of both species. From Eq. (8.4.1) it can be seen that convex wave fronts propagate slower than planar waves. Thus, for the frequency range analysed ($0.09 < f_2 < 0.11$), the frequency of circular waves is two times f_2, since only every second activation is successful. Due to this low frequency, the influence of the secondary waves onto the primary waves is negligible. Irregular patterns are only observed for frequency regime I, where primary waves detach from the bridge. Here, the secondary waves do not influence the pattern and excitation patterns are observed, as if only the primary pacemaker is active. Thus, circular excitation wave fronts for the secondary pacemaker result in more regular patterns due to the low frequency of excitations and the symmetric shape of the front after crossing the bridge.

In the case of the spiral wave as secondary pacemaker, generation of spiral waves was first tested in homogeneous 2D tissue (without bridge). From a stable spiral wave, observed after crossfield-stimulation[4], the u, v-distribution for a certain time instant is taken and used as initial condition in region L. In this way, a spiral wave is initiated, which has a constant rotation frequency of 0.09. As for the point source, due to the low frequency of the secondary waves, only irregularity type I is observed. But in contrast to the circular waves, the secondary waves emitted by the spiral wave interact with the primary waves

[4] After an initially planar first stimulus, a second stimulus perpendicular to the first one, is applied. Because of the refractory tail of the first stimulus a wave front with open end is generated, which can evolve into a spiral wave.

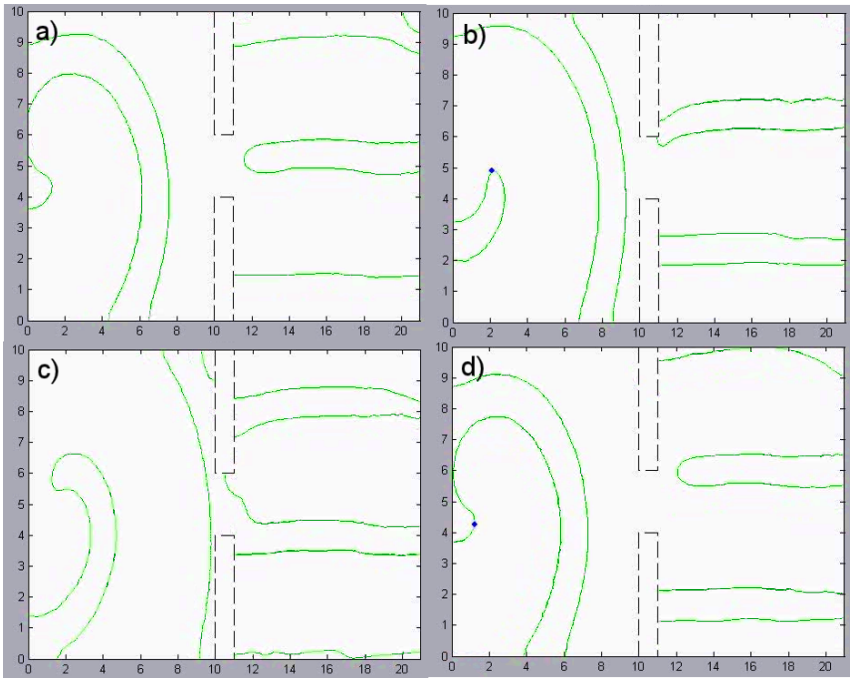

Figure 8.20: Excitation pattern for irregularity type I with spiral wave as secondary pacemaker ($f_2 \approx 0.09$) and $f_1 = 0.11$ for different time steps a) 72, b) 75, c) 81.5, and d) 85. Contour lines, where $u = -0.8$, are shown, representing the activation and the refractory front of the excitation waves. Detachment of primary waves from the bridge is seen in a) followed by a curling of the open end of the wave front in b), and a merging with the secondary wave in c). The pattern in d) almost resembles the one in a), with a small offset of the primary wave front already passing the bridge in $+y$ direction.

and patterns resembling the ones observed for planar, secondary waves for irregularity type I can be seen (Fig. 8.20).

8.5 Influence of bridge width on occurrence of irregular patterns

The observed conduction block in the pBOCF-re variant is a well-known phenomena for waves passing a small isthmus. The occurrence of the conduction block thereby depends on the specific electro-physiological model, the width of the isthmus, the frequency and excitability of the medium. For example, the conduction block can be observed for the pBOCF-re variant due to the lower excitability compared to the pBOCF model but it is not found for the pBOCF model. Furthermore, also the size of the isthmus can play a role for the occurrence of detachment. Here, smaller widths of the bridge are tested for the different models.

At first the dependence of the excitation patterns on the bridge width will be discussed for the FHN model. Increasing the bridge width from $w_b = 2$ up to 4 does not influence the occurrence of the irregularities. Only the strength of the irregularity quantified by S is slightly increased for type I and II. This is caused by the larger interaction zone near the bridge, leading to an enlarged area enclosing the irregular pattern. If the bridge width is decreased, the occurrence of irregularities does not change, as long as the bridge width is larger than a critical bridge width w_{cbl}. For $w \leq w_{cbl}$ a total, complete conduction block occurs at the bridge, i.e. every secondary or primary wave front passes the bridge, but it cannot propagate further into region R or L, respectively. This is due to the curvature of the wave front when leaving the bridge. The curvature is increased so strongly that the conduction velocity $c(K)$ according to Eq. (8.4.1) becomes zero or negative. The corresponding width w_{cbl} of the bridge can be determined by setting $c(K) = 0$. With $c(0) \approx 1$ and $D = 0.1$ for the parameters used in the simulation, $w_{cbl} = 0.05$. In this case, the excitation patterns in region R and L are generated by the respective pacemaker and there is no interference between the secondary and primary wave fronts. Thus only regular patterns are observed.

For slightly larger $w = 0.1 > w_{cbl}$, a frequency dependent conduction block is observed. In this case, wave fronts, generated with $f \geq 0.11$, are all blocked at the bridge. For $f < 0.11$, every second wave front arriving at the bridge is blocked. Hence, the frequency of waves, which have crossed the bridge, is $0.5f_2$ or $0.5f_1$. Increasing the bridge width further to $w = 0.2$ results in a 2:1 transfer of waves across the bridge independent of the frequency of wave fronts (down to $f = 0.0625$). The transfer function, i.e. the relation between wave fronts arriving at the bridge and wave fronts which successfully cross the bridge, depends thereby on the frequency and the bridge width. This was shown also for isolated cardiac muscle and in simulations of the Luo-Rudy model by Cabo *et al.* [237]. It can happen that every wave front is blocked or only every second, third etc. Considering the interplay of the two pacemakers, the same patterns are observed as for larger bridge widths but now the effective frequency of secondary waves in region R is $f_2/2$, and the effective frequency of primary waves in region L is $f_1/2$. Thus, regular patterns in region R are observed for $f_2 < f_1$, while irregularity type III occurs for $f_2 > f_1$. In this respect, no new patterns or irregularities occur due to reduced bridge width in the FHN model. Furthermore, detached wave fragments, as observed in the pBOCF-re variant in the case of the transient conduction block, are not seen in the FHN model.

For the pBOCF model similar results were obtained. Figure 8.21 shows the strength of irregularity, measured by Φ, in dependence of f_2, the frequency of the secondary pacemaker for various fixed values of the width $w = 0.1$ cm (black), 0.5 cm (red), 1 cm (green), and 2 cm (blue). Results are compared for the pBOCF model (upper panel) and the pBOCF-re variant (lower panel). In the pBOCF model, changing the bridge width leads to minor changes of the

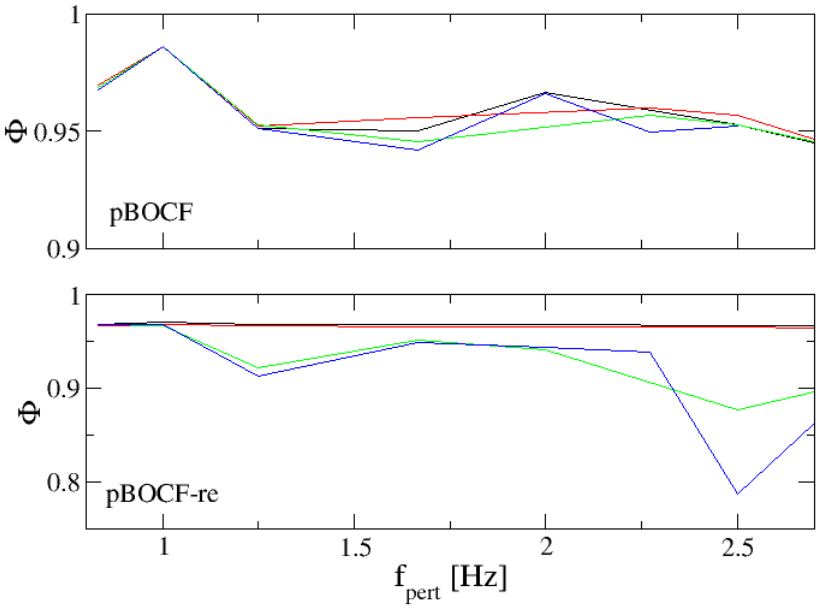

Figure 8.21: Strength of irregularity, measured by Φ, in dependence of frequency f_2 of the secondary pacemaker for $f_1 = 1$ Hz and various fixed bridge widths $w = 0.1$ cm (black), 0.5 cm (red), 1 cm (green) and 2 cm (blue). In the upper panel results for the pBOCF model are shown and in the lower panel for the pBOCF-re variant.

strength of irregularity in the domain of type III irregularity. For bridge widths $w \leq 1\,\mathrm{mm}$, the resulting patterns were not altered significantly. Upon further decrease to $0.6 \lesssim w \lesssim 0.8\,\mathrm{mm}$, a frequency-dependent conduction block was seen, i.e. for high frequencies ($f \approx 3\,\mathrm{Hz}$) only every second wave front could pass the bridge. For smaller frequencies $f \lesssim 2.7\,\mathrm{Hz}$, no conduction block occurred and all wave fronts propagated through the isthmus. This does not cause the generation of irregular patterns, since it only reduces the effective frequency of the secondary wave fronts after passing the bridge. For very small widths $w < w_{cbl} \lesssim 0.4\,\mathrm{mm}$, a total conduction block arose, which led to an effective separation of the two regions R and L with regular patterns. The critical isthmus width w_{cbl} is slightly larger than the theoretically predicted value $w_{cbl}^{th} \approx 0.27\,\mathrm{mm}$, which is given by $w_{cbl}^{th} = D/c_0$ [238] with $D = 1.882\,\mathrm{cm}^2/\mathrm{s}$ and $c_0 = 69\,\mathrm{cm/s}$ the conduction velocity of a plane wave. This indicates a non-linear relationship of conduction velocity on wave front curvature or a discontinuity in this relationship. For heart tissue, the exact dependence of conduction velocity on wave front curvature is not known [239]. Transient conduction blocks or detached wave fronts, as in the pBOCF-re variant, were not observed.

For the pBOCF-re variant, in contrast, a reduction of the bridge width from 2 cm to 1 cm reduces the strength of irregularity (increases of Φ). Already for the largest tested bridge width $w = 2$ cm, a frequency-dependent conduction block is observed. This bridge width is larger than in the case of the pBOCF model, where the frequency-dependent conduction block occurs for $w < 0.8$ mm, due to the decreased excitability. For $w < w_{cbl} = 5\,\mathrm{mm}$, the total conduction block occurred. In this case Φ is independent of f_2, since only the primary wave fronts generate the excitation pattern in R. The bridge width value for the total conduction block is about ten times larger than the theoretically predicted value [238] $w_{cbl}^{th} = D/c_o = 0.52\,\mathrm{mm}$ with $D = 1.882\,\mathrm{cm}^2/\mathrm{s}$ and $c_0 = 36\,\mathrm{cm/s}$. This is caused by the fact that the excitability is not accounted for in the formula, as pointed out by Wellner and Pertsov [236]. They derived a formula for the wave front speed, which takes into account the influence of the excitability and the frequency of waves for a modified FHN model. Two more terms are added, based on the variation of the conduction velocity c by the frequency ω and by the excitability ϵ, namely $\omega/c(\partial c/\partial\omega)_\epsilon$ and $\epsilon/c(\partial c/\partial\epsilon)_\omega$. However, these terms are not known for the BOCF model and thus the critical bridge width for the total conduction block cannot be compared to the corresponding analytical value, when considering the pBOCF-re variant. For the pBOCF model, the formula derived by Zykov agreed well with the values observed in the simulation.

8.6 Discussion

The interplay between two pacemakers located in separate regions, which are only connected by a small isthmus, was studied. Regular excitation patterns are observed in both, the FHN and BOCF models, for a large range of frequency ratios f_1/f_2. This could be expected, since the heart is typically working in a stable manner without irregularities. In Tab. 8.1 the irregularities, which occurred in the different models, are summarized as well as the frequency regimes, where they occur.

In both, the FHN and BOCF model, the same type of irregularity is observed if $f_2 > f_1$, where the secondary wave fronts expel the primary wave fronts. Due to the activation of the primary pacemaker in between the secondary wave fronts in region R, irregular excitation patterns appear. Thereby, the patterns remain relatively regular for the BOCF model because of the extinction of curled primary wave fronts at the boundary of the simulation area. In contrast, in the FHN model, the secondary wave fronts become curled in this region and spiral wave type behaviour can be observed. However, in both models the strength of the irregularity is quite low and the patterns do not resemble fibrillatory excitation patterns in the atria. Thus, the relevance of irregularity type III for the initiation of AF is thought to be low. Furthermore, the question arises, if the activation of the primary pacemaker in between the secondary wave fronts can occur in real tissue, which will depend very much

Table 8.1: Types of irregularities found in certain frequency ranges of the different models

model	frequency range	observed irregularities	classification of pattern in R
FHN	$f_1 > f_{\text{det}}^{\text{FHN}}$	Type I: detachment of primary waves	irregular
	$f_2 > f_1$ $f_2 > f_{\text{det}}^{\text{FHN}}$	Type II: detachment of secondary waves	irregular
	$f_2 > f_1$ $f_2 < f_{\text{det}}^{\text{FHN}}$	Type III: wave fragments at lower boundary in R	irregular
pBOCF	$f_2 > f_1$	Type III: wave fragments at lower boundary in R	weakly irregular
rBOCF	$f_2 > f_1$	Type III: wave fragments at lower boundary in R	weakly irregular
pBOCF-re	$f_1 > f_{\text{tbl}}^{pm}$	wave breaks and reentry in L	regular
	$f_2 > f_1$ $f_2 < f_{\text{tbl}}^{pm}$	Type III: wave fragments at lower boundary in R	weakly irregular
	$f_2 > f_1$ $f_2 > f_{\text{tbl}}^{pm}$ $f_2 < f_{\text{sbl}}^{pm}$	Type IV:conduction block with wave breaks/ re-entry	irregular
	$f_2 > f_1$ $f_2 > f_{\text{sbl}}^{pm}$	conduction block with 2:1 conduction	regular

on the characteristics of the pacemaker cells. In the model, the activation is externally applied and its strength is independent of the previous activations. Sinus node cells, in contrast, are cells with an unstable resting state, continuously producing activations. These activations and the course of the APs depend on previous activations of the cell and APs of the neighbouring cell. It is unclear, if an activation can be generated by the pacemaker cells in between high-frequency activation of the surroundings. This should be studied in further investigations.

Different experimental studies [240–242] showed that during AF, the sinus node automaticity is still present in AF or high-frequency pacing of the atria, although its properties (frequency, ERP etc.) can be changed by the overdrive pacing. Fedorov *et al.* [240] found that the connection between the sinus node and atrial tissue is based on special connection pathways which act as low-pass filter with an entrance conduction block[5] thus preventing the sinus node from overdrive pacing. Due to these findings, a sinus node activity during AF can be assumed and thus activation in between secondary wave fronts by the sinus node. This would be a necessary prerequisite for the occurrence of irregularity

[5]Waves entering the sinus node are blocked.

type III.

In the FHN model two more types of irregularities occur, which are caused by the detachment of high-frequency paced waves at sharp corners. Thereby, wave fragments and re-entry patterns are observed, which resemble fibrillatory patterns observed in the atria. The strength of irregularity in such situations is quite large. Thus, the relevance of these mechanisms for the initiation of AF could be quite high. However, this detachment of waves is not observed in the pBOCF or rBOCF model. The phenomenon of detachment from sharp corners due to high-frequency pacing is known for different electro-physiological models, as for variations of the FHN model [226, 228] or the Luo-Rudy model for ventricular tissue [60, 227, 229]. However, Azene *et al.* studied the detachment of waves from obstacles due to reduced excitability or high-frequency pacing in the Luo-Rudy model, but could not observe detachment for the high-frequency pacing. Furthermore, detachment of waves was shown also in experimental preparations of isolated sheets of cardiac tissue. Therefore, sharp corners or obstacles were introduced by cutting the tissue. Other mechanisms, creating similar source-sink mismatches resulting in detachment, are possible, as e. g. abrupt changes in fibre orientation, thickness of the tissue or electrical properties of the cells at intersections of special muscle bundles with the atrial wall. Detachment and conduction block were found in atrial tissue at the Pectinate Muscles [62] or Bachmanns Bundle [243]. In computational models, inhomogeneity of tissue or the interaction with another wave front were found to be further factors for detachment and conduction blocks [244].

Why the detachment from obstacles for high-frequency pacing is not occurring in the BOCF model, is still unclear. In the mentioned models and experimental preparations, ventricular tissue was studied. It might be, that the parameter set for atrial tissue used in the BOCF model changes the properties of the tissue in that way that detachment is prevented. Thus, it should be studied, which parameters are enabling or preventing detachment in dependence on the type of tissue. If detachment of waves from obstacles occurs for atrial tissue, irregularity type I and II can be candidates for the initiation of AF. Type I can describe situations with high heart rates, as, for example, during sports or excitement. Type II would occur for high-frequency perturbation sources, almost independent of the sinus node frequency.

Another type of irregularity, type IV, is found in the pBOCF-re variant, but not in the FHN, pBOCF or rBOCF model. For this type, a transient or intermittent conduction block at the small isthmus occurs. Shortly after the conduction block, small detached wave fragments evolve after passing the bridge, which, in combination with the primary wave fronts, yield quite irregular excitation patterns with high frequencies. In experiments with large sections of atrial tissue without additional cuttings, similar results were observed. Berenfeld *et al.* [243] isolated the right atria including Bachmans Bundle and the right ventricle of sheep hearts and applied a pacing with different frequencies at the left side of Bachmanns Bundle. For small pacing frequencies, a 1:1

conduction along Bachmanns Bundle and regular excitation patterns are observed in the right atrium. For frequencies larger than $6.5 - 6.7$ Hz, a broader distribution of activation frequencies and a loss of consistency of beat-to-beat direction of the wave fronts, described as fibrillatory conduction, were observed in the right atria. These were not connected to spatial dispersion of the intrinsic APD. Intermittent block appearance was resolved as mechanism for this behaviour. This is in close resemblance to the numerical results for the pBOCF-re variant and thus identifies this mechanism of transient conduction block as a potential candidate for AF initiation. Here, a reduced excitability is necessary to obtain the detachment of waves and the transient conduction block. Although not observed in the FHN model for the studied parameter range, it should occur also in other electro-physiological models without reduced excitability. The mechanism creating the wave fragments is comparable to the high-frequency detachment of wave fronts from obstacles known from experiments [227, 237] and other electro-physiological models [227]. Further studies in a range of bridge widths close to the conduction block width should further elucidate characteristic features of this mechanism.

The influence of wave front shape, orientation and bridge width on the observed irregularities was studied. Circular wave fronts seem to result in more regular patterns due to their low, shape-related frequency. The interplay of pacemakers, where one of them has a circular shapes, was found to be irrelevant for the initiation of AF. In contrast, for a spiral wave shaped pacemaker similar irregularities as seen for planar waves are observed. In the simulation they resemble planar waves with a tilted orientation near the bridge. Due to their higher frequencies and their often described observation in electrocardial mappings, they are supposed to be relevant as possible secondary pacemaker. Furthermore, as shown by Berenfeld *et al.* [245], they often introduce heterogeneity, which could further enhance the possibility of generating wave fragments and thus the initiation and maintaining of AF.

The wave front orientation influences on the one hand the occurrence of irregularities and on the other hand the strength of irregularity and the detected maximal frequencies. For the 45° rotated wave front orientation, irregularity type IV is not occurring. For the 90° orientation of the wave front, the maximal detected frequencies are larger than for the standard orientation.

The bridge width influences the occurrence of irregular patterns if it is decreased into the range of critical bridge widths, where conduction blocks occur. If sustained conductions blocks with a certain conduction ratio, such as 2:1, 3:1 etc. or complete conduction blocks are present, more regular excitation patterns are observed. In the range of transient or frequency-dependent conduction blocks, irregular patterns can occur. No transition of 2:1 to 1:1 conduction is seen in the pBOCF model for the analysed frequencies. Thus, a reduction of isthmus size may help to prevent AF if tuned in the right range. This was also shown in experiments [246], where fibrillatory patterns and high-frequency pacing could be regularized due to conduction block at the isthmus.

In this case, regular activations with lower frequencies were observed at the other side of an isthmus.

The different behaviours of the pBOCF model and the pBOCF-re variant with respect to detachment and conduction block properties may be caused by differences in the wave length WL=CV/ERP (WL). To test this, modified WLs for pBOCF model and pBOCF-re variant were tested by altered conductivities κ (see Fig. 8.11). Changing κ does almost not affect ERPs but CV and thus WL. For $\kappa = 0.016$ S/m in the pBOCF model, one obtains a WL almost the same as in the pBOCF-re variant with $\kappa = 0.065$ S/m. In simulations of the pBOCF model for this smaller κ, waves still do not detach, and synchronization changes only very little. For strongly increased κ (0.1533 S/m) and a conductivity decreased by 30% from the normal value ($\kappa = 0.046$ S/m), the same type of behaviour is seen. For very small conductivity $\kappa = 0.016$ S/m, the critical isthmus width for the total conduction block is decreased to $w_{cbl} = 0.2$ mm, and the onset of the frequency-dependent conduction block is shifted to 0.4 mm in the pBOCF model. From these results, the different behaviours according to detachment and conduction block cannot be associated by WL differences, but likely result from the differences in the ERP.

It is worth here to mention that the study here differs from previous studies about detachment of waves from sharp corners or conduction block, since not only one pacemaker was involved but two, whose frequencies could be tuned. Thus, it allowed to study the influence of a second source on the detachment and conduction block phenomenon. The generation of irregular states exhibited a clear dependence on the frequencies of the two pacemakers. Furthermore, also a regularization of irregular patterns, caused by the primary source, could be found. Let me further mention that the present study differs from previous studies on AF generation also because homogeneous tissue is considered. Nevertheless, irregular patterns could be observed. Thus, heterogeneity of tissue is not a necessary condition for the generation of irregular patterns.

The findings of the modelling offers some implications for the therapy of AF. High-frequency secondary sources should be suppressed as well as high-frequency activations by the sinus node. Typically, AF is treated with ablation therapy, if it could not be terminated by medication. Thereby, ablations, i.e. lesions or 'cuts', are applied to the atrial tissue to eliminate re-entry pathways and ectopic activity. Different protocols for the sites of ablation exits. The maze procedure applies grid-like pattern of lesions, yielding a high success rate for AF termination combined with large modifications of the atrial tissue. The conventional, standard method [247] for catheter ablation is based on a two-step process, where first the pulmonary veins are isolated from the atrial tissue and then targeting sites of complex fractionated atrial electrocardiograms (CFAE), especially in patients with persistent AF. These sites are thought to potentially represent AF substrate sites. Based on the mechanism studied in this thesis, it is proposed to not target CFAEs, since they are assumed to arise from the interplay of different pacemakers (here near the

bridge), but rather search for localized sources. These can be identified by a high frequency (but may have lower frequencies than CFAEs) and regular activation. Indeed, Narayan *et al.* [231] compared catheter ablation outcomes for the conventional strategy with that based on the ablation of localized sources, called focal impulse and rotor modulation (FIRM) ablation. They showed that termination of AF during ablation could be achieved in 86% of FIRM-guided cases, whereas with the conventional strategy only for 20% of the patients AF was terminated. Furthermore, freedom from AF was higher for patients with FIRM-guided ablation than for conventional ablation procedure.

As for all studies, there are some limitations. First of all, the atrial tissue was assumed to be two-dimensional due to the small thickness of atrial walls. Thus, the study of breakthroughs, i.e. activations propagating from epicardial (outside) to endocardial (inside atrium), or the other way round, are not taken into account. Breakthroughs are discussed as one mechanism for the initiation of AF. However, taking into account the thickness of the atrial wall and allowing breakthrough patterns would have complicated the overall set-up and thus impeded the analysis of mechanism responsible for the generation of irregularities due to the interplay of these two pacemakers.

The second assumption was to take into account only one bridge connecting the two atria. This assumptions is based on experimental findings [220, 222, 248], which showed that the left atrium activation is predominantly initiated by Bachmanns Bundle. In some cases additional activation occurred via the coronary sinus and the fossa ovalis. Markides *et al.* [220] showed that in the case of AF, multiple connections can play a role for activation initiation in the left atrium. However, for the study of the interplay of two pacemakers, additional pathways are thought to increase only the irregularity of excitation. The mechanism of detachment or conduction block is believed to be the same for all conduction pathways and to depend on their size and shape.

The third assumption is the bridge with the sharp corners. In atrial tissue sharp corners are not expected but rather a smooth transition from the fibre bundles into the muscle tissue. However, Markides *et al.* [220] determined a line of functional conduction block in the left atrial tissue occurring in all studied patients during sinus rhythm and showed some variations in its extent and completeness in different pacing conditions. These could be correlated with an abrupt change of fibre orientation and wall thickness in the left atrium, already described 1914 by Papez *et al.* [249]. That means, abrupt changes, corresponding to the sharp corners of the bridge in the study here, occur also in anatomical tissue. Mendez *et al.* [250] performed measurements at the connection of the Purkinje fibres to the ventricular tissue. They showed that conduction block can occur due to the progressive change of a cable-like system to a two- or three-dimensional system at the border between Purkinje fibre and ventricular tissue. Furthermore, Azene *et al.* [60] studied by numerical calculations of the Luo-Rudy model the influence of the shape of obstacles onto the detachment of waves from it. They determined the range, where

detachment of waves from the obstacle occurred, in dependence of the radius of the obstacle and the reduction of excitability in the model. Detachment occurred even for large radius, i.e. very smooth 'corners'. Only the range of the excitability for the occurrence of this detachment was reduced.

Another limitation of this study is the use of the BOCF model for system-specific simulations, since it belongs to the class of generic models. Thus, for special cases, as the study of the conduction block or the detachment, simulations were carried out with the system-specific CRN model, invented for the description of atrial tissue. In these simulations, no significant changes of the behaviour between the two models were found. However, in both models detachment from sharp corners did not occur although known from experiments and simulations. This could be a model-specific effect. As was shown by Wilhelms *et al.* [230], already differences in the ability to initiate a spiral wave pattern by cross-field stimulation are observed between different atrial cell models. Therefore, detachment of waves should be studied in different atrial cell models as well as in experiments with atrial tissue to unravel the requirements of its occurrence and its relevance for AF initiation.

Furthermore, only phase coherence and entropy of the distribution of local frequencies are used as measures for the regularity of the patterns. Nevertheless, they measure different properties of the time series. While the frequency takes into account only the time between the action potentials, the phase synchronization considers also the shape of the time series. The results were tested against another measure for the irregularity, which is based on the fractal dimension of the time series (see Appendix 11). Therefore, the fractal dimension was calculated for each point in the simulation area and the entropy of its distribution is taken as measure for the irregularity, analogous to that of the local frequencies. Similar results were observed for the fractal dimension, only the amount of irregularity, i.e. the deviation of the entropy for irregular patterns in comparison with the one for regular patterns, is different. This can be caused by the different sensitivity of each measure for the irregular patterns or by differences in the normalization of the measures. Since all three measures yield similar results, phase coherence and entropy of the distribution of local frequencies seem to be adequate as measures for the irregularity of the patterns.

Part of the presented results in this chapter were published in Refs. [120, 251].

Chapter 9

Diffusive coupling of multiple oscillators

In this chapter, results about the coupling of multiple units, called spots and the resulting patterns will be presented. Each of these spots is either excitable or self-oscillatory and has a well-defined size and shape. Consequently, a patterned excitable media is formed by networks of discrete excitable units, in which it is possible to control precisely the number density of excitable units, the degree of heterogeneity and the coupling strength between them.

With this system it will be studied, if a reduced coupling strength or heterogeneity in the system can yield irregular patterns. Thereby, the underlying discreteness [252] of excitable media can lead to wave propagation failure [253] or diverse wave front shapes [174]. In particular, fibrosis, which reduces the coupling between cardiac cells, is thought to be a mechanism for the occurrence of atrial fibrillation. Thus, it will be studied if a weak coupling and/or heterogeneity of the arrays can yield irregular patterns as, for example, wave fragments, multiple spiral waves and similar. Results from the experiments of the Belousov-Zhabotinsky reaction (BZR) will be shown and compared to calculations of the FHN and the Rovinsky model. System-specific and generic features can thus be determined.

9.1 Results from BZR experiments

In this section, results from experiments with spot arrays undergoing the BZR will be presented. Thereby, the spot diameter d is determined from the first picture of each experiment as described in ch. 6.2. Since diameter variations occur for the same number of applied Ferroin drops due to deviations in the spotting accuracy and of the immobilisation properties, the concentration of Ferroin inside the spot is calculated by

$$c_F = \frac{M N_d V_d}{\pi/4 d^2}, \tag{9.1.1}$$

with the concentration $M = 0.0125\text{mol/l}$ of the Ferroin solution, the number of drops N_d applied per spot, the volume $V_d = 0.4\text{nl}$ of each drop and the determined spot diameter d. Two concentration ranges are defined for the silica gels including PSS-co-PM, which are $0.5 - 1 * 10^{-3}$ mol/m^2 and $1.1 - 2.5 * 10^{-3}$mol/m^2, and two ranges for pure silica gels: $1.0 - 1.9 * 10^{-3}$ mol/m^2 and $2.9 - 3.9 * 10^{-3}$mol/m^2. Only arrays of spots within the same concentration range are compared, since for these the reaction parameters are similar. Thus, for some spot-to-spot distances, spot diameters and concentrations no experimental data could be obtained. The spot-to-spot distance is the distance between the spot centres.

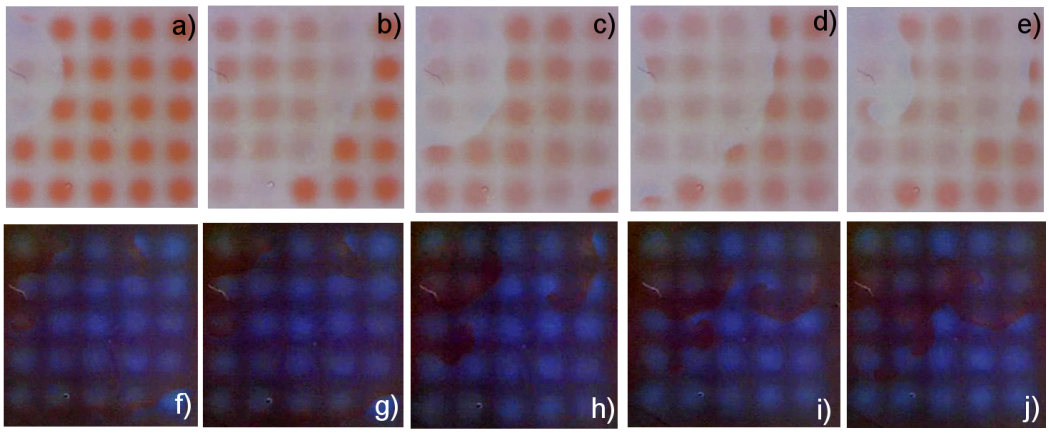

Figure 9.1: Excitation pattern occurring on a 5×5 spot array in standard gels undergoing the BZR. Panels a)-e) show the time instants directly after oscillation starts. Panels f)-j) show a later time of the experiments. Colour saturation was enhanced in a)-e) and colours were inverted in f)-j) to enhance visibility. Time evolution is also shown in movie S10 in the Supporting Material.

In Fig. 9.1 snapshots of an 5×5 spot array on a standard gel[1] are shown to give an illustration of the occurring excitation patterns (and in movie S10 in the Supporting Material). Thereby in the first row, the first waves after initiation of the BZR by adding the reaction solution are shown. A circular shaped wave front can be seen, emerging from the upper left corner and propagating to the right without disturbance [Fig. 9.1 a)-b)]. Interestingly, in most of the experiments initial wave fronts start from the border of the spot array. The second wave front propagates in a similar way across the array [Fig. 9.1 d)]. Thereby, wave fronts seem to propagate slower on the Ferroin spots than in between them. This can be seen by the concave wave front shape on the spot, e.g., right spot in the bottom row in c) or at the shape for the second wave front in d) and e). The third wave front, starting in Fig. 9.1 e), evolves into a re-entrant pattern, which is extinguished by its own refractory tail. More

[1] silica gel with 0.1 g PS-co-PM

re-entrant patterns evolve later on, rotating around the centre of a spot, but all are extinguished by collision with their refractory tail. The lower row shows the excitation patterns at a later time. Since the contrast decreases during the reaction due to fast activation and some diffusion of Ferroin, the colours were inverted to enhance the visibility. Wave fragments are visible. The upper ones evolve into spiral waves, which rotate around the spot centre [Fig. 9.1 g)-j)]. All re-entrant patterns are stable only for a short-time. These irregular patterns, consisting of multiple wave fragments and re-entrant patterns, are observed for most of the experimental realisations on the standard gels after a certain time of the running reaction, almost independent of spot size or spot-to-spot distance.

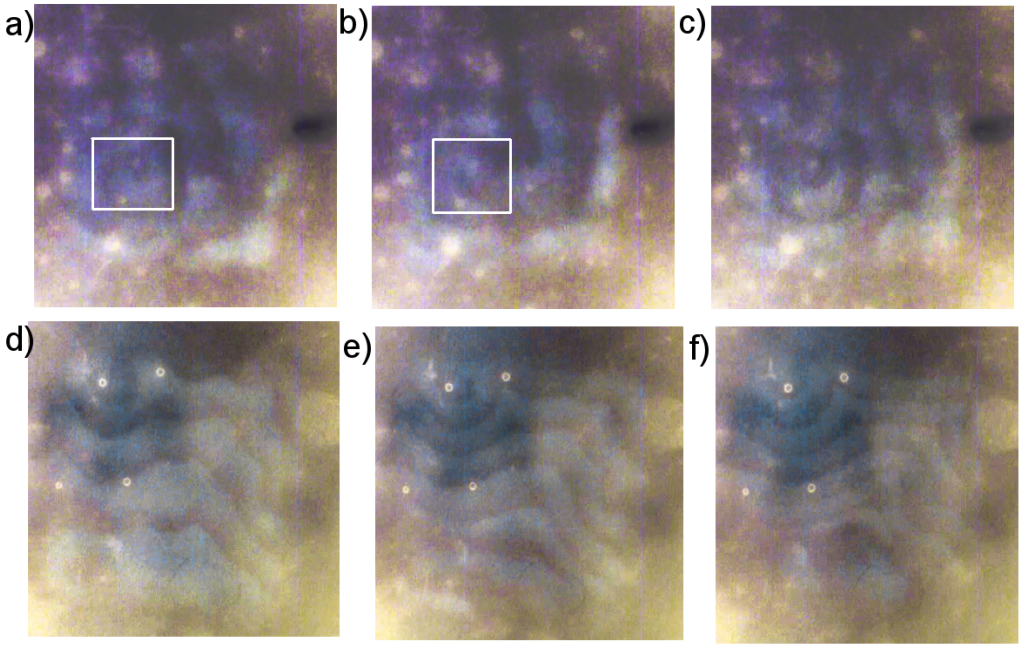

Figure 9.2: Excitation pattern occurring on two experiments of 4×4 spot array in pure silica gel undergoing the BZR. Panels a)-c) show a spiral wave. The tip of the spiral wave is inside the white box. Panels d)-f) show two target patterns. The wavelength of the waves emerging the target pattern (upper left and right corner) is decreasing with time. Colour range was enhanced and colours inverted for better visibility. Time evolutions are shown in movie S11 and S12 in the Supporting Material.

In contrast to this, for pure silica gels, wave front propagate faster on the spot than in between the spots, which can be seen on the wave front curvature (shown in Fig. 9.2 and movie S11 and S12 in the Supporting Material). In these systems, spiral waves (Fig. 9.2 upper row, movie S11) and target patterns (Fig. 9.2 lower row, movie S12) evolve for small spot-to-spot distances. For large spot-to-spot distances, oscillations of the spots seem to be independent of each other. In some cases, if multiple sources are present, wave fragmentation

can be observed. These regularize later on, since only a few pacemaker sources, i.e. 1-2 pacemaker or spirals, survive and dominate the excitation patterns than.

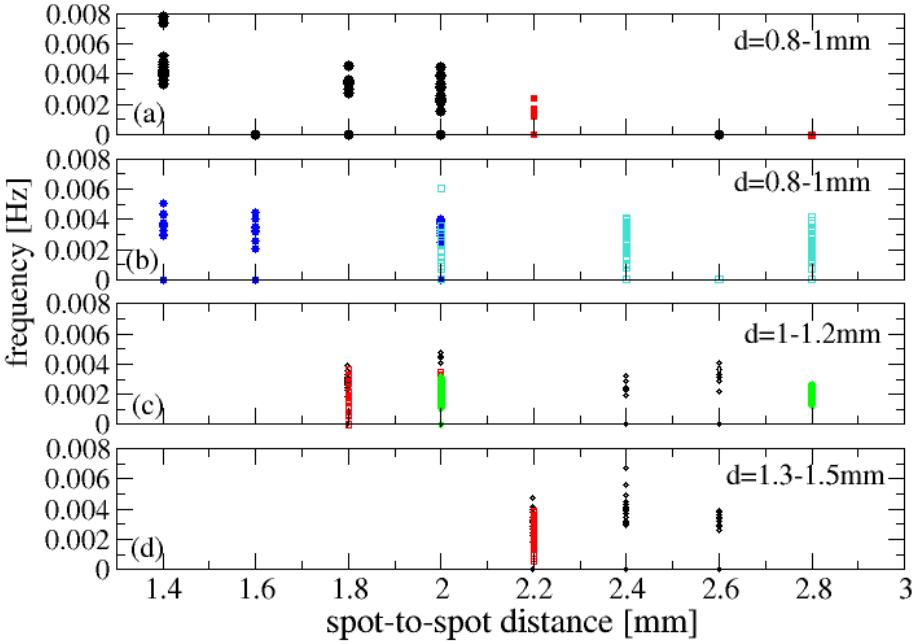

Figure 9.3: Frequency of all individual spots in spot arrays in standard gels in dependence of spot-to-spot distance for 5×5 (black), 10×10 (red, blue) and 20×20 (green, cyan) arrays, concentration and spot diameter $d = 0.8 - 1$ mm (a) and (b), $1 - 1.2$ mm (c) and $1.3 - 1.5$ mm (d). Concentration is $0.5 - 1 * 10^{-3}$ mol/m^2 (a), (c) and (d) and $1 - 2 * 10^{-3}$ mol/m^2 (b).

In Fig. 9.3 frequencies f of all individual spots in one spot array, determined from the time series of colour changes, are shown in dependence of the spot-to-spot distances l in the array for different spot diameters d. The values are from experiments with the standard gels, i.e. silica gels including PSS-co-PM, for 5×5 (black), 10×10 (red and blue) and 20×20 (green and cyan) spot arrays, the low concentration regime and the standard reaction solution (see Tab. 6.1). It can be seen in (a) that small spots ($d = 0.8 - 1$ mm) do not oscillate ($f = 0$ Hz) for large spot-to-spot distances $l > 2.2$ mm. For smaller spot distances, oscillations occur. This resembles the emergence of oscillations observed in biological and chemical systems due to coupling [82, 254–261]. In the oscillating regime ($l \leq 2.2$ mm), the mean value of the frequency distribution increases with decreasing l. In panel (b), the frequency distributions in dependence of the spot-to-spot distance is shown for the small spot diameter $d = 0.8 -$

1 mm and a higher Ferroin concentrations inside the spot ($1.1 - 1.8 * 10^{-3}$ mol/m^2) than in (a). In this case, oscillations of spots are observed for all tested spot-to-spot distances and a broadening of the frequency distribution for some experiments (see, e.g., $l = 2.4$ mm middle panel). For larger spot diameters d [(c) and (d)], oscillating spots are observed for all tested spot-to-spot distances. Interestingly, for some realizations and spot-to-spot distances, as for example $l = 2.2$ mm or 2.4 mm for large spots or $l = 1.8$ mm for middle sized spots, a broadening of the frequency distribution and increased values of the maximal observed frequency are visible. A clear dependence on spot-to-spot distance or spot size of this effect cannot be deduced from the experimental data. There seems to be no dependence on the number of spots in the array, in particular when comparing 5×5 and 10×10 spot arrays. For 20×20 spot arrays, the frequency distribution seems to be more narrow. However, due to the low number of experiments with 20×20 spot arrays in this concentration range, this was not studied in detail.

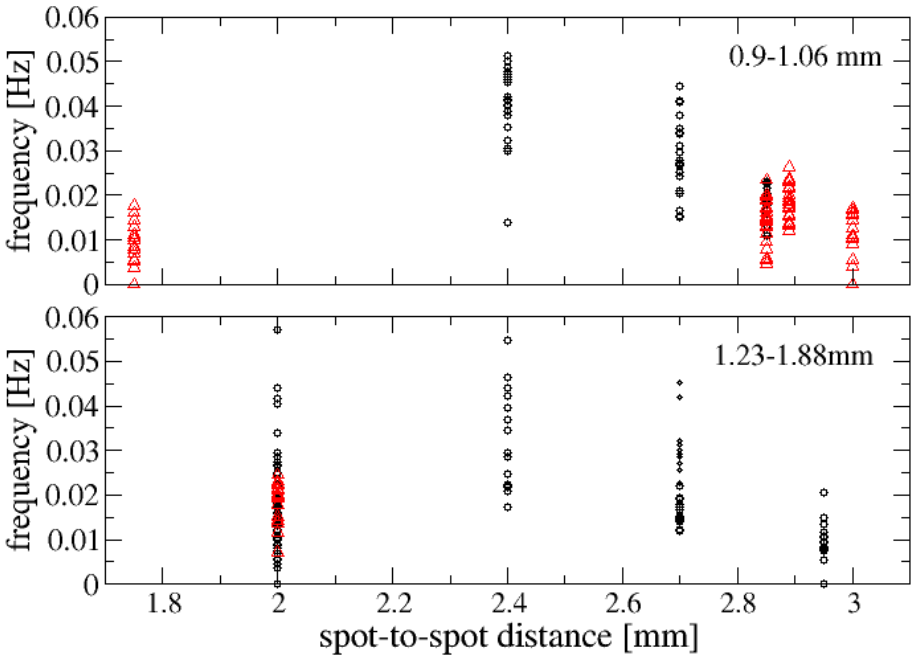

Figure 9.4: Frequency of all individual spots in 4×4 spot arrays in dependence of spot-to-spot distance and spot diameter $d = 0.9 - 1.06$ mm (upper panel) and $1.2 - 1.9$ mm (lower panel) for two different concentration regimes $c_F = 1 - 2 * 10^{-3}$ mol/m^2 (black) and $c_F = 2.9 - 4 * 10^{-3}$ mol/m^2 (red).

In Fig. 9.4 the same is shown for pure silica gels, i.e. frequency of individual spots vs. the spot-to-spot distance. Thereby, two different spot diameters are

shown and two different concentration ranges, $1-2*10^{-3}$ mol/m^3 (black) and $2.9-4*10^{-3}$ mol/m^3 (red). About 10 times higher frequencies are determined for spots on the pure silica gels. This would be expected from comparison of Fig. 9.1 and 9.2, where it is seen, that waves propagate slower on the spots than in between them for standard gels, whereas the wave front speed is comparable or even larger on the spot than in between them when considering the pure silica gels. Since the diffusion coefficient for water is similar for both gels (see NMR measurements ch. 6.1), the reaction rate has to be different between the two gels. Thereby, the compositions of the reaction solution differ only slightly for the two different gels, i.e. [H_2SO_4]= 0.19 mol/l for pure silica gels and 0.2 mol/l for standard gels, [$NaBrO_3$]= 0.11 mol/l for pure silica gels and 0.085 mol/l for standard gels and [mal]= 0.38 mol/l for pure silica gels and 0.53 mol/l for standard gels. An influence of PSS-co-PM on the reaction rate is possible, since it interacts with Ferroin and may thus influence also the BZR.

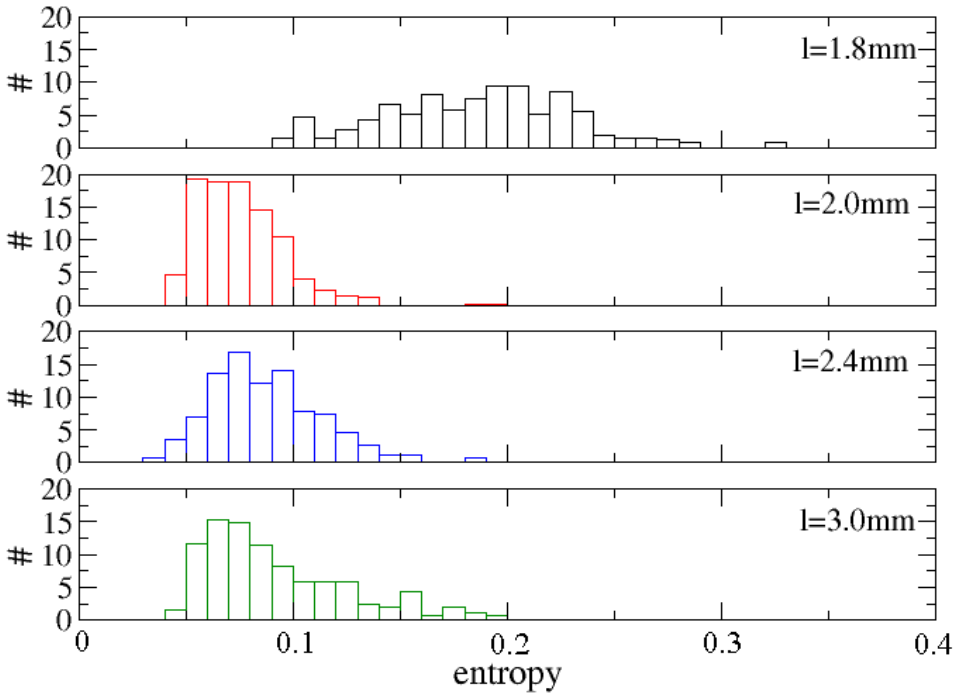

Figure 9.5: Histogram of entropy, calculated for each spot pair, for spot radius 1.3-1.58 mm and different spot-to-spot distances. A decrease of synchronization can be seen.

To determine the coupling regime between the spots, i.e. weak or strong coupling, the synchronization between all pairs of spots is determined on the basis of the entropy of the time-dependent phase difference between the two spots. In Fig. 9.5 the distribution of the entropy is shown in dependence of the spot-to-spot distance for 4×4 spot arrays on pure silica gels and an

average spot diameter of $1.3 - 1.58$ mm. A broad distribution of the entropy can be observed for the smallest spot-to-spot distance $l = 1.8$ mm with an average value of ≈ 0.19. This value is quite low due to large noise in the time series. Nevertheless, the coupling strength is assumed in the intermediate regime for this spot distance, since in the recorded excitation patterns wave fronts propagating across multiple spots are observed, forming spiral wave and target patterns. These can occur only for coupled spots. Thereby, patterns span only parts of the spot array, not the whole array. It can be deduced that this spot-to-spot distance corresponds to a medium coupling range, since for strong coupling, one pattern like a spiral wave or a comparable one is expected to span the whole array. For larger spot-to-spot distances $l \geq 2$ mm, a decrease of the mean value of entropy and a movement of the whole distribution to lower values is observed. For this range, only weak coupling between the spots occurs and they (more or less) oscillate independently of each other. Since the coupling strength is typically calculated by $C = 2D/l^2$ [262] with the diffusion coefficient D of the species responsible for coupling, a critical coupling strength can be determined, separating the medium range from the weak coupling range. In this set-up bromide ions and the other reactants are thought to drive the coupling between spots. Due to the small size of these molecules, the diffusion coefficient for water, determined by NMR for these gels, can be used as approximation for D. Thus the critical coupling strength is given by $C_{\text{crit}} = 2 * (2 * 10^{-9}\, m^2/s)/(2 * 10^{-3}\, m)^2 = 1 * 10^{-3}\, 1/s$. If one expects the same critical coupling strength, separating the medium from the weak coupling regime, the spot-to-spot distance should be similar for the standard gels for the BZR experiments (PSS-co-PM gels), since the diffusion coefficient is almost the same for silica gels and PSS-co-PM gels with 0.1 g PSS-co-PM (see Fig. 6.5). From the synchronization results for these gels, the spot-to-spot distance l_{crit} correlated with the critical coupling strength is estimated to be $l = 2.2$ mm, which is slightly larger than for the silica gels. This difference might occur due to the short experiments with silica gels and the low stability of Ferroin spots in them. Thus, spots cannot synchronize during the time course of the experiment, although it would be expected for this spot-to-spot distance.

Since the quiescence (no oscillation) of small spots occurs for $l > l_{\text{crit}}$, it seems to be a property of uncoupled (or only weakly coupled) spots and oscillations can be obtained by increasing the spot diameter or the concentration of Ferroin inside the spot. Thus, experiments with a single spot of different size and for different reaction solutions are performed on pure silica gels. The spot size was set by varying the amount of Ferroin droplets applied to the gel and is varied between $d \approx 2$ mm (500 drops of Ferroin) over 1.5 mm (250 drops) to $0.5 - 1$ mm (100 drops). Indeed, for the large spot size oscillations occur for the standard composition of the reaction solution for pure silica gels, whereas the small and medium sized spots did not oscillate. Note, that propagating wave fronts occur on the single spots and sometimes even a spiral wave like

pattern is observed on one single spot. Changing the concentration of sodium bromate in the reaction solution (1.5 ml of 0.5, 1 and 2 mol/l sodium bromate solution) did not result in the absence of oscillations for the large spot sizes or occurrence of oscillations for smaller spots. Increasing the concentration of all reactants by skipping the 3.9 ml of water, typically added in the standard composition, resulted in the absence of oscillations even for larger spots.

Spots, oscillating on their own without external stimulus, are called oscillators or oscillating units in the following. Spots, which do not oscillate by their own, are termed excitable units. The correlated property is the self-excitability. The previously described results indicate that it depends on the spot size and the reaction parameters like the concentration of Ferroin.

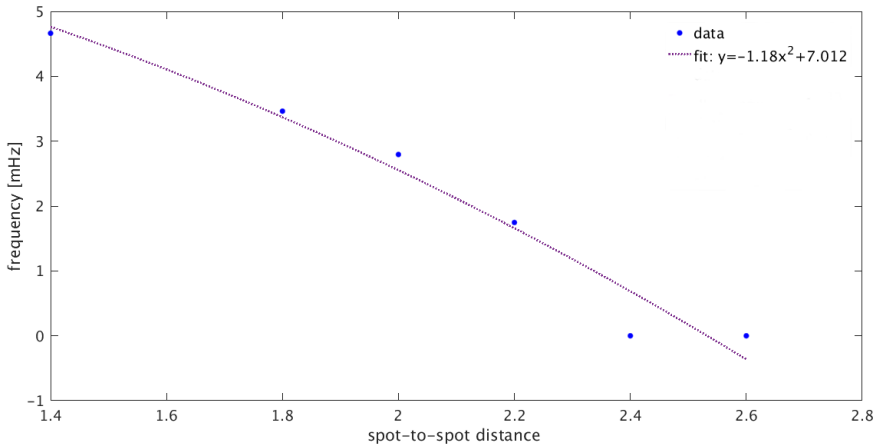

Figure 9.6: Mean of frequency of individual spots in 5×5 spot arrays of spot diameter $0.8 - 1$mm in dependence of spot-to-spot distance determined from BZR experiments. Mean value was determined only of non-zero frequency values. Best fit of the curve is shown, given by $f = -1.18x^2 + 7.022$.

For the strong to intermediate coupling regime the mean frequency in dependence of spot-to-spot distance is shown in Fig. 9.6. Therefore, the mean value of oscillating spots (without zero frequency values) is calculated and plotted in dependence of the spot-to-spot distance. The spot-to-spot distance in the experiments includes the spot radius (centre-to-centre distance), i.e. $l \propto l_{\mathrm{th}} + 2r$. In Fig. 9.6 results are shown for the standard gels and in Fig. 9.7 results are shown for pure silica gels. For standard gels, $f \propto l^2$ can be determined. In contrast, for pure silica gels $f \propto x^6$ or $\propto x^{12}$. This difference might be explainable by a different relationship between reaction rate and diffusion time. However, due to the few data points, the determination of the dependence of the frequency on the spot-to-spot distance has to be taken with caution.

To obtain an understanding of the presented results, i.e. dependence of self-excitability on spot size and reaction parameters as well as the dependence of frequency distribution and coupling on spot size, spot-to-spot distance and

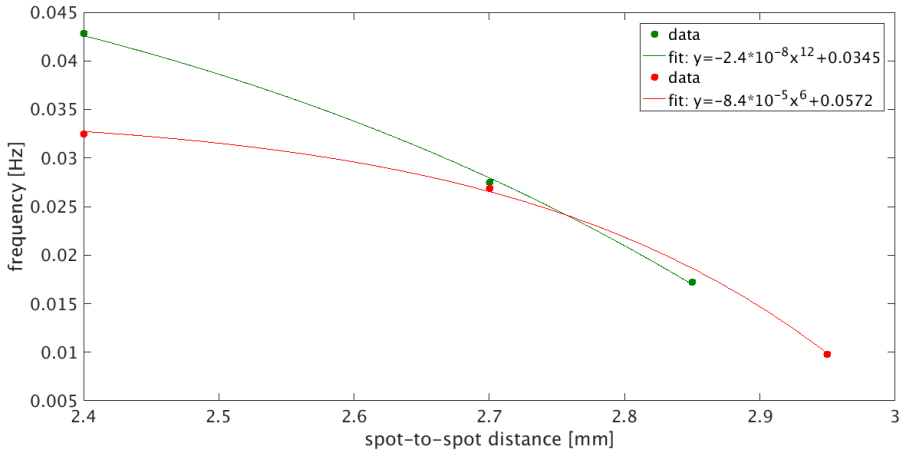

Figure 9.7: Mean of frequency of individual spots in 4×4 spot arrays of spot diameter $0.8 - 1$ mm (red) and $1.3 - 1.6$ mm (green) in dependence of spot-to-spot distance determined from BZR experiments for pure silica gels. Best fit of the curve are shown.

reaction parameters, numerical calculations of the FHN model are performed and their results are presented in the next chapter.

9.2 Results from FHN simulations

9.2.1 Properties of single spots

Before coupled spot arrays are studied, properties of single spots and their dependence on spot size, shape and reaction parameters will be discussed. Thus, with the simulation set-up shown in ch. 5.2.2, a 1×1 spot array was studied. Fig. 9.8 shows the dependence of the oscillation frequency of a single spot in dependence of its radius for two different situations: first, simulations with reaction and diffusion term solved inside the spot radius, but without diffusion term outside of the spot radius (red squares). And second, diffusion and reaction term solved inside the spot radius and only diffusion is allowed around the spot (black circles).

Furthermore, calculations of the FHN model without diffusion term, named 1D simulations in the following, are performed to obtain the dependence of the oscillation frequency on the reaction parameters (a, b, c in the FHN model). If diffusion (inside the spot) is introduced, it can have two effects. First, it results in a faster loss of activation due to the coupling to neighbouring cells and the spread of excitation. Thus, larger oscillation frequencies would be expected since the resting state is reached faster than without diffusion. In this case, the frequency is expected to be dependent on $1/r^2$. For this it is assumed that the frequency increases due to the diffusion of activation from the spot

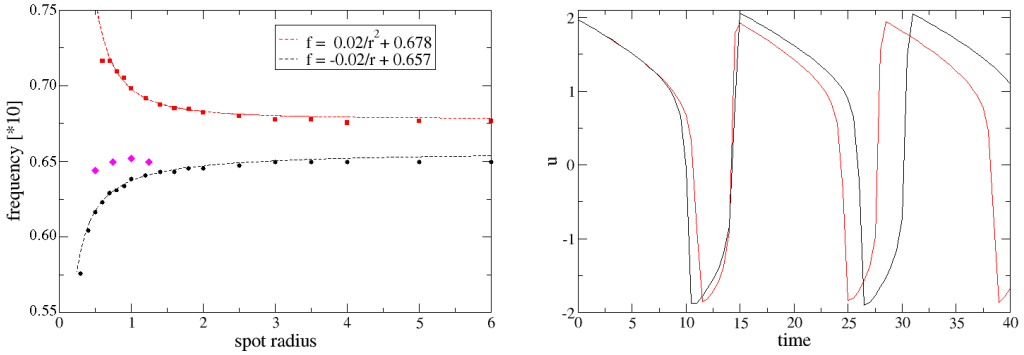

Figure 9.8: *Left:* Frequency of a single spot in dependence of spot radius without (red squares) and with (black dots) diffusion outside the spot radius. In the latter case, width of the diffusion layer is varied from zero (black dots) and 2 (magenta diamonds). *Right:* Action potential shape for oscillating single spot with diffusion only inside the spot (red) and diffusion everywhere (black).

centre to the perimeter. Thereby, the diffusion time can be calculated from $r = \sqrt{2Dt}$. One would expect that there exists a constant frequency for very large spots since then the diffusion time is larger than the frequency and thus the influence is negligible. For this scenario the frequency is expected to follow

$$f = f_0 + a/r^2 \tag{9.2.1}$$

with f_0 the frequency of large spots and a a coefficient proportional to the diffusion coefficient. The second effect, though, is acting in opposite direction. Due to the spread of activation to neighbouring cells and the regularisation effect of diffusion, the self-excitation of a spot is slower since the increase of u is slowed down by the diffusion of u to the neighbours. This would account to a decreased oscillation frequency in comparison to the case without diffusion. It is similar to the conduction velocity reduction due to curvature of the wave front or can be analysed according to the source-sink relationship. The diffusion loss to the passive media is larger for small spot sizes (each cell has more passive neighbours for small spots), slowing down the activation and thus decreasing the frequency. For very small spots oscillation should be even suppressed. Thus the dependence of the the frequency (in analogy to the conduction velocity dependence) is expected to be

$$f = f_0 - a/r\,. \tag{9.2.2}$$

For the two situations, i.e. diffusion only inside the spot or diffusion everywhere, the dependence of the frequency on the spot size differs, as shown in Fig. 9.8. In the first case, where diffusion occurs only inside the spot (red squares), the oscillation frequency of the spots is for small spot sizes larger

than the value for 1D simulations. It decreases with increasing spot size until eventually saturating at a certain value. In the second case with diffusion everywhere (black circles), the frequency is always smaller than the value observed for 1D simulations. It increases with increasing spot size. Fitting the values (dotted line in Fig. 9.8) according to Eq.(9.2.1) or Eq.(9.2.2) reveals that single spots with diffusion only inside the spot behave like case 1 and spots with diffusion also outside the spot like case 2. Thereby, the fitting coefficient a is in both cases almost equal ($a \approx 0.02$), which corresponds to $2D/10$. The saturation frequency differs, $f_0 = 0.678$ for diffusion only inside the spot and $f_0 = 0.657$ for diffusion everywhere. This is caused by the passive media outside the spot (diffusion everywhere), which introduces an offset in the frequency.

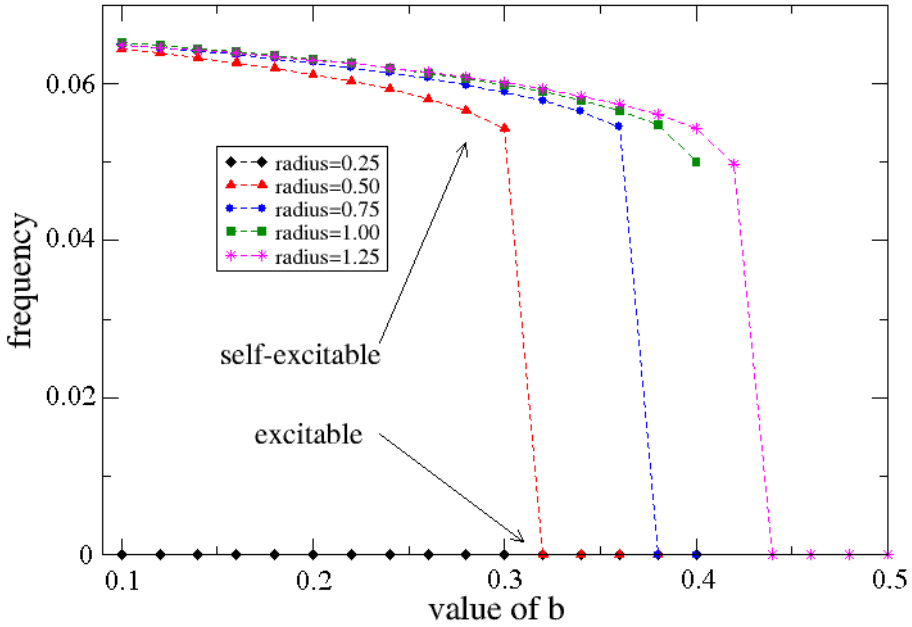

Figure 9.9: Frequency of a single spot in dependence of the value of parameter b in the FHN model for different spot sizes $r = 0.25$ (black), 0.5 (red), 0.75 (blue), 1.0 (green) and 1.25 (pink).

Since the self-excitability is an important property of the spots, as seen from the experimental results, parameter b of the FHN model is of particular importance for the simulations, because b controls the self-excitability of the spots [6]. For a single spot, an oscillation occurs if $b < b_c$ (see Fig. 9.9), i.e. the spot is an oscillator. For $b > b_c$ a single spot stays in the resting state but is excitable by a stimulus of sufficient strength and thus represents an excitable unit. The value of b_c for time-dependent simulations without diffusion is 2/3, as was shown by Winfree [6] and FitzHugh [202]. If diffusion is introduced, it

is effectively reduced. As was pointed out by Cartwright, the influence due to diffusion can be treated as an external signal z acting on the spot in the FHN equations, which is given by

$$z = D \sum_{i=1}^{n} u_i - u_s. \tag{9.2.3}$$

Here, u_s is the variable u on the spot, and u_i describes the neighbouring points. To obtain the influence of the spot radius onto the self-excitability analytically, Eq. (9.2.3) has to be summed over all points (indexed i) lying within the coupling range, which is determined by the diffusion coefficient. The coupling range can be estimated when comparing the diffusion time $t_d = x^2/2D$ with the oscillation frequency. Numerically, the dependence on the spot radius r can be revealed from single spot simulations with varying r and b. As can be seen in Fig. 9.9, b_c decreases with decreasing spot size thus reducing the oscillating regime. This can be explained by the increase of diffusive loss of activation for smaller spots, since less points contribute to the activation but the sink, i.e. the in-excitable surrounding, is comparable. This influence is enlarged for larger b values, since for these the oscillation frequency is smaller and thus a larger region acts as sink for the spot. For very small spots ($r < 0.25$) no oscillation occurs even for small b values. For $r_c = 0.25$ and $D = 0.1$ this quiescence is observed. It can be used to calculate the speed of planar waves $c(0)$ in this system by $c(r) = 0 = c(0) - D/r_c$ [see Eq. (8.4.1)], resulting in $c(0) = 0.4$. Indeed, for $D = 0.05$ oscillations are observed for $r = 0.25$, since $r_c = 0.125$ in this case.

From the explanation above, it is clear that the value of the diffusion coefficient plays an important role for the dependence of the frequency on b. As shown in Fig. 9.10, decreasing the diffusion coefficient results in a decrease of the critical b value. Furthermore, the influence of the boundary conditions on the single spot behaviour is analysed since it might influence the diffusion. Therefore, a single spot with diffusion outside of the spot is simulated for different widths d_{diff} of the diffusion layer and d_{BL} of the absorbing boundary layer (see Fig. 5.2 for a schematic representation of the simulation area with diffusion layer and boundary layer). Results are shown in the inset of Fig. 9.10. If the width of the diffusion layer is equal to zero, i.e. the boundary layer starts directly at the border of the spot, higher frequencies are observed (black dots in Fig. 9.10). In this case, the frequency of the spot still decreases with the spot size but approaches the saturation value for smaller spot sizes [see magenta diamonds in Fig. 9.8]. Increasing the width d_{diff} of the diffusion layer to a non-zero value results in a smaller frequency. However, there is no dependence of the frequency on increasing the width of the diffusion layer further. The same is true for the dependence of f on b. For non-zero values of d_{diff} smaller frequencies are observed and the oscillation regime is slightly increased, but the exact value of d_{diff} does not influence the frequency values any more. Interestingly, the width d_{BL} of the boundary layer does not influence the frequency

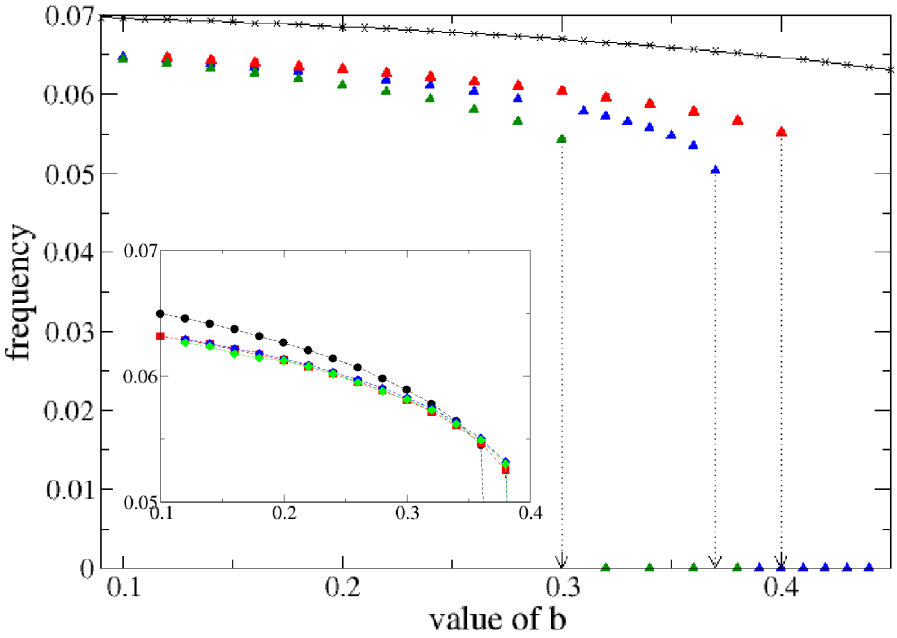

Figure 9.10: Frequency of a single spot (spot radius 0.5) in dependence of b in the FHN model and $D = 0.01$ (red), 0.05 (blue) and 0.1 (green). The curve from 1D simulations (black) is shown for comparison. *Inset:* Frequency of a single spot in dependence of the value of parameter b in the FHN model with (black, red) and without boundary layer (blue, green, orange) and with different sizes $d_{\text{diff}} = 0$ (black), 2 (red, blue), 4 (green) and 10 (orange) of the diffusion region between spot and boundary layer.

of the spot.

The influence of the spot shape on the oscillation frequency is determined from single spot simulations, where the spot is either circular, square, rhombic[2] and triangular (with equilateral edges). In Fig. 9.11, the dependence of the oscillation frequency of a single spot on b is shown for different spot shapes. If the size of the edges is similar to the radius of the circular shaped spots (black circles), b_c is larger for squares (blue squares) and smaller for triangles (green triangles in Fig. 9.11) and diamonds (red diamonds) than for circles. If the spot area is similar for the different spot shapes, b_c is similar for all four spot shapes and only slight variations in the dependence of the frequency on the b values are observed. These variations could be caused by the discretization of the spots in the simulation. The dependence on the spot area is expected, when considering the summation in Eq. (9.2.3). Here, the area of activated spots is compared to the area of the coupled passive media, also known as source-sink relationship.

[2]like square but rotated by 45° according to the boundaries

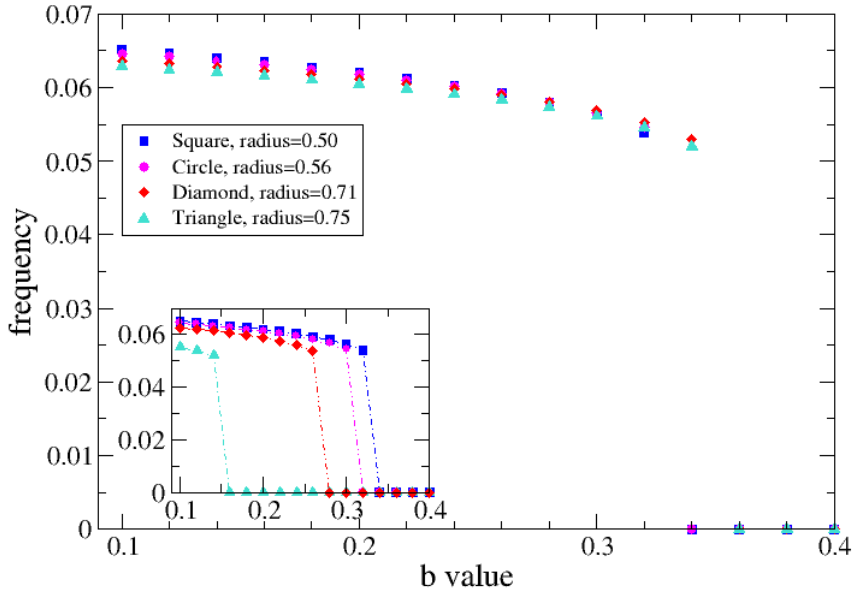

Figure 9.11: Frequency of a single spot in dependence of the value of parameter b in the FHN model for different spot shapes: circle (magenta), diamonds (red), squares (blue) and triangles (turquoise). Area of spots is equal for the different shapes. *Inset:* Spot shapes have the same characteristic length, i.e. radius of circle is equal to side length of square, diamond or triangle, but spot area is different.

The difference between pure silica gels and the standard gels indicates that the relationship between reaction rate and diffusion time has a strong influence on the wave front propagation and the occurrence of irregular patterns. The reaction rate and oscillation frequency in the FHN model are influenced by parameter c of the FHN model. In Fig. 9.12 left side the action potential shape is shown in dependence of parameter c from 1D simulations without diffusion term. Larger c values yield a slower decrease of u and a longer refractory period. Thereby, the influence is stronger on the refractory period than on the initial decrease of the action potential. On the right side of Fig. 9.12, the dependence of the oscillation frequency of a single spot is shown in dependence of parameter b for different c values: $c = 5.5$ (black), 10.5 (red), 15.5 (blue) and 20.5 (green). Increasing c results in a strongly reduced frequency for the same b value. Furthermore, for c values larger than 5.5 the dependence of f on b is changed, i.e. f is almost constant. The transition between the oscillating and the excitable regime does not occur for larger c values in the analysed range of b.

In the following, regular arrays of coupled spots will be studied. The study

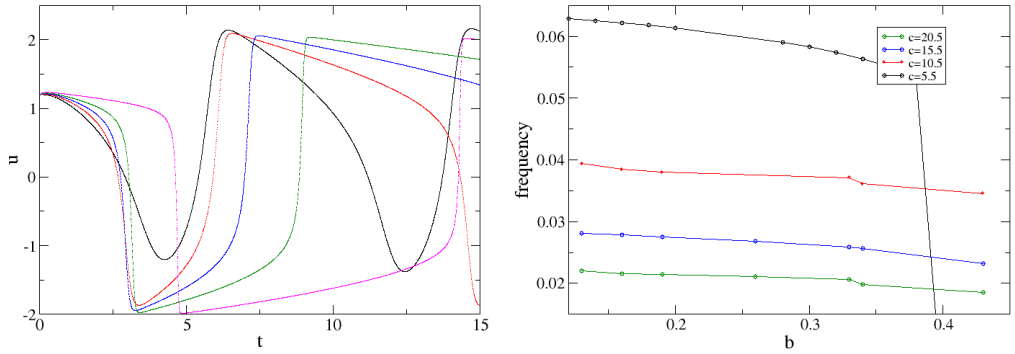

Figure 9.12: *Left:* Time course of u in dependence of parameter c of the FHN model increasing from $c = 5.5$ (black) to $c = 20.5$ (purple). An increase of the action potential duration due to a larger recovery time is visible. The activation time, i.e. the initial decrease of u, is only slightly affected by the change of c. *Right:* Frequency of single spot in dependence of parameter b for different values of c. The transition from the oscillatory to the excitable regime is only observed for the lowest $c = 5.5$.

will be divided into two parts. First, spot arrays in the oscillating regime, i.e. $b < b_c$, are considered, followed by the investigation of spots arrays composed of excitable units.

9.2.2 Regular arrays of oscillators

In this section excitation patterns of regular arrays of coupled oscillators are investigated. As shown before, spots are oscillators, i.e. self-excitable, if $b < b_c$. The spot-to-spot distance is here the distance between the boundaries of the spot, in contrast to the experiments, where the spot-to-spot distance is measured from spot centre to spot centre. To allow the distinction between both, the theoretical value is marked with index th. In Fig. 9.13, mean frequency and phase coherence are shown in dependence of spot-to-spot distance for 5×5 spot arrays with spot radius $r = 1.0$ and $b = 0.1$. For each simulation, random initial conditions were used, i.e. the u, v values for each spot were drawn from a uniform distribution including possible u, v pairs during the course of one action potential (see ch. 5.2.2 for details).

From the course of frequency, synchronization and the excitation patterns one can deduce different coupling regimes:

- weak coupling for $l_{\text{th}} \geq 1$,
- intermediate coupling $l_{\text{th}} = 0.5 - 1$ and
- strong coupling for $l_{\text{th}} < 0.5$.

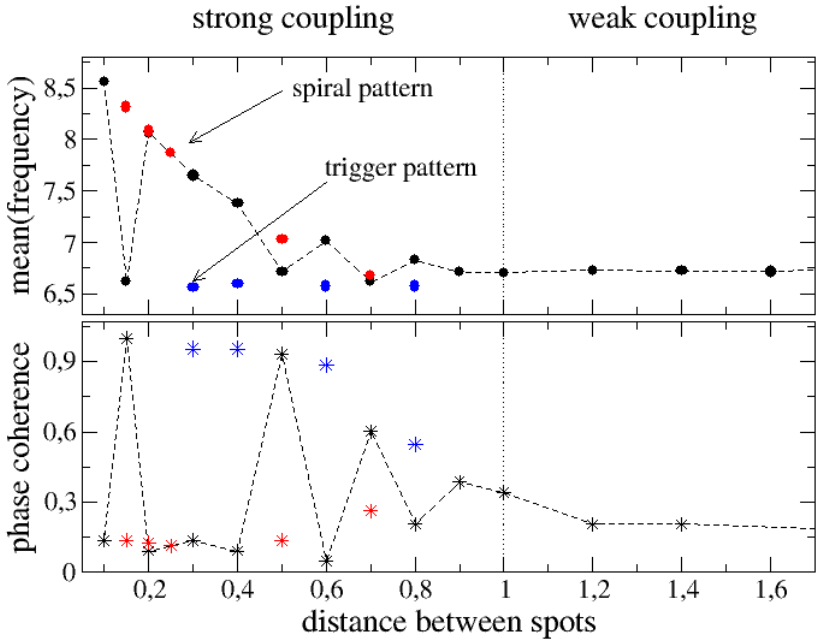

Figure 9.13: Mean frequency and phase coherence in dependence of spot-to-spot distance and final excitation pattern for 5×5 spot arrays, spot diameter 1 and $b = 0.1$. The initial values of u, v for each spot were drawn from a uniform distribution for each realization. Red values correspond to spiral wave patterns and blue to target patterns.

In the range of weak coupling, oscillations occur, which seem to be independent, and all parameters (frequency, synchronization) remain constant for the spot-to-spot distance changes. Thereby, the frequency value is dependent on the spot size and corresponds to the value obtained in single spot experiments. Synchronization, entropy and correlation (not shown) are independent of the spot size in this range and their values thus describe the 'intrinsic' correlation and phase synchronization of the system. This is measured, although there is no real correlation or synchronization occurring in the system. The reason might be the small width of the frequency distribution. No specific excitation pattern can be determined. Representative time evolution is shown in movie S16 in the Supporting Material.

In the range of strong coupling, only one excitation pattern like a spiral wave spanning across the whole array is observed, whereas for intermediate coupling, the array splits up into small subgroups. The spots in the subgroups can synchronize and belong to one excitation pattern. Spots can belong to a spiral wave or a target pattern as shown in Fig. 9.14 (see time evolutions of both in movie S13 and S14 in the Supporting Material). In the case of a target pattern, one spot acts as a pacemaker and wave fronts emerging this source

propagate across all spots without changing the direction. In the case of a spiral wave pattern, the rotation vector and velocity of wave fronts remains constant across the spot array. In the intermediate regime, due to this split-up into subgroups, irregular patterns can be observed, in particular at the border between two subgroups. Since this mechanism for the generation of irregular excitation patterns was already thoroughly studied in the literature [178, 263–265], it will not be investigated further in this work. A representative time evolution is shown in movie S15 in the Supporting Material.

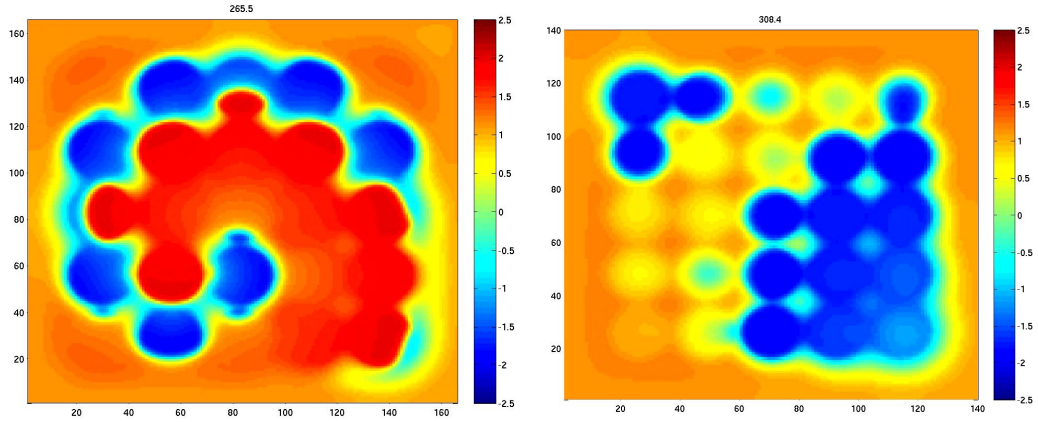

Figure 9.14: Excitation patterns for strongly coupled spots: Spiral wave (a) and target pattern (b). Time evolution is shown in Movie S13 (target pattern) and S14 (spiral wave pattern) in the Supporting Material.

For the strong and intermediate coupling regime, the values of frequency and synchronization do not follow a clear dependence (black dots). However, one can divide the values into two groups, one with a high frequency, high synchronization and low correlation and the other one with low frequency, low synchronization and high correlation. The distinction between both becomes clear, if one takes a look at the excitation patterns. In Fig. 9.13 frequency and phase coherence values are coloured according to the excitation pattern, which evolved on the spot array. The group with low frequency, high correlation and phase coherence corresponds to a target pattern [see Fig. 9.14 (b)], where one spot acts a pacemaker for the whole array. In this case, the mean frequency does not depend on the spot distance, but depends only on the spot size of the pacemaker spot.

The second group with higher frequencies, lower correlation and lower phase coherence corresponds to spiral wave patterns [see Fig. 9.14 (a)]. In this case, the frequency decreases with increasing the spot-to-spot distance until reaching a constant value for the weak coupling regime. The dependence of the frequency on the spot-to-spot distance can be addressed to the circulation of the spiral wave around the in-excitable, passive region in between the excitable spots. The period of oscillation can either be determined by the circumference of the circle, surrounded by four spots, and the velocity of the spiral wave.

This yields $f \propto v/r_k$ with r_k the radius of the circle surrounded by the spiral wave. On the other hand, the period of oscillation is dependent on the diffusion time along the paths between the spots. Since the diffusion time is given by $t = x^2/2D$, in this case $f \propto 1/l^2$. In Fig. 9.15, the mean frequency of spiral wave patterns in dependence of the spot-to-spot distance and the spot size in spot arrays with circular shaped spots is shown. The best fit to these curves

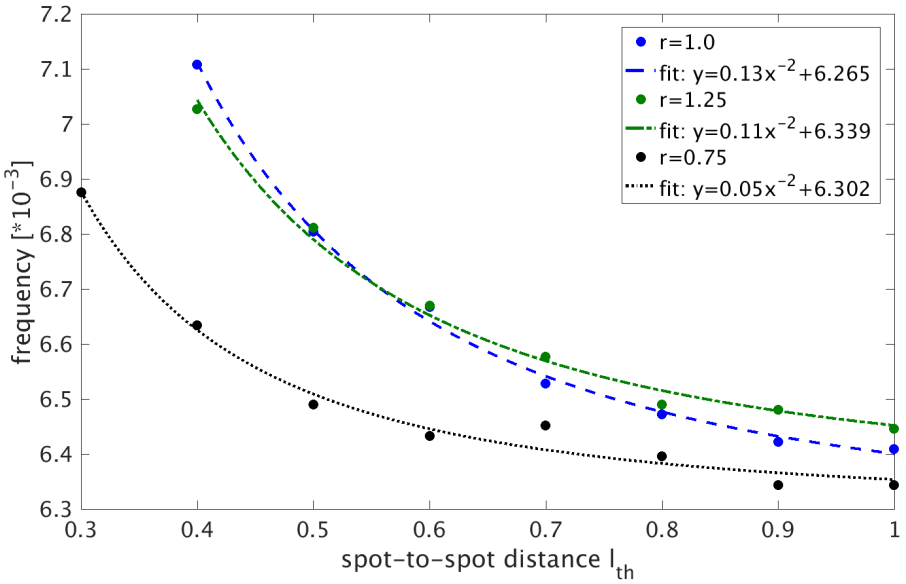

Figure 9.15: Mean frequency in dependence of spot-to-spot distance for spiral wave patterns on circular spots of different size. The best matching fit curves, given by $f = a_{fit} * x^{-2} + b$, are shown.

is given by

$$f = a_{fit}/x^2 + f_0. \tag{9.2.4}$$

Thereby, f_0 is the frequency of independent oscillations or a single spot of same size, respectively. a_{fit} is a fit parameter. It is not equal to $2D$ but deviates from this value and changes with the spot size. These deviations become even more pronounced, if the dependence of the mean frequency of spiral wave patterns on the spot-to-spot distance occurring on different spot shapes is fitted by this formula Eq. (9.2.4), as shown in Fig. 9.16.

The frequency dependence is similar for different spot shapes (circles, squares and diamonds) as given by Eq. (9.2.4) and shown in Fig. 9.16. The frequency is ordered thereby according to the area of the spot, i.e. the maximal frequency is observed for the largest area (squares with $a_s/2 = 1$), and decreasing with decreasing spot area. Thereby the order of spot area beginning with the maximal one is: square ($a_s/2 = 1$), circles ($r = 1$), squares ($a_s/2 = 0.75$), diamonds ($h_d = 1$) and circles ($r = 0.75$). The range of the fit parameter a strongly differs for the different spot shapes, i.e. a(circles)$\approx 1/2 * a_{fit}$(squares) and

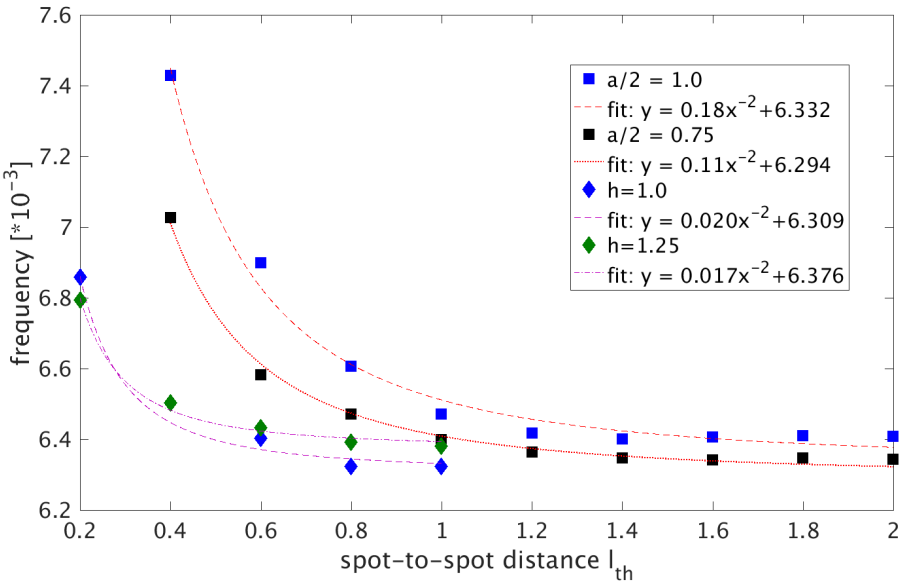

Figure 9.16: Mean frequency in dependence of spot-to-spot distance for spiral wave patterns on different spot shapes. The best matching fit curves are shown.

a_{fit}(circles)$\approx 20 * a_{fit}$(diamonds). The difference of a_{fit} for differing spot size and shape can be accounted to different wave front velocities due to differing wave front shape. Note, that values for spot-to-spot distances below 0.4 were not taken into account for the fit. For these distances, the spiral wave do not rotate around 4 spots but propagates around a larger, rectangular area surrounded by 3x2 spots.

The question arises if it can be predicted which excitation pattern evolves (spiral wave or target pattern) from the initial conditions. When considering different spot shapes, the following can be stated. For random initial conditions, where u, v pairs are drawn from a uniform distribution, spiral wave patterns are observed more often on circular and square shaped spots (in the coupling regime) as on rhombic or triangular shaped spots. It is supposed that this is caused by the different wave front curvatures due to the spot shape. Thus, spiral waves favour slightly convex or planar wave fronts to strongly convex. Furthermore, in large arrays different excitation patterns can evolve for the same initial condition, if the spot shape is varied (see movies 17a-c in the Supporting Material). The final excitation pattern is thereby similar for square and circular shaped spots, but the time until the final state is reached is longer for circular shaped spots. This is expected since due to the curvature of the wave fronts the effective coupling between spots is reduced for circular spots. In contrast, for the diamond shaped spots even after longer simulation time, the same pattern is not observed, as shown in Fig. 9.17. While a single spiral evolves on square and circular shaped spots, two pacemaker spots and a spiral wave is observed for rhombic spots. This spiral wave is unstable and

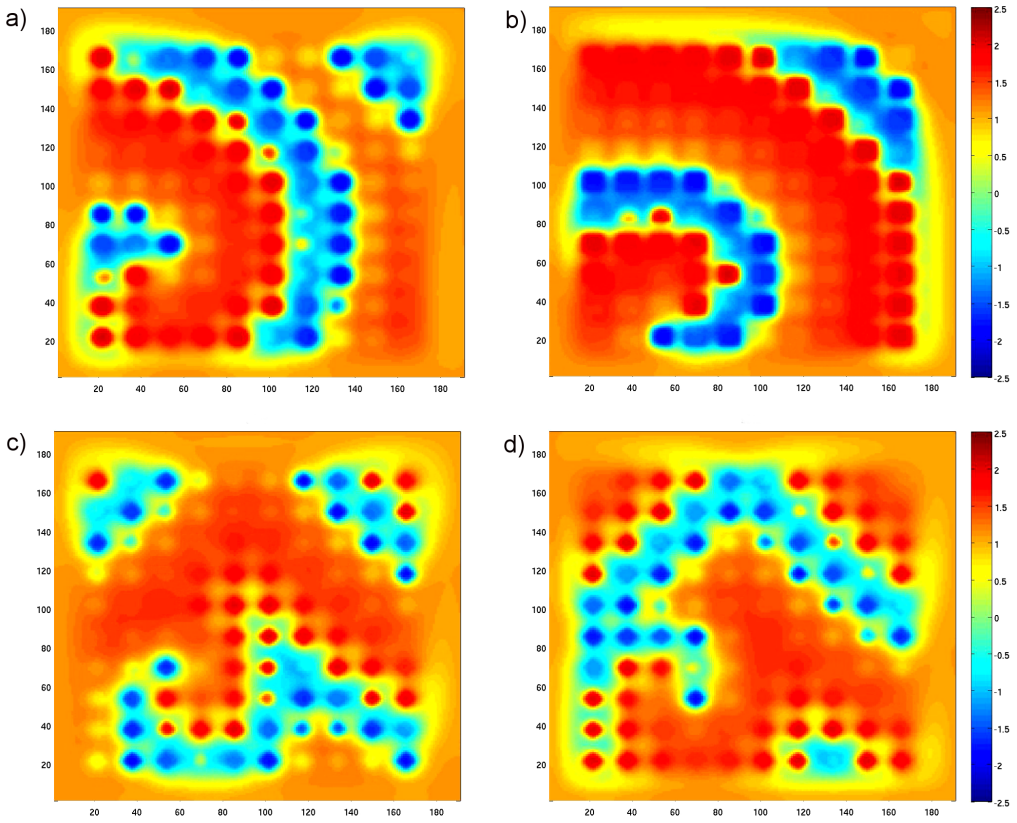

Figure 9.17: Snapshots of excitation pattern evolving from the same initial condition on 10×10 spot arrays of different spot shape a) circular spots, b) square spots, c) and d) rhombic spots (two time instants).

is suppressed by the target pattern after some time. This arises due to the effectively decreased coupling strength in comparison with square or circular shaped spots, reducing thus also the frequency of the spiral wave. Hence, it can be suppressed by the target patterns.

In the next step, it is studied, which excitation patterns occur for a selected initial condition, for which the evolving excitation pattern is known for a certain spot size and spot-to-spot distance. Therefore, an initial condition resulting in a spiral wave for example for spot size $r = 1$ (circular spots) and spot-to-spot distance $l = 0.1$ was taken as initial condition for other spot sizes and spot-to-spot distances. The resulting patterns were classified as spiral wave type or target pattern type. It should be noted here, that the arising excitation pattern cannot be seen from the initial condition already. It resembles an random activation of spots and evolves after some time into a specific excitation pattern due to the interaction of spots and their given properties. In Fig. 9.18, results are shown for one initial condition yielding a target pattern and in Fig. 9.19 for another one yielding a spiral wave. The spot size and spot-to-spot distance, on which the resulting pattern was first observed, is

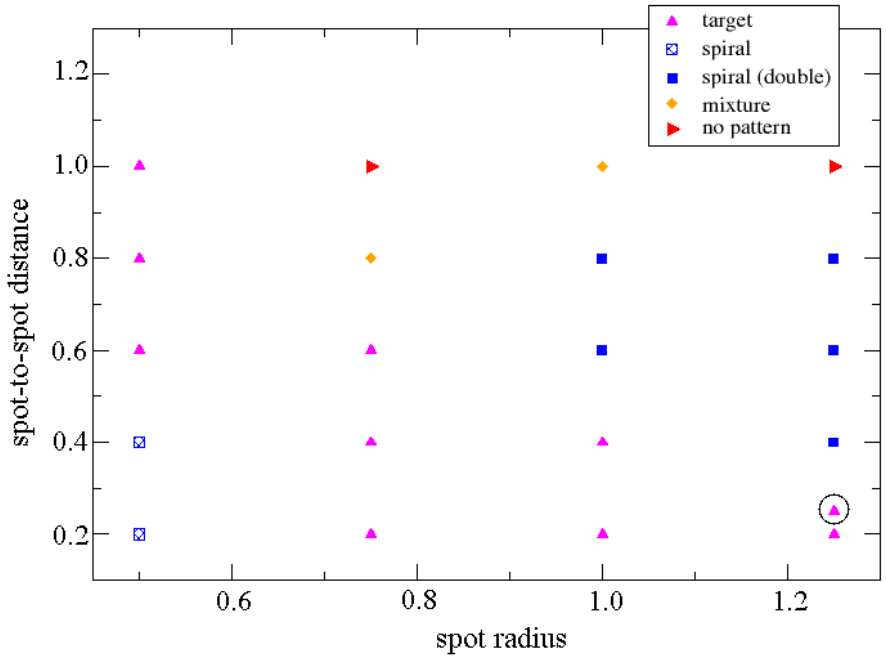

Figure 9.18: Classification of evolving excitation pattern for a given initial condition (marked by circle), yielding a target pattern, in dependence of spot size and spot-to-spot distance. Blue represents spiral wave type patterns (single spiral: open square, double spiral: full square), pink represents target patterns, red corresponds to independent oscillations of the spots and orange indicates mixtures of target and spiral wave patterns.

marked by a circle. It can be seen that an initial condition resulting in a target pattern for a certain spot size and spot-to-spot distance yields target patterns for smaller spot sizes as well. The range of spot-to-spot distances, for which target patterns evolve, increases with decreasing spot size. Nevertheless, for very small spot sizes and spot-to-spot distances spiral wave patterns occur. In contrast, for initial conditions resulting in a spiral wave pattern, these patterns are observed for larger spot-to-spot distances for the same spot size and larger spot sizes. From Fig. 9.19, it looks like spiral wave patterns also occur for smaller spot sizes in the same range of the spot-to-spot distances. However, from the results obtained with another initial condition resulting in a spiral wave (not shown), one can deduce that this is not generally the case. For larger spot sizes and spot-to-spot distances spiral wave patterns are evolving. It should be noted here that despite the classification into a spiral wave pattern, the excitation patterns which evolved are not equal for the different spot sizes and spot-to-spot distances. For example, instead of a double spiral a single spiral wave occurs or the symmetry axis of the double spiral wave changes with spot size or spot-to-spot distance. Furthermore, initial conditions, taken

from a very small spot size $r = 0.5$, did not result in spiral wave patterns for larger spot sizes or spot-to-spot distances. This can be explained from the fact that the frequency of single spots is smaller for smaller spot sizes. Thus, it could be possible to evolve a target pattern for larger spot sizes, since their frequency is higher than for the smaller spot sizes, where it was too low to dominate the spot array. This effect is suppressed for initial conditions taken from larger spot sizes, since there the difference in the oscillation frequency is negligible when increasing the spot size.

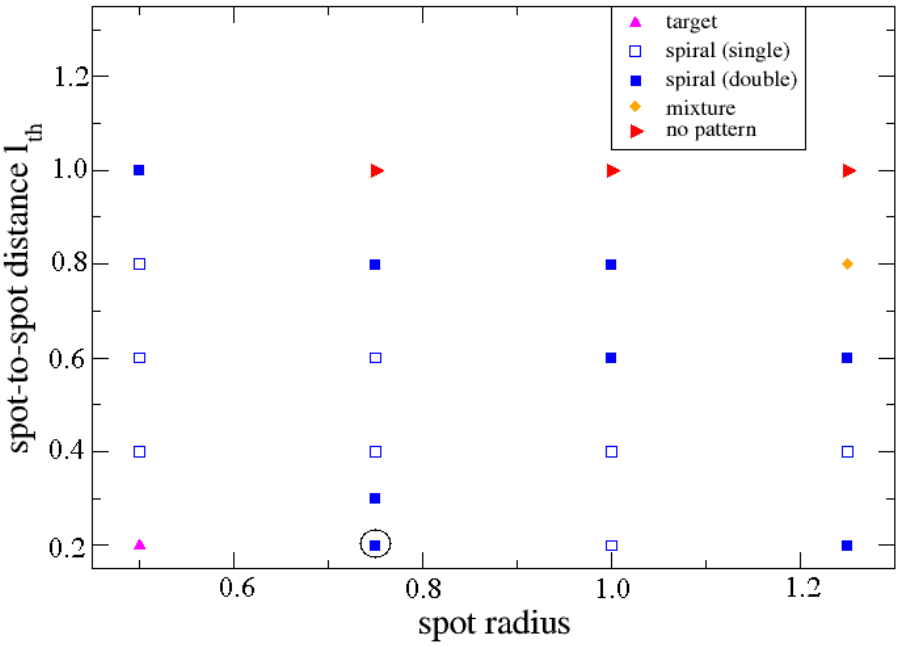

Figure 9.19: Classification of evolving excitation pattern for an initial condition (marked by circle), yielding a spiral wave, in dependence of spot size and spot-to-spot distance. Blue represents spiral wave type patterns (single spiral: open square, double spiral: full square), pink represents target patterns, red corresponds to independent oscillation without a clear patterns and orange indicates mixtures of target and spiral wave patterns.

In all examples shown, mixtures of spiral and target patterns occur for larger spot-to-spot distances (see Movie S18 in Supporting Material for a quite complex mixture of patterns). These can be either coexisting patterns caused by synchronized subgroups of spots or an intermediate state of the system which will evolve into either a spiral wave or a target pattern if the simulation time goes to infinity. In the first case, even for very large simulation times, it should not be possible to determine just one excitation pattern. The latter case is caused by the reduced coupling strength for larger spot-to-spot distances, reducing thus the influence of neighbouring spots onto each other. This increases the time until synchronized states or a single excitation pattern

evolves. Simulations with longer simulation times could clarify to which case the mixture patterns belong.

To summarize, one can predict from a known initial condition (values for spots drawn initially from random distribution) which pattern will evolve on a spot array with a different spot size or spot-to-spot distance. Thereby, target patterns will be reproduced on smaller spot sizes. Thereby, the range of spot-to-spot distance increases with decreasing spot size. Spiral wave patterns are observed for larger spot-to-spot distances and for larger spot sizes. In the latter case, the range of spot-to-spot distances decrease with increasing spot size, since the coupling regime changes to weak coupling. The previous conclusions can be drawn only for strong or intermediate coupling. Due to the limited amount of initial conditions tested, the presented interpretations are not intended as general statements, are phenomenologically drawn and should be accepted with caution. More initial conditions and a statistical analysis should be pursued to allow general statements.

In contrast to the results for random initial conditions, no spiral wave patterns evolve if all spots are initially in the resting state. In experimental realizations of the BZR, spiral wave patterns occur, although all spots are initially in the resting state. This discrepancy might be an effect of a too small variation of the frequency by variation of b compared to the experiments. For $b = 0.1$ and the restriction of a uniform distribution, the distribution of b is limited to the range [0.01,0.19]. This is comparable to a width $\Delta f = 0.001$ of frequency distribution peaked at $f = 0.064$.

9.2.3 Regular arrays of excitable units

In this section excitation patterns occurring on regular arrays of excitable units will be discussed. Excitable units do not oscillate by themselves but can be excited by an external stimulus. In Fig. 9.20 the frequency of individual spots in a 5×5 spot array is shown in dependence of spot-to-spot distance l_{th} and b value for $r = 0.75$. As initial conditions, a resting state is assumed. For $b = 0.3$ spots are in the oscillating regime, whereas for $b \geq 0.4$ spots should be excitable according to the single spot results. In the oscillating regime and in the range of strong coupling, target patterns evolve and spots exhibit the same frequency. For larger spot-to-spot distances, spots oscillate independently of each other with almost the same frequency, due to the small variation in b. For b values far in the excitable regime ($b = 0.45$) spots do not oscillate for weak coupling, i.e. $f = 0$ for large spot-to-spot distance $l_{\mathrm{th}} > 1$ (see Fig. 9.20 lower panel, $b = 0.45$). If the spot-to-spot distance is decreased, i.e. coupling strength increased, coupling induced oscillation starts without any external stimulus. In this case, target patterns evolve and only a narrow frequency distribution is observed. For the intermediate value of $b = 0.4$, which corresponds to excitable but not self-excitable spots according to the single spot analysis, coupled oscillations occur for strong coupling as for the

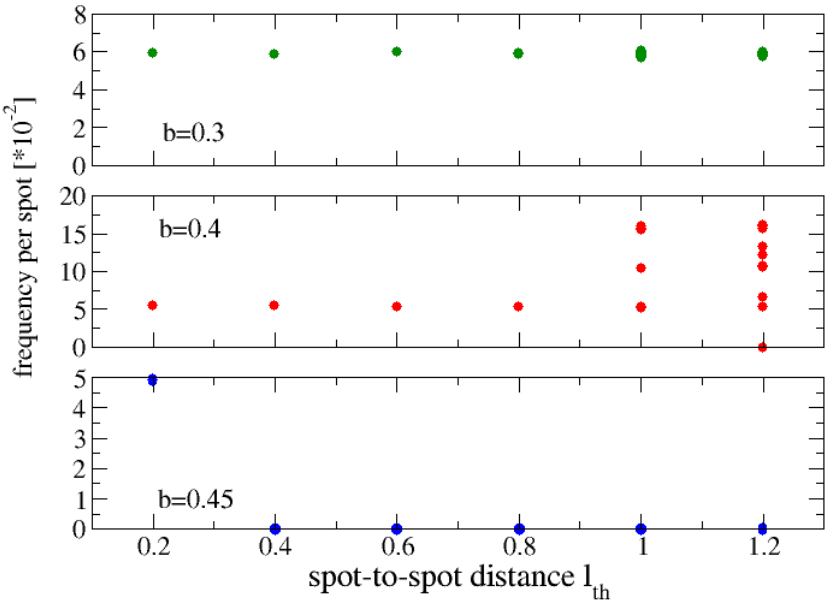

Figure 9.20: Frequency of individual spots in dependence of spot-to-spot distance l_{th} and b value for spot size $r = 0.75$ in a 5×5 spot array. For $b = 0.3$, spots are self-excitable, whereas for $b = 0.4$ and $b = 0.45$ spots are excitable.

larger b value. However, in contrast to the observations for the larger b values, even for weak coupling oscillations are observed. Furthermore, the frequency distribution is broadened and much larger frequencies are observed compared to the other two cases. The spot-to-spot distance l_{c2}, for which the broadening of the frequency distribution is observed is larger than the one, where the oscillation emerges for the uncoupled, non-oscillating spots (l_{c1}). Since the coupling strength is not only depending on the distance between two spots but also on the source-sink relationship of the spot with is passive surrounding, the spot-to-spot distances for the emergence of oscillation and for the occurrence of the broadening of the frequency distribution depend also on r and b. Both effects arise in a small range of b above b_c, whose width is dependent on the diffusion coefficient. For $D = 0.1$, l_{c2} is proportional to $r^{1/2}$. Interestingly, even for $r = 0.25$ and $D = 0.1$ oscillations occur due to coupling, although in single spot simulations no oscillations were observed. A dependence of the emergence of oscillation and the broadening of the frequency distribution on the number of spots in the array is not observed for 5×5, 10×10 and 20×20 spot arrays. Only the synchronization time is longer for larger arrays.

The question arises which excitation patterns correspond to the broadening of the frequency distribution with strongly increased maximal frequency values. Beside normal oscillations, three different excitation patterns can be

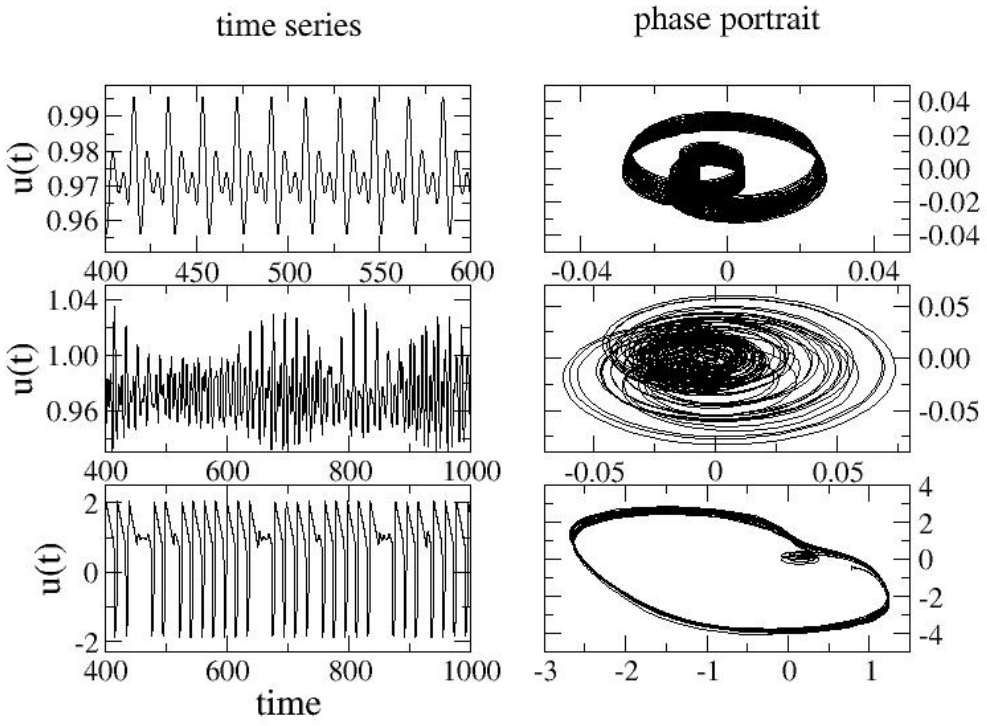

Figure 9.21: *Left:* Oscillation modes ($u(t)$) observed for large spot-to-spot distances in 5×5 spot arrays. *Right:* Corresponding paths in the phase space for different oscillation modes.

distinguished. These are not spatial patterns but time-dependent ones. In Fig. 9.21 these patterns are shown (left side) together with the corresponding path in the phase space (right side). Multi-period oscillations can be seen in Fig. 9.21 (upper panel), amplitude modulated oscillations in Fig. 9.21 (middle panel) and transient dynamics, also known as mixed-mode oscillations, in Fig. 9.21 (lower panel). A representative evolution for an array, where non-normal oscillation modes occur, is shown in movie S19 in the Supporting Material.

Multi-period oscillations are characterized by a path in the phase space, where multiple circles of different size are run through before returning to the starting point [see Fig. 9.21 upper panel]. The occurrence and pattern of multi-period oscillations was studied by considering a row of $N_s \times 1$ spots ($N_s \leq 5$). In these, multi-period oscillations arise from the forced oscillation of an excitable unit by an oscillating spot in combination with the damped oscillation dynamics of the excitable unit [see Fig. 9.22]. In this case, the excitable unit is situated at the border of the array and has only the oscillating unit as neighbour. It exhibits damped oscillations forced by the activation of the oscillator on its side and thus is not self-exciting but is externally stimulated.

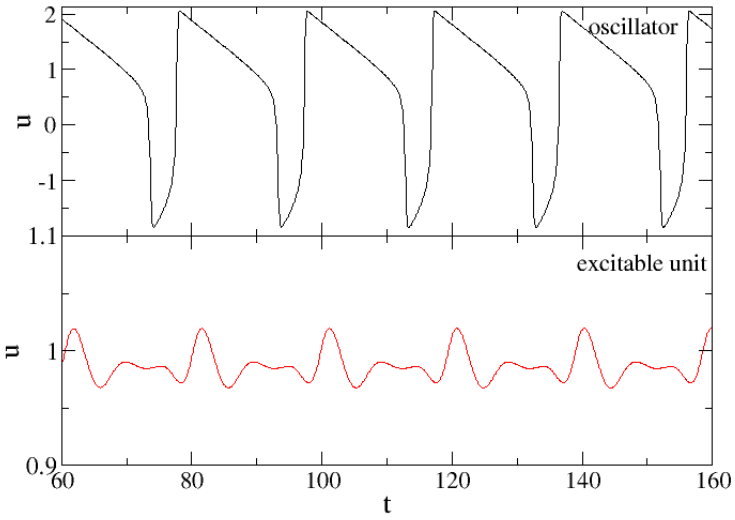

Figure 9.22: Time course of u of an excitable unit (lower panel) neighboured by an oscillating unit (upper panel) in an 5×1 spot array. The excitable unit is situated at the border of the array. It exhibits forced, damped oscillations due to the activation by the neighbouring spot.

Amplitude oscillation (Fig. 9.21 (middle panel)), i.e. modifications of the peak height of u, are caused by a similar mechanism. In this case, the excitable unit is neighboured by two oscillators. Thus, the activations by the neighbouring spots are superposed and result in the amplitude-modulated oscillation of the excitable unit [see Fig. 9.23]. In both cases, multi-period oscillation and amplitude-modulated oscillation, a higher frequency of oscillation is observed whereas the maximal value of the action potential is strongly decreased.

Mixed-mode oscillations are characterized by low amplitude oscillations (LAO) alternating with high amplitude oscillations (HAO). It is different from multi-period oscillations because distinct paths are followed in the phase space for the two different oscillation modes [see Fig. 9.21 lower panel], whereas for multi-period oscillation one path is followed which includes multiple oscillation cycles [see Fig. 9.21 upper panel]. The alternation between LAO and HAO can occur with a regular manner, like 5 LAO followed by 2 HAO, or it can be chaotic. A simple explanation for the occurrence of the mixed-mode oscillations, as for the amplitude-modulated or multi-period oscillations, can not yet be given.

Patterns can be characterized by their synchronization and the number of spots exhibiting the three described oscillation modes, termed non-normal oscillation modes in the following. The latter are determined by the maximum value of the action potential in comparison to the resting state value, denoted

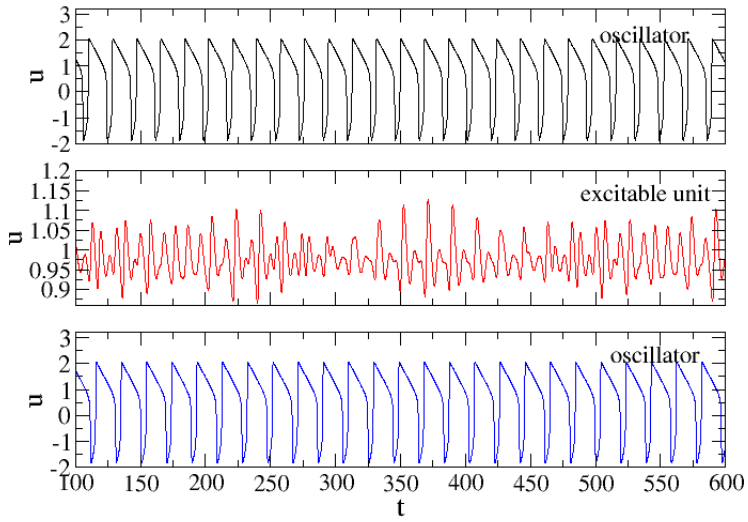

Figure 9.23: Time course of u of an excitable unit (lower panel) neighboured by two oscillating unit (upper panel) in an 5×1 spot array. It exhibits forced, damped oscillations due to the activation by the neighbouring spots, whose activations are superposed.

by AP. For $AP > 2$ normal oscillations occur, whereas $0 < AP < 2$ corresponds to non-normal oscillations. In Fig. 9.24 the frequency of individual spots, synchronization characterized by Φ and the number of spots exhibiting the non-normal oscillation modes are shown in dependence of the spot-to-spot distance l_{th} for spot size 0.5. As in the case of arrays of oscillators, the synchronization is decreasing for increasing spot-to-spot distance and saturating at a certain value, indicating a reduction of coupling strength as expected. However, if the non-normal oscillation modes occur ($l_{\mathrm{th}} > 1$), synchronization is increased. This is expected, since the excitable unit follows the activations of the oscillator. The number of spots exhibiting the non-normal oscillation modes is strongly dependent on the b value. While for $b = 0.3$ only 2 of 25 spots can be counted into this class, for $b = 0.35$ up to 21 of 25 spots exhibit the non-normal oscillation modes. Since $b = 0.35$ is more far in the excitable regime than $b = 0.3$ (compare Fig. 9.9), more spots are expected to be only excitable and thus showing the non-normal oscillation modes.

Following the explanation for the generation of the non-normal oscillation modes, a minimal heterogeneity in b has to be present for the non-normal oscillation modes to occur, since the self-excitability of spots is tuned by b. However, in simulations with strongly reduced variation of b, i.e. only one b value for all spots, frequency broadening and non-normal oscillation modes are still observed, as shown in Fig. 9.25. In this case, only for $l = 1$ non-normal

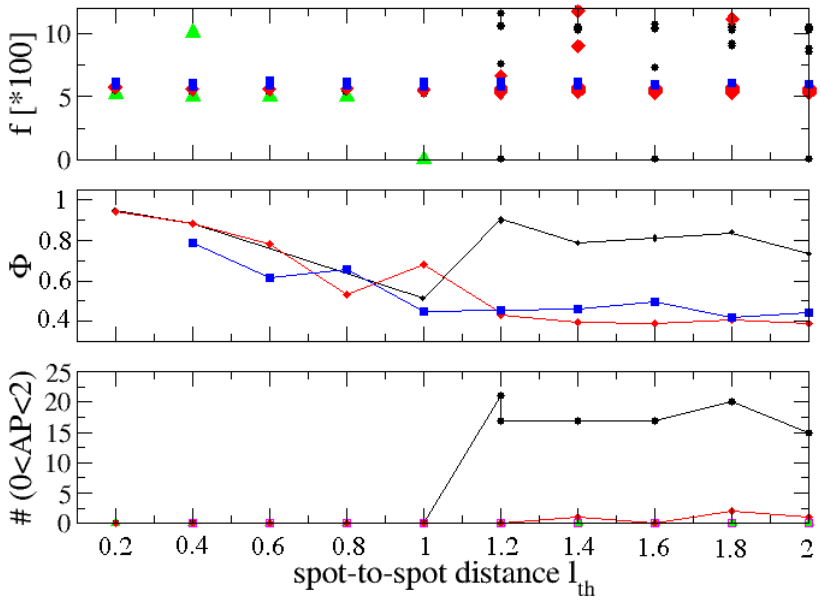

Figure 9.24: Frequency of individual spots, synchronization characterized by Φ and number of spots ($r = 0.5, D = 0.1$) exhibiting non-normal oscillation modes for spot size $r = 0.5$ in a 5×5 spot array in dependence of spot-to-spot distance l_{th} and $b = 0.2$ (blue), 0.3 (red), 0.35 (black) and 0.4 (green).

oscillation modes occur, whereas for larger heterogeneity ($b = 0.4 \pm 0.03$) these are observed for a larger range of spot-to-spot distances, where $1 \leq l < 4.5$. Since for the occurrence of the non-normal oscillations modes a minimum of heterogeneity is necessary, the question arises, what generates the heterogeneity if b is not varied. The number of neighbours or the distance to the boundary layer could be possible reasons. Thereby the first one does not influence the frequency of a spot, since spots are separated by the passive media and, thus, the amount of activation lost due to diffusion is similar for different number of neighbours. The distance to the boundary condition, in particular, the diffusion layer between the spot and the boundary layer, can change the frequency of oscillation, as was shown for single spots (see Fig. 9.10). For very small diffusion layers, higher frequencies are observed for single spots. Thus, spots at the border of the array should exhibit slightly higher oscillations frequencies and a different oscillation range. This introduces the heterogeneity necessary for the occurrence of the non-normal oscillation modes. If a large diffusion layer is introduced, these oscillation modes should not occur if b is similar for all spots.

The critical coupling strength, below which the broadening of the frequency distribution occurs, should depend on the diffusion coefficient. It can be cal-

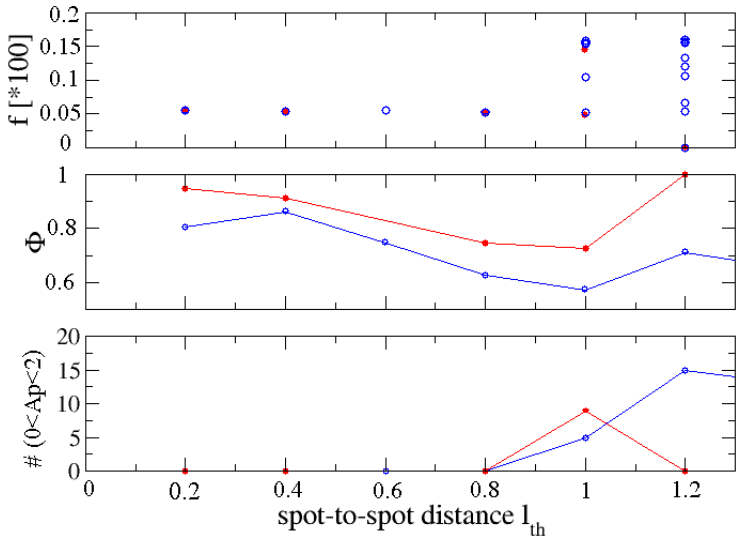

Figure 9.25: Frequency, synchronization and number of spots with $0 < AP < 2$, i.e. in non-normal oscillation mode, in 5×5 spot array ($r = 0.75$, $b = 0.4$, $D = 0.1$) in dependence of spot-to-spot distance and width of b distribution: $\Delta_b = 0.03$ (blue) and $\Delta_b = 0$ (red). Even for b values similar for all spots, broadening of the frequency distribution and non-normal oscillation modes are observed.

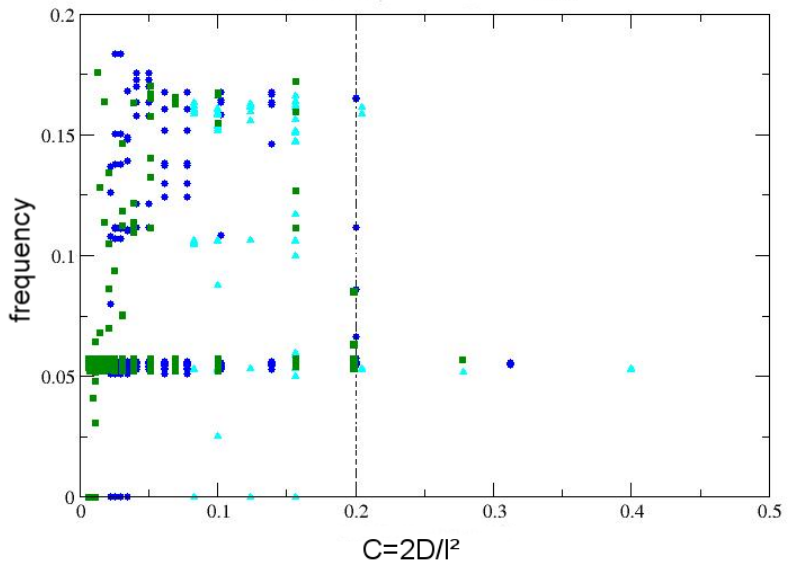

Figure 9.26: Frequency of individual spots ($r = 1.0, b = 0.4$) in a 5×5 spot array in dependence of coupling strength shown for three different diffusion coefficients $D = 0.1$ (blue), 0.2 (cyan) and 0.05 (green).

Table 9.1: Critical spot-to-spot distance, above which non-normal oscillation modes occur in dependence of the spot shape

shape	characteristic length (r)	area	l_{crit}
circular	radius=0.5	$\pi r = 0.785$	1.2
square	half side length=0.44	$4r^2 = 0.774$	1.2
diamond	height=0.62	$2r^2 = 7688$	1.0
triangle	half side length=0.67	$\sqrt{3}r^2 = 0.777$	0.8

culated by $C = 2D/l_{\text{th}}^2$ [262]. Indeed, when varying the diffusion coefficient, the spot-to-spot distance for which broadening of the frequency distribution occurs, is varied. In Fig. 9.26 the frequency of individual spots in a 5×5 spot array with spot size $r = 1$ is shown in dependence of the coupling strength for three different diffusion coefficients $D = 0.1$ (blue), 0.2 (cyan) and 0.05 (green). As can be seen, the critical coupling strength, below which the broadening of the frequency distribution occurs, is similar for the three different diffusion coefficient. Thus, the formula describes the coupling strength well for this case. Furthermore, different spot sizes exhibit similar critical coupling strengths $C_{\text{crit}} \approx 0.2$.

In contrast, for different spot shapes the spot-to-spot distance, above which frequency broadening occurs, is different (see Tab. 9.1). In this case, the spot area is similar for the different spot shapes and, thus, their oscillation frequency should be similar, as determined from the single spot simulations. The critical spot-to-spot distance changes in dependence on the spot shape, possibly since the conduction velocity (due to wave front shape) is different for the different shapes.

It is expected, that there exists a second critical coupling strength, below which the non-normal oscillation modes are not observed any more. In this range, the coupling becomes too weak to allow the oscillators to influence the excitable units. In this case, the spot-to-spot distance is so large, that the diffusive spread of the activation from the oscillator results in such a strong reduction of u that it resembles the resting state value. Thus no activation should be observable at the excitable units. As shown in Fig. 9.27, in this range of no coupling only two frequency values are observed. The one of oscillating units, which are dependent on the spot size, and $f = 0$ for the excitable units. The corresponding value of spot-to-spot distance $l_{\text{th}} = 3.4$ ($r = 1.0$, $D = 0.05$, $b = 0.4$) is unexpectedly large and dependent on the spot size (e.g. $l = 5$ for $r = 0.75$). It means, that the diffusive coupling covers a range up to 5 length units in the system, and is thus, in comparison with the spot size and the typical spot-to-spot distance, a non-local coupling. Furthermore, for $D = 0.1$ one would expect the spot-to-spot distance for uncoupling to be $l_{\text{th}} = 12.5$ for $r = 0.75$ and $l_{\text{th}} = 5.75$ for $r = 1.0$. Indeed, up to the largest tested spot-to-spot distance $l_{\text{th}} = 7$ for $r = 0.75$ and $l_{\text{th}} = 4$ for $r = 1.0$ non-normal oscillation

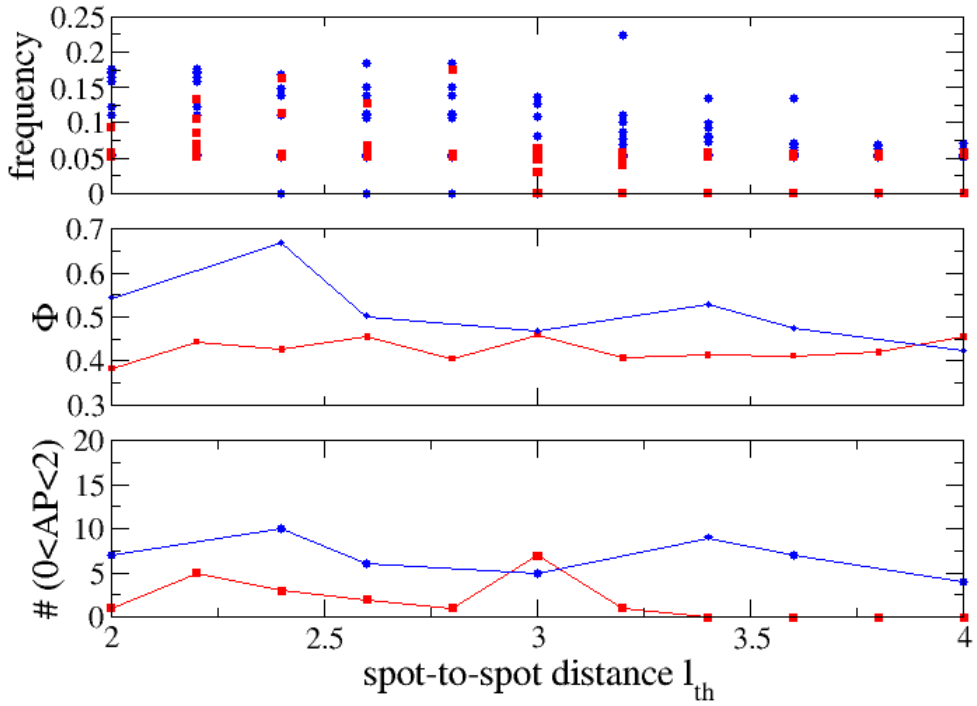

Figure 9.27: Frequency of individual spots, synchronization and number of spots exhibiting non-normal oscillation modes ($0 < AP < 2$) in $5x5$ array ($r = 1.0, b = 0.4$) in dependence of spot-to-spot distance for different diffusion coefficients $D = 0.1$ (blue) and $D = 0.05$ (red). For $D = 0.05$ spots become uncoupled if $l_{\mathrm{th}} > 3.2$, whereas for $D = 0.1$ spots are still coupled for $l_{\mathrm{th}} = 4$, as can be seen from the number of spots in non-normal oscillation modes.

modes are observed, i.e. spots are still coupled. Larger spot-to-spot distances could not be tested due to the size of the array fitting on the GPU memory. Larger simulations would require multi-GPU simulations.

9.3 Comparison of theory and experiment

In this chapter, results from the FHN simulations (see previous section) will be compared to BZR experiments, to reveal if the experimental observations can be described by the model. In Fig. 9.28 the frequency of individual spots is shown in dependence of the spot-to-spot distance for different spot sizes. On the left side, results from the BZR experiments are shown and on the right side, results from the FHN simulations. For small spot sizes, no oscillations are observed for large spot-to-spot distances ($l > 2.2$ mm and $l_{\mathrm{th}} > 1$) for both, experiment and simulation, whereas for small spot-to-spot distances oscillations emerge upon coupling. Thereby, a decreasing mean frequency is observed in the experiments, when increasing the spot-to-spot distance. The same behaviour

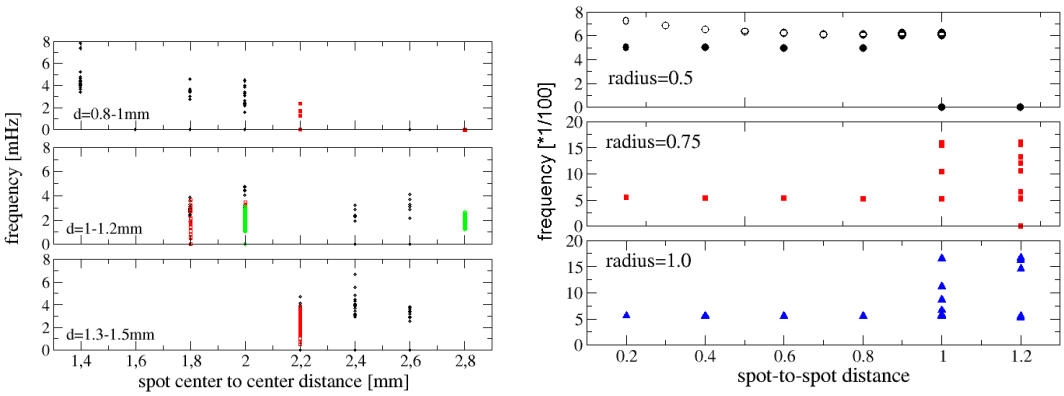

Figure 9.28: Frequency of individual spots in 5×5 spot array in dependence of spot-to-spot distance l and spot sizes determined from the BZR experiments (left) and simulations of the FHN model (right). For experiments, the concentration of Ferroin was $0.5 - 1 * 10^{-}3$ mol/m^2. In simulations, $b = 0.35$ (full symbols) and $b = 0.1$ (open symbols).

is observed in the simulations, if spiral wave patterns are present on the spot array (see Fig. 9.28 right open circles). Spiral waves are observed quite often in the experiments, whereas in the FHN simulations these only occur for random initial conditions. In the FHN simulations, the frequency of spiral waves is proportional to $f = a_{fit}/l_{\mathrm{th}}^2 + b_{fit}$ for spots in the oscillating regime. Thereby, the spiral wave rotates around the in-excitable region surrounded by 4 spots and b is similar to the frequency of a single spot of same size.

In the experiments, the mean value of frequency is proportional to $a_{fit}x^2 + b_{fit}$ for standard gels or $a_{fit}x^6 + b_{fit}$ for pure silica gels. Note, the spot-to-spot distance in the experiments includes the spot radius (centre-to-centre distance), i.e. $l \propto l_{\mathrm{th}} + 2r$. The tip of spiral waves, observed in the experiments, mainly rotates around the centre of one spot. In this case, the frequency is not limited by the diffusion across the gaps but rather by the reactive part of the RD system or the velocity on the spot, respectively. For the pure silica gels, spiral waves rotating around the passive media in between spots are also observed. Most of the spirals still rotate around the spot centre. Thus the dependence of the frequency on the spot-to-spot distance differs from the one obtained from the simulations. In the simulations, spiral waves rotating on a spot are not observed. Since a spiral wave can only be stable if the rotation time, given by the circumference of the rotation path divided by the wave front speed, is at least as large as the action potential duration. Otherwise, the tip of the spiral catches its own refractory tail and is thus extinguished. For the spiral waves rotating around the in-excitable media in between four spots, a minimal spot-to-spot distance of 0.4 is necessary to obtain a stable spiral wave. For smaller spot-to-spot distance the rotation path is larger by propagation around 6 spots. For the parameter range used in the simulations

the speed of a wave front on a spot, i.e. on active media, is much higher than between spots, i.e. passive media. To obtain spiral waves rotating on a spot in the simulations either the spot radius has to be increased strongly or the wave front velocity has to be decreased for example by reducing the excitability (increasing parameter c in FHN model). Another reason for spirals rotating around the spot centre can be the concentration distribution inside the spot, which is not equal everywhere but increases from the boundary to the spot centre.

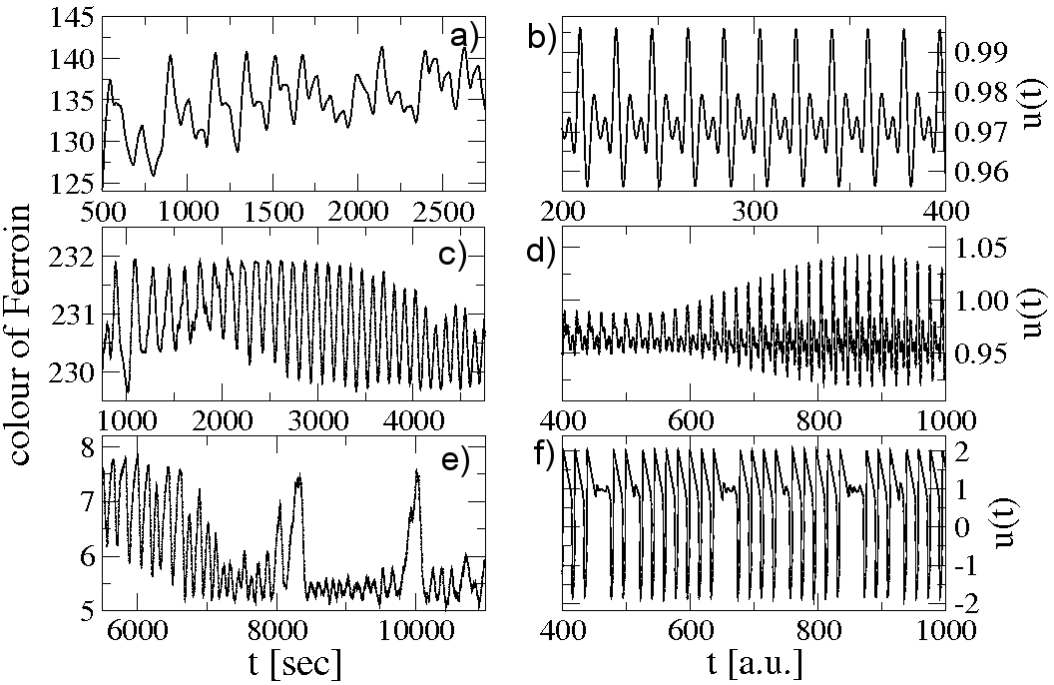

Figure 9.29: Oscillation modes observed for weak coupling in the BZR experiment (left) and FHN model (right): multi-period oscillations [(a) and (b)], amplitude-modulated oscillations [(c) and (d)] and mixed-mode oscillations [(e) and (f)].

For larger spot sizes, broadening of the frequency distribution combined with an increase of the maximal frequency is observed. In the FHN model three oscillation modes could be identified for this regime, which are multi-period, amplitude-modulated and mixed-mode oscillations. As shown in Fig. 9.29 on the left side, similar oscillation modes are observed in the BZR experiments. However, due to the large noise and the low amplitude of these oscillation modes, these oscillation modes could only be detected using the knowledge from the simulations. From the comparison of the results it can be concluded that in the BZR experiments, spots are in the excitable regime, since the non-normal oscillation modes and the emergence of oscillation upon coupling occurs in a small range of excitability, where spots are excitable but the excitability is close to the threshold of the oscillating regime.

Between the experiments on pure silica gels and PSS-co-PM gels one large difference occurred. This is the break-up of wave fronts at the spots on PSS-co-PM gels resulting in irregular patterns. Thereby, the wave front shape is changed to a concave shape on the spots, whereas on the pure silica gels it is convex. Since diffusion times of the small molecules of the reaction solution should be similar for both gel types, a reduced reaction rate or longer action potential might cause this behaviour. To test, if a break-up of wave fronts

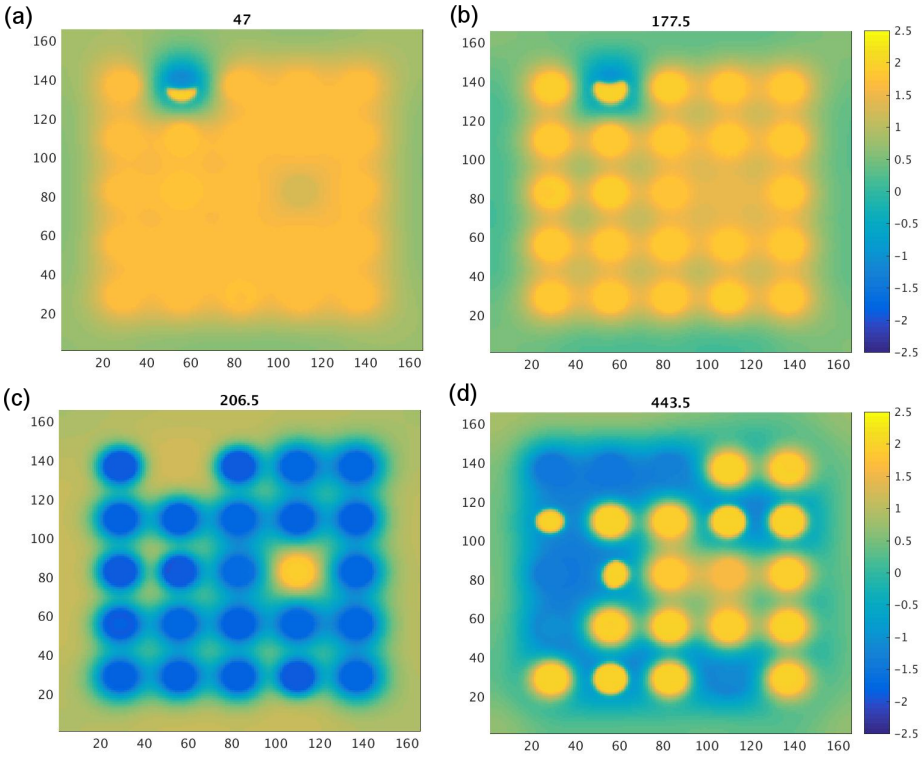

Figure 9.30: Snapshots of excitation patterns on 5×5 spot arrays of oscillators ($r = 0.75, D = 0.1, b = 0.1, l = 0.8$) for strongly increased action potential duration by increasing c to 20.5 (standard value 5.5). Blue corresponds to the resting state, whereas yellow represents the excited state. A change of wave front curvature along one spot is visible [(a) and (b)]. Spots oscillate independently with two spots exhibiting a different period [(c) and (d)].

can occur in the FHN simulations for longer action potentials, parameter c is increased. As shown in Fig. 9.30 [(a) and (b)] for an array of self-excitable spots ($b = 0.1$), a distortion of the wave front on the spot, as was seen in the experiments, is observed for some spots. The other spots are excited mainly by itself, which can be seen by the activation of the spot starting in the spot centre [see (c) and (d)]. Two spots exhibit a different behaviour. The influence of the other spots onto these can be seen for the upper spot (first row, second column). Propagating wave fronts are observed. However, despite the similarity of wave front shape, a break-up of wave fronts as in the experiments

does not occur. Spots are strongly coupled even for spot-to-spot distances $l_{\mathrm{th}} = 1.2$, which can be seen by the synchronization of spots with time. In all simulations, target patterns evolve, pacing the whole spot array. Similar results are observed for an array of spots with larger b values. These would be only excitable for $c = 5.5$ but are still self-excitable for the larger c values, as determined from the single spot simulations (ch. 9.2.1). To obtain a break-up of wave fronts increasing the spot size could be necessary to increase the further increase the curvature of the wave fronts until it eventually breaks up. Alternatively, a break-up of the wave fronts might be possible if the coupling between spots is reduced by either increasing the spot-to-spot distance or decreasing the diffusion coefficient. Simulations with a spot size $r = 1.5$ and 3.0 did not show a break-up of wave fronts at the spot.

9.3.1 Dependence on concentrations of reactants

In this section the patterns on spot arrays will be analysed for different compositions of the reaction solution, i.e. concentration of Ferroin, sodium bromate, sulphuric acid and malonic acid. Increasing the concentration of Ferroin in the BZR experiments resulted in an oscillation of small spots, which did not oscillate for the lower concentration. Since not only the self-excitability but also the oscillation frequency is dependent on the composition of the reaction solution, BZR experiments for different concentrations of sulphuric acid and sodium bromate are performed, which are thought to influence the oscillation behaviour most. Therefore, either sodium bromate or sulphuric acid concentration is changed by adding or reducing the amount without changing the values of the other components of the reaction solution. In Fig. 9.31 frequencies of individual spots in 5×5 (black) or 10×10 (red) spot arrays are shown in dependence of the amount of sodium bromate (Na_2BrO_3, upper panel) or sulphuric acid (H_2O, lower panel). The mean frequency and the width of the frequency distribution decreases when decreasing the amount of Na_2BrO_3. If the amount of Na_2BrO_3 is increased compared to the standard value, the mean frequency and the width of the frequency distribution remain almost the same (slight increase). The behaviour is different, when the amount of sulphuric acid is changed. Here a decrease of the mean frequency distribution and the width of the frequency distribution is observed for increasing amount of H_2SO_4.

In the FHN model, an equivalent for the Ferroin concentration is hard to determine. Therefore, 1D simulations (without diffusion) of the Rovinsky model are performed. In this model, parameters and variables are related to the concentrations of the experiments. In Fig. 9.32, the frequency is shown in dependence of the initial concentrations of Ferroin (parameter c), sulphuric acid and sodium bromate (parameter a). Sulphuric acid concentration is introduced in the model by the acidity function h, whereby low h values correspond to high concentrations of sulphuric acid. Increasing the concentration of sodium bromate or sulphuric acid results in an increase of the oscillation frequency. In

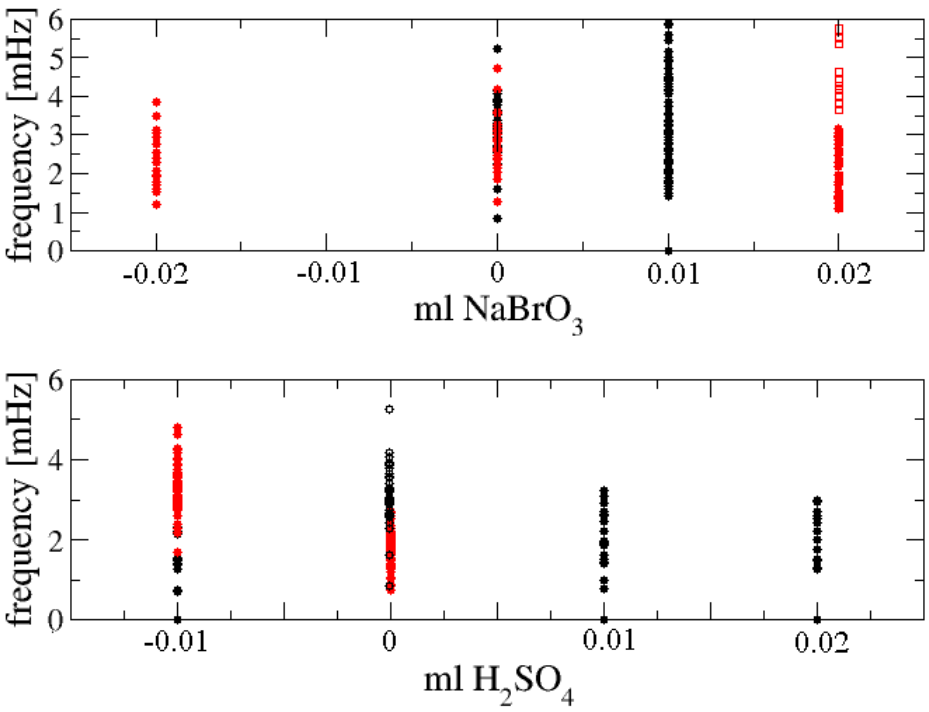

Figure 9.31: Frequency of the individual spots in 5×5 (black) and 10×10 spot arrays (500 drops and spot-to-spot distance 2 mm) for different amounts of sodium bromate $NaBrO_3$ (upper panel) or sulphuric acid H_2SO_4 (lower panel) added to the standard composition of the reaction solution.

contrast, if the concentration of Ferroin is increased the oscillation frequency decreases. A jump of the frequency to zero, as observed for varying the b value in the FHN model, is not observed in the analysed parameter range. Winfree [6] determined the parameter f in the Oregonator model to be the one determining the self-excitable regime. In resemblance to the Oregonator model, parameter $\alpha =$ in the Rovinsky model should have the same effect. It is given by $\alpha = k_4 K_8 B_R / k_1^2 A_R^2 h_0^2$ with the rate constants k_4, K_8 and k_1. Further parameters are proportional to the concentrations of reactants, i.e B_R is proportional to the concentration of malonic acid, A to the one of sodium bromate and h_0 is the acidity function correlated to the concentration of sulphuric acid. Thus, either increasing B_R or decreasing A_R or h_0 should yield a transition to the oscillating regime. In the analysed parameter regime, it could not be observed.

Increasing the concentration of Ferroin [blue curve in Fig. 9.32 (a)] results in a decrease of the oscillation frequency. However, below $c = 0.001$ in the Rovinsky model and the larger a value, oscillations do not occur. In this range, increasing the concentration of Ferroin, i.e. parameter c_R in the Rovinsky model, would move the spots from an excitable to a self-oscillating regime.

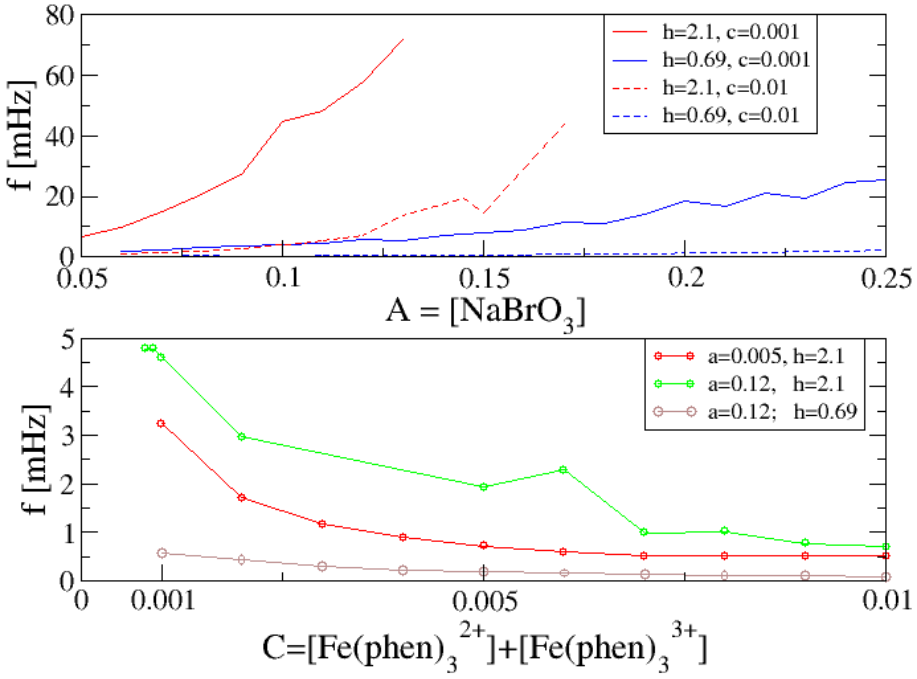

Figure 9.32: Frequency in dependence of concentration of sodium bromate (A_R=[$NaBrO_3$]), sulphuric acid (given by acidity h_0) and Ferroin/Ferriin (C_R=[$Fe(phen)_3^{2+}$]+[$Fe(phen)_3^{3+}$]) calculated with the Rovinsky model.

This could be an explanation for the oscillation of small spots in the BZR experiments for higher concentrations.

Increasing the concentration of sodium bromate, resulted in an increase of oscillation frequency as observed in the BZR experiments of spot arrays. The width of the frequency distribution increases also since small variations of a result in larger variations of the frequency due to steeper slope for larger sodium bromate concentrations. Both effects are visible in the experimental data. Decreasing the concentration of sulphuric acid, i.e. increasing h_0, results in a decrease of the oscillation frequency, which is similar to the observations in the BZR experiments [see Fig. 9.31 (b)].

9.3.2 Arrays with varying parameters

In this section, the influence of a varying coupling strength is tested by increasing the spot size or spot distance within one spot array (see Fig. 9.33). BZR experiments are performed with a 10×10 and 20×20 spot array. The spot distance is varied by increasing it for each row by Δl from the initial value of l_0. Its value in dependence of row i is given by $l_i = l_0 + (i-1) * \Delta l$

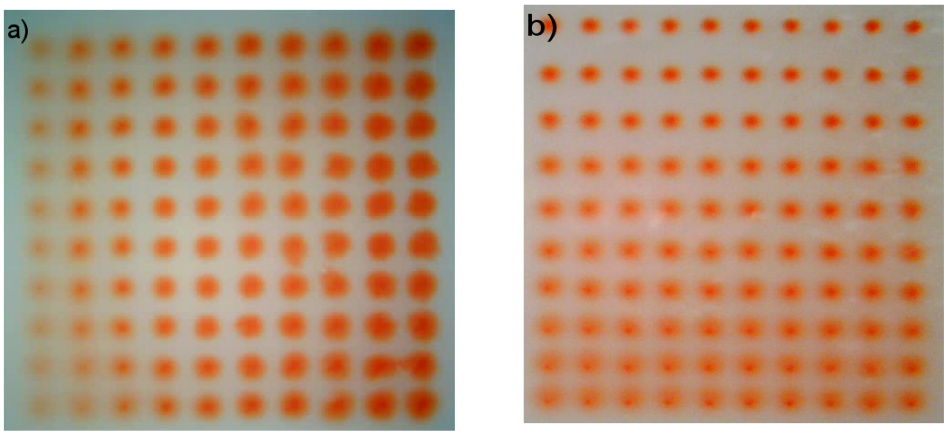

Figure 9.33: Snapshot of 10×10 spot array directly after spotting with varying number of drops per spot (a) and varying spot distance (b). In (a) drop number per spot increases from left to right with each row by 20 (initially 50 drops per spot) and spot-to-spot distance 2.4 mm. In (b) initial spot distance is 2.1 mm and increases by $\Delta l = 0.1$ mm per row (bottom to top). The number of drops per spot is 100.

with $i = 1...N_s - 1$ and N_s the number of spots in the experiments as well as in the simulations. The first spot-to-spot distance is thereby between row 0 and 1. The spot size is varied along the spot array in the experiments by increasing the number of drops per spot for each row by ΔN_d from the initial value N_d^0. The number of drops per spot in a certain row i is then given by $N_d^i = N_d^0 + (i-1)\Delta N_d$ with $i = 1...N_s$. As it can be seen in Fig. 9.33, increasing the number of drops per spot results in the expected increase of spot size. In the simulations, the spot size increases by Δr according to $r_i = r_0 + (i-1) * \Delta r$ with $i = 1...N_s$ the row number.

In Fig. 9.34 the frequency of individual spots in 10×10 and 20×20 spot arrays is shown in dependence of Δl for varying spot distance (lower panel) and ΔN_d for varying spot size (upper panel) as determined from BZR experiments. In the experiments for varying spot distance, the mean frequency is decreased with increasing Δl, whereas the width of the frequency distribution remains almost constant. A representative time evolution of patterns in the BZR experiments is shown in movie S21 in the Supporting Material. If the number of drops per spot increases, i.e. the spot size, the mean frequency per spot array remains nearly the same and a slight decrease of the width of the frequency distribution is observed.

In Fig. 9.35 results for varying spot-to-spot distance are shown for the FHN simulations, i.e. mean value and standard deviation of the frequency distribution (left) as well as the frequency of individual spots (right) is shown in dependence of the spot-to-spot distance and the increase Δl for spot size 0.5 (left) and 0.75 (right). For the small spot size 0.5, the same effect, as seen in the experiments, is observed for $l_{\mathrm{th}} > 0.6$ and $\Delta l > 0.2$. In this case, the width of

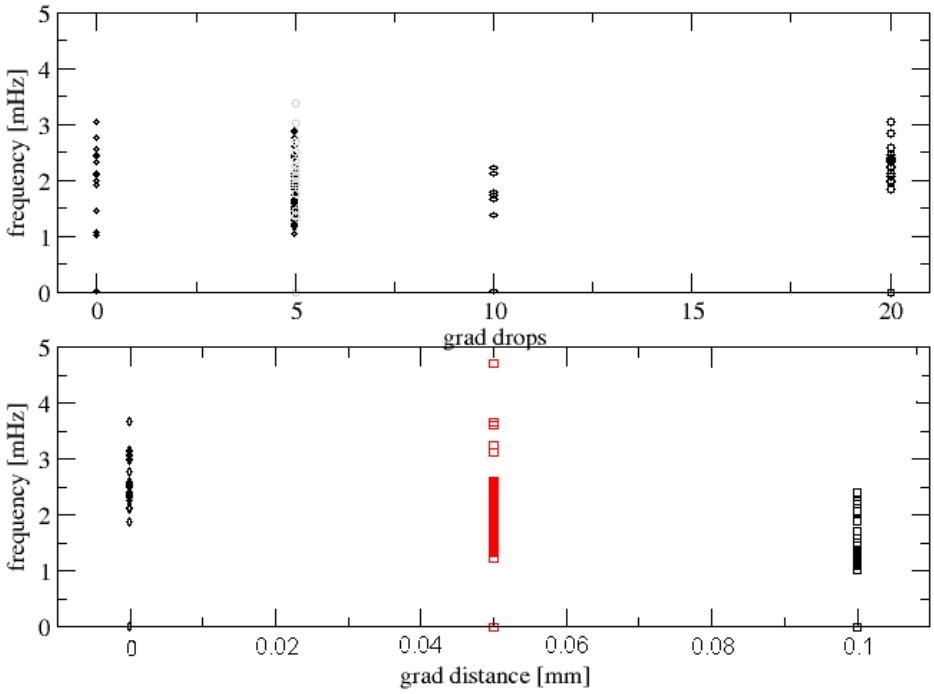

Figure 9.34: Frequency of the individual spots in spot array with varying spot size (upper panel) and varying spot distance (lower panel) in the BZR experiments in dependence of ΔN (drops) or Δl. In the experiments 10×10 (black) and 20×20 (red/grey) spot arrays are used. For a varying spot size, a spot distance of 2.4 mm and an initial number of drops per spot of 50 is used (upper panel). For varying spot distance, the number of drops is 50 and the initial spot distance $l_0 = 2.1$ mm (10×10 array) and $l_0 = 2.05$ mm (20×20 array).

the frequency distribution is slightly reduced and non-oscillating spots occur. Due to the latter one the mean frequency decreases. Furthermore, the critical spot distance, for which non-normal oscillation modes occur, is decreased if Δl is increased, i.e. $l_{\text{crit}} = 0.8$ for $\Delta l = 0.2$ and 0.6 for $\Delta l = 0.3$. For larger $\Delta l = 0.4$, in contrast, it is increased to larger values again. This can be an effect of the initial conditions resulting in more stable conditions for the smaller spot-to-spot distances. A separation of rows with large spot-to-spot distance from the excitation pattern occurring on the more closely coupled spots can be observed. Thus, effects like a reflection of a spiral wave can be observed, as shown in Fig. 9.36 for a 5×5 spot array and in movie S22 in the Supporting Material. Thereby, a spiral wave pattern is rotating on the three rows with the smaller spot-to-spot distance. The other two rows are effectively decoupled, i.e. wave fronts of the spiral wave do not extend onto these rows. They are excited by two pace making spots with a frequency much smaller than the spiral wave.

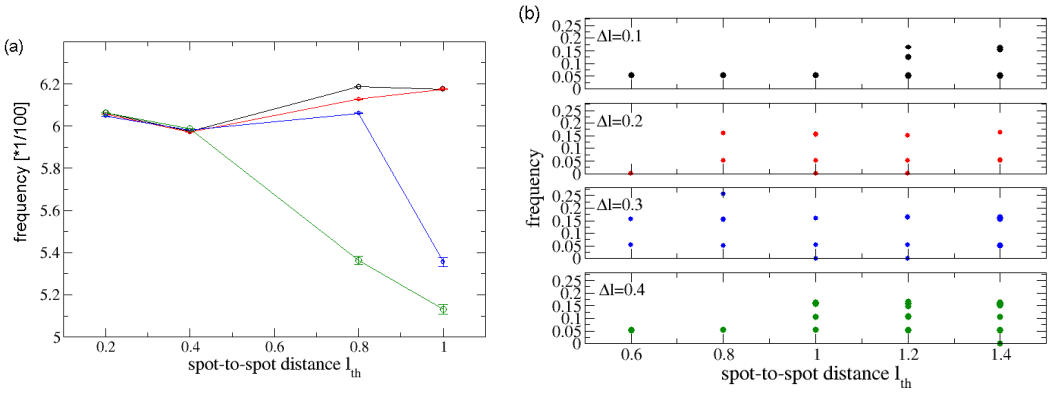

Figure 9.35: (a) Mean and standard deviation (reduced to 10% of its value) of frequency distribution in a 5×5 spot array of radius 0.5 is shown in dependence of spot-to-spot distance and increase Δl of l_{th} with $\Delta l = 0.1$ (black), 0.2 (red), 0.3 (blue) and 0.4 (green). (b) Frequency of the individual spots in a 5×5 spot array in dependence of spot-to-spot distance l_{th} and increase Δl of spot-to-spot distance for $r = 0.75, b = 0.4, D = 0.1$ in FHN simulations.

Without the increase in spot-to-spot distance, this target patterns would be suppressed by the spiral wave due to its higher frequency.

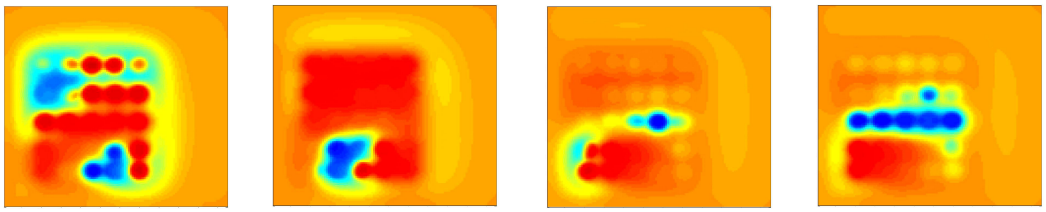

Figure 9.36: Excitation pattern for a 5×5 spot array ($r = 0.5, D = 0.1, b = 0.4$) with increasing spot distance ($l_0 = 1.0, \Delta l = 0.4$) from bottom to to top. The upper two rows are effectively decoupled from the lower rows. A spiral wave pattern on the lower rows does not extend onto the upper two rows.

For smaller increases (Δl) of the spot distance the excitation patterns are comparable to spot arrays without varying spot distance. If the spot size is increased to 0.75 (right side of Fig. 9.35), the behaviour is different. In this case, a reduction of the mean frequency or the width of the frequency distribution is not observed even for $\Delta l = 0.4$. Patterns resemble the ones from regular arrays. The difference for different spot sizes is caused by the dependence of the diffusion time $T_d = l_{\mathrm{th}}^2/a_{fit}$ for propagation across the gap l_{th} between spots on the spot size. Here, a_{fit} is the value determined from the frequency dependence of spiral waves in the simulation (see Fig. 9.15). Small spots exhibit a larger diffusion time ($T_d \propto 20l^2$) than larger spots ($T_d \propto 7.7l^2$), i.e. the effective coupling is weaker for small spots, since the diffusion time has to be smaller than oscillation period of self-excitable spots to influence the

neighbouring spots. Thus, the increase of spot-to-spot distance affects spot arrays with small spots more than the ones with large spots.

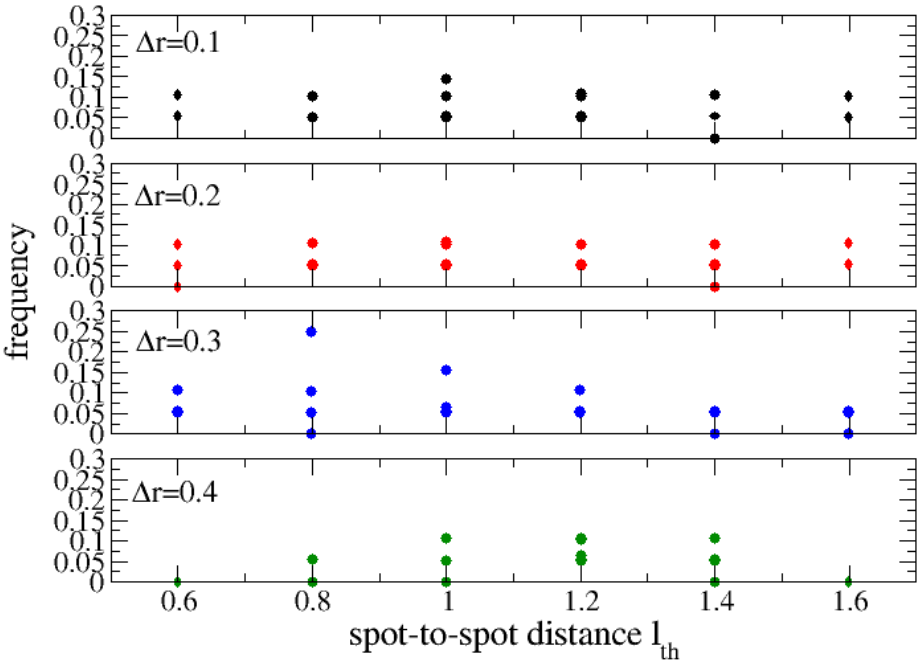

Figure 9.37: Frequency of the individual spots in 5×1 spot arrays in dependence of spot-to-spot distance l_{th} and increase Δr of spot radius for initial spot radius 0.5 in FHN simulations ($b = 0.35$).

Increasing the spot size in the simulations results in a decrease of the critical spot-to-spot distance for non-normal oscillation modes to $l = 0.6$ even for a slight increase of the spot size, i.e. $\Delta r = 0.1$. This is shown in Fig. 9.37, where the frequency of individual spots in a 5×1 spot array with spot size 0.5 is plotted against the spot-to-spot distance for different increases of spot size Δr. This is possibly due to the broader frequency distribution due to the different size of the spots. If $\Delta r = 0.4$, the range of spot-to-spot distances for which non-normal oscillation modes occur, is decreased again. That means, the critical spot-to-spot distance above which non-normal oscillation modes occur is increased to 0.8, which is still smaller than for spot arrays without increasing spot size. Furthermore, the second critical spot-to-spot distance above which spots are uncoupled and non-normal oscillation modes do not occur is decreased to 1.6. In spot arrays without increasing spot radius this value is 3.5. This is surprising, since the coupling strength, i.e. the distance between spots, is not changed.

9.4 Discussion

In this chapter, excitation patterns occurring on multiple, coupled units were studied to reveal if a reduced coupling or heterogeneity yield irregular patterns in this system. The units could be either self-excitable or excitable. Three different mechanisms for the occurrence of irregular patterns could be identified. Mechanism I is a reduced coupling strength in arrays of oscillators, which results in the generation of synchronized subgroups with irregular patterns at the borders of the subgroups. Mechanism II, occurring in arrays of excitable units, yields irregular oscillation modes for weak coupling and heterogeneity in the array properties. Mechanism III describes the case of reaction kinetics slower than the diffusion time. Thereby irregular patterns result from break-up of wave fronts at the spots, i.e. at higher concentrations of the catalyst.

Before discussing all three mechanisms in detail a closer look will be taken at the self-excitability, the property distinguishing between mechanism I and II. The self-excitability and its dependence on the spot and reaction properties was studied in single spot experiments and in the FHN simulations. As was deduced by Winfree and shown by others [266], parameter a and b control the self-excitable regime in the FHN model. In this work, b was varied to tune the self-excitability. In the Rovinsky model parameter $\alpha \propto B_R/(A_R^2 h_0^2)$ with B_R the concentration of malonic acid, A_R the concentration of sodium bromate and h_0 the acidity determined by the concentration of sulphuric acid, should be determining the self-excitability. This is proposed from the similarity to the Oregonator model [156, 157] and the studies of Winfree [6], who showed that the parameter before the term coupling u and z in the Oregonator model controls the self-excitability. However, in 1D simulations without diffusion term the transition between excitable and oscillatory regime could not be determined. The system was always oscillating.

The influence of diffusion onto the self-excitable regime was discussed by Winfree [6]. Diffusion should reduce the critical b value. This was observed in the single spot simulations of the FHN model for increasing D. In this work, b_c decreases with decreasing spot diameter, possibly due to a lower influence of the diffusion for larger spot sizes. In this case, the source-sink relationship is reduced with the spot size. The same argument can explain the influence of the spot shape onto b_c. If the spot areas are similar, b_c and the oscillation frequency are independent of the spot shape. The dependence of the oscillation frequency on the size of the BZR oscillator was studied by Yoshikawa *et al.* [267] and Maselko *et al.* [268] for polymer-resin beads loaded with Ferroin. Both observed a decrease of oscillation frequency with decreasing radius of the bead. Furthermore, they showed a critical radius, below which the beads were only excitable, as was observed in this work, too. Yoshikawa *et al.* could deduce the dependence of the oscillation period $T = 1/f$ on the bead size r and the amount of sulphuric acid in the reaction solution to be $f/[H_2SO_4]^\gamma \propto (1-\eta/r)$. Due to the dibasicity of sulphuric acid and the fact that sulphuric acid takes

part in the BZR, $1 \leq \gamma \leq 2$ is introduced. This is similar to the results from the FHN model for single spots in this work. Studies about the influence of the spot diameter on b_c could not be found. Particularly interesting would be theoretical studies with increasing Ferroin concentration from spot boundary to the spot centre, since in the BZR experiments spiral wave like patterns are observed even on single Ferroin spots. These are thought to be caused by the varying Ferroin concentration inside the spot. Since a larger concentration results in a lower oscillation frequency, the high-concentration region can act as anchor side for the high-frequency activation in the low-concentration range.

The occurrence of irregular patterns due to a weak coupling and/or heterogeneity was studied in two regimes: first for coupled oscillators (type I) and second for coupled excitable units (type II). The coupling strength is thereby influenced by the diffusion coefficient, the spot-to-spot distance, the spot diameter and the spot shape.

Type I irregularity occurs in arrays of self-excitable units for weak coupling. If the coupling strength for coupled oscillators is decreased by increasing the distance between spots or decreasing the diffusion coefficient, multiple, coexisting excitation patterns and a separation of spots into synchronized subgroups is observed. At the border of these subgroups, irregular activations can occur due to a switching of oscillations between the different clusters. A further increase of the spot distance results in independent oscillations of spots. This clustering of oscillations with irregular patterns in between the clusters was described previously by Wang *et al.* for globally coupled electrochemical oscillators [182], by Taylor *et al.* for globally coupled photochemical BZR oscillators [269, 270] and by Maselko *et al.* for diffusively coupled Ferroin loaded beads in BZR solution [268]. The theoretical description was pioneered by Kuramoto, Crawford and Strogatz [271–273]. In the experiments, Maselko *et al.* showed that the regularity of patterns can be tuned by the bromate concentration, i.e. low concentration corresponds to regular patterns, whereas larger concentrations result in irregular ones. The critical concentration for the occurrence of irregular patterns decreased with increasing bead size. The loss of coherence in population of coupled BZR oscillators was also studied by Toth *et al.* [263]. Thereby, catalyst loaded beads were placed in BZR solution in different densities and compositions of the reaction solution. In dependence of the number of neighbours and the composition of reaction solution, either regular wave patterns were observed or irregular ones. Here, the composition of the reaction solution seemed to play a more important role than the number of neighbours. The frequency distribution for coupled beads was dependent on the number of neighbours for the reaction solution yielding irregular patterns, whereas is was independent on the number of neighbours for the reaction solution yielding regular patterns. Due to the experimental set-up, it could not be deduced if the occurrence of irregular patterns was dependent on the density of beads or the composition of reaction solution.

Type II irregularity occurs for arrays of coupled excitable units for weak

coupling. In the strong coupling regime similar excitation patterns are observed as for coupled oscillators. For weak coupling, though, either quiescence or non-normal oscillation modes occur. The emergence of oscillation upon coupling of excitable units is known from diverse systems as beta pancreatic cells, responsible for insulin secretion [274], yeast cells, the slime mold Dictyostelium discoidium and other biological systems [254, 255], Ferroin-loaded beads in BZR solution [256], neurons [257], electrotonic systems [258] or other chemical excitable media [259, 260, 275] and numerous theoretical studies [82, 261]. It typically occurs, if the system is near a oscillation bifurcation. In this work, experimental studies on the dependence of the emergence of oscillation on the coupling strength could be studied due to the possibility to tune the coupling strength by changing the spot-to-spot distance and the spot size. This is new in comparison to the previously mentioned experiments, since there the density of units was controlled but not the positioning of the units.

The non-normal oscillation modes cause a broadening of the frequency distribution and an increase of maximal frequency by two to three times. Three types of oscillation modes could be identified, multi-period oscillations, amplitude-modulated oscillations and mixed-mode or multi-mode oscillations. The first two can be explained by the interaction of excitable and oscillating spots, whereas for the latter one a simple explanation could not be found. These non-normal oscillation modes are related with a higher frequency of oscillation and a strongly decreased maximal value of the action potential. However, if these oscillation modes may play a role for irregular patterns in biological systems is unclear. In biological systems, cells react according to a all-or-nothing behaviour, i.e. stimuli lower than the threshold do not result in a response by the cell. Yet, nerve cells in the brain, for example, possess also a summing function. That means, a number of incoming impulses are summed up until the threshold for activation is reached. In this case, the low amplitude oscillations of the non-normal oscillation modes might play a role for the system behaviour. The occurrence of non-normal oscillation modes is restricted to a small regime between the excitable and the oscillating regime. This regime is thereby defined by the self-excitability parameter and the spot size. The coupling strength, i.e. the diffusion coefficient and the spot-to-spot distance, spans thereby a large range of values. The occurrence of the non-normal oscillation modes, in particular the mixed-mode oscillation, is known from systems as the BZR, electrochemical oscillators, enzyme reaction systems or networks of light emitting diodes [16, 142, 276–279]. In these cases, either they occurred due to a certain set of reaction parameters (introducing different chemicals) or by coupling [266]. The latter one was studied for example by Postnov *et al.* [266] with focus on resource-mediated coupling. Sometimes this term is used in the BZR for beads in a common reaction medium, but it mostly describes the case of stirred reactors introducing a global coupling [181]. Postnov *et al.* studied electrotonic oscillators coupled by a common power supply. As for the diffusive and more locally coupled BZR excitable units in this work,

multi-mode oscillations are observed for weak coupling and a certain amount of heterogeneity. In the system studied in this work, the non-normal oscillation modes occurred also for vanishing heterogeneity. Heterogeneity seemed to play a minor role in the generation of these patterns, but it increased the range, where these modes occur.

The spatial patterns for spot arrays exhibiting non-normal oscillation modes are rather regular, i.e. they resemble independent oscillation patterns or coupled oscillation patterns. Thus, the generation of wave breaks or fragments or propagation failure [252, 253] due to the underlying discreteness or the reduced coupling strength could not be observed. Nevertheless, if a gradient of the coupling strength is introduced, in particular when increasing the spot-to-spot distance inside the spot array, spatial patterns are disturbed. That means, rows of the spot array become more or less independent from the rest of the array. Thus, spiral wave patterns could be observed on a part of the array, whereas the rest of the array was activated by a different frequency. In larger spot arrays and with larger variations of the coupling strength along the array, propagation failure or even irregular spatial patterns with wave breaks are expected. Indeed for a decrease of the coupling strength due to a reduced density of spots Steinbock *et al.* showed the occurrence of irregular, spatial patterns. In cardiac tissue, a reduced conduction near fibrotic tissue is thought to stabilize atrial fibrillation [280]. This was shown by Bub *et al.* [281] on monolayer preparations of embryonic chick heart cells. In this preparations, they could change the cell density in the preparation step and the coupling between cells by addition of a drug blocking gap junction connections. A reduction of cell density as well as a reduction of the gap junction between cells, i.e. the coupling strength, resulted thereby in irregular activation patterns including wave fragmentation. In this experiment, the sites of reduced gap junctions and the heterogeneity of cells could not be addressed. In numerical models of heterogeneous tissue, consisting of excitable and in-excitable elements, similar results could be observed. For an increased amount of heterogeneity, wave fragmentation occurs [70, 281]. Thus, the reduction of the coupling strength is conceivable as cause for irregular patterns in biological (cardiac) or chemical systems. From the theoretical studies in this work, it can be concluded that heterogeneity enhances the irregularity and increases the range of occurrence but is not the cause for the occurrence of the irregular patterns.

Another type of irregularity, type III, was observed in the experiments with silica gels including PSS-co-PM. Here, wave fronts seem to propagate faster at the border of the spots than at the spot centre. This resulted in the break up of wave fronts at the spot centre. This type of irregularity mechanism was not observed for pure silica gels but for a large range of configurations (spot-to-spot distance and spot size) in the PSS-co-PM gels. This could be caused by reaction rates, i.e. the inverse of the activation time or the refractory period, which are smaller for the PSS-co-PM gels than for the pure silica gels, if diffusion times are similar. In this case, the propagation from spot to spot

across the in-excitable gap would be faster than the subsequent activation of the whole spot. This results in a stronger curvature of the wave front. The change of reaction rates could be caused by an interaction of the PSS-co-PM with the Ferroin. Indeed, in the gel optimization experiments it could be shown that PSS-co-PM interacts with Ferroin and similar diffusion times for water in both gels were measured by NMR [224]. Another reason for this propagation pattern can be a varying Ferroin concentration inside the spot, since the frequency of oscillation should be lower for the higher Ferroin concentration. In this case, the high concentration in the spot centre acts as an obstacle for the wave propagation, which can yield a break-up of the wave front. As a third mechanism it could be possible that a small amount of Ferroin diffused out of the spot and thus the gaps between the spots are also excitable. To reveal this mechanism, FHN simulations with longer action potential duration, i.e. larger activation and recovery times, were done by increasing parameter c in the model. This moves the transition from self-excitable to excitable behaviour, which could not be observed for single spots in the tested range of b values any more. Spot arrays with large c values exhibit changes to the wave front shape as seen in the experiments. That means, concave wave fronts are observed on the spots. Despite of the similar curvature for simulations and experiments, a break-up of wave fronts at the spots did not occur in the simulations. Due to the changes of c, the coupling between spots is modified, too, i.e. spots are still strongly coupled for $l > 1$, whereas for small c values spots are only weakly coupled. The break-up of waves might be prevented by the strong coupling between spots. Thus, simulations with large spot-to-spot distance ore reduced diffusion coefficient should be done to clarify this. Alternatively, it is possible that a break-up of wave fronts might occur for larger spot sizes. In this case the curvature of the wave front should be increased until it eventually ruptures. However, simulations with up to four times larger spots did not show a rupture of the wave fronts at the spot. Due to the small amount of parameters tested in this sense, this should be tested in further simulations with larger spot sizes or BZR experiments will smaller spot sizes. From the comparison with the simulations, the break-up of waves at the spots most likely occurs due to the larger Ferroin concentration inside the spots, acting as an obstacle for the wave front. Thus the part of the wave front propagating in the centre of the spot is slowed down in comparison with the outer parts, resulting eventually in the rupture of the wave. This is known for in-excitable obstacles and leads to a detachment of the wave front from the obstacles. However, a high concentration of Ferroin, acting as an obstacle for the wave front, was not yet described.

Beside the types of irregularity and due to the possibility of controllable changing spot size and distance, the dependence of other effects as the emergence of oscillations and the patterns in the strong coupling regime could be studied in more detail. Considering spot arrays of strongly coupled oscillators/excitable units, these typically exhibit either a spiral wave pattern or a

target pattern. Thereby the frequency of the spiral wave pattern is much larger than the one of the target patterns. In the simulations it is depending on the diffusion time across the in-excitable gaps between the spots, whereas in the experiments spirals most often rotate on a spot around the spot centre. Thus, different frequency dependences on the spot-to-spot distance are observed. This difference occurs also for single spot experiments and simulations, since in the experiments also re-entrant patterns on single spots are observed. It should be studied in further work if the inhomogeneous Ferroin concentration inside the spot or the large spot size in comparison to the wave front width enables these patterns. Increasing the spot size results in larger rotation frequencies for small spot-to-spot distances in the FHN simulations, whereas in the experiments it changes the dependence on l. However, due to the small experimental data set, this should be validated in further studies. Changing the spot shapes result in different rotation frequencies of the spiral wave due to changing wave front speed with curvature and thus a change of coupling strength. Steinbock *et al.* [174] observed different wave front shapes in dependence of the spot shape, which could be observed also in the simulations of large spot arrays. Furthermore, the spot shape is important for the evolving pattern, when considering similar initial conditions. This can be explained by reduced coupling strength for triangular and rhombic spots. The evolving pattern can be predicted in a limited range for certain initial conditions, if it is known for a certain spot size and distance between spots. This analysis of evolving patterns and their properties might be useful for optimizing catalysis processes, which exhibit similar dynamics, as for example CO oxidation on Platinum catalyst or proton exchange membrane (PExM) fuel cells. Using patterned structures of the catalyst can have advantages for these reactions. If one can structure the catalyst in a way that favours spiral wave patterns, i.e. square units, the effectiveness of the catalyst might increase, due to the higher frequency of spiral wave patterns. This is only true, if the reaction of the catalyst is still the same. Furthermore, with this approach, a reduction of catalyst material might be possible. Although the area of catalyst available would be less, the higher frequency of catalysis could compensate this. However, the typical usage of, for example, a Platinum catalyst for CO oxidation is done in a flow reactor, i.e. there is a gas flow along the catalyst. This would introduce another coupling component acting on a large (spatial) range in the model, which changes the dynamics of the system. It should be studied in further work if an increase of effectiveness can be achieved in these systems by patterned catalyst structures.

Limitations of this work are that mainly FHN simulations were done to compare with the experimental data. Only time-dependent simulations of the Rovinsky model were conducted, since it exhibited a low stability, when solved with the Euler-method. In particular, the results of different gel systems would be interesting to study in system-specific models to reveal the mechanism of the lower propagation of wave fronts on the spots than in between. Despite

this, experiment and numerical studies exhibited close similarities.

In the experiments, although the immobilisation of Ferroin was enhanced by optimizing the silica gels for this purpose, still some Ferroin could diffuse during the experiment and sometimes out of the gel into the reaction solution. In the latter case, the BZR can evolve in between spots and in the reaction solution, resulting in more complicated propagation patterns, since the propagation speed should be different in the gel system and the reaction solution. Furthermore, 3D wave patterns are possible, which cannot be resolved by the camera pictures. However, the diffusion of Ferroin in the reaction solution was quite well visible and experiments, in which this was observed, were excluded from the analysis. After the end of the experiments, the reaction solution was removed from the gel and distilled water was added. In most of the experiments, slightly red spots became visible by this procedure. This indicates, that the Ferroin is still immobilized in the gels and the reduction in contrast is caused by the decomposition of Ferroin by the components of the reaction solution, as was described already by [268].

The influence of the gel onto the BZR patterns was not studied in detail in this work. Since both gel systems exhibited similar diffusion coefficients for water, their influence on the propagation of waves seems similar. Furthermore, the concentration of immobilized Ferroin is in the same range, since similar spot sizes are observed for the same amount of Ferroin drops applied. The observed difference of wave propagation on spots is thus probably due to the interaction of PSS-co-PM with Ferroin. A comparison of different gel systems onto propagating waves in the BZR was done by Yamaguchi *et al.* [173], where agar gels, silica gels, polyacrylamide gels, alginate gels and anion exchange resins were compared. Neumann *et al.* [282] studied the influence of the composition of silica gels on wave front propagation. In both cases, changing the gel system or the composition could be used to tune the properties of the BZR and the propagation of waves. Since in this work, always results from similar gels were compared, their influence on the patterns should be similar, since the reproducibility in particular for the PSS-co-PM gels was high.

Furthermore, the influence of the surrounding environment, in particular temperature and oxygen, were not controlled. But since the experiments were performed in the clean room area, where the temperature is kept constant, an influence due to changing temperature is negligible. A heating of the reaction solution due the ongoing reaction or the illumination was not observed. Although it is known, that oxygen diffusing into the reaction solution from the environment can suppress the BZR [64], the experiments were performed in an open reactor. To reduce the influence of the oxygen, a larger amount of reaction solution was poured onto the gels. To reduce the influence of varying spot size, distance or concentration due to the plotting procedure and the immobilization properties of the gels, spot size and distance were determined before initiation of the BZR and only experiments with similar spot size, distance and concentration of Ferroin were compared.

Summary and Conclusions

Chapter 10

Conclusions

From the studies of the interaction of two pacemakers in active tissue located in separate regions, which are only connected by a small isthmus, one can conclude that fibrillatory-like patterns can be generated. The similarity to results from medical studies and the increased efficiency of catheter ablation treating these sources supports the conjecture that this mechanism constitutes a novel generating mechanism for atrial fibrillation. It is important to note that heterogeneity is not necessary for the occurrence of the irregular patterns. Necessary are the separation of the pacemaker in two regions and the small isthmus connecting both regions. The dependence on the frequencies of the pacemakers together with the naturally occurring variation of pacemaker frequencies in the human heart can be an explanation for the episodic behaviour of atrial fibrillation. Results from this study also have relevance for other reaction-diffusion systems, if the interplay of oscillators in combination with geometrical constraints on the wave front propagation in active tissue is considered. Detachment of waves with subsequent re-entrant patterns is known from many other systems as, amongst others, the BZR. For an example of detachment of waves in the BZR, see movie S9 (spot (first row, 3-4th column) in the Supporting Material.

From the studies of multiple coupled oscillators or excitable units it can be concluded that irregular patterns can be generated by three different mechanisms. In particular interesting are the mechanism of weak coupling of excitable units, resulting in so termed 'non-normal' oscillation modes, and the mechanism of break-up of wave fronts at the spots, occurring for the PSS-co-PM gels. While the first mechanism could only be identified due to the possibility to experimentally control the coupling strength, spot size and other properties, the second mechanism could be revealed by the comparison of the different gel systems. Both mechanisms are relevant for the study of BZR dynamics for coupled oscillators. Because of the generic origins of the mechanisms, they will be important also for similar systems like catalysis processes or in biological systems.

The simple method to obtain structured systems by plotting a substance

(here Ferroin) and subsequently immobilize it in an easily producible gel support offers a fast and effective way to study tailored, structured systems. These can be, BZR waves in corrugated channels or controlled catalyst patterns of other type or, similarly controlled structures in other fields, as, for example, cell growth in different nutrition or cell compositions. In the latter case either the nutrients or a chosen type of cells can be immobilized in the gel and (another) cell type, which shall be studied, can be added by plotting. Thereby, a possible route to improve the immobilization of substances in silica gels was presented, which is based either on the change of the gels' microstructure or the interaction of certain substances with the immobilized agent. In particular interesting for the BZR is the possibility to tune the relationship between reaction rate and diffusion time by addition of substances into the gel. This offers new ways to experimentally address regions of the phase space exhibiting interesting dynamics, which could yet only be studied by the help of simulations. The coupling of multiple oscillators or excitable units and the observed mechanisms are not only relevant for the BZR. It can be also interesting for biological systems, where oscillators or excitable units are a model for cells, whose coupling is constricted. A possible system for coupled oscillators might be the formation (coordination or perturbation) of a multicellular slug of the slime mold Dictyostelium discoideum, which is controlled by waves of chemicals emitted by the individual cells. The weakening in the coupling strength of cardiac cells due to ageing or diseases and the resulting disturbances in the electrical activation is an example for weakly coupled excitable units.

Considering the system-specificity and universality of the different mechanisms it can be stated that in the case of cardiac tissue a strong system-specificity is observed. That means, although some features and mechanisms observed in the generic model occur also in the system-specific model, as the conduction block or irregularity type III, other effects and mechanisms differ strongly for the system-specific and the generic model, as e.g. the detachment from sharp corners. Thus, it is possible to gain some understanding of observations from cardiac tissue by the help of the generic model. But one will not get a complete picture without the use of system-specific models. Furthermore, it is advisable to use not only one system-specific model but compare different ones, since they can differ quite much in important effects as e.g. stability of re-entrant waves or detachment from corners [230, 283].

In contrast, the system-specificity is smaller for the chemical reaction-diffusion system, i.e. results from the generic model describe quite well the occurring features in the BZR. When considering in particular the Ferroin-catalysed BZR, modelling the system by the generic model seems to be sufficient for understanding the mechanisms generating the irregular patterns. Simulations with system-specific models support the study by identifying interesting parameter ranges for the experimental studies.

These conclusions are drawn from the comparison of the results from the FHN model as generic one and the system-specific ones (BOCF model, Rovin-

sky model or BZR experiments). The FHN model already exhibits a closer similarity to the BZR system-specific model (Rovinsky model) than to the cardiac tissue model (BOCF model). Thus, a different generic model might lead to other conclusions regarding the system-specificity. The importance of system-specificity can be derived from the difference in dynamical behaviour and properties of another system in comparison with the FHN dynamics. To obtain a first guess about the applicability of the FHN model for a specific system one can take a look at the restitution properties and the action potential shape of the new system. Nevertheless, the use of a generic model is helpful to gain an understanding of the underlying mechanisms, which is much more complicated for system-specific models due to their typically higher complexity. Thus, it is harder to determine, what is the cause of an observed effect due to the the number of variables and their mutual dependencies.

Chapter 11

Summary

In this work, the transition between regular and irregular states in reaction diffusion systems was studied with the focus on the coupling between two or more oscillators and their properties. Determining the system-specificity and the universality of the mechanisms yielding this transition was one objective of this work. Therefore, numerical simulations of generic and system-specific models have been performed and compared to data from medical studies of AF and experiments of the BZR. Two mechanisms were studied, which are suggested to yield irregular patterns.

The first mechanism was proposed by myself on the basis of medical studies of atrial fibrillation. It is based on the interaction of two active sources located in separate regions, which are interacting by the active tissue they are connected to. In this work it was found that in dependence on the relation of the frequencies of the active sources, irregular patterns of different types occurred. One type is a general one, occurring in the generic as well as the system-specific simulations. Three other types occurred only in either the generic model or the system-specific one. Their properties and dependence on the simulation set-up as well as system properties was studied with respect to their relevance as generating mechanism for atrial fibrillation. The mechanism, interplay of two pacemakers under geometrical constraints, was found to be an explanation for the generation and the often episodic occurrence of AF, because changes in the frequency of either the sinus node or the perturbation source can move the system into a region of the phase space, where irregular patterns occur. Similar effects, like detachment of waves and conduction blocks, which cause the generation of irregular patterns, are observed also for the BZR and other reaction-diffusion systems. Accordingly, the novel mechanism is relevant also for these systems when situations occur, where pacemakers interact under geometrical constraints for wave propagation in active tissue.

The second mechanism is based on the coupling of multiple oscillators. In this case, either a reduced coupling or heterogeneity were thought to cause irregular patterns. This mechanism was investigated systematically by both, theoretical investigations and experiments of the BZR, in which the coupling

strength and properties of the oscillators could be tuned.

Irregular patterns were found in the BZR for the weak coupling regime in case of arrays of oscillators and excitable units due to different effects. In the case of the oscillators, a loss of coherence or synchronization yields irregular patterns, whereas in the case of excitable units, the long-range diffusive interaction between the spots was the reason for the irregularities. Another type of irregularity was determined, where a break-up of wave fronts at the spot centres is observed, which was not yet described in the literature. The influence of the size, shape and coupling strength of the coupled units on the irregularities was investigated as well as the properties of the irregularities itself. Changing the coupling strength along the array could result in stronger irregularity, as known from former studies. The interplay of experiment and simulation, whereby in both the properties of the spots and the coupling strength could be tuned in a controllable way, allowed the distinction between the different types of irregularities and the determination of the mechanism generating them. These mechanism seem to be not only relevant for the BZR system but also for other systems, which are similar to the BZR, as the CO oxidation on a Pt catalyst or in PEM fuel cells. Furthermore, the observations might be relevant also for biological systems, consisting of multiple oscillators, as, e.g., the brain or hair cells in the ear, or of excitable units like the cardiac tissue or the pancreatic beta cells. In particular interesting is that a weakening of the coupling between cardiac cells can cause atrial fibrillation.

In both studied systems, i.e. AF and BZR, the generic model could reproduce features observed in the experiments or medical studies. Furthermore, experiments and medical studies show in certain cases similar effects. Despite of this, there are some features, which could not be reproduced by the generic FHN model. In these cases the system-specific approach has to be applied. Concluding, due to the similarity between the systems and the observed features, starting with the generic approach to understand underlying mechanisms and then becoming more and more system-specific to reveal the relevance for the actual system seems to be an effective and promising route to understand the complex pattern-generating systems.

Bibliography

[1] J. R. Anderson, "Cognitive psychology and its implications," (Springer New York, New York, NY, 1990) p. 519.

[2] M. Shermer, Scientific American **299**, 48 (2008).

[3] I. Wickelgren, Science **256**, 1520 (1992).

[4] W. Gruber, H. Oberhummer, and M. Puntigam, *Wer nichts, weiß muss alles glauben* (Ecowin Verlag, 2010).

[5] J. E. Pearson, Science **261**, 189 (1993).

[6] A. T. Winfree, Chaos **1**, 303 (1991).

[7] A. M. Turing, Phil Trans. R. Soc. B **237**, 37 (1952).

[8] V. K. Vanag and I. R. Epstein, Int. J. Dev. Biol. **53**, 673 (2009).

[9] I. R. Epstein and K. Showalter, J. Chem. Phys. **100**, 13132 (1996).

[10] F. X. Witkowski, J. L. Leon, P. A. Penkoske, W. R. Giles, M. L. Spano, W. L. Ditto, and A. T. Winfree, Nature **392**, 78 (1998).

[11] R. A. Gray and J. Jalife, Chaos **8**, 65 (1998).

[12] A. T. Winfree, J. theor. Biol. **138**, 353 (1989).

[13] A. R. Mani, S. Montagnese, C. D. Jackson, C. W. Jenkins, I. M. Head, R. C. Stephens, K. P. Moore, and M. Y. Morgan, American Journal of Physiology - Gastrointestinal and Liver Physiology **296**, G330 (2009).

[14] M. P. Griffin and J. R. Moorman, Pediatrics **107**, 97 (2001).

[15] D. Kessler and H. Levine, (1993).

[16] I. Z. Kiss and J. L. Hudson, AIChE Journal **49**, 2234 (2003).

[17] M. S. Spach and J. P. Boineau, PACE **20**, 397 (1997).

[18] K. H. W. J. Ten Tusscher and A. V. Panfilov, Europace , 38 (2007).

[19] H. Zhang, C. J. Garratt, S. Kharche, and A. V. Holden, Physica D **238**, 976 (2009).

[20] R. F. Bosch, J. B. Grammer, V. Kühlkamp, and L. Seipel, Z. Kardiol. **89**, 795 (2000).

[21] R. Clayton, O. Bernus, E. Cherry, H. Dierckx, F. H. Fenton, L. Mirabella, A. V. Panfilov, F. B. Sachse, G. Seemann, and H. Zhang, Prog. Biophys. Mol. Biol. **104**, 22 (2011).

[22] G. W. Albers, J. E. Atwood, and J. Jirsh, Ann. Intern. Med. **115**, 727 (1991).

[23] M. D. Ezekowitz and J. A. Levine, J. Am. Med. Assoc. **281**, 1830 (1999).

[24] A. J. Camm, P. Kirchhof, G. Y. H. Lip, U. Schotten, I. Savelieva, S. Ernst, I. C. Van Gelder, N. Al-Attar, G. Hindricks, B. Prendergast, H. Heidbuchel, O. Alfieri, A. Angelini, D. Atar, P. Colonna, R. De Caterina, J. De Sutter, A. Goette, B. Gorenek, M. Heldal, S. H. Hohloser, P. Kolh, J.-Y. Le Heuzey, P. Ponikowski, and F. H. Rutten, Eur. Heart J. **31**, 2369 (2010).

[25] V. Fuster, L. E. Rydén, D. S. Cannom, H. J. Crijns, A. B. Curtis, K. A. Ellenbogen, J. L. Halperin, J.-Y. Le Heuzey, G. N. Kay, J. E. Lowe, S. B. Olsson, E. N. Prystowsky, J. L. Tamargo, S. Wann, S. C. Smith, A. K. Jacobs, C. D. Adams, J. L. Anderson, E. M. Antman, S. A. Hunt, R. Nishimura, J. P. Ornato, R. L. Page, B. Riegel, S. G. Priori, J.-J. Blanc, A. Budaj, A. J. Camm, V. Dean, J. W. Deckers, C. Despres, K. Dickstein, J. Lekakis, K. McGregor, M. Metra, J. Morais, A. Osterspey, and J. L. Zamorano, Europace **8**, 651 (2006).

[26] X. Gao, L. Dong, H. Wang, H. Zhang, Y. Liu, W. Fan, and Y. Pan, Phys. Plasmas **23**, 083526 (2016).

[27] B. P. Belousov, "Eine periodische reaktion und ihr mechanismus," (Verlag Harri Klein, Frankfurt am Main, 1981) pp. 73–82.

[28] B. P. Belousov, "Eine periodische oxydationsreaktion in flüssiger phase," (Verlag Harri Klein, Frankfurt am Main, 1964) pp. 83–89.

[29] S. Tobias and E. Knobloch, Phys. Rev. Lett. **80**, 4811 (1998).

[30] M. Bär and M. Eiswirth, Phys. Rev. E **48**, R1635 (1993).

[31] S. Jakubith, H. H. Rotermund, W. Engel, A. von Oertzen, and G. Ertl, Phys. Rev. Lett. **65**, 3013 (1990).

[32] G. Ertl, Science **254**, 1750 (1991).

[33] M. G. Clerc, D. Escaff, and V. M. Kenkre, Phys. Rev. E **72**, 056217 (2005).

[34] L. S. Schulman and P. E. Seiden, Science **233**, 425 (1986).

[35] V. Mendez and J. E. Llebot, Phys. Rev. E **56**, 6557 (1997).

[36] F. M. Schneider, E. Schöll, and M. A. Dahlem, Chaos **19**, 015110 (2009).

[37] G. F. Webb, J. Math. Anal. App. **84**, 150 (1981).

[38] J.-G. Barbara, Biochim. Biophys. Acta **1600**, 12 (2002).

[39] M. D. Graham, M. Bär, I. Kevrekidis, K. Asakura, J. Lauterbach, H.-H. Rotermund, and G. Ertl, Phys. Rev. E **52**, 76 (1995).

[40] J. Lechleiter, S. Girard, E. Peralta, and D. Clapham, Science **252**, 123 (1991).

[41] S. Kondo and R. Asai, Nature **376**, 765 (2002).

[42] J. D. Murray, *Mathematical Biology*, 2nd ed. (Springer, Berlin, 1993).

[43] J. D. Murray and M. R. Myerscough, J. theor. Biol. **149**, 339 (1991).

[44] H. Meinhardt and M. Klingler, J. theor. Biol. **126**, 63 (1987).

[45] P. W. Ingham, Nature **335**, 25 (1988).

[46] A. Runions, M. Fuhrer, B. Lane, P. Federl, A.-G. Rolland-Lagan, and P. Prusinkiewicz, ACM Trans. Graphics **24**, 702 (2005).

[47] J. M. Köhler and S. C. Müller, J. Phys. Chem. **99**, 980 (1995).

[48] D. Cocks, *Mathematical modelling of dune formation*, Ph.D. thesis, University of Oxford (2010).

[49] P. W. Barlow, J. S. Parker, and P. Brain, COSPAR **14**, 149 (1994).

[50] R. Hanke-Rauschenbach, S. Kirsch, R. Kelling, C. Weinzierl, and K. Sundmacher, J. Electrochem. Soc. **157**, B1521 (2010).

[51] A. E. Blanchard and T. Lu, BMC systems biology **9**, 59 (2015).

[52] I. Lymperopoulos and G. Ioannou, Evolving Systems **7**, 207 (2016).

[53] M. Yamaguchi, E. Yoshimoto, and S. Kondo, PNAS **104**, 4790 (2007).

[54] W. Koehler, *Musterbildung und Mustererkennung* (Haug Verlag, 1999).

[55] W. Ebeling, J. Freund, and F. Schweitzer, *Komplexe Strukturen, Entropie und Information* (Teubner Verlag, Stuttgart, 1998).

[56] S. Sick, S. Reinker, J. Timmer, and T. Schlake, Science **652** (2006).

[57] A. D. Economou, A. Ohazama, T. Porntaveetus, P. T. Sharpe, S. Kondo, M. A. Basson, A. Gritli-Linde, M. T. Cobourne, and J. B. A. Green, Nat. Genet. **44**, 348 (2012).

[58] E. J. Crampin, Com. on Theor. Biol. **6**, 229 (2001).

[59] I. Stoop, D. Lagrange, P. M. Terwagne, D. Reis, and J. Dunkel, Nature Materials **14**, 337 (2015).

[60] E. M. Azene, N. A. Trayanova, and E. Warman, Ann. Biomed. Eng. **29**, 35 (2001).

[61] D. Olmos-Liceaga, World Acad. Sci. Eng. Techn. **59**, 137 (2011).

[62] T.-J. Wu, M. Yashima, F. Xie, C. A. Athill, Y.-H. Kim, M. C. Fishbein, Z. Qu, A. Garfinkel, J. N. Weiss, H. S. Karagueuzian, and P.-S. Chen, Circ. Res. **83**, 448 (1998).

[63] J. D. Murray, C. R. Biologies **326**, 239 (2003).

[64] A. M. Zhabotinsky, S. C. Müller, and B. Hess, Chem. Phys. Lett. **172**, 445 (1990).

[65] C. Zhang, H. Zhang, Q. Ouyang, B. Hu, and G. Gunaratne, Phys. Rev. E **68**, 036202 (2003).

[66] H. Sevcikova and M. Malik, Physica D **9**, 140 (1983).

[67] C. Luengviriya, S. C. Müller, and M. J. B. Hauser, Phys. Rev. E **77**, 015201 (2008).

[68] J. Carballido-Landeira, V. K. Vanag, and I. R. Epstein, PCCP **12**, 3656 (2010).

[69] S. Alonso, R. Kapral, and M. Bär, Phys. Rev. Lett. **102**, 238302 (2009).

[70] S. Alonso, K. John, and M. Bär, J. Chem. Phys. **134**, 094117 (2011).

[71] V. K. Vanag and I. R. Epstein, Chaos **18**, 026107 (2008).

[72] V. Zykov and K. Showalter, Phys. Rev. Lett. **94**, 068302 (2005).

[73] Y. Kobayashi and H. Kori, New J. Phys. **11**, 033018 (2009).

[74] V. Zykov, H. Brandtstädter, G. Bordiougov, and H. Engel, Phys. Rev. E **72**, 065201 (2005).

[75] R. A. Gray, Chaos **12**, 941 (2002).

[76] J. Schlesner, V. S. Zykov, H. Brandtstädter, I. Gerdes, and H. Engel, New J. Phys. **10**, 015003 (2008).

[77] K. Agladze, M. W. Kay, V. Krinsky, and N. Sarvazyan, Am. J. Physiol. Heart Circ. Physiol. **20037** (2011).

[78] F. Xie, Z. Qu, A. Garfinkel, and J. N. Weiss, Am. J. Physiol. Heart Circ. Physiol. **280**, H535 (2001).

[79] M. F. Crowley and I. R. Epstein, J. Chem. Phys. **93**, 2496 (1989).

[80] J. M. Davidenko, R. Salomonsz, A. M. Pertsov, W. T. Baxter, and J. Jalife, Circ. Res. **77**, 1166 (1995).

[81] E. P. Zemskov, K. Kassner, and M. J. B. Hauser, Phys. Rev. E **77**, 036219 (2008).

[82] J. H. E. Cartwright, Phys. Rev. E **62**, 1149 (2000).

[83] D. Horváth, S. Tóth, and Á. Tóth, Phys. Rev. Lett. **97**, 194501 (2006).

[84] K. Showalter and I. R. Epstein, Chaos **25**, 097613 (2015).

[85] S. Kondo and T. Miura, Science **329**, 1616 (2010).

[86] E. Meron, Phys. Reports **218**, 1 (1992).

[87] F. M. Weber, *Personalizing Simulations of the Human Atria*, Dissertation, Karlsruher Institut für Technologie (2011).

[88] H. J. Jongsma and R. Wilders, Circ. Res. **86**, 1193 (2000).

[89] A. G. Kléber and Y. Rudy, Physiol. Rev. **84**, 431 (2004).

[90] M. B. Rook, A. C. van Ginneken, B. de Jonge, A. el Aoumari, D. Gros, and H. J. Jongsma, Am. J. Physiol. **263**, C959 (1992).

[91] R. H. Hoyt, M. L. Cohen, and J. E. Saffitz, Circ. Res. **64**, 563 (1989).

[92] D. D. J. Streeter, H. M. Spotnitz, D. P. Patel, J. J. Ross, and E. H. Sonnenblick, Circ. Res. **24**, 339 (1969).

[93] W. J. Hucker, C. M. Ripplinger, C. P. Fleming, V. V. Fedorov, A. M. Rollins, and I. R. Efimov, J. Biomed. Optics **13**, 054012 (2008).

[94] G. B. Sands, D. A. Gerneke, D. A. Hooks, C. R. Green, B. H. Smaill, and I. J. Legrice, Microsc. Res. Tech. **67**, 227 (2005).

[95] R. M. Smith, A. Matiukas, C. W. Zemlin, and A. M. Pertsov, Microsc. Res. Tech. **71**, 510 (2008).

[96] R. H. Anderson and S. Y. Ho, J. Cardiovasc. Electrophysiol. **9**, 1233 (1998).

[97] J. A. Cabrera, D. Sanchez-Quintana, S. Y. Ho, A. Medina, and R. H. Anderson, J. Cardio-vasc. Electrophysiol. **9**, 1186 (1998).

[98] S. H. Gilbert, A. P. Benson, P. Li, and A. V. Holden, Eur. J. Cardiothor. Surg. **32**, 231 (2007).

[99] S. Y. Ho, R. H. Anderson, and D. Sanchez-Quintana, Cardiovasc. Res. **54**, 325 (2002).

[100] C. Zywietz, Brit. Med. J. **1**, 720 (1950).

[101] T. Hennig, P. Maass, J. Hayano, and S. Heinrichs, J. Biol. Phys. **32**, 383 (2006).

[102] W. Zeng and L. Glass, Phys. Rev. E **54**, 1779 (1996).

[103] M. A. Allessie, P. A. Boyden, A. J. Camm, A. G. Kléber, M. J. Lab, M. J. Legato, M. R. Rosen, P. J. Schwartz, P. M. Spooner, D. R. V. Wagoner, and A. L. Waldo, Circ. **103**, 769 (2001).

[104] S. Nattel, Nature **415**, 219 (2002).

[105] T. Lewis and H. G. Schleiter, Heart **3**, 173 (1912).

[106] T. Lewis, A. N. Drury, and C. C. Iliescu, Heart **8**, 361 (1921).

[107] T. W. Engelmann, Arch. Gesamte Psychol. **62**, 543 (1896).

[108] H. Winterberg, Z. Exp. Pathol. Ther. **3**, 182 (1906).

[109] C. J. Rothberger and H. Winterberg, Pflugers Arch Gesamte Physiol. Menschen Tiere **160**, 42 (1915).

[110] W. E. Garrey, Physiol. Rev. **4**, 215 (1924).

[111] G. R. Mines, J. Physiol. **46**, 349 (1913).

[112] G. K. Moe and J. A. Abildskov, Am. Heart J. **58**, 59 (1959).

[113] G. K. Moe, W. C. Rheinboldt, and J. A. Abildskov, Am. Heart J. **67**, 200 (1964).

[114] M. A. Allessie, W. Lammers, and F. Bonke (Grune and Stratton Inc., New York, 1985) pp. 265–275.

[115] P. Jais, M. Haisaguerre, D. C. Shah, S. Chouairi, L. Gencel, M. Hocini, and J. Clementy, Circ. **95**, 572 (1997).

[116] M. Haisaguerre, P. Jais, D. C. Shah, A. Takahashi, M. Hocini, G. Quiniou, S. Garrigue, A. Le Mouroux, P. Le Métayer, and J. Clémenty, N. Engl. J. Med. **339**, 659 (1998).

[117] D. Li, T. K. Leung, and S. Nattel, Circ. **98**, I209 (1998).

[118] K. Matsuo, Y. Tomita, K. Uno, C. M. Khrestian, and A. L. Waldo, Circ. **98**, I209 (1998).

[119] A. Bueno-Orovio, E. M. Cherry, and F. H. Fenton, J. theo. biol. **253**, 544 (2008).

[120] C. Lenk, F. M. Weber, M. Bauer, M. Einax, P. Maass, and G. Seemann, J. Theor. Biol. **366**, 13 (2015).

[121] G. Seemann, P. Carillo, D. L. Weiss, M. W. Krueger, O. Dössel, and E. P. Scholz (2009) p. 144.

[122] Y. Ruan, N. Liu, and S. G. Priori, Nat. Rev. Cardiol. **6**, 337 (2009).

[123] D. F. Gudbjartsson, D. O. Arnar, A. Helgadottir, S. Gretarsdottir, H. Holm, A. Sigurdsson, A. Jonasdottir, A. Baker, G. Thorleifsson, K. Kristjansson, A. Palsson, T. Blondal, P. Sulem, V. M. Backman, G. A. Hardarson, E. Palsdottir, A. Helgason, R. Sigurjonsdottir, J. T. Sverrisson, K. Kostulas, M. C. Y. Ng, L. Baum, W. Y. So, K. S. Wong, J. C. N. Chan, K. L. Furie, S. M. Greenberg, M. Sale, P. Kelly, C. A. MacRae, E. E. Smith, J. Rosand, J. Hillert, R. C. W. Ma, P. T. Ellinor, G. Thorgeirsson, J. R. Gulcher, A. Kong, U. Thorsteinsdottir, and K. Stefansson, Nature **448**, 353 (2007).

[124] D. G. Katritsis, Europ. Heart J. **27**, 886 (2006).

[125] C. J. Boos and G. Y. H. Lip, Heart **94**, 133 (2008).

[126] A. W. Teh, J. M. Kalman, G. Lee, C. Medi, P. M. Heck, L.-H. Ling, S. Kumar, S. J. Spence, J. B. Morton, and P. M. Kistler, Europace **14**, 46 (2012).

[127] R. B. Neuman, I. Bloom, H. L. Shukrullah, L. A. Darrow, D. Kleinbaum, D. P. Jones, and S. C. J. Dudley, Clin. Chem. **53**, 1652 (2007).

[128] A. M. De Jong, A. H. Maass, S. U. Oberdorf-Maass, D. J. Van Veldhuisen, W. H. Van Gilst, and I. C. Van Gelder, Cardiovasc. res. **89**, 754 (2011).

[129] A. Isomura, M. Hörning, K. Agladze, and K. Yoshikawa, Phys. Rev. E **78**, 066216 (2008).

[130] A. T. Stamp, G. V. Osipov, and J. J. Collins, Chaos **12**, 931 (2002).

[131] R. Schuessler, J. Cardiovasc. Electrophysiol. **12**, 875 (2001).

[132] P. Jais, M. Haissaguerre, D. C. Shah, S. Chouairi, L. Gencel, M. Hocini, and J. Clémenty, Circ. **95**, 572 (1997).

[133] A. Harada, K. Sasaki, T. Fukushima, M. Ikeshita, T. Asano, S. Yamauchi, S. Tanaka, and T. Shoji, Ann. Thorac. Surg. **61**, 104 (1996).

[134] T. Sueda, H. Nagata, H. Shikata, K. Orihashi, S. Morita, M. Sueshiro, K. Okada, and Y. Matsuura, Ann. Thorac. Surg. **62**, 1796 (1996).

[135] J. Sahadevan, R. Kyungmoo, L. Peltz, C. M. Khrestian, R. W. Stewart, A. H. Markowitz, and A. L. Waldo, Circ. **110**, 3293 (2004).

[136] P. Sanders, O. Berenfeld, M. Hocini, P. Jais, R. Vaidyanathan, L.-F. Hsu, S. Garrigue, Y. Takahashi, M. Rotter, F. Sacher, C. Scavee, R. Ploutz-Snyder, J. Jalife, and M. Haisaguerre, Circ. **112**, 789 (2005).

[137] R. Mandapati, A. Skanes, J. Chen, O. Berenfeld, and J. Jalife, Circ. **101**, 194 (2000).

[138] J. Chen, R. Mandapati, O. Berenfeld, A. C. Skanes, R. A. Gray, and J. Jalife, Cardiovasc. Res. **48**, 220 (2000).

[139] A. Skanes, R. Mandapati, O. Berenfeld, J. Davidenko, and J. Jalife, Circ. **98**, 1236 (1998).

[140] C. A. Morillo, G. J. Klein, D. L. Jones, and C. M. Guiraudon, Circ. **91**, 1588 (1995).

[141] R. Yoshida, Sensors **10**, 1810 (2010).

[142] C. Zong, Q. Gao, Y. Wang, J. Feng, S. Mao, and L. Zhang, Sci. in China B **50**, 205 (2007).

[143] A. Arneodo, F. Argoul, J. Elezgaray, and P. Richetti, Physica D **62**, 134 (1993).

[144] A. M. Zhabotinsky and A. B. Rovinsky, J. Stat. Phys. **48**, 959 (1987).

[145] K. Agladze, V. I. Krinsky, and A. M. Pertsov, Nature **308**, 834 (1984).

[146] I. R. Epstein, J. a. Pojman, and O. Steinbock, Chaos **16**, 037101 (2006).

[147] N. Manz and O. Steinbock, Chaos **16**, 037112 (2006).

[148] V. K. Vanag and I. R. Epstein, PNAS **100**, 14635 (2003).

[149] C. Qiao, Y. Wu, X. Lu, C. Wang, Q. Ouyang, and H. Wang, Chaos **18**, 026109 (2008).

[150] C. Luengviriya, U. Storb, G. Lindner, S. Müller, M. Bär, and M. Hauser, Phys. Rev. Lett. **100**, 148302 (2008).

[151] T. Bánsági, V. K. Vanag, and I. R. Epstein, Science **331**, 1309 (2011).

[152] S. Alonso, F. Sagues, and A. S. Mikhailov, Science **299**, 1722 (2003).

[153] A. T. Winfree, Science **266**, 1003 (1994).

[154] R. Yoshida, E. Kokufuta, T. Yamaguchi, and H. Ichijo, J. Am. Chem. Soc. **118**, 5134 (1996).

[155] R. Yoshida, E. Kokufuta, T. Yamaguchi, and H. Ichijo, Chaos **9**, 260 (1999).

[156] R. J. Field and R. M. Noyes, Nature **237**, 390 (1972).

[157] R. J. Field and R. M. Noyes, J. Chem. Phys. **60**, 1877 (1974).

[158] R. J. Field, E. Koros, and R. M. Noyes, JACS **94**, 8649 (1972).

[159] M. Woltering, *Chaos und Turbulenz in der Belousov-Zhabotinsky-Reaktion*, Dissertation, Universität Dortmund (2001).

[160] M. Woltering and M. Markus, Phys. Rev. E **64**, 045601 (2001).

[161] M. Vinson, S. Mironov, S. Mulvey, and A. Pertsov, Nature **386**, 477 (1997).

[162] R. J. Field and R. M. Noyes, J. Am. Chem. Soc. **96**, 2001 (1974).

[163] W. Sontag, Bioelectromagnetics **27**, 314 (2006).

[164] A. M. Zhabotinsky, L. Gyorgyi, M. Dolnik, and I. R. Epstein, J. Phys. Chem. **98**, 7981 (1994).

[165] O. Steinbock and Müller, Phys. Rev. E **47**, 1506 (1993).

[166] H. Kitahata, K. Fujio, J. Gorecki, S. Nakata, Y. Igarashi, A. Gorecka, and K. Yoshikawa, J. Phys. Chem. A **113**, 10405 (2009).

[167] J. Gorecka and J. Gorecki, PCCP **7**, 2915 (2005).

[168] I. R. Epstein, I. B. Berenstein, M. Dolnik, V. K. Vanag, L. Yang, and A. M. Zhabotinsky, Phil.l trans. A **366**, 397 (2008).

[169] A. J. Steele, M. Tinsley, and K. Showalter, Chaos **18**, 026108 (2008).

[170] S. Steinbock and S. C. Müller, "Control and perturbation of wave propagation in excitable systems," (Cambridge University Press, Cambridge, UK, 2000) pp. 387–408.

[171] A. Toth, V. Gaspar, and K. Showalter, J. Phys. Chem. **98**, 522 (1994).

[172] S. Martens, J. Löber, and H. Engel, Phys. Rev. E **91**, 022902 (2015).

[173] T. Yamaguchi, L. Kuhnert, Z. Nagy-Ungvarai, S. C. Mueller, and B. Hess, J. Phys. Chem. **95**, 5831 (1991).

[174] O. Steinbock, P. Kettunen, and K. Showalter, Science **269**, 1857 (1995).

[175] K. Suzuki, T. Yoshinobu, and H. Iwasaki, Jpn. J. Appl. Phys. **38**, 345 (1999).

[176] K. Suzuki, T. Yoshinobu, and H. Iwasaki, J. Phys. Chem. A **104**, 5154 (2000).

[177] H. Fukuda, N. Tamari, H. Morimura, and S. Kai, J. Phys. Chem. A **109**, 11250 (2005).

[178] H. Fukuda, H. Morimurab, and S. Kai, Physica D **80**, 205 (2005).

[179] J. N. Gorecka, J. Gorecki, and Y. Igarashi, J. Phys. Chem. A **111**, 885 (2007).

[180] J. Gorecka and J. Gorecki, TJ. Chem. Phys. **124**, 084101 (2006).

[181] R. Toth, A. F. Taylor, and M. R. Tinsley, J. Phys. Chem. B **110**, 10170 (2006).

[182] W. Wang, I. Z. Kiss, and J. L. Hudson, Chaos **10**, 248 (2000).

[183] V. K. Vanag and I. R. Epstein, PCCP **11**, 897 (2009).

[184] A. Malevanets and R. Kapral, Phys. Rev. E **55**, 5657 (1997).

[185] P. Kohl, D. Noble, R. Winslow, and P. J. Hunter, Philos. Trans. R. Soc. A **358**, 579 (2000).

[186] D. Noble, Bioessays **24**, 1155 (2002).

[187] A. L. Hodgkin and A. F. Huxley, J. Physiol. **117**, 500 (1952).

[188] Y. Jiang, A. Lee, J. Chen, V. Ruta, M. Cadene, B. T. Chait, and R. MacKinnon, Nature **423**, 33 (2003).

[189] Y. Jiang, V. Ruta, J. Chen, A. Lee, and R. MacKinnon, Nature **423**, 42 (2003).

[190] M. Courtemanche, R. J. Ramirez, and S. Nattel, Am. J. Physiol. **275**, H301 (1998).

[191] A. Nygren, C. Fiset, L. Firek, J. W. Clark, D. S. Lindblad, R. B. Clark, and W. R. Giles, Circ. Res. **82**, 63 (1998).

[192] M. M. Maleckar, J. L. Greenstein, N. A. Trayanova, and W. R. Giles, Prog. Biophys. Mol. Biol. **98**, 161 (2008).

[193] J. T. Koivumaki, T. Korhonen, and P. Tavi, PLoS Comput. Biol. **7**, e100106 (2011).

[194] E. Grandi, S. V. Pandit, N. Voigt, A. J. Workman, D. Dobrev, and J. Jalife, Circ. Res. **109**, 1055 (2011).

[195] C. H. Luo and Y. Rudy, Circ. Res. **68**, 1501 (1991).

[196] D. Noble, J. Physiol. **160**, 317 (1962).

[197] I. Prigogine and R. Lefever, J. Chem. Phys. **48**, 1695 (1968).

[198] A. B. Rovinsky, J. Phys. Chem. **90**, 1984 (1986).

[199] J. X. Zhang and R. Datta, J. Electrochem. Soc. **152**, A1180 (2005).

[200] K. Krischer, M. Eiswirth, and G. Ertl, J. Chem. Phys. **96**, 9161 (1992).

[201] R. Fitzhugh, J. gen. physiol. **43**, 867 (1960).

[202] R. Fitzhugh, Biophysi. J. **1**, 446 (1961).

[203] B. van der Pol, Phil. Mag. **2**, 978 (1926).

[204] M. Cross and P. Hohenberg, Rev.Mod. Phys. **65**, 851 (1993).

[205] A. Gierer and H. Meinhardt, Kybernetik **12**, 30 (1972).

[206] R. R. Aliev and A. V. Panfilov, Chaos, Solitons & Fractals **7**, 293 (1996).

[207] A. Pertsov, E. Ermakova, and A. Panfilov, Physica D **14**, 117 (1984).

[208] D. Barkley, Physica D **49**, 61 (1991).

[209] R. D. Simitev and V. N. Biktashev, Biophys. J. **90**, 2258 (2006).

[210] O. C. Zienkiewicz and Y. K. Cheung, *The Finite Element Method in Structural and Continuum Mechanics* (McGraw Hill, 1967).

[211] A. Zimmer and P. Groth, *Elementmethode der Elastostatik* (Oldenburg Verlag, München, 1969).

[212] G. Seemann, F. Sachse, M. Karl, D. Weiss, V. Heuveline, and O. Doessel, "Framework for modular, flexible and efficient solving the cardiac bidomain equations using petsc," (Springer, Berlin, Heidelberg, 2010) p. 363.

[213] S. Balay, S. Abhyankar, M. F. Adams, J. Brown, P. Brune, K. Buschelman, L. Dalcin, V. Eijkhout, W. D. Gropp, D. Kaushik, M. G. Knepley, L. C. McInnes, K. Rupp, B. F. Smith, S. Zampini, H. Zhang, and H. Zhang, "PETSc Web page," `http://www.mcs.anl.gov/petsc` (2016).

[214] S. Balay, S. Abhyankar, M. F. Adams, J. Brown, P. Brune, K. Buschelman, L. Dalcin, V. Eijkhout, W. D. Gropp, D. Kaushik, M. G. Knepley, L. C. McInnes, K. Rupp, B. F. Smith, S. Zampini, H. Zhang, and H. Zhang, *PETSc Users Manual*, Tech. Rep. ANL-95/11 - Revision 3.7 (Argonne National Laboratory, 2016).

[215] S. Balay, W. D. Gropp, L. C. McInnes, and B. F. Smith, in *Modern Software Tools in Scientific Computing*, edited by E. Arge, A. M. Bruaset, and H. P. Langtangen (Birkhäuser Press, 1997) pp. 163–202.

[216] T. Ikeda, M. Yashima, T. Uchida, D. Hough, and M. C. Fishbein, Circ. Res. **81**, 753 (1997).

[217] S. Iravanian, Y. Nabutovsky, C.-R. Kong, S. Saha, N. Bursac, and L. Tung, Am. J. Physiol. Heart Circ. Physiol. **285**, H449 (2003).

[218] T. Ikeda, L. Czer, A. Trento, C. Hwang, J. J. C. Ong, D. Hough, M. C. Fishbein, W. J. Mandel, H. S. Karagueuzian, and P.-S. Chen, Circ. **96**, 3013 (1997).

[219] S. Y. Ho, R. H. Anderson, and D. Sánchez-Quintana, Cardiovasc. res. **54**, 325 (2002).

[220] V. Markides, R. J. Schilling, S. Y. Ho, A. W. C. Chow, D. W. Davies, and N. S. Peters, Circ. **107**, 733 (2003).

[221] R. Lemery, L. Soucie, B. Martin, A. S. L. Tang, and J. Green, M.and Healey, Circ. **110**, 2083 (2004).

[222] F. X. Roithinger, J. Cheng, A. SippensGroenewegen, R. J. Lee, L. A. Saxon, M. M. Scheinman, and M. D. Lesh, Circulation **100**, 1791 (1999).

[223] M. Chauvin, D. C. Shah, M. Haissaguerre, L. Marcellin, and C. Brechenmacher, Circulation **101**, 647 (2000).

[224] C. Lenk, C. Mattea, S. Stapf, and J. M. Köhler, J. Por. Mat. , 1 (2016).

[225] A. Pikovsky, M. Rosenblum, and J. Kurths, in *Cambridge Nonlinear Science Series 12*, edited by B. Chirikov, P. Cvitanovic, F. Moss, and H. Swinney (Cambridge, 2001).

[226] K. Agladze, J. P. Keener, S. C. Müller, and A. Panfilov, Science **264**, 3 (1994).

[227] C. Cabo, A. M. Pertsov, J. M. Davidenko, W. T. Baxter, R. A. Gray, and J. Jalife, Biophys. J. **70**, 1105 (1996).

[228] J. M. Starobin, Y. I. Zilberter, E. M. Rusnak, and C. F. Starmer, Biophys. J. **70**, 581 (1996).

[229] C. Cabo, A. M. Pertsov, J. M. Davidenko, and J. Jalife, Chaos **8**, 116 (1998).

[230] M. Wilhelms, H. Hettmann, M. M. Maleckar, J. T. Koivumäki, O. Dössel, and G. Seemann, Front. Physiol. **3**, 487 (2012).

[231] S. M. Narayan, D. E. Krummen, K. Shivkumar, P. Clopton, W.-J. Rappel, and J. M. Miller, J. Am. Coll. Cardiol. **60**, 628 (2012).

[232] J. Jalife, O. Berenfeld, and M. Mansour, Cardiovasc. res. **54**, 204 (2002).

[233] R. A. Gray, A. M. Pertsov, and J. Jalife, Circ. **94**, 2649 (1996).

[234] A. C. Skanes, R. Mandapati, O. Berenfeld, J. M. Davidenko, and J. Jalife, Circ. **98**, 1236 (1998).

[235] V. S. Zykov, Biofizika **25**, 888 (1980).

[236] M. Wellner and A. M. Pertsov, Phys. Rev. E **55**, 7656 (1997).

[237] C. Cabo, A. M. Pertsov, W. T. Baxter, J. M. Davidenko, R. A. Gray, and J. Jalife, Circ. Res. **75**, 1014 (1994).

[238] V. S. Zykov and O. L. Morozova, Biophysics **24**, 739 (1979).

[239] V. G. Fast and a. G. Kléber, Cardiovasc. res. **33**, 258 (1997).

[240] V. V. Fedorov, R. Chang, A. V. Glukhov, G. Kostecki, D. Janks, R. B. Schuessler, and I. R. Efimov, Circ. **122**, 782 (2010).

[241] I. Efimov, V. V. Fedorov, B. Joung, and S.-F. Lin, Circ. Res. **106**, 255 (2010).

[242] A. Elvan, K. Wylie, and D. P. Zipes, Circ. , 2953 (1996).

[243] O. Berenfeld, A. Zaitsev, V. S. F. Mironov, A. M. Pertsov, and J. Jalife, Circ. Res. **90**, 1173 (2002).

[244] P. Kuklik and J. J. Zebrowski, Chaos **15**, 033301 (2005).

[245] O. Berenfeld, Arch. Cardiol. Mex. **80**, 301 (2010).

[246] D. De La Fuente, B. Sasyniuk, and G. K. Moe, Circ. **44**, 803 (1971).

[247] H. Calkins, J. Brugada, D. L. Packer, R. Cappato, S.-A. Chen, H. J. G. Crijns, R. J. Damiano, D. W. Davies, D. E. Haines, M. Haissaguerre, Y. Iesaka, W. Jackman, P. Jais, H. Kottkamp, K. H. Kuck, B. D. Lindsay, F. E. Marchlinski, P. M. McCarthy, J. L. Mont, F. Morady, K. Nademanee, A. Natale, C. Pappone, E. Prystowsky, A. Raviele, J. N. Ruskin, and R. J. Shemin, Europace **9**, 335 (2007).

[248] R. J. Schilling, N. S. Peters, and D. W. Davies, Circ. **98**, 887 (1998).

[249] J. W. Papez, Am J Anat. **27**, 0255 (1920).

[250] C. Mendez, W. J. Mueller, and X. Urguiaga, Circ. Res. **26**, 135 (1970).

[251] C. Lenk, M. Einax, and P. Maass, Phys. Rev. E **87**, 042904 (2013).

[252] N. M. Shnerb, Y. Louzoun, E. Bettelheim, and S. Solomon, Proc. Nat. Acad. Sci. **97**, 10322 (2000).

[253] J. P. Keener, SIAM J. App. Math. **47**, 556 (1987).

[254] P. M. Dean and E. K. Matthews, Nature **219**, 389 (1968).

[255] M. Perez-Armendariz, C. Roy, D. C. Spray, and M. V. Bennett, Biophys. J. **59**, 76 (1991).

[256] M. Tinsley, A. Taylor, Z. Huang, and K. Showalter, Phys. Rev. Lett. **102**, 158301 (2009).

[257] S. Tanabe and K. Pakdaman, Biol. Cybern. **85**, 269 (2001).

[258] D. E. Postnov, S. K. Han, T. G. Yim, and O. V. Sosnovtseva, Phys. Rev. E **59**, R3791 (1999).

[259] S. Kadar, J. Wang, and K. Showalter, Nature **391**, 770 (1998).

[260] S. Alonso, I. Sendina-Nadal, V. Perez-Munuzuri, J. M. Sancho, and F. Sagues, Phys. Rev. Lett. **87**, 078302 (2001).

[261] M. A. Zaks, A. B. Neiman, S. Feistel, and L. Schimansky-Geier, Phys. Rev. E **68**, 066206 (2003).

[262] V. K. Vanag and I. R. Epstein, Phys. Rev. E **84**, 066209 (2011).

[263] R. Toth and A. F. Taylor, J. Chem. Phys. **125**, 224708 (2006).

[264] A. F. Taylor, P. Kapetanopoulos, B. J. Whitaker, R. Toth, L. Bull, and M. R. Tinsley, Eur. Phys. J. Spec. Top. **165**, 137 (2008).

[265] A. T. Winfree, Science **298**, 2336 (2002).

[266] D. E. Postnov, O. V. Sosnovtseva, P. Scherbakov, and E. Mosekilde, Chaos **18**, 1 (2008).

[267] K. Yoshikawa, R. Aihara, and K. Agladze, J. Phys. Chem. A **102**, 7649 (1998).

[268] J. Maselko, J. S. Reckley, and K. Showalter, J. Phys. Chem. **93**, 2775 (1989).

[269] A. Taylor, P. Kapetanopoulos, B. Whitaker, R. Toth, L. Bull, and M. Tinsley, Phys. Rev. Lett. **100**, 214101 (2008).

[270] A. F. Taylor, M. R. Tinsley, F. Wang, and K. Showalter, Angew. Chemie **50**, 10161 (2011).

[271] Y. Kuramoto and D. Battogtokh, arXiv preprint cond-mat/0210694 (2002).

[272] Y. Kuramoto, Physica D **50**, 15 (1991).

[273] S. H. Strogatz, Physica D **143**, 1 (2000).

[274] M. Perez-Armendariz, C. Roy, D. C. Spray, and M. V. L. Bennett, Biophys. J. **59**, 76 (1991).

[275] W. Zou, D. V. Senthilkumar, R. Nagao, I. Z. Kiss, Y. Tang, A. Koseska, J. Duan, and J. Kurths, Nature Comm. **6**, 7709 (2015).

[276] M. Desroches, J. Guckenheimer, B. Krauskopf, C. Kuehn, H. Osinga, and M. Wechselberger, SIAM Rev. **54**, 211 (2010).

[277] M. J. B. Hauser and J. A. C. Gallas, J. Phys. Chem. Lett. **5** (2014).

[278] D. Bakes, L. Schreiberová, I. Schreiber, and M. J. B. Hauser, Chaos **18**, 015102 (2008).

[279] M. Brøns, T. J. Kaper, and H. G. Rotstein, Chaos **18** (2008).

[280] R. Morgan, M. A. Colman, H. Chubb, G. Seemann, and O. V. Aslanidi, Front Physiol. **7**, 474 (2016).

[281] G. Bub, A. Shrier, and L. Glass, Phys. Rev. Lett. **94**, 8 (2005).

[282] B. Neumann, Z. Nagy-Ungvarai, and S. C. Müller, Chem. Phys. Lett. **211**, 36 (1993).

[283] D. M. Lombardo, F. H. Fenton, S. M. Narayan, and W.-J. Rappel, PLOS Comp. Biol. **12**, e1005060 (2016).

[284] N. Marwan, M. Carmenromano, M. Thiel, and J. Kurths, Phys. Rep. **438**, 237 (2007).

[285] P. Babinec, M. Kučera, and M. Babincová, Harm. Fract. Im. Anal. **3**, 87 (2005).

Part IV: Appendix

Recurrence plots and fractal dimension

Recurrence plots (RP) are a graphical representation method for certain properties of dynamical systems. In particular, the recurrence of the system in certain states like action potentials can be studied. The calculation of recurrence plots is based on the evaluation of the distance between two points $\Delta u(t, t') = u(t') - u(t)$, which correspond to different time steps of the time series $u(t)$. For so-called unthresholded RP (UTRP) this distance is plotted colour-coded with t as the x axis and t' as the y axis. For the presentations, which are typically called recurrence plots, a threshold u_c[1] is chosen and points are designated the colour black or white, depending on the their relation to the threshold, i.e. RP$= 1$ (black) for $\Delta u < u_c$ or RP $= 0$ (white) else. The distribution of the black points yields information about, amongst others, the determinism of the analysed system and the noise, as described for example in [284].

One method to quantify this distribution is to determine the fractal dimension of black regions, for example, by a box-counting algorithm. The fractal dimension gives the relation between the change of the value of one property, e.g. length, in dependence on the scale used to quantify this property. The application of the fractal dimension of recurrence plots was demonstrated, for example, by Babinec *et* al. [285] for analysing ECG data, who observed a smaller fractal dimension for older people in comparison to younger ones.

The box-counting algorithm is based on the fractionation of the curve, here the black-and-white RP, into boxes and the subsequent counting of boxes needed to cover the black regions. This is done for different sizes of the boxes, corresponding to different scales for measuring the black regions. For a fractal object, the number of boxes N in dependence of their size r is given by

$$N(r) = Cr^D, \tag{.0.1}$$

with the constant C and the fractal dimension D. The fractal dimension is determined according to

$$D = -\frac{\log(N(r))}{\log(r)}. \tag{.0.2}$$

[1]The threshold u_c is often chosen to be 10% of the maximal Δu

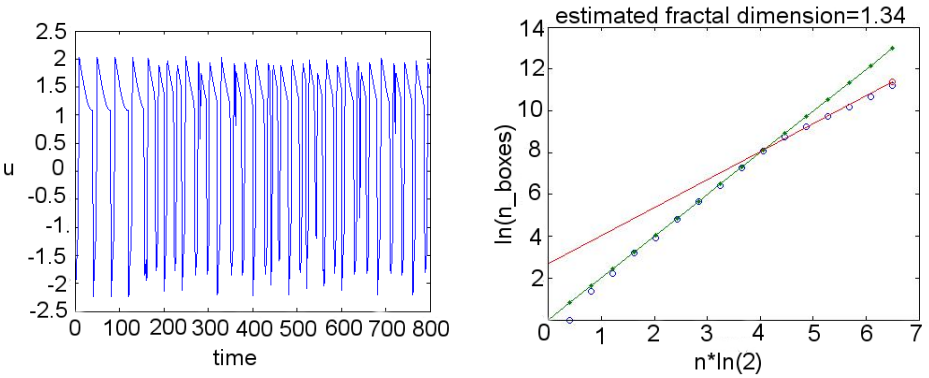

Figure 1: *Left:* Time series from FHN model. *Right:* Determination of fractal dimension of this time series as increase of $D = \log(n_{Boxes})/(n \log(2))$, where n is the number of reductions steps and n_{Boxes} describes the number of the boxes for covering the black part of the RP. Blue circles correspond to the determined number of boxes per box size. The green curve represents a fractal dimension of two (for an area) and the red line is the fit for determining D. Here $D = 1.34$.

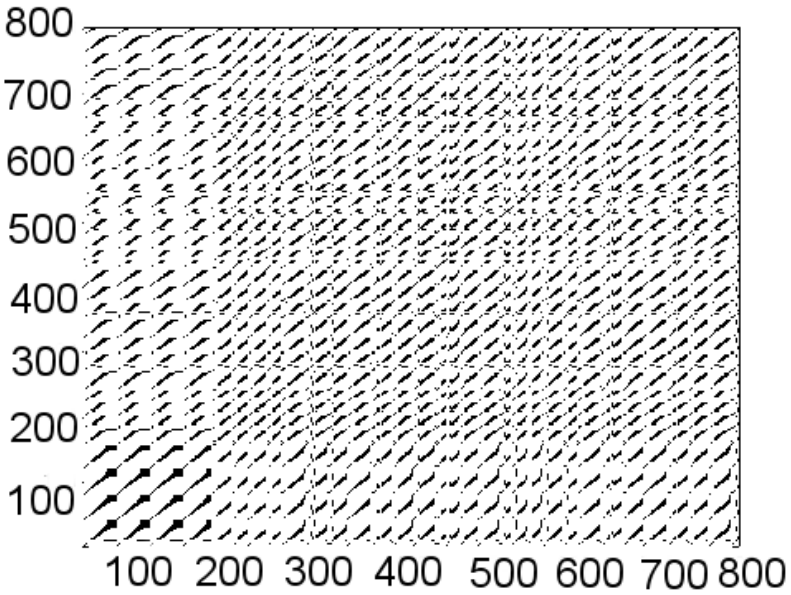

Figure 2: Thresholded recurrence plot of the time series (with itself) in Fig. 1.

In Fig. 1 the logarithm of the number of boxes N, which contain black regions, are plotted against the corresponding step $n \log(2)$ of reduction of box size for 13 steps. At the beginning, for large boxes, the slope is equal to two, corresponding to a division of the boxes into halves and still all boxes containing a section of the black pattern. In this case, the boxes are much larger than the pattern to be covered. The slope of 2 corresponds to the fractal dimension of an area or plane, 1 to a linear curve and 3 to a volume

(as a sphere). For very small boxes a slope of 0 is observed. Thereby, the size of the boxes is smaller than the resolution of the structure. The fractal dimension of the structure corresponds to the value of the slope between these two ranges.

Two different algorithms for determination of the fractal dimension are applied, both usable with Matlab. On the one hand, the *'boxcount'* toolbox from F. Moisy (Uni. Paris Sud). This toolbox just needs the image (RP) as input but it does not allow to modify the settings as the step size of box size reduction. This results sometimes in a too small number of data points in the region of small boxes, where the fractal dimension is determined. On the other hand, the *'boxcount'* toolbox from B. Flemisch (Uni. Stuttgart TU) was tested. Here, the number n of reduction steps can be set. Since the slope changes with the reduction steps, as described above, the routine used for fitting the curve and determining the slope has to be optimized to obtain the right value for the fractal dimension.

Analogously to the distribution of local frequencies, the Shannon entropy can be calculated from the distribution of fractal dimension as another measure for the regularity of the excitation patterns. The order parameter s_{fd} can be determined according to

$$s_{fd} = -\frac{\sum_{l=1}^{N_\mathrm{b}} \tilde{p}_l \ln \tilde{p}_l}{\ln N_\mathrm{b}} \tag{.0.3}$$

with $\tilde{p}_l$ being the probability to observe the fractal dimension in a pre-defined interval (analogue to the definition of the frequency distribution). Correspondingly, a broader distribution results in higher values of s_{fd}, describing less regular patterns.